Study of Cu-based Cathode Materials for High-energy All-solid-state Fluoride-ion Batteries

Datong Zhang

Study of Cu-based Cathode Materials for High-energy All-solid-state Fluoride-ion Batteries

Datong Zhang

Graduate School of Human and Environmental Studies

Kyoto University

Supervised by

Prof. Dr. Yoshiharu Uchimoto

Contents

Chapter 1 General Introduction

1.1 Background

Large-scale application of traditional fossil fuels has given considerably contributed to the modernization of our society, and it has facilitated industrial civilization represented by combustion engines.[1-5] However, inefficient and unplanned mining and burning of these fossil fuels have led to severe environmental pollution that threatens general ecosystem. The large amounts of carbons deposited over millions of years are rapidly released to the atmosphere, leading to significant global warming and climate crisis such as frequent extreme weathers and sea level rise. To save energy, reduce emissions, and protect the environment, academic and industrial circles are concentrating on the development of new energy sources as replacements for fossil fuels.

The development of new and clean energy devices can be important for large developing economies, including China, Brazil, and southeast Asian nations, etc., who are facing intense challenges in balancing the rate and quality of economic growth. For instance, China, as the largest developing country, has been making her contribution for global environment-protection movements. At the general debate of the 75th session of UN General Assembly, Chinese President Xi Jinping officially annouced that China will strive to reach peak CO_2 emissions before 2030 and achieve carbon neutrality before 2060.[6] To accomplish this significant goal, one of the most important policies is to establish new industries related to new energy devices and firmly supressed the use of conventional fuel vehicles.[1-3] Motivated by the goal of "innovative, coordinated, green, open, and shared development",[7] China is now endeavoring to develop electric vehicles (EV) and gradually taking global leading positions in terms of both R&D expenditures and market share. This process is highly in line with the tendency to reduce utilization of fossil fuels and develop new industries using clean energy. Represented by high-tech enterprises like CATL, BYD, etc., it is promising to simultaneously achieve emission reduction and establish value-added industries.

Vehicles, including buses and private cars, have been playing key roles in the transportation field, particularly in daily urban commuting or urban/rural passenger transport. To replace conventional fuel vehicles in practical transportation, EVs should meet some vital requirements. In terms of practicability, EVs must possess superior mileages and battery lives;

that is, they should realize sufficient travel distances after discharging while ensuring the deterioration of capacity to be limited to an acceptable extent. With respect to user experiences, EVs should also have fast charging rates, robust climbing/accelerating capabilities, and powerful batteries even on cold days.

Certainly, there are some ideal energy-storage devices such as high-efficiency, low-cost, and environmentally-friendly hydrogen-based systems. Nevertheless, at the current stage, all these ideal systems are under development; thus, it is inevitable to employ relatively well-developed chemical batteries in EVs. Specifically, Li-ion batteries (LIBs) are one of the most established chemical batteries. Due to some intrinsic merits, including light atomic weight (M = 6.94 g mol^{-1}), small ionic radius (r_{Li^+} = 0.76 Å), and lowest standard electrode potential (-3.04 V vs standard hydrogen electrode), of Li element, Li-based battery chemistries were considered as viable solution for EV applications. Ever since SONY successfully developed the commerlizable prototypes of LIBs in 1991,[8] LIBs have rapidly become the first choice of energy sources for smart devices owing to the much higher energy/power density than those of conventional energy storage devices. Recently, because of the increasing requirements of environmental protection, conventional fuel vehicles are being quickly replaced by EVs. Furthermore, LIBs have occupied the majority of power-cell markets. The status quo is as follows: not only many new EV-enterprises (for example, BYD, TESLA, and NIO, etc.) are budding, but also several developed auto enterprises are transforming to the "new normal", that is, investing more in the R&D of EVs. The famous business data platform *Statista* has predicted a LIBs production capacity of ~2.3 TWh in 2030.[9] The Korean consulting organization *SNE Research* has even estimated a battery shipment of 3.5 TWh in 2030.[10]

Despite the increasing market performances of LIBs that have attracted the attentions of many investors and consumers, some hidden risks, particularly the fact that LIBs have almost reached their physicochemical limits in terms of energy/power densities, have been noticed by scientists and leading companies. Energy and power densities are the most important indices of a chemical battery which have been defined in equations (1-1) and (1-2),

$$Energy\ density = capacity \times voltage \qquad (1-1)$$

$$Power\ density = capacity \times voltage \times C_{rate} \qquad (1-2)$$

where C_{rate} refers to the charge/discharge rate[11] (x C indicates that the battery can be fully charged/discharged within $1/x$ h, for example, 5 C implies that the battery can be fully charged/discharged within 12 min). The energy/power densities of a LIB is determined by the

following factors: 1) overall capacity, where in the cases of widely used LIB systems, the capacities of cathode are substaintially lower than those of the anodes; 2) overall potential, which are directly depended on the differences between standard electrode potentials of cathodes and anodes; 3) the performance of battery under high-current-density conditions, where cathode materials usually suffer from sluggish kinetics compared with anode material because of complex topotactic lattice configurations. Therefore, the performances of cathode materials become the bottleneck of the overall performances of LIBs.

At the current levels of LIBs, the energy density of the battery package is merely 220–250 Wh kg^{-1}. Such energy density of commercialized LIBs hinder the replacement of conventional fuel vehicles by EVs. Chinese government issued a national strategic plan, *Made in China 2025*, and sunsequently, four departments jointly launched a more detailed *Action Plan for Promoting the Development of Automobile Power Battery Industry*, in which the purposes of developing LIBs wtih energy densities of 300 and 500 Wh kg^{-1} by 2020 and 2025, respectively, were proposed.[12,13] The U.S. Department of Energy also issued a *Battery500 Consortium* for the construction of next-generation Li-metal batteries with energy densities up to 500 Wh kg^{-1} by composing world-class scientists, engineers, and many U.S. National Laboratories and extraordinary universities.[14]

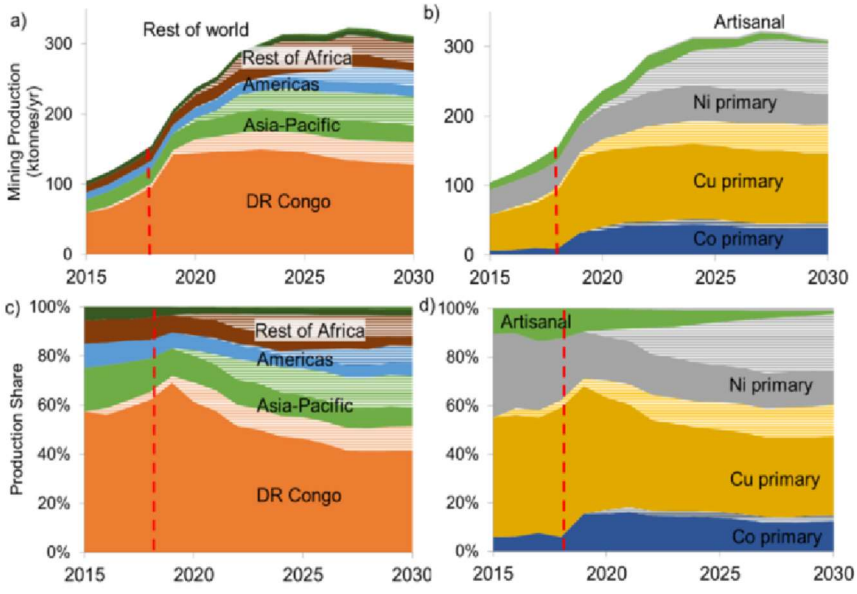

Figure 1.1 Estimates of Co supply from primary mined sources by (a,c) country and (b,d) principal metal plotted in terms of (a,b) mining production and (c,d) production share.[15]

In addition to the issues of energy density, the application of LIBs are constrained by some other problems, such as inferior low-temperature performances, thermal instabilities,

potential risk of spontaneous combustion due to short circuit, and the geopolitical considerations arising from the globally inhomogenuous distributions of Ni/Co/Li mines (**Figure 1.1**); these problems strongly impede further applications of LIBs. [15]

Consequently, the explorations to new possibilities involving both improvements on LIBs and developments of new replacements are no longer a nicety but a necessity. Except for the cases of some totally different systems (including solar and fuel cells), scientists and engineers have been exploring "post LIBs", for instance, batteries employing cations including Na^+, K^+, Mg^{2+}, Zn^{2+}, Ca^{2+}, and Al^{3+}, even anions such as F^- and Cl^- as charge carriers instead of Li^+, with working principles similar to those of LIBs.[16-27] Among them, the concep of F-ion batteries (FIBs) was proposed in the 1970s; nevertheless, the laboratorial prototype did not emerge until 2011 when Fichtner et al. designed tysonite-type $La_{0.9}Ba_{0.1}F_{2.9}$ as a reliable solid electrolyte.[18] All-solid-state FIBs possess several advantages: 1) multielectron reactions induced by simple fluorination processes, leading to high capacities and high potentials of these FIBs; 2) supreme safety due to the chemical stability of F anions and the inflammable nature of the inorganic solid electrolyte. Therefore, recently, the studies on FIBs have attracted extensive attention; however, there are still numerous unresolved questions related to fundamental theories of fluorination reactions.

In this thesis, we investigated all-solid-state batteries using F^- as charge carriers starting from principles of basic metal/metal fluoride conversions and finally approaching the design and discussion of all-solid-state devices with high energy densities. In the subsequent sections of this chapter, initially, the typical working principles of LIBs are discussed; then, the requirements of new battery devices until the current research stages of FIBs are introduced; finally, the logic and reasons of topic selection and research process of this doctoral thesis are revealed.

1.2 Lithium-ion batteries and their fundamental principles

1.2.1 Working principles

In the 1970s, Prof. M. S. Whittingham, who at that time worked for Exxon,[28] constructed the LIB prototype $Li|LiClO_4|TiS_2$,[29] and reported the electrochemically Li-inserted phase Li_xTiS_2. Nearly in the same period, Prof. J. B. Goodenough and Prof. A. Yoshino further developed $LiCoO_2$ cathode material, C anode materials and a carbonate-based liquid electrolyte, which considerably improved the lifespan and increased the working potentials of LIBs,

thereby successfully promoting the commercialization of LIBs.[30-32] Owing to their significant contributions to various aspects of LIB research, these three esteemed professors were awarded the Nobel Prize in Chemistry 2019.

Generally, a working LIB, where "working" means "providing electricity", namely, discharging, is driven by the potential difference between the cathode and the anode. During this process, a Li ion (positive charge) moves from the cathode to the electrolyte inside the battery, along with oxidation at the cathode to maintain charge neutrality and the release of one electron (negative charge). Immediately, the released electron travels from the positive to the negative electrode via the circuit outside the battery, also allowing charge neutrality of the anode, which exactly accepted a Li^+ coming from electrolyte. In the cathode, charge compensation is accomplished by the oxidation/reduction of transition metal species, whereas the Li atoms in the topotactic crystallographic structure of the cathode connect and form successive pathways; consequently, Li^+ can reversibly (de)intercalate from bulk, driven by potentials between cathode and anode. Similarly, in the anode, Li^+ can be accepted/released by insertion (for example, layered structure in graphite) or conversion (for example, alloy-type materials) reactions. From a macroscale perspective, it is similar to the back and forth shuttling of Li^+ from the cathode to the anode. This working principle of LIBs are described as "rocking-chair batteries" (**Figure 1.2**).[33]

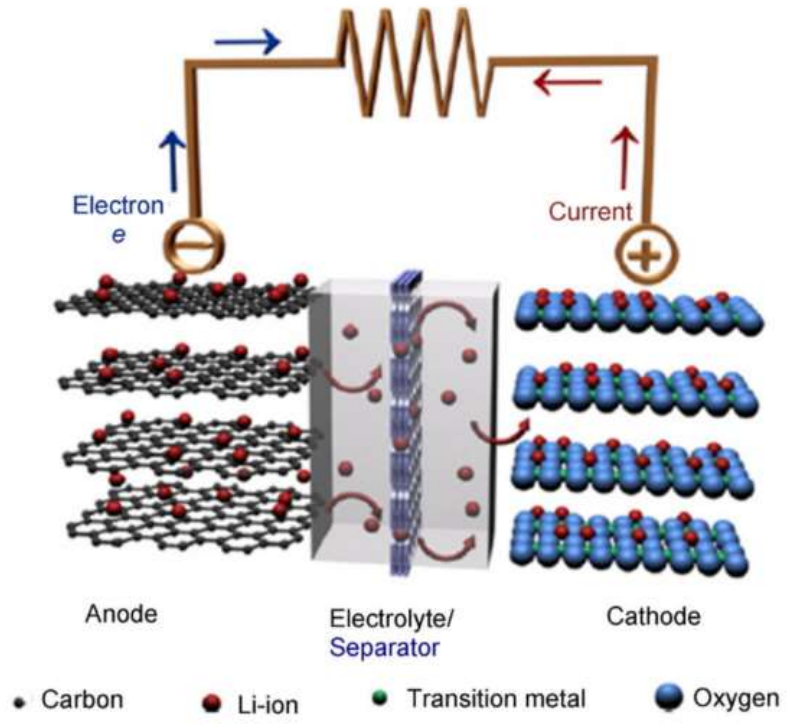

Figure 1.2 Working principle of a "rocking-chair" lithium-ion battery (charging).[33]

Based on this working principle, we summarized several factors that would significantly affect the overall performance of a LIB. First, the capacity of the electrode material, which is the provider/receiver of Li^+, is directly determined by the maximum number of Li-storage sites in its structure. Second, the number of gained/lost electrons and the ease of transition metals to maintain charge neutrality also influence the Li^+ (de)intercalation process. Third, the Gibbs free energy change ΔG of transition metal oxidation/reduction determines the electromotive force of this redox reaction via the equation (1-3):

$$\Delta G = -nFE_{cell} \qquad (1-3)$$

where n is the number of transferred electrons, F is the Faraday's constant, and E_{cell} is the standard-state cell potential (or the electromotive force between two half-cells). Moreover, electronic structures and some kinetic factors determine the rate of Li^+ (de)intercalations, which usually affect the high-current-densities performances (known as "rate capability") and battery polarization (known as "voltage hysteresis"). Additionally, factors including the interactions between electrode materials and the electrolyte, crystal defects, and crystal anisotropies contribute to the overall performances of LIBs.

1.2.2 Typical technology roadmaps

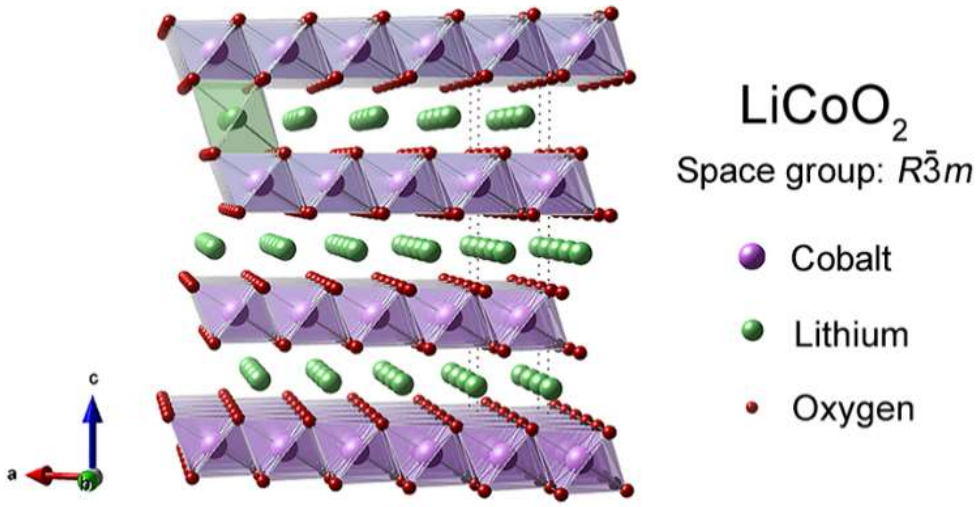

Figure 1.3 Crystal structures of $LiCoO_2$ material.

Typically, two representative materials that have been widely industrialized for LIBs: Li transition metal oxides ($LiTmO_2$, Tm = transition metal) and polyanionic Li transition metal phosphates ($LiTmPO_4$). The most common $LiTmO_2$-type material is $LiCoO_2$, which possesses

an α-$NaFeO_2$ structure (space group: $R\bar{3}m$) with [CoO_6] and [LiO_6] octahedra arranged as highly ordered Li-O and Co-O slabs (**Figure 1.3**). $LiCoO_2$ has high potentials (over 3.5 V vs. Li/Li^+) and a high theoretical capacity (~274 mAh g^{-1} under fully delithiated condition). Li ions are believed to diffuse along the *a*-*b* planes with rapid diffusivities. Nevertheless, if the voltage is higher than ~4.2 V (corresponding to approximately x > 0.5-0.55 in $Li_{1-x}CoO_2$ formula), unmodified $LiCoO_2$ loses its cycling stability[34] because of several reasons: i) half delithiation of $LiCoO_2$ causes transition from a hexagonal phase of $LiCoO_2$ to a monoclinic phase, which has inferior structural stabilities;[34-37] ii) the formation of an increasing number of Co^{4+} (smaller ionic radii than that of Co^{3+}) leads to the migration of Co^{4+} from original Co-O slabs to Li-O slabs followed by undesired dissolution in liquid electrolytes;[38,39] iii) the t_{2g} bands of the 3*d* orbitals in Co^{4+} slightly overlap with the top of the O 2*p* orbital, resulting in electron loss and oxidation of surficial O until O releases and the lattice collapses.[40,41]

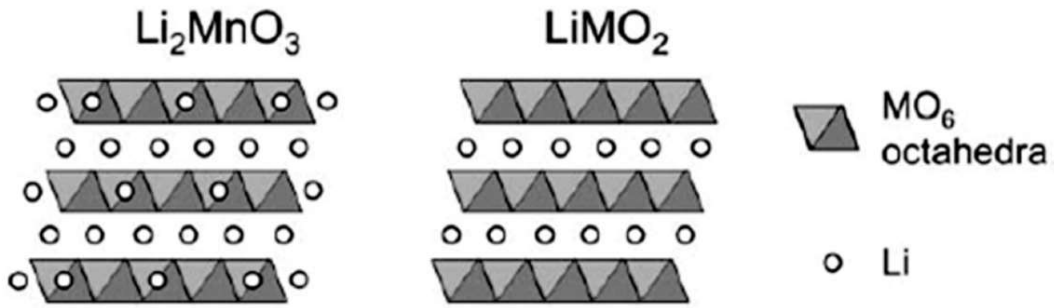

Figure 1.4 Layered structures and lattice coherency of Li_2MnO_3 and $LiTmO_2$ (Tm = Co, Ni, Mn). [42]

Ternary-type layered $LiTmO_2$ have been designed to tune the band structures and transition metal valences, in which Co has been co-substituted with Ni/Mn or Ni/Al; these ternary compounds are known as NCM or NCA materials. By adjusting the ratios of the three main transition metals in ternary compounds and via some doping or surficial engineering strategies, ternary NCM or NCA materials with higher capacities of ~200 mAh g^{-1} and high output voltage similar to those of $LiCoO_2$ can be obtained. Another strategy for improving the performances of $LiTmO_2$ is to induce a Li_2MnO_3 phase that is highly compatible with $LiTmO_2$ lattices and consequently forms a Li-rich layered $xLi_2MnO_3{\cdot}(1-x)LiTmO_2$ phase. Li-rich materials possess higher Mn contents than those of conventional NCM or NCA materials; consequently, Li-rich materials have higher thermal stabilities, lower costs, and better environmental friendliness. As shown in **Figure 1.4**,[42] a high lattice coherency between Li_2MnO_3 (monoclinic $C2/m$ phase) and $LiTmO_2$ (hexagonal $R\bar{3}m$ phase) components can be noticed due to their high structural compatibility with each other.[43-45]

In addition to the highly ordered layered phase $LiTmO_2$, a rock-salt phase with highly mixed $[CoO_6]$/$[LiO_6]$ local structures (space group: $Fm\bar{3}m$) is considered electrochemically inactive because of the completely isolated Li sites in its lattice. However, these Li sites can be connected by many strategies, such as by adjusting the Li/Tm ratios, tuning the degrees of order/disorder, and inducing heteroatoms, owing to the high flexibility of $[LiO_6]$ and $[TmO_6]$ octahedra in the rock-salt structure (**Figure 1.5**).[46,47] Recently, partially ordered rock-salt $Li_{1+y}Tm_zO_{2-\delta}$ materials with the best capacity of ~360 mAh g^{-1} were developed, and the kinetic factors were investigated by theoretical calculations.[48]

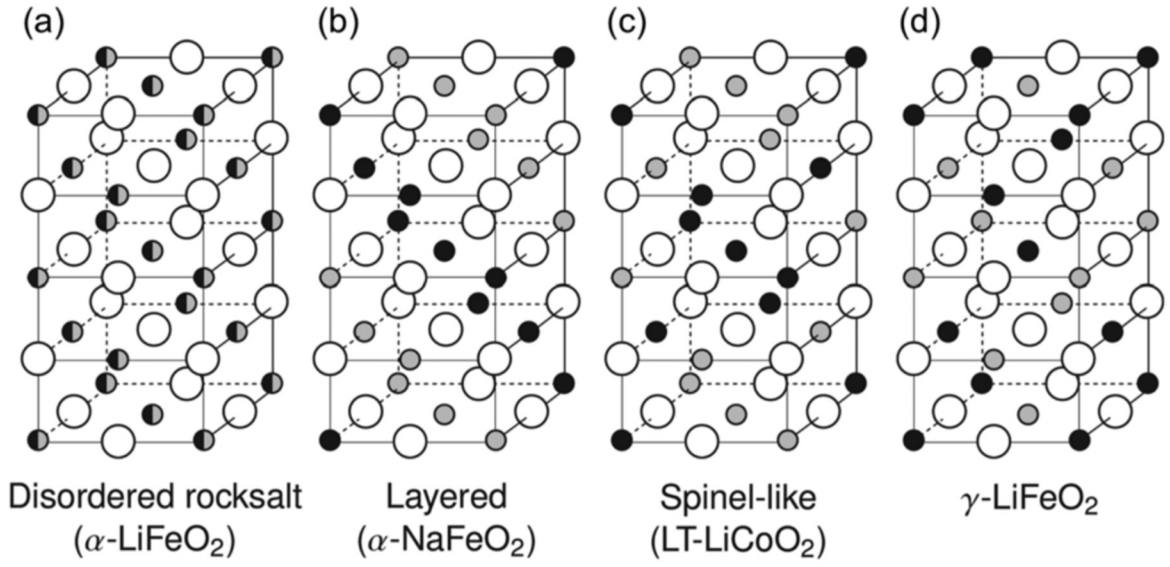

Figure 1.5 Common rock-salt-type Li transition metal oxide crystal structures: (a) disordered rocksalt α-$LiFeO_2$ structure in which all cation sites are equivalent, (b) layered α-$NaFeO_2$ structure, (c) spinel-like low-temperature $LiCoO_2$ structure, and (d) γ-$LiFeO_2$ structure. Large empty circles indicate O sites, small gray and black filled circles stand for lithium and transition metal sites, respectively. Adapted with permission from Urban et al.[47]

Deeper understandings on charge compensations, voltage decays and structural stabilities of $LiTmO_2$ were obtained by researchers since 2016, following the O redox behavior has extensively attracted attentions.[49,50] While discussing charge compensations and atomic interactions, the Fermi level, which refers to a hypothetical energy level that has a 50% possibility of being occupied at thermodynamic equilibrium in the band structure of solids should be considered. In the cases of $Li_{1+y}Tm_zO_2$ materials with high oxidation-state redox species or large Li/Tm ratios, it is highly possible that the Fermi level will be located at states where O 2*p* orbitals and high-energy Tm 3*d* split orbitals overlap with each other. Therefore, at a high state-of-charge (SOC), O tend to participate in redox reactions and significantly contributes to charge compensation. Although there are some stereotypes that the reaction rate

of O redox might be sluggish and hardly reversible based on some previous studies on $LiCoO_2$ or related materials, many recent studies have demonstrated that anionic redox is rapid, smooth, and highly reversible[46,48,51] provided the particles and its intrinsic electronic structures were properly controlled and modified. Nevertheless, several problems in terms of voltage hysteresis or voltage decay need to be resolved before meeting the demands of commercialization, and realization of high energy/power densities via reliable anionic redox reactions is still in experimental stage.

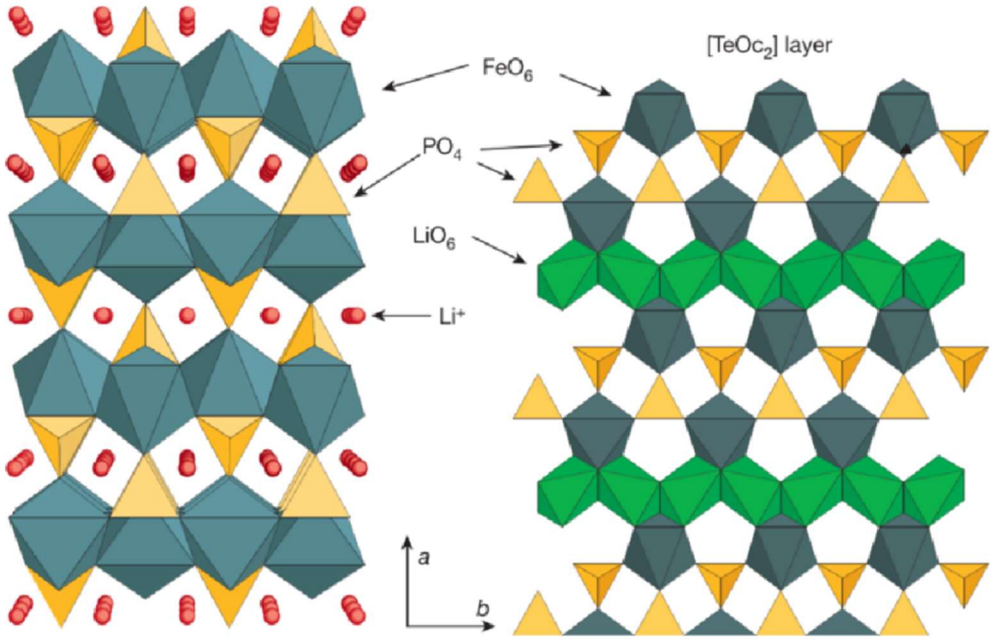

Figure 1.6 Crystal structure of olivine $LiFePO_4$ in projection along [001]. $[TeOc_2]$ refers to the repeated units of $[PO_4]$−$[FeO_6]$−$[LiO_6]$ tetra-octa-octahedral layers. [52]

Pioneering studies on polyanionic phosphate compounds, Represented by olivine-type $LiFePO_4$, have been performed by Padhi et al.[53-56] $LiFePO_4$ with a conformal thin C coating, which substantially enhances the inferior electronic conductivity if $LiFePO_4$, has become one of the most successfully commercialized cathode materials for LIBs. In the $LiFePO_4$ lattice, O atoms are arranged as a slightly distorted hexagonal close-packed (*hcp*) sublattice. Half of the octahedral sites in the O sublattice are occupied by Fe, forming the corner-sharing $[FeO_6]$ arrays; one-eighth of the octahedral sites in O sub-lattice are occupied by Li and form the edge-shared $[LiO_6]$ arrays, and tetrahedral sites in the O sub-lattice are filled by P, forming $[PO_4]$ arrays (**Figure 1.6**).[52] Owing to the stabilization effects of $[PO_4]$ tetrahedrons on $[LiO_6]$ and $[FeO_6]$, $LiFePO_4$ has extraordinary thermal and structural stabilities, leading to its ultralong lifespan; the integrity of the $LiFePO_4$ lattice remains intact at ultrahigh current densities (even

at 100 C-rate[57]). The Fe^{2+}/Fe^{3+} redox contributes to charge compensation along with a two-phase $LiFePO_4/FePO_4$ transition, resulting in a stable output voltage. However, unlike $Li_{1+y}Tm_zO_2$, the Li content of $LiFePO_4$ cannot be further increased constrained by its crystal structure, thus the theoretical capacity of ~170 mAh g^{-1} cannot be improved; that is, there is almost no scope for the enhancement of the energy density of $LiFePO_4$. Orthosilicate compounds (Li_2MSiO_4, M = Fe, Mn, Co) comprise two Li atoms per unit formula; therefore, they have theoretical capacities of over 320 mAh g^{-1}.[58-60] Nevertheless, problems including unstable Fe^{3+}/Fe^{4+} redox in Li_2FeSiO_4, severe distortion caused by Jahn−Teller effects, ion dissolution due to $Mn^{3+} \rightarrow Mn^{2+} + Mn^{4+}$ disproportionation reaction, and lattice amorphization in Li_2MnSiO_4, hinder the further industrialization of orthosilicate materials.[61,62]

1.2.3 Prospects and considerations

Comprehensively considering the various factors such as mileage, charge/discharge rate, low-temperature performance deterioration, and safety, it is currently difficult to realize LIB-driven EVs with performances higher than those of conventional fuel vehicles. For example, in August 2017, *Tesla* unveiled a P100D-type *Model S* vehicle, in which a 100 kWh battery with approximately 500–600 km mileage and a weight of 625 kg in a 0.40 m^3 volume was employed. These performances, which is in the top level among those of the current-stage batteries, are still insufficient for replacing conventional fossil fuels. The present technical roadmaps (introduced in Section 1.2.2) cannot produce a qualitative leap in the energy/power densities of LIBs. To date, revolutionary materials for LIBs, in particular those with high volumetric energy density considering the practical application conditions where there is limited space to accommodate battery packs, have not been reported.[63,64]

As a result, researchers have to pay attention to other systems including post-LIBs, metal/S batteries, metal/air batteries, and fuel cells. In terms of volumetric energy densities, batteries, for example, batteries employing multivalent cations (Mg^{2+}, Ca^{2+}, or Al^{3+}) as charge carriers, involving multielectron processes can easily achieve high capacities in limited redox centers. [17,19,22,24,26-27] Among these diverse systems, FIBs utilizing monovalent F ions as charge carriers have become more attractive because of the intrinsic multielectron characteristics of many fluorination reactions. [18,65] Therefore, FIBs can theoretically deliver extraordinary energy densities up to 5000 Wh L^{-1}, which are higher than the theoretical capacities of Li–air batteries and conventional LIBs.[65,70,77]

1.3 Fluoride-ion batteries

1.3.1 Fluorination reactions and fluoride-ion batteries

Describing an anion-transfer chemical battery using a "rocking-chair" mechanism similar to that in the case of LIBs is difficult. In the cases of LIBs, (de)lithiation can be achieved via either topotactic or non-topotactic ways, where the term *topotactic* refers to the reversible (de) intercalation of Li with no diffusive rearrangements of other host atoms and with only lattice parameter changes. [51] Topotactic lattices usually possess stable O sublattices as a framework; at least one non-Li cation species helps to neutralize the negative charges of O ions and cooperates with O to maintain the integrity of the host structure in a highly delithiated state, for example, delithiated Li_0FePO_4, $Li_{1-x}CoO_2$, and $Li_4Ti_5O_{12}$. There are also many non-topotactic conversion-type or alloying-type (de)lithiation reactions, in which the parent phase (compound or elemental substance) is completely converted to one or several new phases, such as Li–Si alloys and Li-TmO, with large-scale atomic rearrangements, as presented in equation (1-4):[66]

$$2Li + TmO \leftrightarrow Li_2O + Tm\ (Tm = Co, Fe, Ni, Cu) \qquad (1-4)$$

Non-topotactic reactions might lead to higher voltage polarizations or inadequate cycle lives of batteries because of intense volumetric changes and large Gibbs formation energies. However, the high utilization rate and thorough conversions of the parent phase lead to multielectron reactions and thus high capacities.

(1) Fluorination with non-topotactic pattern

Non-topotactic pattern of fluorination can be generally supposed considering the most fundamental fluorination of elemental substances (M/MF_x transitions). These fluorinations are similar to oxidation reactions (including rusting of metals), where the starting materials lose electrons and form ionic or covalent bonds with F atoms. To fabricate a chemical battery using fluorination reactions, it is necessary to evaluate the fluorination from electrochemical standpoints. Clemens et al. have provided an interesting explanation of the potentials of FIB using a LIB as an example in their previous study,[67] which can be further described as follows.

In the laboratory studies of a LIB, a Li-metal half-cell is widely used for evaluating the properties of electrode materials because the redox of Li^+ directly being plated on Li, namely Li/Li^+ redox, possesses the lowest electrode potential (-3.04 V vs. standard H electrode) among

those of various solid-state redox species. Therefore, electrodes with low potentials vs. that of Li/Li^+ should be appropriate anode materials, whereas those with high potentials vs. that of Li/Li^+ should be suitable cathode materials. It is convenient to employ Li because it acts as a uniform standard for various electrode materials. In the cases of Li half-cells, the reactions occurring on each electrode can be expressed as equations (1-5)–(1-7). In the reaction (1-7), Tm gradually reduced with the insertion of Li into the $Li_{1-x}TmO_2$ lattices; a reduction limit was achieved and Li plating occurred with the insertion of more Li into the $Li_{1-x}TmO_2$ lattices.

$$Cathode:\ LiTmO_2 \leftrightarrow Li_{1-x}TmO_2 + xLi^+ + xe^- \qquad (1-5)$$

$$Anode:\ xLi^+ + xe^- \leftrightarrow xLi \qquad (1-6)$$

$$Overall:\ LiTmO_2 \leftrightarrow Li_{1-x}TmO_2 + xLi \qquad (1-7)$$

Similarly, in the cases of a FIB, we can hypothesize a F_2-gas half-cell; nevertheless, a gaseous F anode does not exist. When a certain M/MF_x couple is combined with the F_2/F^- electrode in a FIB, its electrode reactions can be expressed as equations (1-8)–(1-10).

$$Cathode:\ \frac{2}{x}M + 2F^- \leftrightarrow \frac{2}{x}MF_x + xe^- \qquad (1-8)$$

$$Anode:\ F_2 + xe^- \leftrightarrow 2F^- \qquad (1-9)$$

$$Overall:\ \frac{2}{x}M + F_2 \leftrightarrow \frac{2}{x}MF_x \qquad (1-10)$$

Unlike the case of reaction (1-7), in the reaction (1-10), M was oxidized upon fluorination; correspondingly, an oxidation limit was reached and F_2 was released with the excessive fluorination of M/MF_x. Via the oxidation/reduction relationships in the reactions (1-8) and (1-9), we can calculate the cell voltage ($E^{\ominus}$) for the reaction (1–10) based on the speculated F_2/F^- electrode by the Nernst equation, as shown in the equation (1-11).

$$E^{\ominus} = \frac{RT}{nF}\ln a^{\ominus}(F_2) \qquad (1-11)$$

where R, T, n, and F represent the gas constant, temperature (Kelvin), the number of transferred electrons ($n = 2$ for the reaction (1-10)), and Faraday constant, respectively. In the reaction (1-10), the activities of solid-state M and MF_x under standard temperature and pressure (STP) conditions were considered as 1; thus, only the activity of F_2 gas ($a^{\ominus}(F_2)$) was evaluated using the equation (1-11). The calculated cell voltages are actually the standard electromotive forces of several M/MF_x vs. F_2/F^- redox. The results of $E^{\ominus}$ are presented in **Table 1.1** and **Figure 1.7**;

the $a^{\ominus}(F_2)$ values were calculated by Motohashi et al.[68] via *MALT for Windows*[69] thermodynamic database. The distances between the top of each pillar to the F_2-release level are the exact $E^{\ominus}$ values (Figure 1.7). Compared to that of the Li/Li^+ redox, the electrode potential of the F_2/F^- redox (+2.866 V vs. standard H electrode) is almost the highest among those of all redox species. Therefore, electrodes with slightly lower potentials than that of the hypothesized F_2/F^- electrode shall be appropriate cathode materials, whereas those with considerably lower potentials than that of the speculated F_2/F^- electrode shall be suitable anode materials.

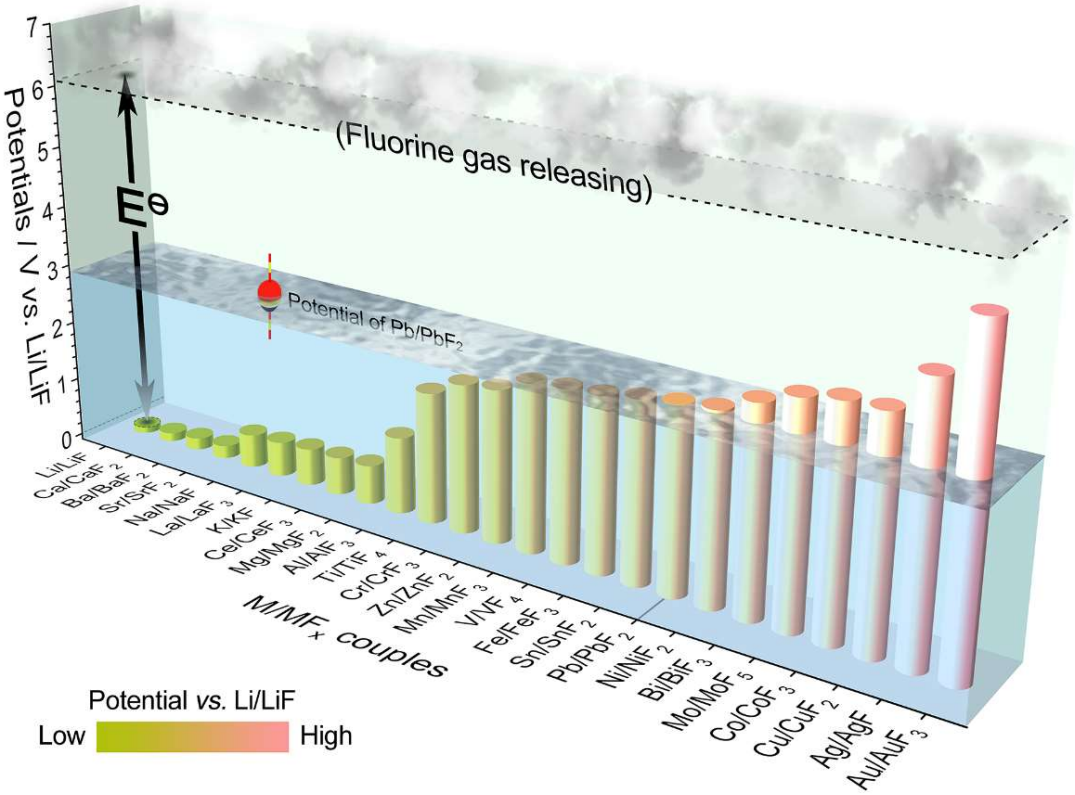

Figure 1.7 Schematic illustration of standard electrode potentials of various M/MF_x couples. Water level in the graph represents the potential of Pb/PbF_2 which is widely used as counter or reference electrode in FIB-related studies.

As a gaseous F_2 electrode does not exist in practical studies of FIB, we have to choose two couples of M/MF_x as the cathode and anode and construct a full cell. The full-cell voltage can also be measured by the Nernst equation.

$$E_{full\ cell} = \frac{RT}{2F} \ln \frac{a^{\ominus}(F_2, anode)}{a^{\ominus}(F_2, cathode)} \qquad (1-12)$$

Among all M/MF_x, Li/LiF is regarded as a theoretically ideal anode for FIBs because of its extremely high capacity and lowest $E^{\ominus}$. Moreover, Pb/PbF_2 has been widely utilized as a reliable reference electrode in many studies because of its stable and smooth electrochemical properties. Therefore, the potentials vs. Li/LiF and potentials vs. Pb/PbF_2 of all M/MF_x were also calculated using the equation (1-12) and are provided in **Table 1.1**. The practical reaction environments are significantly more complex than STP; however, for some previously reported M/MF_x couples (M = Cu, Co, Ni, Bi, Pb, La, Ba, Ce), [65,70-77] the actual electrochemical behaviors appropriately correspond with the predictions presented in Table 1-1.

Table 1.1 Standard electrode activities and potentials of various M/MF_x couples

M/MF_x Couples	$a^{\ominus}(F_2)$	$E^{\ominus}$	E vs. Li/LiF	E vs. Pb/PbF_2	M/MF_x Couples	$a^{\ominus}(F_2)$	$E^{\ominus}$	E vs. Li/LiF	E vs. Pb/PbF_2
			(V)					(V)	
Li/LiF	1.17×10^{-206}	6.091	0	-2.893	Ti/TiF_4	2.57×10^{-137}	4.040	2.051	-0.842
Ca/CaF_2	3.13×10^{-205}	6.049	0.042	-2.851	In/InF_3	6.00×10^{-131}	3.852	2.239	-0.654
Ba/BaF_2	2.17×10^{-203}	5.995	0.097	-2.797	Cr/CrF_2	8.81×10^{-130}	3.817	2.274	-0.619
Sr/SrF_2	8.59×10^{-203}	6.036	0.114	-2.779	Cr/CrF_3	8.32×10^{-128}	3.759	2.332	-0.561
Sm/SmF_3	2.39×10^{-199}	5.875	0.216	-2.677	Ga/GaF_3	1.72×10^{-127}	3.750	2.342	-0.552
Y/YF_3	7.87×10^{-193}	5.682	0.409	-2.484	Ta/TaF_5	2.96×10^{-126}	3.713	2.378	-0.515
Er/ErF_3	1.56×10^{-191}	5.644	0.447	-2.446	Zn/ZnF_2	1.08×10^{-125}	3.696	2.395	-0.499
Na/NaF	3.64×10^{-191}	5.633	0.458	-2.435	Nb/NbF_5	8.53×10^{-120}	3.522	2.569	-0.324
Tb/TbF_3	4.40×10^{-191}	5.631	0.461	-2.433	Fe/FeF_2	7.33×10^{-118}	3.465	2.627	-0.267
Ho/HoF_3	9.20×10^{-191}	5.621	0.470	-2.423	Mn/MnF_3	1.64×10^{-117}	3.454	2.637	-0.257
La/LaF_3	2.16×10^{-190}	5.610	0.481	-2.412	V/VF_4	1.81×10^{-115}	3.394	2.697	-0.196
Gd/GdF_3	3.13×10^{-190}	5.605	0.486	-2.408	Fe/FeF_3	2.94×10^{-114}	3.358	2.733	-0.160
Dy/DyF_3	2.68×10^{-189}	5.578	0.514	-2.380	Cd/CdF_2	3.37×10^{-114}	3.356	2.735	-0.159
K/KF	3.73×10^{-189}	5.574	0.518	-2.376	Co/CoF_2	4.12×10^{-114}	3.354	2.738	-0.156
Pr/PrF_3	4.24×10^{-189}	5.572	0.519	-2.374	Sn/SnF_2	4.42×10^{-111}	3.264	2.827	-0.066
Ce/CeF_3	6.58×10^{-189}	5.566	0.525	-2.368	Pb/PbF_2	7.73×10^{-109}	3.198	2.893	0
Mg/MgF_2	3.09×10^{-188}	5.547	0.545	-2.349	Ti/TiF	3.29×10^{-107}	3.150	2.942	0.048
Lu/LuF_3	5.02×10^{-188}	5.540	0.551	-2.342	Ni/NiF_2	1.46×10^{-106}	3.131	2.961	0.067
Nb/NbF_3	5.08×10^{-188}	5.540	0.551	-2.342	Cr/CrF_4	4.47×10^{-102}	2.998	3.094	0.200
Rb/RbF	1.16×10^{-185}	5.470	0.621	-2.272	Bi/BiF_3	5.43×10^{-98}	2.877	3.214	0.321
Cs/CsF	7.43×10^{-185}	5.446	0.645	-2.249	Mo/MoF_3	1.03×10^{-96}	2.839	3.252	0.359
Sc/ScF_3	2.01×10^{-182}	5.375	0.717	-2.177	Mo/MoF_5	1.47×10^{-90}	2.657	3.434	0.541
Eu/EuF_3	3.52×10^{-176}	5.190	0.902	-1.992	Co/CoF_3	3.69×10^{-87}	2.557	3.535	0.641
Th/ThF_4	1.15×10^{-175}	5.175	0.917	-1.977	Cu/CuF_2	4.62×10^{-87}	2.554	3.538	0.644
Vb/YbF_3	2.82×10^{-175}	5.163	0.928	-1.965	Pd/PdF_2	6.58×10^{-75}	2.194	3.897	1.004

Be/BeF_2	2.60×10^{-172}	5.075	1.016	-1.878	Ag/AgF	3.83×10^{-66}	1.935	4.156	1.263
Al/AlF_3	3.61×10^{-167}	4.923	1.168	-1.725	Ru/RuF_3	1.74×10^{-55}	1.620	4.472	1.578
Hf/HfF_4	4.51×10^{-161}	4.743	1.348	-1.545	Au/AuF_3	6.15×10^{-35}	1.012	5.079	2.186
Ti/TiF_3	8.47×10^{-160}	4.705	1.386	-1.507					
Zr/ZrF_4	2.82×10^{-159}	4.690	1.402	-1.492					
V/VF_3	5.21×10^{-144}	4.238	1.853	-1.040					
Mn/MnF_2	4.35×10^{-142}	4.181	1.910	-0.984					

In the abovementioned discussion, we evaluated the oxidative limits (F_2 release) of M/MF_x from the viewpoint of electrode. However, from the viewpoint of electrolyte, it is also necessary to discuss the reductive limits (decomposition of MF_x and generation of metal). It is interesting that the thinking logic of FIB is exactly opposite to that of LIB, in which the oxidative limits are typically used for electrolyte research, whereas the reductive limits are employed for electrode research. The $E^{\ominus}$ values presented in Table 1-1 also help to predict the electrochemical windows in the cases where one fluoride compound is selected as a F ion conductor; the MF_x compound with larger $E^{\ominus}$ values will be decomposed later. Note that some solid-state fluoride compounds with wide electrochemical windows exhibit high F^- ionic conductivities. The existence of these solid-state conductors directly facilitate the construction of an all-solid-state FIB, which has been discussed in Section 1.3.2.

(2) Fluorination with topotactic pattern

Topotactic fluorination is a reversible F (de)intercalation that does not vary the fundamental framework of the host material. Topotactic fluorination in perovskite-related, infinite−layer-, and Ruddlesden−Popper structures by chemical methods (that is, calcination with fluorinating agents such as poly (vinylidene fluoride) (PVDF), XeF_2, and CaF_2) has been extensively reported, [78-82] where the basic requirement for the host materials is the presence of anionic deficiencies surrounding the central cation of a certain coordination polyhedron. In many cases, for example, $Sr_2CuO_2F_{2+\delta}$ (prepared using Sr_2CuO_3 and gaseous F_2) and $Sr_2TiO_3F_2$ (produced by Sr_2TiO_4 and PVDF or NH_4F), fluorinations are partially topotactic because a few oxide anions are inevitably substituted by F ions. [83-85] Perfectly topotactic fluorinations have also been reported, for instance, in the cases of $LaSrMnO_4F$ [86] and $La_{1.2}Sr_{1.8}Mn_2O_7F$, [87] where all F ions are located at interstitial sites with no replacement of oxide ions. An intercalation-based cathode material for FIB, which is highly similar to the extensively used $LiCoO_2$-based LIB, can be obtained from these topotactic fluorination reactions if the insertion of F can be

achieved by electrochemical methods. Numerous efforts have been devoted to these concepts, which have been discussed in the following sections.

1.3.2 Electrolytes

The proof-of-principle of FIB starts from the transport of F ions, enabling the back-and-forth shuttling of these ions from the positive and negative electrodes. Since the 1970s, several pioneering studies have been reported on the development of F-ion conductors for application in the fields of gas sensor, gas-phase electrolysis,[88-90] and F-ion galvanic cells;[91-93] furthermore, in 1981, the term "solid-state fluoride-ion battery" was coined for the first time by J. Schoonman.[94-96] Thereafter, little progress has been made until Reddy and Fichtner constructed tysonite-type $La_{1-x}Ba_xF_{3-x}$ as a solid electrolyte for all-solid-state FIBs in 2011 (**Figure 1.8**).[18] It is believed that the selective transport of F ions can be facilely realized in solid conductors than that in the cases of liquid systems.

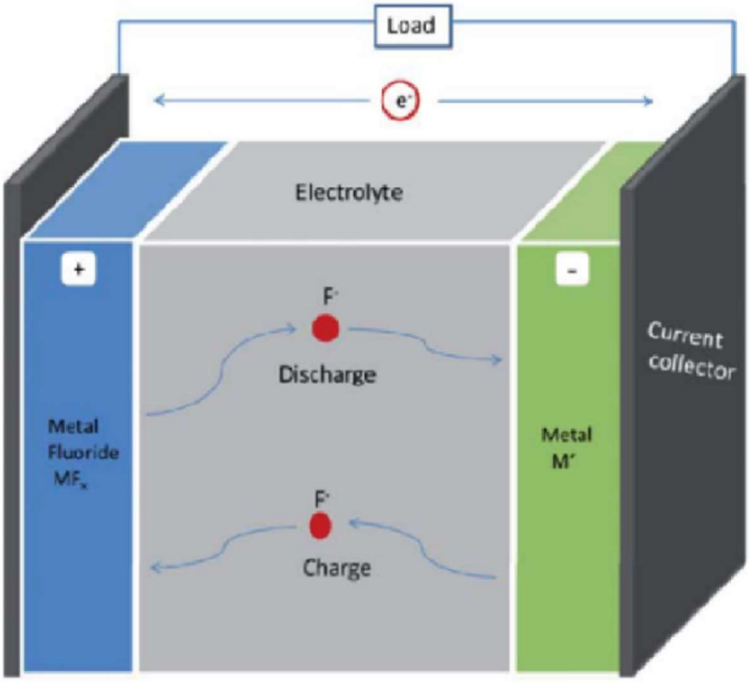

Figure 1.8 Schematic of the architecture of a fluoride-ion battery. [18]

(1) Tysonite- and fluorite-type compounds

For solid F-ion conductors, alkaline-earth element-containing fluorite-type compounds ($M_{ae}F_2$, M_{ae} = alkaline-earth metals (Ca, Sr, Ba)) and rare-earth element-containing tysonite-

type compounds ($M_{re}F_3$, M_{re} = rare-earth metals (La, Ce)) are potential candidates at elevated temperatures (usually above 423 K). Schoonman and Fichtner reported the ionic conductivities of LaF_3 and $La_{1-x}Ba_xF_{3-x}$ solid solutions using various La/Ba ratios, respectively. The continuous tysonite-to-fluorite phase transition of $La_{1-x}Ba_xF_{3-x}$ with conductivities ranging from 10^{-7} to 10^{-4} S cm^{-1} and activation energies (E_a) of 0.65–0.57 eV was investigated. As demonstrated in Section 1.3.1 (1), the formation of La and Ba in La- and Ba-based fluoride compounds occurs at extremely low potentials, ensuring wide electrochemical windows (~5.5 V vs. Li/LiF) of $La_{1-x}Ba_xF_{3-x}$ electrolytes. [97] Wang et al. developed flexible polyethylene oxide-composited $La_{0.95}Ba_{0.05}F_{2.95}$, which exhibited a conductivity of 5.13×10^{-6} S cm^{-1} and a wide electrochemical stability window of 4.7 V vs. Li/LiF at 70 °C.[74] Among the various $La_{1-x}Ba_xF_{3-x}$ compositions, $La_{0.9}Ba_{0.1}F_{2.9}$ was deemed as a reliable solid electrolyte because of its relatively high ionic conductivity (2×10^{-4} S cm^{-1} at 150 °C), a substantially wide electrochemical stability window, and superior thermal stability. Moreover, Dieudonné et al.[98,99] fabricated $Sm_{1-x}Ca_xF_{3-x}$ and $Ce_{1-x}Sr_xF_{3-x}$ materials with high room-temperature (RT) ionic conductivities of ~10^{-4} S cm^{-1}. The increased anionic vacancies created by Sr (in CeF_3) and Ca (in SmF_3) dopants is believed to facilitate F ion conduction because the decreased cationic coordination and enhanced mutual repulsions among cations would lead to smoother anionic transport.

(2) Sn-based compounds

Derivatives of SnF_2, namely, $M_xSn_{2-x}F_4$ (M = Pb, Ba, Sr), demonstrate ultrahigh ionic conductivities owing to their special structures. F ions are located in the M-Sn and Sn-Sn layers, which consist of arrays of modulated -M-M-Sn-Sn-M-M- chains along the *c*-axis. Stereoactivities of the Sn(II) lone pairs of electrons affect the fluoride sublattice, resulting in large amounts of disorders and defects at the F ion sites; these disorders and defects are believed to be major contributors to mass transfer in $M_xSn_{2-x}F_4$ materials.[88,100-103] $PbSnF_4$ has four configurations: orthorhombic (*o*-), tetragonal (α- and β-), and cubic (γ-), where tetragonal phases show particularly high RT ionic conductivities of 2–3 mS cm^{-1}.[102,104] Owing to the presence of toxic Pb in $PbSnF_4$, significant attention has recently been paid to isostructural α-$BaSnF_4$ with an RT ionic conductivity of 3.5×10^{-4} S cm^{-1}. The high ionic conductivities of $BaSnF_4$ and $PbSnF_4$ (from ~10^{-4} to ~10^{-3} S cm^{-1} at 298 K) facilitate the development of RT-operable all-solid-state FIBs. Nevertheless, the limited electrochemical stability windows of $M_xSn_{2-x}F_4$ are considerably influenced by the high formation potential of Sn.

(3) Liquid electrolytes

For liquid electrolytes of FIBs, the usual strategy is to dissolve a F-containing salt in a solvent. Very few studies have been reported on aqueous FIB systems because of the unstable electrochemical characteristics of F ions in aqueous systems. Li et al.[105] designed an aqueous dual-ion battery involving both F and K ions as charge transfer agents, and the BiF_3 electrode with a $Bi_7F_{11}O_5$ buffering phase delivered a high capacity (218 mAh g^{-1} at a current density of 1 A g^{-1}) and exhibited a long lifespan (over 1000 cycles). Ionic liquid solvents allow the transport of selective ions when specific salt species are employed; however, the solubilities of most inorganic fluoride compounds are limited (typically less than 0.05 M).[25] Anion acceptors (AAs) are widely utilized to increase the dissolutions of inorganic F-containing salts.[106,107] Many studies have been reported on the application of B-containing compounds as AAs because the B ions in AA attract F ions, as demonstrated in LIB-related studies. CsF dissolved in ether-based ionic liquid solvents using B-containing AAs shows acceptable RT ionic conductivities; for example, an electrolyte comprising a saturated CsF salt dissolved in tetraglyme (G4) with triphenylboroxine (TPhBX) as an AA and lithium bis (oxalato) borate (LiBOB) as an additive, denoted as LiBOB/TPhBX/CsF/G4, exhibited an ionic conductivity of 1.20 mS cm^{-1} and a wide electrochemical stability window of 4.1 V; a Py/KF/G4 electrolyte (Py: pyridine-related compound) showed an ionic conductivity of 1.02×10^{-5} S cm^{-1}.[106,108-112]

The roles of AAs in liquid systems are indefinite due to the difficulties in controlling the undesired dissolution of fluoride electrodes (including BiF_3 and PbF_2).[110,113,114] Recently, AA-free ionic liquid electrolytes have also been reported, and a typical ionic conductivity of $\sim 10^{-3}$ S cm^{-1} was measured in a CsF/GBL (GBL: γ-butyrolactone) electrolyte.[115] Davis et al. synthesized a liquid tetraalkylammonium-in-ether electrolyte with a high ionic conductivity, wide operating voltage, and robust chemical stability, which enabled highly reversible cycling of Cu@LaF_3 core-shell cathode materials.[25]

1.3.3 Electrodes

Basic non-topotactic (de)fluorinations have been extensively employed as promising electrode reactions because of their multielectron nature. Typically, M/MF_x-type cathode materials for FIB can theoretically deliver extraordinary energy densities of 2000 Wh kg^{-1} or 5000 Wh L^{-1}.[65,77] Topotactic (de)fluorinations have also been utilized to design intercalation-type cathode materials, which show excellent structural reversibilities and high F ion tolerances.

(1) Metal/metal fluoride (M/MF_x) systems

The intrinsic multielectron process of M/MF_x systems leads to high capacities and high utilizations of active materials. Among the various M/MF_x couples, Cu/CuF_2, Co/CoF_2, Ni/NiF_2, Bi/BiF_3, Pb/PbF_2, Zn/ZnF_2, Mg/MgF_2, Ca/CaF_2, Ce/CeF_3, and La/LaF_3 have been evaluated as electrode materials in pioneering studies.[65,70-77] Bi/BiF_3 has been extensively used as an electrode material in early studies of both liquid and all-solid-state systems, where initial charge and discharge capacities of approximately 300 and less than 100 mAh g^{-1} (theoretical value: 384 mAh g^{-1}), respectively, with fast capacity deterioration have been achieved. Cu/CuF_2 is regarded as a promising cathode material due to its high theoretical capacity (843 mAh g^{-1}) and high electrode potential (~3.5 V vs. Li/LiF, Table 1-1). Thieu et al. reported an all-solid-state $CuF_2|La_{0.9}Ba_{0.1}F_{2.9}|La$ cell with an initial capacity of 68% that of the theoretical value and 30 reversible cycles.[77]

In terms of the reaction mechanism, it is commonly considered that M/MF_x (de)fluorination proceeds in a two-phase-transition pattern. Ideally, a direct phase transition occurs between M and MF_x without the generation of other intermediate phases or solid solutions. Haruyama et al. [116] have conducted density functional theory calculations and proved that the solid-solution pattern is unreasonable because one fluoride vacancy introduces one electron, whereas if this electron is doped in an MF_x supercell, it is far from the Fermi level (E_{Fermi}) and its escape is difficult, making it unstable, owing to the large band gap between M n*s* and F 2*p* orbitals. Recent studies on the microscopic observations of the Cu/CuF_2 system also supported the two-phase hypothesis.[76,117] The theoretical capacities of several M/MF_x couples are presented and compared in **Table 1.2**.

Table 1.2 Theoretical capacities* and reported performances of various M/MF_x couples

M/MF_x Couples	Gravimetric capacity / mAh g^{-1}	Volumetric capacity / mAh cm^{-3}	M/MF_x Couples	Gravimetric capacity / mAh g^{-1}	Volumetric capacity / mAh cm^{-3}
Li/LiF	3861	2062	V/VF_4	2105	11336
Ca/CaF_2	1337	2073	Fe/FeF_3	1440	3301
Ba/BaF_2	390	1402	Sn/SnF_2	452	2936
Sr/SrF_2	612	1554	Pb/PbF_2	259	8129
Na/NaF	1166	1132	Ni/NiF_2	913	3751
La/LaF_3	579	3560	Bi/BiF_3	385	14275
K/KF	685	591	Mo/MoF_5	1397	8095
Ce/CeF_3	574	3885	Co/CoF_2	910	12143

Mg/MgF_2	2205	3832	Co/CoF_3	1364	7558
Al/AlF_3	2980	8052	Cu/CuF_2	843	2608
Ti/TiF_4	2240	10167	Ag/AgF	248	7887
Cr/CrF_3	1546	11117	Au/AuF_3	408	11336
Zn/ZnF_2	820	5847			
Mn/MnF_3	1463	10874			
V/VF_4	2105	12859			

*The capacities are calculated based on metal (M) mass instead of the metal fluoride (MF_x) mass.

(2) Intercalation-type topotactic host materials

As abovementioned in Section 1.3.1 (2), host materials with perfect topotactic fluorination behaviors can be regarded as ideal candidates for $LiCoO_2$-like intercalation-type materials. Clemens et al. have reported the first electrochemical fluorination of perovskite-type $BaFeO_{2.5}$ utilizing an all-solid-state $BaFeO_{2.5}||MgF_2$ (or CeF_3) cell, and the formation of $BaFeO_{2.5}F_{0.5}$ and three reversible cycles have been demonstrated.

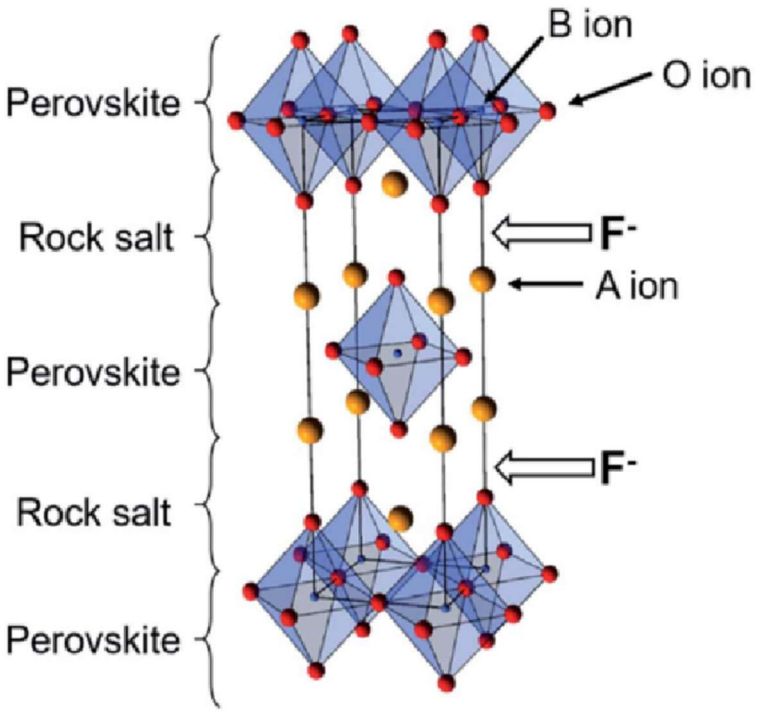

Figure 1.9 The K_2NiF_4-type structure consists of alternating layers of perovskite and rock-salt sub-units. Theoretically, F anions can be stored inside the rock-salt layers.[118]

Ruddlesden−Popper compounds and their derivatives have also been investigated as promising intercalation-type materials. The Ruddlesden−Popper compounds with the general

formula A_2BX_4 (a typical K_2NiF_4 structure, **Figure 1.9**) comprise two repeated layers, the perovskite layer ABX_3, and the rocksalt layer AX; large amounts of anionic deficiencies exist in the AX layer. [118] Nowroozi et al. developed $LaSrMnO_4$, La_2CoO_4, and $La_2NiO_{4+\delta}$ as intercalation-type cathode materials and theoretically proved the possibility of the application of these materials as intercalation-type cathode materials.[67,118,119] Recently, topotactic F^- (de)intercalation in Schafarzikite-type $FeSb_2O_4$ materials with tunnel-like structures has been reported; however, data on successful battery cycling are still lacking. [120,121] Recently, an interesting electrochemical oxidative fluorination of ReO_3, which possesses an A-site vacant perovskite structure, has been reported. In this study, F^- was inserted into the A site of the perovskite structure, resulting in the migration of Re ions to tetrahedral sites and the formation of $[ReO_3F]$ tetrahedra.[79]

1.3.4 Bottlenecks and outlooks of fluoride-ion batteries

Ever since FIBs again attracted attention in 2011, several major studies related to electrolytes and electrode materials for FIBs have been reported. Nevertheless, compared with the cases of highly mature LIB systems, various concerns related to the application of FIBs are worth considering.

First, a suitable electrolyte system for FIBs is lacking. The ionic conductivities of both liquid and solid electrolytes fail to meet the requirements of high-performance secondary batteries. Second, for both the electrolyte and the electrode, recent studies have focused on limited material repertoires, and consequently, promising candidates for application as electrolytes and electrodes are few. Thus, more categories of materials should be developed. Third, *in situ* techniques applicable to all-solid-state batteries are urgently needed. Fourth, the fluorination of oxide compounds leads to intrinsic mixed-anion characteristics, which will provide new insights into the kinetics and electronic structures of materials.

In terms of battery performance, cathode materials play significant roles because they determine the overall capacities and cell voltages, which are directly related with energy densities; the rate capabilities of electrode materials also determine the power densities of batteries. However, the current research on cathode materials for FIBs is still in its infancy and approximate. Problems such as the undesired cycling lives of M/MF_x materials due to their large volumetric expansions and low capacities and unclarified mechanisms of intercalation-type materials still remain unsolved. It is believed that the designs and studies of high-

performance cathode materials for FIBs are of vital importance, and more efforts should be devoted to understanding the fundamental mechanisms of fluorination reactions.

1.4 Objective

In this chapter, we focused on the fundamental principles and recent progress of FIBs and found that new understandings and continuous development of electrode and electrolyte materials are required. Cu-based materials have attracted our attention because of the high fluorination potential of the Cu/CuF_2 couple. $Cu/Cu^+/Cu^{2+}$ redox species possess high fluorination potentials, resulting in high cell voltages and thus high energy densities; nevertheless, to date, except for the simple Cu/CuF_2 material, no studies have been reported on Cu-based cathode materials. The $[Ar]3d^{10}4s^1$ electronic configuration of Cu renders a distinctive monovalent Cu cation, potentiating a series of compounds with low coordination numbers (**Figure 1.10**), for instance, 4-fold CuCl with tetrahedral $[CuCl_4]$, 2-fold $LaCuO_2$, Cu_2O, and Cu_3N with linear [X-Cu-X] (X = O, N). The existence of numerous anion vacancies around low-coordination Cu^+ facilitates F (de)intercalation; this structural diversity of Cu-containing materials substantially broadens the range of promising cathode materials for FIBs.

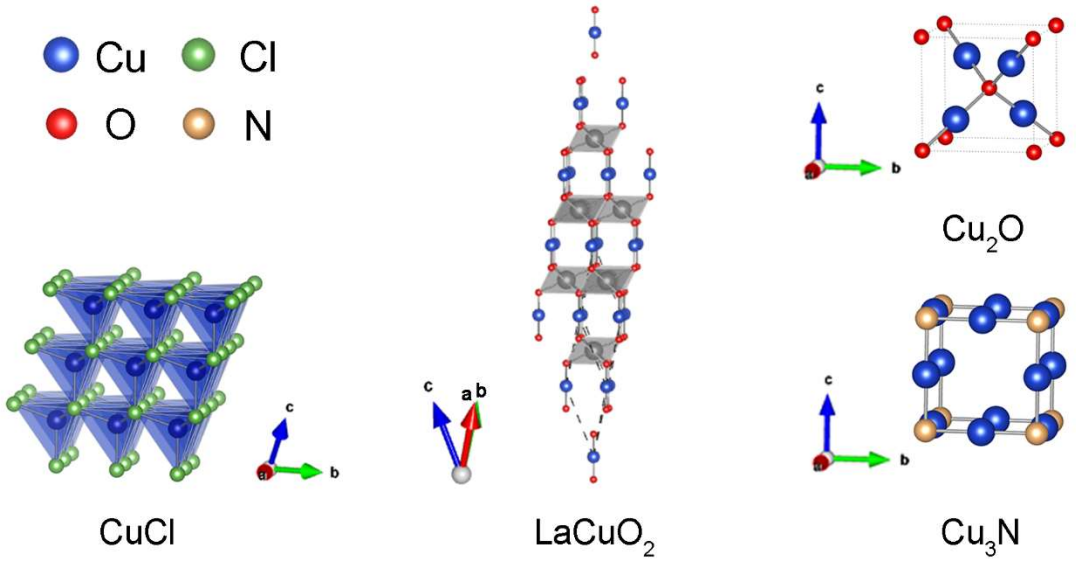

Figure 1.10 Typical Cu-containing materials with low coordination numbers of Cu^+ center.

Additionally, it is inevitable to test all-solid-state systems at elevated temperatures because the ionic conductivities of solid electrolytes are lower than those of liquid electrolytes; however, high thermal stabilities and active-material compatibility of solid electrolytes enable independent and accurate evaluations of electrode behaviors. Moreover, flexible and compact

devices can be easily acquired using all-solid-state batteries, which is also consistent with the purpose of intelligentization. Therefore, all-solid-state cells were employed in our study.

In this thesis, cathode materials for FIBs with high energy densities were designed and studied. The research project focused on diverse Cu-containing material systems, ranging from basic 3d transition metal systems to reversible open lattices until topotactic infinite-layer-related oxide materials, involving both cationic (Cu) and anionic redox. Furthermore, kinetic factors of solid electrolytes are analyzed and discussed. The corresponding (de)fluorination mechanisms, electronic/local structures, and crystal evolutions of cathode materials have been clarified based on the electrochemical behaviors and synchrotron X-ray spectroscopy. We believe that the present thesis will offer new insights with exciting possibilities for high-energy-density FIB cathode materials.

1.5 Outline of the present thesis

This thesis consists of eight chapters, which report the designs and studies of various Cu-based cathode materials for all-solid-state FIBs and a quantitative analysis of the kinetics of electrode/electrolyte interfacial reactions.

In Chapter 1, the fundamental principles of batteries are briefly described. Via a comparison of FIBs that utilize anions as charge carriers with the widely used LIBs that employ cations as charge carriers, the working principle, research progress, and current bottlenecks of FIBs are introduced. Particularly, the current bottlenecks that restrain the further progress of FIBs and the efforts to overcome these limitations are presented.

In Chapter 2, excellent electrochemical properties of fundamental Cu, Co, and Ni cathodes are reported, which are supported by the ideal environments created by thin-film cells. Owing to the near theoretical electrochemical behaviors of these cathodes, it is possible to obtain and understand the entire phase transition process via X-ray absorption spectroscopy (XAS). The two-phase reaction pattern of M/MF_x has been experimentally verified for the first time.

In Chapter 3, a rational design of Cu–Pb nanocomposites with high electrochemical performances at RT is reported. The PbF_2 composites self-generated in advance from Pb were retained in the subsequent cycles and acted as fast F ion conductors, consequently enhancing the kinetics of the rest of the Cu/CuF_2 phase transition upon cycling. The detailed mechanisms were examined by XAS.

In Chapter 4, the first use of stable and low-cost Cu_2O as a cathode material for all-solid-state FIBs with reversible and fast (de)fluorination behaviors is reported. Via electrochemical behaviors and XAS, the mechanism of phase transition involving the Cu^{+}/Cu^{2+} redox for charge compensation was confirmed. Compared with previously reported materials, Cu_2O shows a superior rate capability, which is expected to deepen our understanding and bring new considerations toward the possibilities of practical applications of all-solid-state FIBs.

In Chapter 5, the utilization of anti-ReO_3-structured Cu_3N as a high-energy cathode material for all-solid-state FIBs is reported. The highly open lattice of Cu_3N provides numerous accessible anionic vacancies for F^{-} (de)intercalation. Interestingly, both cationic (Cu^{+}/Cu^{2+}) and anionic redox (N^{3-}/N^{0}) participate in charge compensation, where the signals of molecular N–N bonds can be detected by resonant inelastic X-ray scattering (RIXS). Thus, high capacity, stable cyclability, and excellent rate capability are achieved.

In Chapter 6, $Ca_{0.85}CuO_2$ with an infinite-layer-related structure was used as a high-energy cathode material for all-solid-state FIBs. In terms of charge compensation, the high-contribution ratio of O redox upon initial charging and the combined contribution of O and Cu redox in the following cycles are clarified. The presence of molecular O–O bonds was clearly observed by RIXS.

In Chapter 7, by comparing β-$Pb_{0.78}Sn_{1.22}F_4$, a promising solid electrolyte material for mild-temperature applications, with representative FIB and LIB solid electrolytes, the rate-determining factor for electrode/electrolyte interfacial reactions in all-solid-state FIBs was investigated using chronoamperometric measurements and Allen-Hickling simulations. Results indicate that mass transfer (electrolyte-side F ion conduction) should be the rate-determining process at the electrode/electrolyte interface of all-solid-state FIBs. It is also believed that superior rate capabilities can be realized in all-solid-state FIBs similar to those in all-solid-state LIBs by developing high-conductivity solid electrolytes.

In Chapter 8, general conclusions are drawn and presented based on the abovementioned discussion; moreover, prospects for the future development of rechargeable all-solid-state FIBs are provided.

Reference

1. Armand, M.; Tarascon, J. M., Building better batteries. *Nature* **2008,** *451* (7179), 652-657.

2. Yabuuchi, N.; Kubota, K.; Dahbi, M.; Komaba, S., Research development on sodium-ion batteries. *Chem. Rev.* **2014,** *114* (23), 11636-11682.

3. Chu, S.; Cui, Y.; Liu, N., The path towards sustainable energy. *Nat. Mater.* **2017,** *16* (1), 16-22.

4. Grey, C.; Tarascon, J., Sustainability and in situ monitoring in battery development. *Nat. Mater.* **2017,** *16* (1), 45-56.

5. Islam, M. S.; Fisher, C. A. J., Lithium and sodium battery cathode materials: computational insights into voltage, diffusion and nanostructural properties. *Chem. Soc. Rev.* **2014,** *43* (1), 185-204.

6. The 75th ordinary session of general assembly of the United Nations. https://journal.un.org/en/meeting/officials/e6d6ab5e-c0de-ea11-9114-0050569e8b67/2020-09-22 (accessed Sep 23, 2021).

7. Fostering a New Development Paradigm and Pursuing Mutual Benefit and Win-win Cooperation, Ministry of Foreign Affairs, the People's Republic of China. https://www.fmprc.gov.cn/mfa_eng/wjdt_665385/zyjh_665391/t1833641.shtml (accessed Sep 23, 2021).

8. SONY Corp. https://www.sony.com/en/SonyInfo/News/Press_Archive/200412/04-060E/ (accessed Sep 23, 2021).

9. Lithium ion battery production capacity by 2028, by company, Statista. https://www.statista.com/statistics/1103401/predicted-lithium-ion-battery-capacity-by-company/ (accessed Sep 23, 2021).

10. Battery Shipment and Installation for EV/ESS, SNE Research. http://www.sneresearch.com/_new/eng/sub/sub2/sub2_01_view.php?id=95901&s_keyword=&f_date=&t_date=&pg=1 (accessed Sep 23, 2021).

11. Merryweather, A. J.; Schnedermann, C.; Jacquet, Q.; Grey, C. P.; Rao, A., Operando optical tracking of single-particle ion dynamics in batteries. *Nature* **2021,** *594* (7864), 522-528.

12. Made in China 2025, MInistry of Industry and Information Technology of the People's Republic of China. https://www.miit.gov.cn/ztzl/lszt/zgzz2025/index.html (accessed Sep 23, 2021).

13. 四部委关于印发《促进汽车动力电池产业发展行动方案》的通知, the State Council, the People's Republic of China. http://www.gov.cn/xinwen/2017-03/02/content_5172254.htm#1 (accessed Sep 23, 2021).

14. Battery500: Progress Update, Office of Energy Efficiency & Renewable Energy, U.S. Department of Energy. https://www.energy.gov/eere/articles/battery500-progress-update (accessed Sep 23, 2021).

15. Fu, X.; Beatty, D. N.; Gaustad, G. G.; Ceder, G.; Roth, R.; Kirchain, R. E.; Bustamante, M.; Babbitt, C.; Olivetti, E. A., Perspectives on Cobalt Supply through 2030 in the Face of Changing Demand. *Environ. Sci. Technol.* **2020,** *54* (5), 2985-2993.

16. Delmas, C.; Braconnier, J. J.; Fouassier, C.; Hagenmuller, P., Electrochemical intercalation of sodium in Na_xCoO_2 bronzes. *Solid State Ionics* **1981,** *3–4* (AUG), 165-169.

17. Aurbach, D.; Lu, Z.; Schechter, A.; Gofer, Y.; Gizbar, H.; Turgeman, R.; Cohen, Y.; Moshkovich, M.; Levi, E., Prototype systems for rechargeable magnesium batteries. *Nature* **2000,** *407* (6805), 724-7.

18. Anji Reddy, M.; Fichtner, M., Batteries based on fluoride shuttle. *J. Mater. Chem.* **2011,** *21* (43), 17059-17062.

19. Xu, C.; Li, B.; Du, H.; Kang, F., Energetic zinc ion chemistry: the rechargeable zinc ion battery. *Angew. Chem. Int. Ed. Engl.* **2012,** *51* (4), 933-935.

20. Zhao, X.; Zhao-Karger, Z.; Wang, D.; Fichtner, M., Metal oxychlorides as cathode materials for chloride ion batteries. *Angew. Chem. Int. Ed. Engl.* **2013,** *52* (51), 13621-13624.

21. Jian, Z.; Luo, W.; Ji, X., Carbon Electrodes for K-Ion Batteries. *J. Am. Chem. Soc.* **2015,** *137* (36), 11566-11569.

22. Lin, M. C.; Gong, M.; Lu, B.; Wu, Y.; Wang, D. Y.; Guan, M.; Angell, M.; Chen, C.; Yang, J.; Hwang, B. J.; Dai, H., An ultrafast rechargeable aluminium-ion battery. *Nature* **2015,** *520* (7547), 325-328.

23. Gao, P.; Reddy, M. A.; Mu, X.; Diemant, T.; Zhang, L.; Zhao-Karger, Z.; Chakravadhanula, V. S.; Clemens, O.; Behm, R. J.; Fichtner, M., VOCl as a Cathode for Rechargeable Chloride Ion Batteries. *Angew. Chem. Int. Ed. Engl.* **2016,** *55* (13), 4285-90.

24. Ponrouch, A.; Frontera, C.; Barde, F.; Palacin, M. R., Towards a calcium-based rechargeable battery. *Nat. Mater.* **2016,** *15* (2), 169-72.

25. Davis, V. K.; Bates, C. M.; Omichi, K.; Savoie, B. M.; Momcilovic, N.; Xu, Q.; Wolf, W. J.; Webb, M. A.; Billings, K. J.; Chou, N. H.; Alayoglu, S.; McKenney, R. K.; Darolles, I. M.; Nair, N. G.; Hightower, A.; Rosenberg, D.; Ahmed, M.; Brooks, C. J.; Miller, T. F., 3rd; Grubbs, R. H.; Jones, S. C., Room-temperature cycling of metal fluoride electrodes: Liquid electrolytes for high-energy fluoride ion cells. *Science* **2018,** *362* (6419), 1144-1148.

26. Wang, M.; Jiang, C.; Zhang, S.; Song, X.; Tang, Y.; Cheng, H. M., Reversible calcium alloying enables a practical room-temperature rechargeable calcium-ion battery with a high discharge voltage. *Nat. Chem.* **2018,** *10* (6), 667-672.

27. Zhao, S.; Han, B.; Zhang, D.; Huang, Q.; Xiao, L.; Chen, L.; Ivey, D. G.; Deng, Y.; Wei, W., Unravelling the reaction chemistry and degradation mechanism in aqueous Zn/MnO_2 rechargeable batteries. *J. Mater. Chem. A* **2018,** *6* (14), 5733-5739.

28. Binghamton University professor wins Nobel Prize in Chemistry, BingUNews, Binghamton University, State University of New York. https://www.binghamton.edu/news/story/2073/binghamton-university-professor-wins-nobel-prize-in-chemistry (accessed Sep 23, 2021).

29. Whittingham, M. S., Electrical energy storage and intercalation chemistry. *Science* **1976,** *192* (4244), 1126-7.

30. Mizushima, K.; Jones, P. C.; Wiseman, P. J.; Goodenough, J. B., Li_xCoO_2 ($0<x<-1$): A new cathode material for batteries of high energy density. *Mater. Res. Bull.* **1980,** *15* (6), 783-789.

31. Nakajima, T.; Sanechika, K.-i.; Yoshino, A. Secondary battery. US4668595A, May 9, 1986.

32. Yoshino, A.; Sanechika, K.; Nakajima, T. 防爆型二次電池. JP2642206, Dec 28, 1989.

33. Zhang, Y.; Li, Y.; Xia, X.; Wang, X.; Gu, C.; Tu, J., High-energy cathode materials for Li-ion batteries: A review of recent developments. *Sci. Chin. Technol. Sci.* **2015,** *58* (11), 1809-1828.

34. Qian, J.; Liu, L.; Yang, J.; Li, S.; Wang, X.; Zhuang, H. L.; Lu, Y., Electrochemical surface passivation of $LiCoO_2$ particles at ultrahigh voltage and its applications in lithium-based batteries. *Nat Commun* **2018,** *9* (1), 4918.

35. Reimers, J. N.; Dahn, J. R., Electrochemical and In Situ X-Ray Diffraction Studies of Lithium Intercalation in Li_xCoO_2. *J. Electrochem. Soc.* **1992,** *139* (8), 2091-2097.

36. Lee, J.-I.; Lee, E.-H.; Park, J.-H.; Park, S.; Lee, S.-Y., Ultrahigh-Energy-Density Lithium-Ion Batteries Based on a High-Capacity Anode and a High-Voltage Cathode with an Electroconductive Nanoparticle Shell. *Adv. Energy Mater.* **2014,** *4* (8), 1301542.

37. Kalluri, S.; Yoon, M.; Jo, M.; Park, S.; Myeong, S.; Kim, J.; Dou, S. X.; Guo, Z.; Cho, J., Surface Engineering Strategies of Layered $LiCoO_2$ Cathode Material to Realize High-Energy and High-Voltage Li-Ion Cells. *Adv. Energy Mater.* **2017,** *7* (1), 1601507.

38. Wizansky, A. R.; Rauch, P. E.; Disalvo, F. J., Powerful oxidizing agents for the oxidative deintercalation of lithium from transition-metal oxides. *J. Solid State Chem.* **1989,** *81* (2), 203-207.

39. Ohzuku, T.; Ueda, A., Solid-State Redox Reactions of $LiCoO_2$ (*R*-3*m*) for 4 Volt Secondary Lithium Cells. *J. Electrochem. Soc.* **2019,** *141* (11), 2972-2977.

40. Gupta, R.; Manthiram, A., Chemical Extraction of Lithium from Layered $LiCoO_2$. *J. Solid State Chem.* **1996,** *121* (2), 483-491.

41. Wang, Z. X.; Dong, H.; Chen, L. Q.; Mo, Y. J.; Huang, X. J., Understanding mechanism of improved electrochemical performance of surface modified $LiCoO_2$. *Solid State Ionics* **2004,** *175* (1-4), 239-242.

42. Thackeray, M. M.; Kang, S. H.; Johnson, C. S.; Vaughey, J. T.; Benedek, R.; Hackney, S. A., Li_2MnO_3-stabilized $LiMO_2$ (M = Mn, Ni, Co) electrodes for lithium-ion batteries. *J. Mater. Chem.* **2007,** *17* (30), 3112-3125.

43. Yoon, W. S.; Kim, N.; Yang, X. Q.; Mcbreen, J.; Grey, C. P., ^{6}Li MAS NMR and in situ X-ray studies of lithium nickel manganese oxides. *J. Power Sources* **2003,** *s119–121* (119), 649-653.

44. Yu, H.; Ishikawa, R.; So, Y. G.; Shibata, N.; Kudo, T.; Zhou, H.; Ikuhara, Y., Direct Atomic - Resolution Observation of Two Phases in the $Li_{1.2}Mn_{0.567}Ni_{0.166}Co_{0.067}O_2$ Cathode Material for Lithium - Ion Batteries. *Angew. Chem.* **2013,** *52* (23), 5969-5973.

45. Yu, H.; So, Y. G.; Kuwabara, A.; Tochigi, E.; Shibata, N.; Kudo, T.; Zhou, H.; Ikuhara, Y., Crystalline Grain Interior Configuration Affects Lithium Migration Kinetics in Li-Rich Layered Oxide. *Nano Lett.* **2016,** *16* (5), 2907-2915.

46. Clément, R. J.; Lun, Z.; Ceder, G., Cation-disordered rocksalt transition metal oxides and oxyfluorides for high energy lithium-ion cathodes. *Energy Environ. Sci.* **2020,** *13* (2), 345-373.

47. Urban, A.; Lee, J.; Ceder, G., The Configurational Space of Rocksalt-Type Oxides for High-Capacity Lithium Battery Electrodes. *Adv. Energy Mater.* **2014,** *4* (13), 1400478.

48. Ji, H.; Wu, J.; Cai, Z.; Liu, J.; Kwon, D.-H.; Kim, H.; Urban, A.; Papp, J. K.; Foley, E.; Tian, Y.; Balasubramanian, M.; Kim, H.; Clément, R. J.; McCloskey, B. D.; Yang, W.; Ceder, G., Ultrahigh power and energy density in partially ordered lithium-ion cathode materials. *Nat. Energy* **2020,** *5* (3), 213-221.

49. Seo, D. H.; Lee, J.; Urban, A.; Malik, R.; Kang, S.; Ceder, G., The structural and chemical origin of the oxygen redox activity in layered and cation-disordered Li-excess cathode materials. *Nat. Chem.* **2016,** *8* (7), 692-697.

50. Yang, W., Oxygen release and oxygen redox. *Nat. Energy* **2018,** *3* (8), 619-620.

51. Huang, J. P.; Zhong, P. C.; Ha, Y.; Kwon, D. H.; Crafton, M. J.; Tian, Y. S.; Balasubramanian, M.; McCloskey, B. D.; Yang, W. L.; Ceder, G., Non-topotactic reactions enable high rate capability in Li-rich cathode materials. *Nat. Energy* **2021,** *6* (7), 706-714.

52. Tarascon, J. M.; Armand, M., Issues and challenges facing rechargeable lithium batteries. *Nature* **2001,** *414* (6861), 359-367.

53. Delmas, C.; Nadiri, A.; Soubeyroux, J. L., The Nasicon-Type Titanium Phosphates $ATi_2(PO_4)_3$ (A = Li, Na) as Electrode Materials. *Solid State Ionics* **1988,** *28-30* (Part 1), 419-423.

54. Manthiram, A.; Goodenough, J. B., Lithium insertion into $Fe_2(SO_4)_3$ frameworks. *J. Power Sources* **1989,** *26* (s 3–4), 403–408.

55. Padhi, A. K.; Nanjundaswamy, K. S.; Goodenough, J. B., Phospho - olivines as Positive - Electrode Materials for Rechargeable Lithium Batteries. *J. Electrochem. Soc.* **1997,** *144* (4), 1188-1194.

56. Padhi, A. K.; Nanjundaswamy, K. S.; Masquelier, C.; Okada, S.; Goodenough, J. B., Effect of Structure on the Fe^{3+}/Fe^{2+} Redox Couple in Iron Phosphates. *J. Electrochem. Soc.* **1997,** *144* (5), 1609-1613.

57. Zou, Y.; Chen, S.; Yang, X.; Ma, N.; Xia, Y.; Yang, D.; Guo, S., Suppressing Fe-Li Antisite Defects in $LiFePO_4$/Carbon Hybrid Microtube to Enhance the Lithium Ion Storage. *Adv. Energy Mater.* **2016,** *6* (24), 1601549.

58. Li, Y.; Sun, W.; Liang, J.; Sun, H.; Di Marco, I.; Ni, L.; Tang, S.; Zhang, J., Understanding the electrochemical properties of A_2MSiO_4 (A = Li and Na; M = Fe, Mn, Co and Ni) and the Na doping effect on Li_2MSiO_4 from first-principles calculations. *J. Mater. Chem. A* **2016,** *4* (44), 17455-17463.

59. Nytén, A.; Abouimrane, A.; Armand, M.; Gustafsson, T.; Thomas, J. O., Electrochemical performance of Li_2FeSiO_4 as a new Li-battery cathode material. *Electrochem. Commun.* **2005,** *7* (2), 156-160.

60. Dominko, R.; Bele, M.; Gaberšček, M.; Meden, A.; Remškar, M.; Jamnik, J., Structure and electrochemical performance of Li_2MnSiO_4 and Li_2FeSiO_4 as potential Li-battery cathode materials. *Electrochem. Commun.* **2006,** *8* (2), 217-222.

61. Cheng, Q.; He, W.; Zhang, X.; Li, M.; Wang, L., Modification of Li_2MnSiO_4 cathode materials for lithium-ion batteries: a review. *J. Mater. Chem. A* **2017,** *5* (22), 10772-10797.

62. Islam, M. S.; Dominko, R.; Masquelier, C.; Sirisopanaporn, C.; Armstrong, A. R.; Bruce, P. G., Silicate cathodes for lithium batteries: alternatives to phosphates? *J. Mater. Chem.* **2011,** *21* (27), 9811-9818.

63. Massé, R. C.; Uchaker, E.; Cao, G., Beyond Li-ion: electrode materials for sodium- and magnesium-ion batteries. *Sci. Chin. Mater.* **2015,** *58* (9), 715-766.

64. Manthiram, A., A reflection on lithium-ion battery cathode chemistry. *Nat. Commun.* **2020,** *11* (1), 1550.

65. Zhang, D.; Yamamoto, K.; Ochi, A.; Wang, Y.; Yoshinari, T.; Nakanishi, K.; Nakano, H.; Miki, H.; Nakanishi, S.; Iba, H.; Uchiyama, T.; Watanabe, T.; Amezawa, K.; Uchimoto, Y., Understanding the reaction mechanism and performances of 3d transition metal cathodes for all-solid-state fluoride ion batteries. *J. Mater. Chem. A* **2021,** *9* (1), 406-412.

66. Zu, C.-X.; Li, H., Thermodynamic analysis on energy densities of batteries. *Energy Environ. Sci.* **2011,** *4* (8), 2614–2624.

67. Nowroozi, M. A.; Wissel, K.; Rohrer, J.; Munnangi, A. R.; Clemens, O., $LaSrMnO_4$: Reversible Electrochemical Intercalation of Fluoride Ions in the Context of Fluoride Ion Batteries. *Chem. Mater.* **2017,** *29* (8), 3441-3453.

68. Motohashi, K.; Nakamura, T.; Kimura, Y.; Uchimoto, Y.; Amezawa, K., Influence of microstructures on conductivity in Tysonite-type fluoride ion conductors. *Solid State Ionics* **2019,** *338*, 113-120.

69. Thermodynamic Database MALT for Windows, Kagaku Gijutsu-Sha. https://www.kagaku.com/malt/index.html (accessed Sep 23, 2021).

70. Rongeat, C.; Reddy, M. A.; Witter, R.; Fichtner, M., Nanostructured Fluorite-Type Fluorides As Electrolytes for Fluoride Ion Batteries. *J. Phys. Chem. C* **2013,** *117* (10), 4943-4950.

71. Düvel, A.; Bednarcik, J.; Šepelák, V.; Heitjans, P., Mechanosynthesis of the Fast Fluoride Ion Conductor $Ba_{1-x}La_xF_{2+x}$: From the Fluorite to the Tysonite Structure. *J. Phys. Chem. C* **2014,** *118* (13), 7117-7129.

72. Rongeat, C.; Reddy, M. A.; Witter, R.; Fichtner, M., Solid electrolytes for fluoride ion batteries: ionic conductivity in polycrystalline tysonite-type fluorides. *ACS Appl. Mater. Interfaces* **2014,** *6* (3), 2103-2110.

73. Zhang, L.; Anji Reddy, M.; Fichtner, M., Development of tysonite-type fluoride conducting thin film electrolytes for fluoride ion batteries. *Solid State Ionics* **2015,** *272*, 39-44.

74. Liu, L.; Yang, L.; Liu, M.; Wang, X.; Li, X.; Shao, D.; Luo, K.; Luo, Z.; Chen, G., A flexible tysonite-type $La_{0.95}Ba_{0.05}F_{2.95}$@PEO-based composite electrolyte for the application of advanced fluoride ion battery. *J. Energy Storage* **2019,** *25*, 100886.

75. Molaiyan, P.; Witter, R., Surface defect-enhanced conductivity of calcium fluoride for electrochemical applications. *Mater. Des. Process. Commun.* **2019,** *1* (4), e44.

76. Fawey, M. H.; Chakravadhanula, V. S. K.; Munnangi, A. R.; Rongeat, C.; Hahn, H.; Fichtner, M.; Kübel, C., First results from in situ transmission electron microscopy studies of all-solid-state fluoride ion batteries. *J. Power Sources* **2020,** *466*, 228283.

77. Thieu, D. T.; Fawey, M. H.; Bhatia, H.; Diemant, T.; Chakravadhanula, V. S. K.; Behm, R. J.; Kübel, C.; Fichtner, M., CuF_2 as Reversible Cathode for Fluoride Ion Batteries. *Adv. Funct. Mater.* **2017,** *27* (31), 1701051.

78. Clemens, O.; Rongeat, C.; Reddy, M. A.; Giehr, A.; Fichtner, M.; Hahn, H., Electrochemical fluorination of perovskite type $BaFeO_{2.5}$. *Dalton Trans.* **2014,** *43* (42), 15771-15778.

79. Bashian, N. H.; Zuba, M.; Irshad, A.; Becwar, S. M.; Vinckeviciute, J.; Rahim, W.; Griffith, K. J.; McClure, E. T.; Papp, J. K.; McCloskey, B. D.; Scanlon, D. O.; Chmelka, B. F.; Van der Ven, A.; Narayan, S. R.; Piper, L. F. J.; Melot, B. C., Electrochemical Oxidative Fluorination of an Oxide Perovskite. *Chem. Mater.* **2021,** *33* (14), 5757-5768.

80. Greaves, C.; Francesconi, M. G., Fluorine insertion in inorganic materials. *Curr. Opin. Solid State Mater. Sci.* **1998,** *3* (2), 132-136.

81. McCabe, E. E.; Greaves, C., Fluorine insertion reactions into pre-formed metal oxides. *J. Fluorine Chem.* **2007,** *128* (4), 448-458.

82. Clemens, O.; Slater, P. R., Topochemical modifications of mixed metal oxide compounds by low-temperature fluorination routes. *Rev. Inorg. Chem.* **2013,** *33* (2-3), 105-117.

83. Ai-Mamouri, M.; Edwards, P. P.; Greaves, C.; Slaski, M., Synthesis and superconducting properties of the strontium copper oxy-fluoride $Sr_2CuO_2F_{2+\delta}$. *Nature* **1994,** *369* (6479), 382-384.

84. Slater, P. R., Poly(vinylidene fluoride) as a reagent for the synthesis of K_2NiF_4-related inorganic oxide fluorides. *J. Fluorine Chem.* **2002,** *117* (1), 43-45.

85. Slater, P. R.; Gover, R. K. B., Synthesis and structure of the new oxide fluoride $Sr_2TiO_3F_2$ from the low temperature fluorination of Sr_2TiO_4: an example of a staged fluorine substitution/insertion reaction. *J. Mater. Chem.* **2002,** *12* (2), 291-294.

86. Aikens, L. D.; Li, R. K.; Greaves, C., The synthesis and structure of a new oxide fluoride, $LaSrMnO_4F$, with staged fluorine insertion. *Chem. Commun.* **2000,** (21), 2129-2130.

87. Aikens, L. D.; Gillie, L. J.; Li, R. K.; Greaves, C., Staged fluorine insertion into manganese oxides with Ruddlesden–Popper structures: $LaSrMnO_4F$ and $La_{1.2}Sr_{1.8}Mn_2O_7F$. *J. Mater. Chem.* **2002,** *12* (2), 264-267.

88. Liu, L.; Yang, L.; Liu, M.; Li, X.; Shao, D.; Luo, K.; Wang, X.; Luo, Z., SnF2-based fluoride ion electrolytes MSnF4 (M = Ba, Pb) for the application of room-temperature solid-state fluoride ion batteries. *J. Alloys Compd.* **2020,** *819*, 152983.

89. Murray, E.; Brougham, D. F.; Stankovic, J.; Abrahams, I., Conductivity and Fluoride Ion Dynamics in α-$PbSnF_4$; ^{19}F Field-Cycling NMR and Diffraction Studies. *J. Phys. Chem. C* **2008,** *112* (14), 5672-5678.

90. Preishuber-Pflügl, F.; Epp, V.; Nakhal, S.; Lerch, M.; Wilkening, M., Defect-enhanced F-ion conductivity in layer-structured nanocrystalline $BaSnF_4$ prepared by high-energy ball milling combined with soft annealing. *Phys. Status Solidi C* **2015,** *12* (1-2), 10-14.

91. Schoonman, J., A Solid-State Galvanic Cell with Fluoride-Conducting Electrolytes. *J. Electrochem. Soc.* **1976,** *123* (12), 1772-1775.

92. Danto, Y.; Poujade, G.; Pistré, J. D.; Lucat, C.; Salardenne, J., A $Pb|PbF_2|BiF_3|Bi$ thin solid film reversible galvanic cell. *Thin Solid Films* **1978,** *55* (3), 347-354.

93. Schoonman, J.; Wapenaar, K. E. D.; Oversluizen, G.; Dirksen, G. J., Fluoride-Conducting Solid Electrolytes in Galvanic Cells. *J. Electrochem. Soc.* **1979,** *126* (5), 709-713.

94. Nowroozi, M. A.; Mohammad, I.; Molaiyan, P.; Wissel, K.; Munnangi, A. R.; Clemens, O., Fluoride ion batteries – past, present, and future. *J. Mater. Chem. A* **2021,** *9* (10), 5980-6012.

95. Schoonman, J.; Wolfert, A., Alloy-anodes in fluoride solid-state batteries. *J. Electrochem. Soc.* **1981,** *128* (7), 1522-1523.

96. Schoonman, J.; Wolfert, A., Solid-state galvanic cells with fast fluoride conducting electrolytes. *Solid State Ionics* **1981,** *3-4*, 373-379.

97. Grenier, A.; Porras-Gutierrez, A. G.; Body, M.; Legein, C.; Chrétien, F.; Raymundo-Piñero, E.; Dollé, M.; Groult, H.; Dambournet, D., Solid Fluoride Electrolytes and Their Composite with Carbon: Issues and Challenges for Rechargeable Solid State Fluoride-Ion Batteries. *J. Phys. Chem. C* **2017,** *121* (45), 24962-24970.

98. Dieudonné, B.; Chable, J.; Mauvy, F.; Fourcade, S.; Durand, E.; Lebraud, E.; Leblanc, M.; Legein, C.; Body, M.; Maisonneuve, V.; Demourgues, A., Exploring the $Sm_{1-x}Ca_xF_{3-x}$ Tysonite Solid Solution as a Solid-State Electrolyte: Relationships between Structural Features and F^- Ionic Conductivity. *J. Phys. Chem. C* **2015,** *119* (45), 25170-25179.

99. Dieudonne, B.; Chable, J.; Body, M.; Legein, C.; Durand, E.; Mauvy, F.; Fourcade, S.; Leblanc, M.; Maisonneuve, V.; Demourgues, A., The key role of the composition and structural features in fluoride ion conductivity in tysonite $Ce_{1-x}Sr_xF_{3-x}$ solid solutions. *Dalton Trans.* **2017,** *46* (11), 3761-3769.

100. Castiglione, M.; Madden, P. A.; Berastegui, P.; Hull, S., The crystal structure of α-PbSnF4 and its anion diffusion mechanism. *J. Phys. Condens. Matt.* **2005,** *17* (6), 845-861.

101. Murakami, M.; Morita, Y.; Yonemura, M.; Shimoda, K.; Mori, M.; Koyama, Y.; Kawaguchi, T.; Fukuda, K.; Ishikawa, Y.; Kamiyama, T.; Uchimoto, Y.; Ogumi, Z., High anionic conductive form of $Pb_xSn_{2-x}F_4$. *Chem. Mater.* **2019,** *31* (18), 7704-7710.

102. Zhang, D.; Nakano, H.; Yamamoto, K.; Tanaka, K.; Yahara, T.; Imai, K.; Mori, T.; Miki, H.; Nakanishi, S.; Iba, H.; Watanabe, T.; Uchiyama, T.; Amezawa, K.; Uchimoto, Y., Rate-Determining Process at Electrode/Electrolyte Interfaces for All-Solid-State Fluoride-Ion Batteries. *ACS Appl. Mater. Interfaces* **2021,** *13* (25), 30198-30204.

103. Dénès, G.; Milova, G.; Madamba, M. C.; Perfiliev, M., Structure and Ionic Transport of $PbSnF_4$ Superionic Conductor. *Solid State Ionics* **1996,** *86-88*, 77-82.

104. Hagenmuller, P.; Reau, J.; Lucat, C.; Matar, S.; Villeneuve, G., Ionic Conductivity of Fluorite-type Fluorides. *Solid State Ionics* **1981,** *3-4*, 341-345.

105. Li, X.; Tang, Y.; Zhu, J.; Lv, H.; Xu, Y.; Wang, W.; Zhi, C.; Li, H., Initiating a Room-Temperature Rechargeable Aqueous Fluoride-Ion Battery with Long Lifespan through a Rational Buffering Phase Design. *Adv. Energy Mater.* **2021,** *11* (14), 2003714.

106. Konishi, H.; Minato, T.; Abe, T.; Ogumi, Z., Charge and Discharge Reactions of a Lead Fluoride Electrode in a Liquid - Based Electrolyte for Fluoride Shuttle Batteries: - The Role of Triphenylborane as an Anion Acceptor - . *ChemistrySelect* **2019,** *4* (19), 5984-5987.

107. Konishi, H.; Minato, T.; Abe, T.; Ogumi, Z., Electrochemical Performance of a Bismuth Fluoride Electrode in a Reserve-Type Fluoride Shuttle Battery. *J. Electrochem. Soc.* **2017,** *164* (14), A3702-A3708.

108. Konishi, H.; Minato, T.; Abe, T.; Ogumi, Z., Electrochemical Properties of Lead Fluoride Electrode in Fluoride Shuttle Battery. *J. Electroanal. Chem.* **2018,** *826*, 60-64.

109. Konishi, H.; Minato, T.; Abe, T.; Ogumi, Z., Triphenylboroxine and Triphenylborane as Anion Acceptors for Electrolyte in Fluoride Shuttle Batteries. *Chem. Lett.* **2018,** *47* (11), 1346-1349.

110. Konishi, H.; Minato, T.; Abe, T.; Ogumi, Z., Electrochemical Performance of A Lead Fluoride Electrode Mixed with Carbon in An Electrolyte Containing Triphenylboroxine as An Anion Acceptor for Fluoride Shuttle Batteries. *Mater. Chem. Phys.* **2019,** *226*, 1-5.

111. Konishi, H.; Minato, T.; Abe, T.; Ogumi, Z., Influence of Electrolyte Composition on the Electrochemical Reaction Mechanism of Bismuth Fluoride Electrode in Fluoride Shuttle Battery. *J. Phys. Chem. C* **2019,** *123* (16), 10246-10252.

112. Celik Kucuk, A.; Yamanaka, T.; Yokoyama, Y.; Abe, T., Low-Cost Fluoride Source for Organic Liquid Electrolyte-Based Fluoride Shuttle Battery. *J. Electrochem. Soc.* **2021,** *168* (1).

113. Rodríguez-Pérez, I. A.; Ji, X., Anion Hosting Cathodes in Dual-Ion Batteries. *ACS Energy Lett.* **2017,** *2* (8), 1762-1770.

114. Celik Kucuk, A.; Minato, T.; Yamanaka, T.; Abe, T., Effects of LiBOB on Salt Solubility and BiF_3 Electrode Electrochemical Properties in Fluoride Shuttle Batteries. *J. Mater. Chem. A* **2019,** *7* (14), 8559-8567.

115. Kawasaki, M.; Morigaki, K.-I.; Kano, G.; Nakamoto, H.; Takekawa, R.; Kawamura, J.; Minato, T.; Abe, T.; Ogumi, Z., Lactone-Based Liquid Electrolytes for Fluoride Shuttle Batteries. *J. Electrochem. Soc.* **2021,** *168* (1).

116. Haruyama, J.; Okazaki, K. I.; Morita, Y.; Nakamoto, H.; Matsubara, E.; Ikeshoji, T.; Otani, M., Two-Phase Reaction Mechanism for Fluorination and Defluorination in Fluoride-Shuttle Batteries: A First-Principles Study. *ACS Appl. Mater. Interfaces* **2020,** *12* (1), 428-435.

117. Nakano, H.; Matsunaga, T.; Mori, T.; Nakanishi, K.; Morita, Y.; Ide, K.; Okazaki, K. I.; Orikasa, Y.; Minato, T.; Yamamoto, K.; Ogumi, Z.; Uchimoto, Y., Fluoride-Ion Shuttle Battery with High Volumetric Energy Density. *Chem. Mater.* **2021,** *33* (1), 459-466.

118. Nowroozi, M. A.; Ivlev, S.; Rohrer, J.; Clemens, O., La_2CoO_4: A New Intercalation Based Cathode Material for Fluoride Ion Batteries with Improved Cycling Stability. *J. Mater. Chem. A* **2018,** *6* (11), 4658-4669.

119. Nowroozi, M. A.; Wissel, K.; Donzelli, M.; Hosseinpourkahvaz, N.; Plana-Ruiz, S.; Kolb, U.; Schoch, R.; Bauer, M.; Malik, A. M.; Rohrer, J.; Ivlev, S.; Kraus, F.; Clemens, O., High Cycle Life All-Solid-State Fluoride Ion Battery with La_2NiO_{4+d} High Voltage Cathode. *Commun. Mater.* **2020,** *1* (1), 27.

120. de Laune, B. P.; Rees, G. J.; Marco, J. F.; Hah, H. Y.; Johnson, C. E.; Johnson, J. A.; Berry, F. J.; Hanna, J. V.; Greaves, C., Topotactic Fluorine Insertion into the

Channels of $FeSb_2O_4$-Related Materials. *Inorg. Chem.* **2017,** *56* (16), 10078-10089.

121. Zaheer, W.; Andrews, J. L.; Parija, A.; Hyler, F. P.; Jaye, C.; Weiland, C.; Yu, Y.-S.; Shapiro, D. A.; Fischer, D. A.; Guo, J.; Velázquez, J. M.; Banerjee, S., Reversible Room-Temperature Fluoride-Ion Insertion in a Tunnel-Structured Transition Metal Oxide Host. *ACS Energy Lett.* **2020,** *5* (8), 2520-2526.

Chapter 2 Reaction Mechanism and Performances of 3*d* Transition Metal Cathode Materials

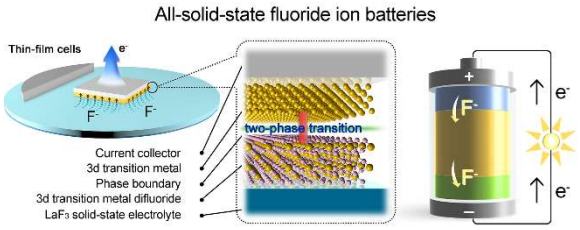

Fluoride ion batteries (FIBs) are regarded as promising energy storage devices, and it is important and urgent to develop cathode materials with high energy densities for use in FIBs. However, systematic investigations of 3d transition metal/metal fluorides have been rarely reported thus far because of the restricted reversibility and unfavorable interfacial compatibility of the 3d transition metal/metal fluorides with solid-state electrolytes. Herein, the 3d transition metals are investigated utilizing thin-film cells with LaF_3 substrates. The highly reversible (de)fluorinations of Cu, Co, and Ni are validated at various temperatures. High capacity utilizations of 79.5%, 100%, and 90.5% are obtained during the initial cycle at 150 °C. By combining results from X-ray absorption spectroscopy (XAS) and electrochemical characterization, the electrochemical behaviors of Cu, Co, and Ni, as well as experimental evidence of the two-phase transition mechanism during the M/MF_2 reaction are reported for the first time. This provides new insights required for future cathode designs for use in all-solid-state FIBs.

2.1 Introduction

Developing electrochemical energy storage devices is a greatly effective and imperative strategy in developing alternative energy sources to fossil fuels, that have been deemed to cause environmental issues and are possibly close to depletion. [1–5] Lithium-ion batteries (LIBs), typical representatives of electrochemical energy storage devices, have been used worldwide in the last several decades. However, the energy densities of highly commercialized LIBs are difficult to improve which have been limited by their intrinsic characteristics. As a result, there have been a strong desire to design new concepts of beyond-LIBs, such as new systems that employ Na^+, K^+, Mg^{2+}, Zn^{2+}, Ca^{2+}, Al^{3+}, F^-, and Cl^- as charge carriers. [6–17] Fluoride ion batteries (FIBs) are among these new systems and have been regarded as promising candidates owing to the electrochemical stability of F anions as charge transfers, which is ensured by the high electronegativity of the F element. [14, 18–25]

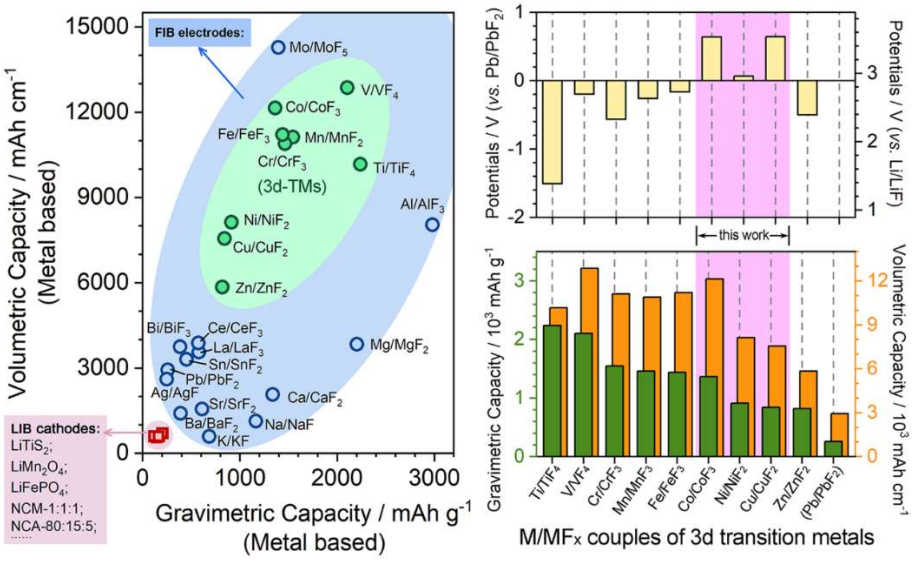

Figure 2.1 Left: comparison of gravimetric/volumetric energy densities of LIB cathode materials (pink),30 FIB metal/metal fluoride cathode material (blue) and FIB 3d transition metal/metal fluoride cathode materials (green). Right: the theoretical working potentials and gravimetric/ volumetric energy densities of 3d transition metal/metal fluoride cathode materials for FIBs.

After the successful application of tysonite-type solid solutions $La_{1-x}Ba_xF_{3-x}$ ($0 \leq x \leq 0.15$) as solid-state electrolytes, [14] the all-solid-state FIBs utilizing metal/metal fluoride (M/MF_x) compounds as electrodes have captured broad attentions because of their extremely high energy densities. Particularly, couples of 3d transition metals and their corresponding metal fluorides (3d-M/MF_x), which are lightweight and multivalent, possess huge theoretical

capacities (approximately 5–10 times that of common LIB cathode materials) and relatively high potentials (usually 1.5–3.5 V *vs.* Li/LiF). Therefore, these couples could provide high energy densities of over 2000 Wh kg^{-1} or 5000 Wh L^{-1}, as shown in **Figure 2.1**. [25–30]

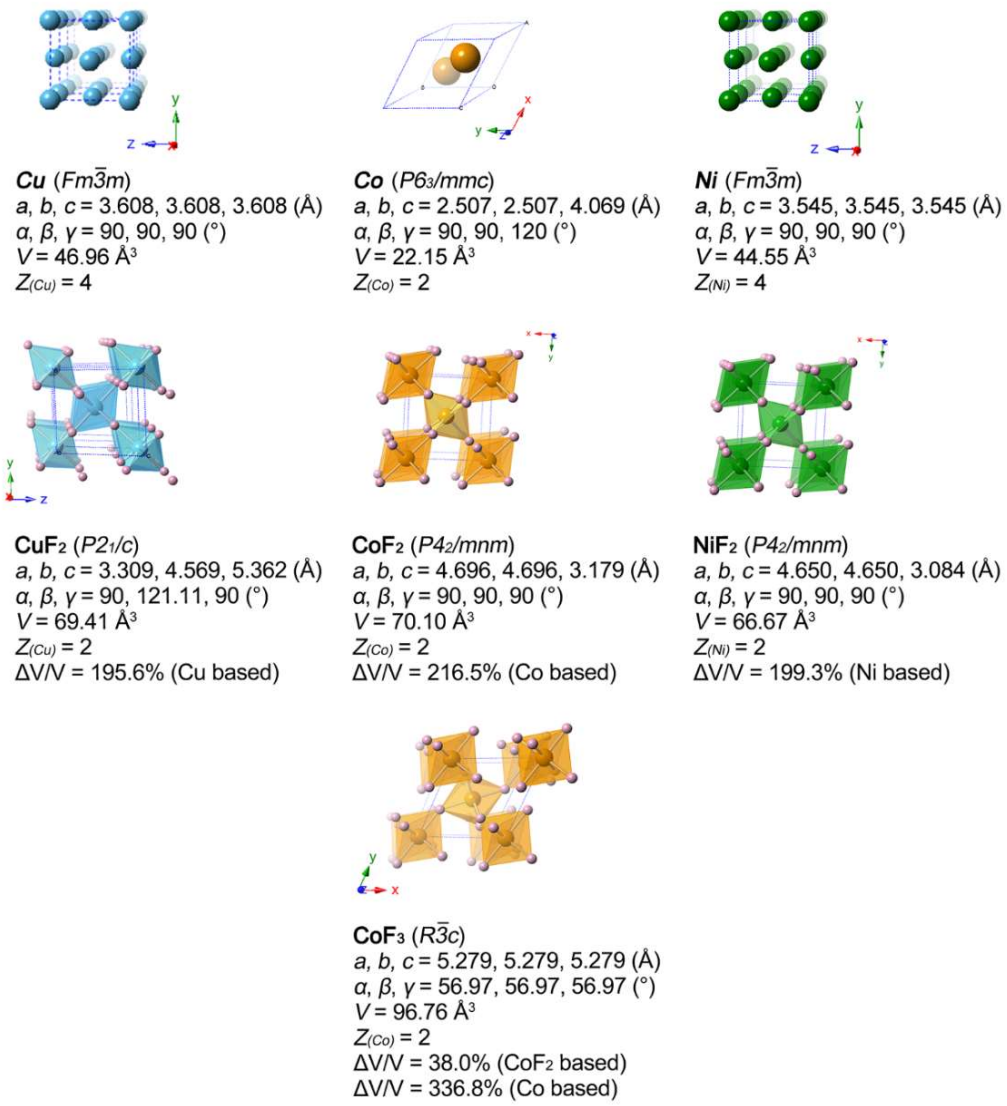

Figure 2.2 Crystallographic models of Cu, Co, Ni, and their fluorides. The volumetric changes are listed below each crystal model. [43-48]

Notwithstanding all these merits in terms of energy densities, there are few reports on the use of 3d-M/MF_x as cathode materials for all-solid-state FIBs. Particularly, systematic discussions on their typical fluorination process and corresponding phase transitions, based on high battery utilizations, are lacking. Although some pioneering works on Cu/CuF_2 have been reported, [26,29,31] most works have focused more on the optimization of solid-state F^- conductors, or on liquid-electrolyte battery systems, without specific perspectives towards the electrode materials of Cu, Zn, Sn, and even Bi. [14,17,25,26,32–42] Therefore, it is urgently important to

establish a database-type understanding of the basic electrochemical information on the use of 3d-M/MF_x as cathode for all-solid-state FIBs. One main hinderance to such investigations might be the inferior cycling reversibility caused by the enormous volumetric expansion/contraction upon (de)fluorination process and sluggish ion transportation of 3d-M/MF_x. [26–28,31] Hence, the widely used bulk-type cell models are not suitable for evaluating these materials in detail. For example, huge volumetric changes of c.a. 200–300% (**Figure 2.2**) lead to drastic damages to the electrolyte/cathode interfacial contacts. [43–48] Therefore, the reaction mechanisms and electrochemical properties of 3d-M/MF_x are still unknown and consequently optimization strategies are unclear. Thin-film models are considered as powerful tools for evaluating 3d-M/MF_x materials, which could be used to control the film thickness to optimize the cathode/electrolyte interfacial compatibility, reduce the internal resistance, and create a nearly ideal reaction environment. [31]

Herein, we introduced 3d transition metals Cu, Co, and Ni as thin-film cathode materials for all-solid-state FIBs, and for the first time, experimentally explored the two-phase-transition process within the difluorination ranges through X-ray absorption spectroscopy (XAS). To the best of our knowledge, this is the first report to investigate the electrochemical properties of Co and Ni as cathode materials for all-solid-state FIBs.

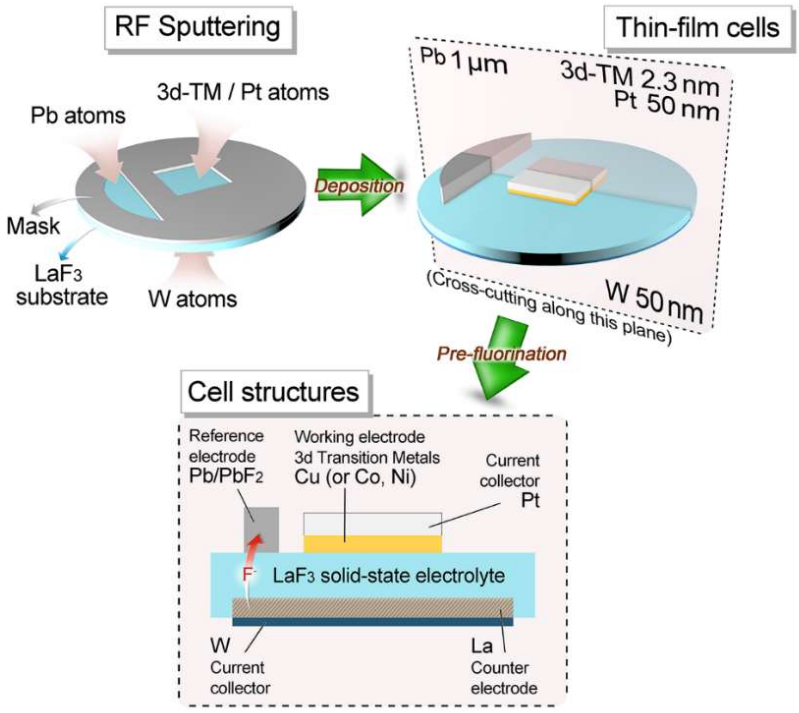

Figure 2.3 Schematic illustrations of the RF sputtering and pre-fluorination processes.

2.2 Expermental

2.2.1 Preparations for thin-film cell

The thin-film preparation procedure is schematically presented in **Figure 2.3**. Typically, the thin-film cells were prepared *via* a radio-frequency magnetron sputtering (RF Sputtering, Eiko, Japan) method by depositing all the necessary metals onto the single-crystal LaF_3 substrate (used as a solid-state electrolyte). The parameters and details of the RF Sputtering are described in **Table 2.1**. The as-deposited thin-film cells were assembled into battery vessels in an argon-filled glovebox (Miwa, Japan). A Pb/PbF_2 reference electrode, which could offer stable reference potentials (**Figure 2.4**), was constructed by the pre-fluorination step after the thicknesses of all the metals had reached their design values. The pre-fluorination was achieved by connecting the as-deposited Pb and W current collector with a current of 8.3 μA for 300 s at 150 °C. As a result, the pure Pb and LaF_3 were fluorinated/defluorinated to Pb/PbF_2 and La/LaF_3, which were employed as the reference and counter electrodes, respectively. The pre-fluorination and galvanostatic tests were processed using a PARSTAT MC2000 battery testing system (Princeton Applied Research, USA). The smoothness and thickness of the as-deposited thin films were also examined by atomic force microscopy (AFM, **Figure 2.5**) and transmission electron microscopy (TEM, **Figure 2.6**). Since it is difficult to observe ultra-thin films with thicknesses of ~2.3 nm, TEM images were acquired from thicker films (c.a. 60 nm).

Table 2.1 The parameters of RF sputtering on LaF_3 substrate

Element	Application	Thickness / nm	RF Sputtering Power / W
Cu	Working electrode	2.3	50
Co	Working electrode	2.3	120
Ni	Working electrode	2.3	100
Pb	Reference electrode	1000	50
Pt	Current collector	50	50
W	Current collector	50	120
RF Sputtering Temperature: Room temperature (~25 ˚C)			
Atmosphere: Argon; Atmosphere pressure: 1.0 Pa			

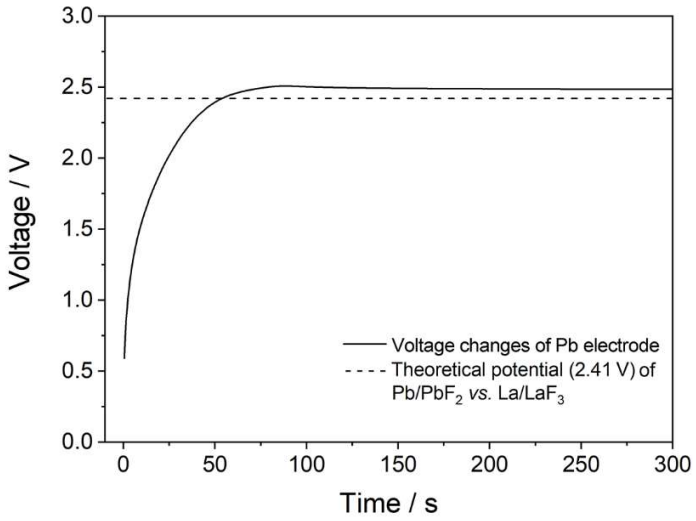

Figure 2.4 The voltage changes of Pb reference electrode versus counter electrode upon pre-fluorination treatment. The dash line represents the theoretical voltage (2.41 V) of Pb/PbF_2 *vs*. La/LaF_3.

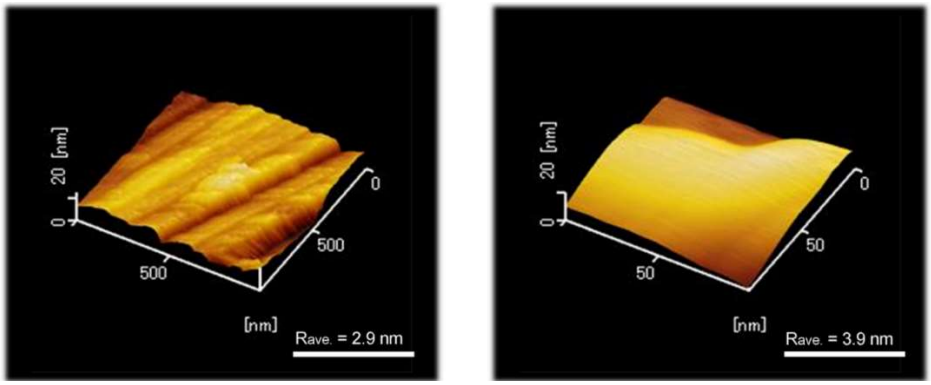

Figure 2.5 Surface smoothness of the substrate. Atomic force microscopy (AFM) images of (a) mirror polished LaF_3 substrate and (b) Cu deposited LaF_3 substrate. The surface roughness of the substrate before and after the Cu deposition are 2.9 and 3.9 nm, respectively.

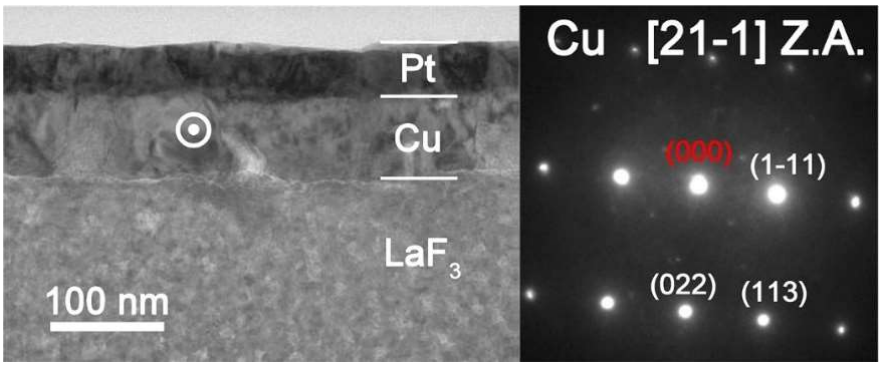

Figure 2.6 The cross-sectional TEM images of Pt, Cu film and LaF_3 substrates, and the nano-area electron diffraction (NAED) patterns of Cu along $[21\bar{1}]$ zone axis.

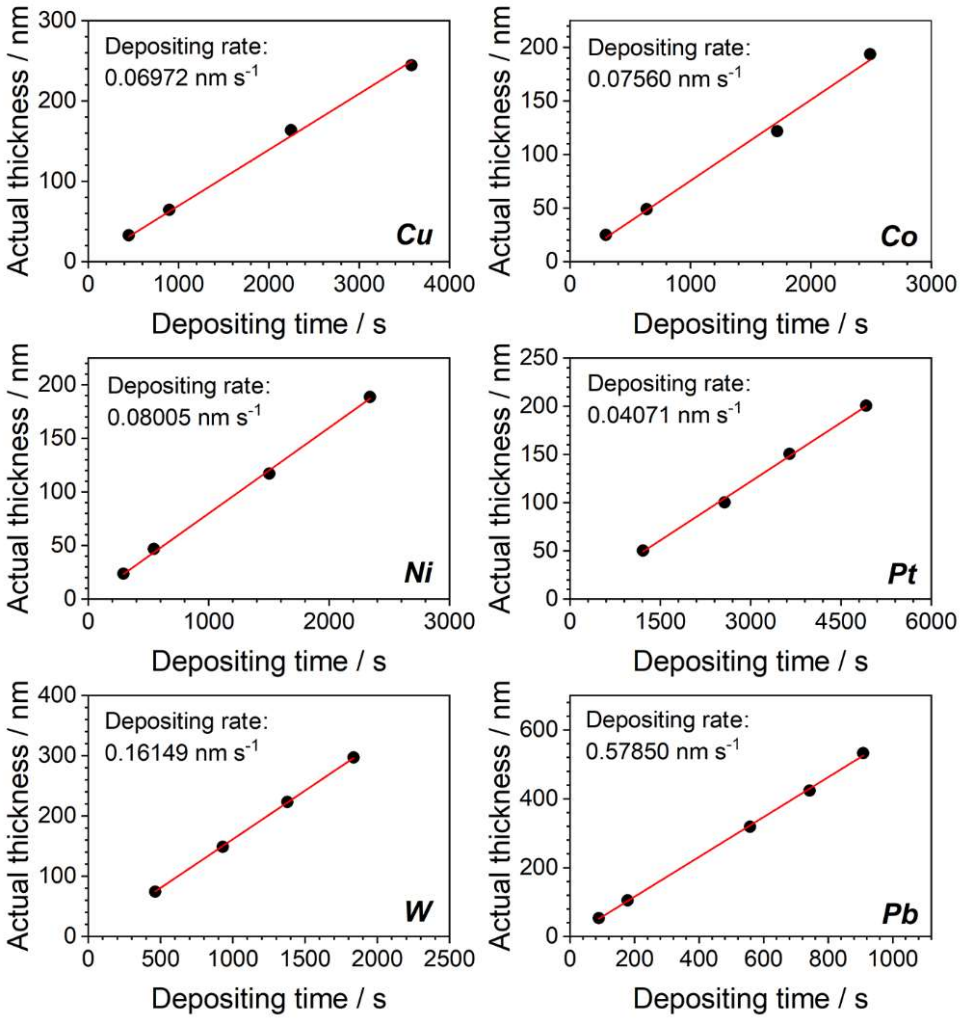

Figure 2.7 The direct proportional fittings (y = kx model) of depositing rates of all utilized metals.

The metal deposition rates were determined *via* a Dektak-8 Stylus Profiler (Veeco, USA) by preparing films of various design thickness and then fitting a linear relationship ($y = kx$) of the actual thickness versus the deposition time, as shown in **Figure 2.7**. Upon preparing the cell, the deposition rates were measured in real-time by the quartz crystal microbalance (QCM) inside the RF Sputtering chamber.

The surface of the single-crystal LaF_3 substrate was treated by reverse sputtering under argon (2.0 Pa) to remove most of the surficial oxidized layers. Then, the surface was annealed in a NF_3 atmosphere (3.6 Pa) at 300 °C for 1 hour to repair the defective lattice (which included remnants of LaOF and La_2O_3 species) based on the following reactions.

$$La_2O_3 + 2NF_3 \xrightarrow{\Delta} 2LaF_3 + N_2 + 1.5O_2 \qquad (2-1)$$

$$3LaOF + 2NF_3 \xrightarrow{\Delta} 3LaF_3 + N_2 + 1.5O_2 \qquad (2-2)$$

2.2.2 Characterizations and electrochemical tests

The X-ray diffraction (XRD) patterns were taken using an X-ray diffractometer (Rigaku Ultima IV, Japan) with Cu-Kα radiation (λ =1.54056 Å). The X-ray adsorption near-edge spectroscopy (XANES) was measured at BL37XU beamline at the SPring-8 synchrotron radiation facilities (Hyogo, Japan). The signals were collected under partial fluorescence yield (PFY) mode by a 19-element solid-state detector.

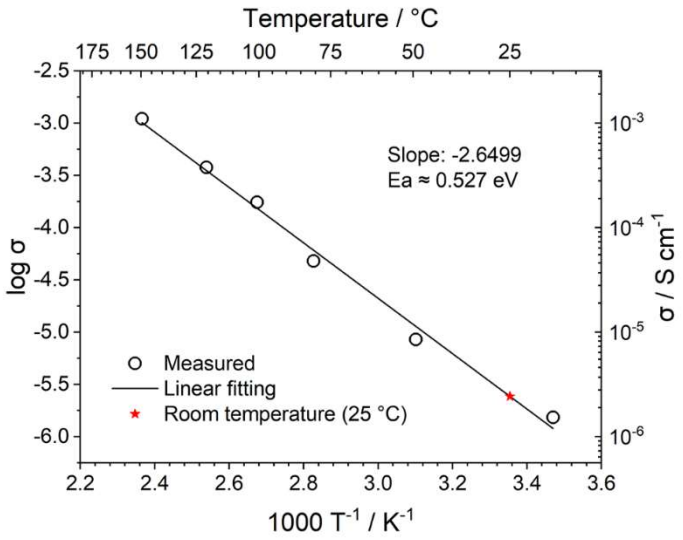

Figure 2.8 The ionic conductivities of LaF_3 substrates at temperatures of 15, 50, 80, 100, 125, 150 ˚C, respectively, and corresponding Arrhenius linear fitting.

The ionic conductivity of LaF_3 was measured by electrochemical impedance spectroscopy (EIS) using a Modulab XM ECS electrochemical test system (Solartron analytical, UK) at a frequency in the range of 10^6 to 10^{-1} Hz and an amplitude voltage of 50 mV at temperatures of 15, 50, 80, 100, 120, and 150 °C. The activation energy (E_a) was calculated using the Arrhenius equation: [35,49]

$$\sigma = Ae^{\frac{-E_a}{k_B T}} \qquad (2-3)$$

where σ, A, E_a, k_B, and T are the ionic conductivity, pre-exponential factor, activation energy, Boltzmann constant, and temperature (K), respectively. Further, this equation can be rearranged to Equation (2-4). Therefore, the E_a can be determined by linear fitting of log σ vs. T^{-1}, as depicted in **Figure 2.8**.

$$\log \sigma = -\frac{E_a}{2.30259 k_B} \cdot \frac{1}{T} + \log A \qquad (2-4)$$

2.3 Results and discussion

2.3.1 Structural analysis of the as-deposited metals

The XRD of the thin films was accomplished by depositing the metals onto quartz substrates instead of LaF_3 substrates to avoid the disturbance of the strong LaF_3 diffraction peaks, as demonstrated in **Figure 2.9**. The diffraction peaks of Cu and Ni were both well indexed with a face-centered cubic (*fcc*) structure (JCPDS#04-0836 and #04-0850, respectively) with a space group of $Fm\bar{3}m$. The metallic cobalt exhibited a rough diffraction with a $P6_3/mmc$ hexagonal close packed (*hcp*) structure (JCPDS#05-0727). Additionally, the Pt and Pb, and W also corresponded well to the cubic structure (JCPDS#04-0802 and #04-0686) and α+β multiphases (JCPDS#04-0806 and #47-1319), respectively.

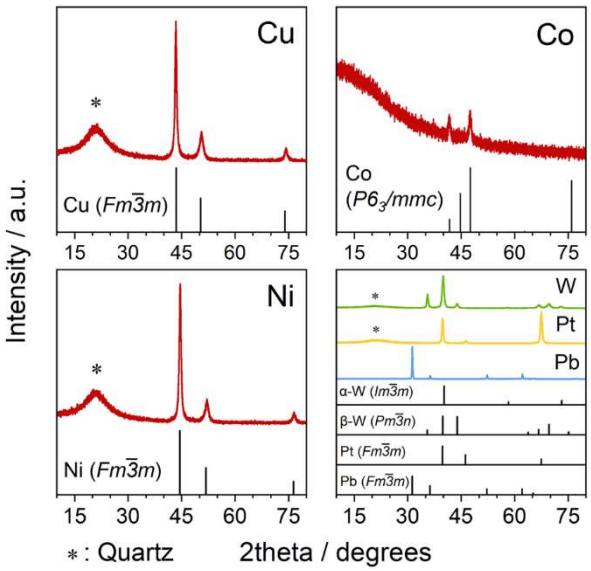

Figure 2.9 XRD patterns of Cu, Co, Ni, W, Pt, and Pb thin films.

2.3.2 Electrochemical properties

To acquire the ideal ionic conductivity of LaF_3, the galvanostatic charging/discharging tests were mainly carried out at 150 °C. The ionic conductivities (σ) the of the LaF_3 at various temperatures and its activation energy (E_a) were measured by EIS and calculated by Arrhenius equations, respectively, as described in the Experimental section. As shown in Figure S6, the $\sigma(LaF_3)$ at 150 °C was approximately 1.1×10^{-3} S cm^{-1}. This was adequate for the smooth electrochemical reactions in the all-solid-state cells. Meanwhile, the calculated E_a was 0.527 eV (the reference value was 0.43–0.46 eV [50,51]). The Pb/PbF_2 reference electrode also provided stable reference potentials of c.a. 2.5 V (theoretically 2.41 V). As shown in Figure 2.4, the

increase in the reference potential from 0 to 75 s was attributed to the generation and growth of La grains from pure LaF_3, and PbF_2 grains from pure Pb, i.e., the reference voltages changed from Pb vs. LaF_3 (0 s) to Pb/PbF_2 vs. La/LaF_3 (75 s). The Cu, Co, and Ni metals exhibited high (de)fluorination reversibility upon cycling as shown in **Figure 2.10**. The initial reversible capacity of Cu, Co, and Ni at 150 °C were 670.5, 1366.6, and 826.9 mAh g^{-1}, which were 79.5%, 100%, and 90.5% of the theoretical values of Cu/CuF_2, Co/CoF_3, and Ni/NiF_2, respectively.

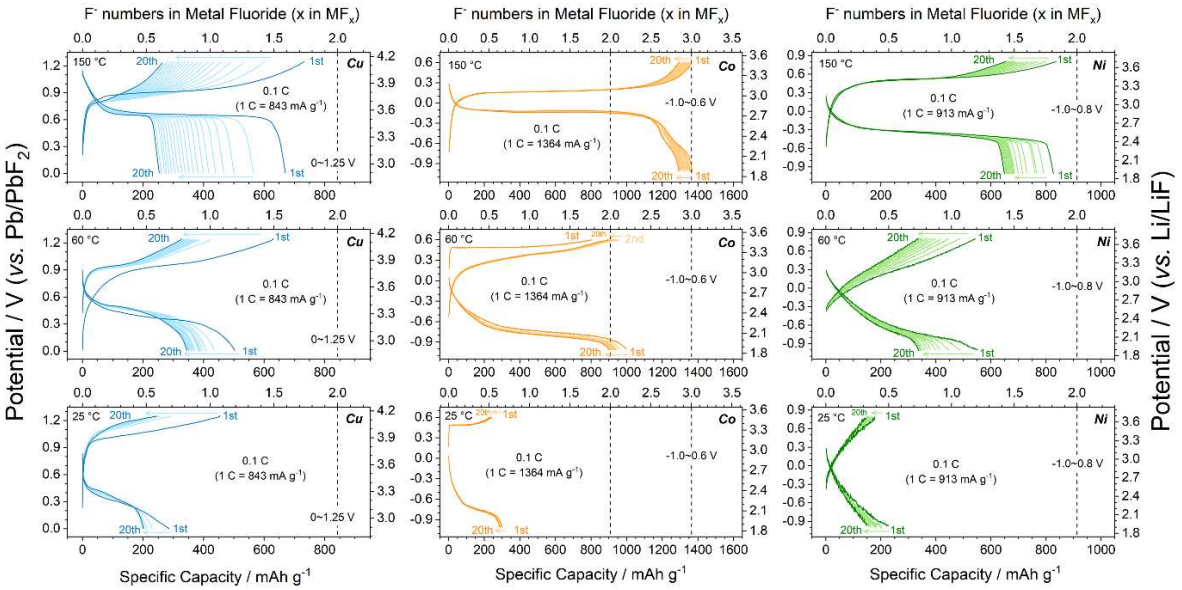

Figure 2.10 Galvanostatic charge/discharge profiles at 0.1 C of Cu (left column), Co (middle column), and Ni (right column) at 150 (upper), 60 (middle) and 25 ˚C (lower). The vertical dashed lines refer to the theoretical capacity of x = 2.0 in MF_x (3.0 for CoF_x additionally).

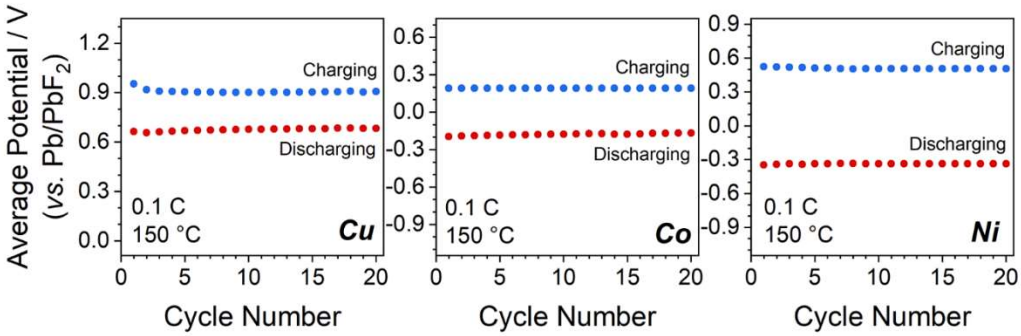

Figure 2.11 The average working potentials in the first 20 cycles of Cu, Co and Ni at 0.1 C and 150 ˚C.

Notice that all the three metals possessed flat single charging/discharging plateaus, which was indicative of the possibility of a phase-transition mechanism upon cycling. The deteriorations in the average working potentials of Cu, Co, and Ni were inappreciable as presented in **Figure 2.11**, with potential changes of 0.047/-0.018 V, 0.001/-0.026 V, and

0.018/-0.012 V during charging/discharging processes after 20 cycles, respectively. In addition, the reversible (de)fluorination of Cu, Co, and Ni at mild temperatures were also verified. Although the $\sigma(LaF_3)$ dropped to 2.1×10^{-5} S cm^{-1} (60 °C) and 2.4×10^{-6} S cm^{-1} (25 °C), the reversible M/MF_x conversion was still achieved at mild temperatures. As shown in Figure 2.10, the 3d-TM cathode materials at 25 °C exhibited considerable capacities compared with typical LIB cathodes, while the polarization became exceedingly large owing to the very limited $\sigma(LaF_3)$ value. But the potentials for wider application of 3d-TMs as FIB cathodes in the future were also revealed.

2.3.3 X-ray absorption spectroscopy and reaction mechanism

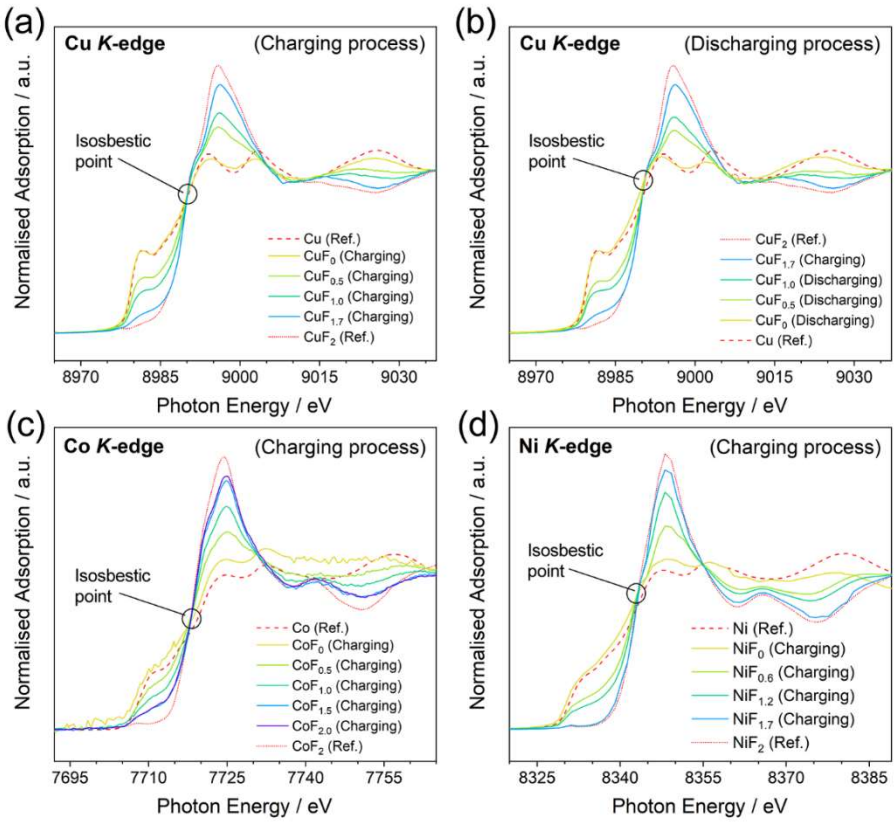

Figure 2.12 Ex situ X-ray absorption near-edge spectra of (a, b) Cu K-edge upon initial charging/discharging, (c) Co K-edge upon initial charging within Co/CoF_2 range and (d) Ni K-edge upon initial charging.

As mentioned above, a two-phase-transition mechanism was thought to be responsible for the reaction based on the electrochemical behaviors. The XANES was conducted to afford firmer experimental evidence. The ex-situ XANES samples were prepared by controlling the state of charge (SOC) into certain F content in the MF_x. It must be emphasized that the MF_x formulas used in this work do not represent the homogeneous solid solutions, but only the intermediate products of $(1 - 0.5x)$ M · $0.5x$ MF_2 ($0 \leq x \leq 2.0$) with a nominal F content of x

according to the two-phase-transition mechanism. The Cu K-edge, Co K-edge, and Ni K-edge spectra are shown in **Figure 2.12**. The spectra of all the pristine metals (CuF_0, CoF_0, and NiF_0) were consistent with the reference (Ref.) spectra of Cu, Co, and Ni. The tendencies of the spectra to transfer from Ref.-M toward Ref.-MF_2 were exhibited upon gradual fluorination. The isosbestic points can be observed in Figure 3a to Figure 3d which are located at c.a. 8990, 7717, and 8342 eV for Cu K-edge, Co K-edge, and Ni K-edge, respectively. The occurrence of the isosbestic points usually indicates the direct transition from phase A toward phase B, [52-55] consequently we linearly fitted the M and MF_2 (M=Cu, Co and Ni) phase amounts versus the F content, as shown in **Figure 2.13**. According to the results from the fitted lines, the phase fraction changes of M and MF_2 were linear in the range of $0 \leq x \leq 2.0$ in the MF_x, which implied the two-phase-transition nature of the M/MF_2 reactions. A recent report by Haruyama J. et al. [56] also concluded the same, in which the authors discussed the thermodynamically favored reaction patterns (i.e., solid-solution or two-phase-coexistent) of various M/MF_x combinations *via* density functional theory calculations. They also discussed both models and concluded that the solid-solution model was unreasonable, because the F vacancy would be uniformly distributed and equally introduce electron dopants, whereas the large forbidden band gap made these doped electrons unstable.

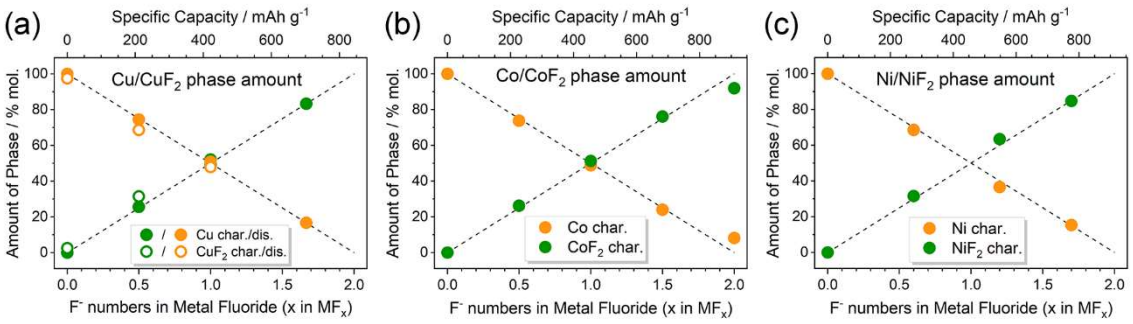

Figure 2.13 Linear fittings of the phase amounts of (a) Cu/CuF_2, (b) Co/CoF_2, and (c) Ni/NiF_2. The dashed lines in (a), (b), and (c) are assistant lines that connect (0, 0) with (2.0, 100%), and (0, 100%) with (2.0, 0), which represent the ideal linear changes of the phase amounts.

The galvanostatic intermittent titration open circuit potentials (OCPs) at various SOC were also analyzed and are shown in **Figure 2.14**(a) to Figure 2.14(c). The OCPs of CuF_x, CoF_x, and NiF_x were almost remained stable in the range of $0 \leq x \leq 2.0$ except at the beginning of the charging. This inferred the phase-transition mechanism because the Gibbs free energy of formation of the M and MF_2 phases remained unchanged during the (de)fluorination process within the phase-transition dominations. [57] Particularly, the Co with a higher metallic character

showed a different mechanism in which the OCPs gradually increased upon further charging in the range of $2.0 \leq x \leq 3.0$ (Figure 2.14(b)). This was inconsistent with the two-phase transition characteristics. Meanwhile, the XANES patterns of the $CoF_{2.5}$ and $CoF_{3.0}$ transferred into higher oxidation states but were still similar to Ref.-CoF_2 spectra (Figure 2.14(d)). For the whole Co/CoF_3 fluorination process, the reaction mechanisms in the initial and later stages (i.e., $0 \leq x \leq 2.0$ and $2.0 \leq x \leq 3.0$) were completely distinct. The mechanism of the CoF_2/CoF_3 has not been clearly elucidated, however a possible reason for the abnormal XANES spectra is that the XANES data were collected through ex-situ approaches which did not adequately shield the chemically unstable samples like CoF_3. Although CoF_3 can exist independently, it is decomposed into CoF_2 by traces of moisture during sample storage or transfer. Considering the ultra-thin thickness employed in this work, small current leakage might also accelerate this decomposition. These facts point to some critical requirements for in-situ measurements on thin-film systems.

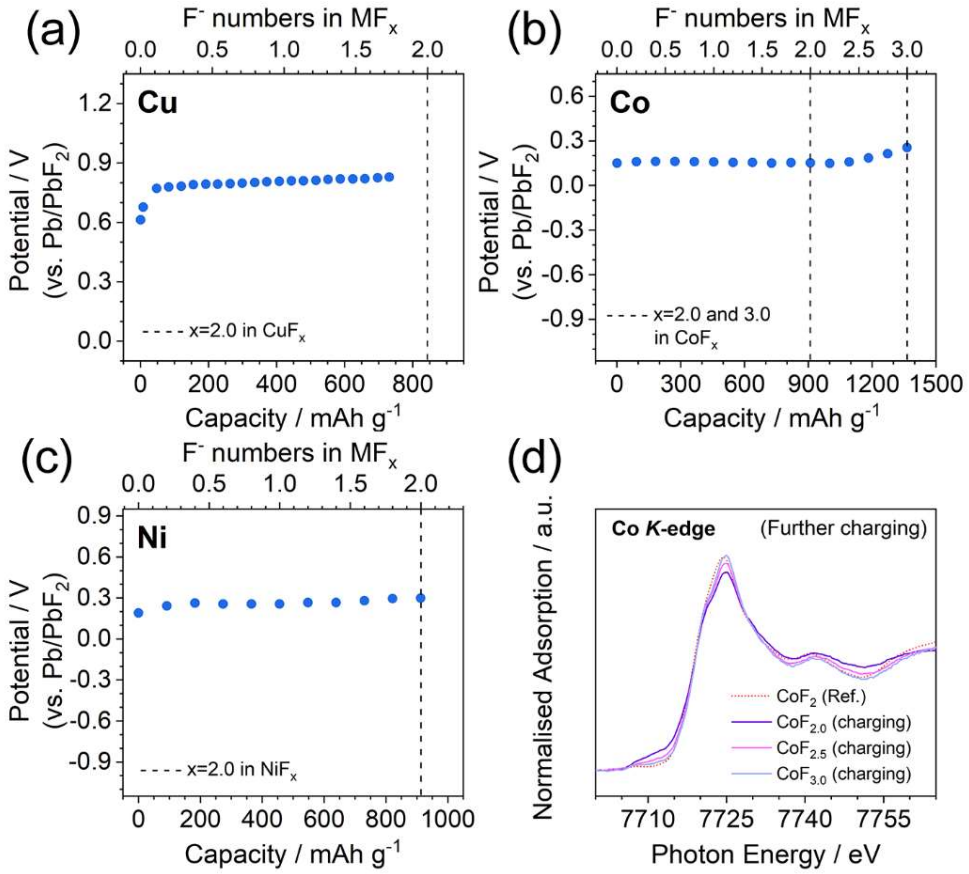

Figure 2.14 (a–c) Galvanostatic intermittent titration open circuit potentials (OCPs) upon initial charging of Cu, Co, and Ni. The vertical dashed lines refer to the theoretical capacities of $x = 2.0$ or 3.0 in the MF_x formula. (d) Ex situ XANES of the Co K-edge upon initial charging with the CoF_2/CoF_3 range.

2.3.4 Discussion and Prospection

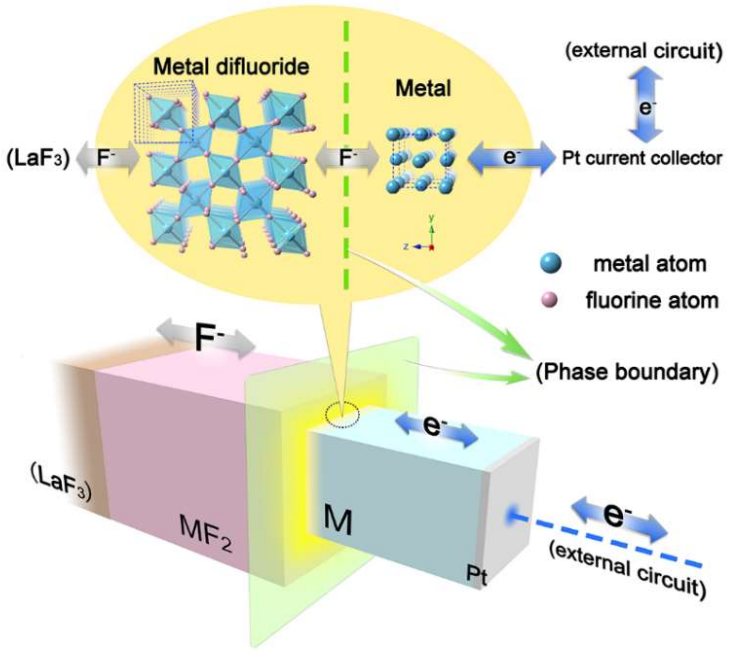

Figure 2.15 Schematic illustration of the two-phase transition mechanism during the M/MF_2 reaction.

A typical charge/mass transferring procedure of M/MF_2 phase transitions (the schematic description is shown in **Figure 2.15**) can be summarized as following categories; i) the interphase F^- transportation, i.e., the F^- diffuses across the M/MF_x phase boundaries, ii) the internal F^- transportation, i.e., F^- inside the MF_x bulks, and iii) the electron transfer toward the current collectors *via* the M bulks. The resistance from the electrode was deemed to be the macroscale rate-determining step, however more microscale contributions from the internal and interphase components (i or ii) could not be identified. [56]

Primary evaluations towards kinetical factors were given by the results of film-thickness-dependent electrochemical properties of Cu as demonstrated in **Figure 2.16**. Thin films of Cu with various thicknesses of 2.3 (this work), 10 and 50 nm were prepared and galvanostatically tested at 150 °C. The samples with 2.3 and 10 nm thicknesses almost delivered capacities near theoretical values, whereas the 50 nm sample only delivered an initial charging capacity of ~170 mAh g^{-1} which was c.a. 20% of theoretical value, corresponding to a diffusion depth of c.a. 10 nm. The specific rate-determining step, factors effecting the (de)fluorination kinetics, and CoF_2/CoF_3 reaction mechanisms will be researched in detail in future works, which are beyond the discussions of this work.

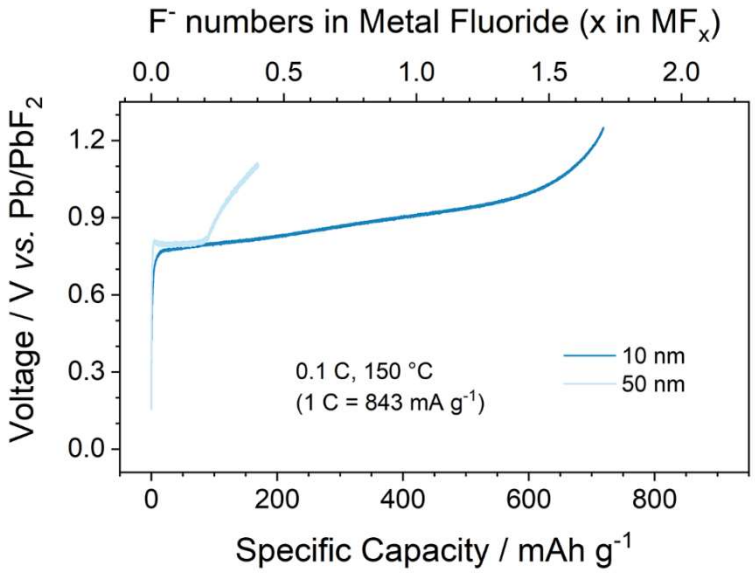

Figure 2.16 The electrochemical properties of Cu with various thicknesses. The 10 nm sample possessed a similar initial performance with 2.3 nm sample in this study, while the thickest sample only delivered an initial charging capacity of 170 mAh g^{-1} which corresponded to c.a. 20% of theoretical values, i.e., diffusion depth of 10 nm out of 50 nm.

2.4 Conclusions

The 3d transition metals Cu, Co, and Ni were investigated as reliable cathode materials for all-solid-state FIBs using the thin-film cell models. The electrochemical properties with buffered polarizations and high reversible capacities were determined and analyzed by the ideal reaction environments created by the thin-film cell models. Based on the thorough fluorination, a possibility was implied that the fluorination of 3d transition metal proceeds *via* two-phase transition by ex-situ XAS analyses and electrochemical assessments. The electrochemical properties of Co and Ni for the uses in FIBs were also reported for the first time. From a wider perspective, the overall performance of the all-solid-state FIB was depended on various aspects, therefore deeper understanding and knowledge are required to design the FIB. Thus, besides the insights acquired in this study, more investigations are appealed to achieve both high reversibility and high energy density in FIBs.

Reference

1. Armand, M.; Tarascon, J. M., Building better batteries. *Nature* **2008,** *451* (7179), 652-657.

2. Yabuuchi, N.; Kubota, K.; Dahbi, M.; Komaba, S., Research development on sodium-ion batteries. *Chem. Rev.* **2014,** *114* (23), 11636-11682.

3. Chu, S.; Cui, Y.; Liu, N., The path towards sustainable energy. *Nat. Mater.* **2017,** *16* (1), 16-22.

4. Grey, C.; Tarascon, J., Sustainability and in situ monitoring in battery development. *Nat. Mater.* **2017,** *16* (1), 45-56.

5. Islam, M. S.; Fisher, C. A. J., Lithium and sodium battery cathode materials: computational insights into voltage, diffusion and nanostructural properties. *Chem. Soc. Rev.* **2014,** *43* (1), 185-204.

6. Delmas, C.; Braconnier, J. J.; Fouassier, C.; Hagenmuller, P., Electrochemical intercalation of sodium in Na_xCoO_2 bronzes. *Solid State Ionics* **1981,** *3–4* (AUG), 165-169.

7. Aurbach, D.; Lu, Z.; Schechter, A.; Gofer, Y.; Gizbar, H.; Turgeman, R.; Cohen, Y.; Moshkovich, M.; Levi, E., Prototype systems for rechargeable magnesium batteries. *Nature* **2000,** *407* (6805), 724-727.

8. Xu, C.; Li, B.; Du, H.; Kang, F., Energetic zinc ion chemistry: the rechargeable zinc ion battery. *Angew. Chem., Int. Ed.* **2012,** *51* (4), 933-935.

9. Zhao, S.; Han, B.; Zhang, D.; Huang, Q.; Xiao, L.; Chen, L.; Ivey, D. G.; Deng, Y.; Wei, W., Unravelling the reaction chemistry and degradation mechanism in aqueous Zn/MnO_2 rechargeable batteries. *J. Mater. Chem. A* **2018,** *6* (14), 5733-5739.

10. Lin, M. C.; Gong, M.; Lu, B.; Wu, Y.; Wang, D. Y.; Guan, M.; Angell, M.; Chen, C.; Yang, J.; Hwang, B. J.; Dai, H., An ultrafast rechargeable aluminium-ion battery. *Nature* **2015,** *520* (7547), 325-328.

11. Jian, Z.; Luo, W.; Ji, X., Carbon electrodes for K-ion batteries. *J. Am. Chem. Soc.* **2015,** *137* (36), 11566-11569.

12. Gao, P.; Reddy, M. A.; Mu, X.; Diemant, T.; Zhang, L.; Zhao-Karger, Z.; Chakravadhanula, V. S.; Clemens, O.; Behm, R. J.; Fichtner, M., VOCl as a cathode for rechargeable chloride ion batteries. *Angew. Chem., Int. Ed.* **2016,** *55* (13), 4285-4290.

13. Zhao, X.; Zhao-Karger, Z.; Wang, D.; Fichtner, M., Metal oxychlorides as cathode materials for chloride ion batteries. *Angew. Chem., Int. Ed.* **2013,** *52* (51), 13621-13624.

14. Anji Reddy, M.; Fichtner, M., Batteries based on fluoride shuttle. *J. Mater. Chem.* **2011,** *21* (43), 17059-17062.

15. Ponrouch, A.; Frontera, C.; Barde, F.; Palacin, M. R., Towards a calcium-based rechargeable battery. *Nat. Mater.* **2016,** *15* (2), 169-172.

16. Wang, M.; Jiang, C.; Zhang, S.; Song, X.; Tang, Y.; Cheng, H. M., Reversible calcium alloying enables a practical room-temperature rechargeable calcium-ion battery with a high discharge voltage. *Nat. Chem.* **2018,** *10* (6), 667-672.

17. Davis, V. K.; Bates, C. M.; Omichi, K.; Savoie, B. M.; Momcilovic, N.; Xu, Q.; Wolf, W. J.; Webb, M. A.; Billings, K. J.; Chou, N. H.; Alayoglu, S.; McKenney, R. K.; Darolles, I. M.; Nair, N. G.; Hightower, A.; Rosenberg, D.; Ahmed, M.; Brooks, C. J.; Miller, T. F., 3rd; Grubbs, R. H.; Jones, S. C., Room-temperature cycling of metal fluoride electrodes: Liquid electrolytes for high-energy fluoride ion cells. *Science* **2018,** *362* (6419), 1144-1148.

18. Kennedy, J. H.; Hunter, J. C., Thin-Film Galvanic Cell $Pb/PbF_2/PbF_2$, CuF_2/Cu. *J. Electrochem. Soc.* **1976,** *123* (1), 10-14.

19. Schoonman, J., A solid-state galvanic cell with fluoride-conducting electrolytes. *J. Electrochem. Soc.* **1976,** *123* (12), 1772-1775.

20. Danto, Y.; Poujade, G.; Pistre, J.; Lucat, C.; Salardenne, J., A $Pb|PbF_2|BiF_3|Bi$ thin solid film reversible galvanic cell. *Thin Solid Films* **1978,** *55* (3), 347-354.

21. Schoonman, J.; Wapenaar, K. E. D.; Oversluizen, G.; Dirksen, G. J., Fluoride−conducting solid electrolytes in galvanic cells. *J. Electrochem. Soc.* **1979,** *126* (5), 709-713.

22. Hagenmuller, P.; Réau, J.-M.; Lucat, C.; Matar, S.; Villeneuve, G., Ionic conductivity of fluorite-type fluorides. *Solid State Ionics* **1981,** *3*, 341-345.

23. Schoonman, J.; Wolfert, A., Solid-state galvanic cells with fast fluoride conducting electrolytes. *Solid State Ionics* **1981,** *3*, 373-379.

24. Kosacki, I., Physical properties and applications of $Cd_{1-x}Pb_xF_2$ superionic crystals. *Appl. Phys. A* **1989,** *49* (4), 413-424.

25. Okazaki, K.-i.; Uchimoto, Y.; Abe, T.; Ogumi, Z., Charge–discharge behavior of bismuth in a liquid electrolyte for rechargeable batteries based on a fluoride shuttle. *ACS Energy Lett.* **2017,** *2* (6), 1460-1464.

26. Thieu, D. T.; Fawey, M. H.; Bhatia, H.; Diemant, T.; Chakravadhanula, V. S. K.; Behm, R. J.; Kübel, C.; Fichtner, M., CuF_2 as reversible cathode for fluoride ion batteries. *Adv. Funct. Mater.* **2017,** *27* (31), 1701051.

27. Reddy, M. A.; Fichtner, M., Chapter 3 - Fluoride Cathodes for Secondary Batteries. In *Advanced Fluoride-Based Materials for Energy Conversion*, Nakajima, T.; Groult, H., Eds. Elsevier: 2015; pp 51-76, DOI: 10.1016/b978-0-12800679-5.00003-8.

28. Gschwind, F.; Rodriguez-Garcia, G.; Sandbeck, D. J. S.; Gross, A.; Weil, M.; Fichtner, M.; Hörmann, N., Fluoride ion batteries: Theoretical performance, safety, toxicity, and a combinatorial screening of new electrodes. *J. Fluorine Chem.* **2016,** *182*, 76-90.

29. Fawey, M. H.; Chakravadhanula, V. S. K.; Munnangi, A. R.; Rongeat, C.; Hahn, H.; Fichtner, M.; Kübel, C., First results from in situ transmission electron microscopy studies of all-solid-state fluoride ion batteries. *J. Power Sources* **2020,** *466*, 228283.

30. Nitta, N.; Wu, F.; Lee, J. T.; Yushin, G., Li-ion battery materials: Present and future. *Mater. Today* **2015,** *18* (5), 252-264.

31. Zhang, L.; Reddy, M. A.; Gao, P.; Diemant, T.; Jürgen Behm, R.; Fichtner, M., Study of all solid-state rechargeable fluoride ion batteries based on thin-film electrolyte. *J. Solid State Electrochem.* **2016,** *21* (5), 1243-1251.

32. Rongeat, C.; Reddy, M. A.; Witter, R.; Fichtner, M., Nanostructured fluorite-type fluorides as electrolytes for fluoride ion batteries. *J. Phys. Chem. C* **2013,** *117* (10), 4943-4950.

33. Rongeat, C.; Reddy, M. A.; Diemant, T.; Behm, R. J.; Fichtner, M., Development of new anode composite materials for fluoride ion batteries. *J. Mater. Chem. A* **2014,** *2* (48), 20861-20872.

34. Zhang, L.; Reddy, M. A.; Fichtner, M., Electrochemical performance of all solid-state fluoride-ion batteries based on thin-film electrolyte using alternative conductive additives and anodes. *J. Solid State Electrochem.* **2017,** *22* (4), 997-1006.

35. Mohammad, I.; Chable, J.; Witter, R.; Fichtner, M.; Reddy, M. A., Synthesis of fast fluoride-ion-conductive fluorite-type $Ba_{1-x}Sb_xF_{2+x}$ ($0.1 \leq x \leq 0.4$): A potential solid electrolyte for fluoride-ion batteries. *ACS Appl. Mater. Interfaces* **2018,** *10* (20), 17249-17256.

36. Grenier, A.; Porras-Gutierrez, A.-G.; Groult, H.; Beyer, K. A.; Borkiewicz, O. J.; Chapman, Karena W.; Dambournet, D., Electrochemical reactions in fluoride-ion batteries: mechanistic insights from pair distribution function analysis. *J. Mater. Chem. A* **2017,** *5* (30), 15700-15705.

37. Grenier, A.; Porras-Gutierrez, A. G.; Body, M.; Legein, C.; Chrétien, F.; Raymundo-Piñero, E.; Dollé, M.; Groult, H.; Dambournet, D., Solid fluoride electrolytes and their composite with carbon: Issues and challenges for rechargeable solid state fluoride-ion batteries. *J. Phys. Chem. C* **2017,** *121* (45), 24962-24970.

38. Mohammad, I.; Witter, R.; Fichtner, M.; Reddy, M. A., Introducing interlayer electrolytes: Toward room-temperature high-potential solid-state rechargeable fluoride ion batteries. *ACS Appl. Energy Mater.* **2019,** *2* (2), 1553-1562.

39. Hou, X.; Zhang, Z.; Shen, K.; Cheng, S.; He, Q.; Shi, Y.; Yu, D. Y. W.; Su, C.-y.; Li, L.-J.; Chen, F., An aqueous rechargeable fluoride ion battery with dual fluoride electrodes. *J. Electrochem. Soc.* **2019,** *166* (12), A2419-A2424.

40. Zhang, Z.; Hu, X.; Zhou, Y.; Wang, S.; Yao, L.; Pan, H.; Su, C.-Y.; Chen, F.; Hou, X., Aqueous rechargeable dual-ion battery based on fluoride ion and sodium ion electrochemistry. *J. Mater. Chem. A* **2018,** *6* (18), 8244-8250.

41. Yamanaka, T.; Nakamoto, H.; Abe, T.; Nishio, K.; Ogumi, Z., Formation and propagation of fluorine-deficient phases in large LaF_3 single crystals during electrochemical defluorination. *ACS Appl. Energy Mater.* **2019,** *2* (5), 3092-3097.

42. Grenier, A.; Porras Gutierrez, A. G.; Groult, H.; Dambournet, D., Modified coin cells to evaluate the electrochemical properties of solid-state fluoride-ion batteries at 150 °C. *J. Fluorine Chem.* **2016,** *191*, 23-28.

43. Owen, E. A.; Yates, E. L., Precision measurements of crystal parameters Locality: synthetic Sample: at T = 18 ˚C. *Philos. Mag.* **1933,** *15*, 472-488.

44. Fischer, P.; Hälg, W.; Schwarzenbach, D.; Gamsjäger, H., Magnetic and crystal structure of copper (II) fluoride. *J. Phys. Chem. Solids* **1974,** *35* (12), 1683-1689.

45. Zemann, J., Crystal structures, 2nd edition. Vol. 1 by R. W. G. Wyckoff. *Acta Crystallogr.* **1965,** *18* (1), 139.

46. Jorgensen, J. E.; Smith, R. I., On the compression mechanism of FeF3. *Acta Crystallogr., Sect. B: Struct. Sci.* **2006,** *62* (Pt 6), 987-992.

47. Costa, M. M. R.; Paixão, J. A.; de Almeida, M. J. M.; Andrade, L. C. R., Charge densities of two rutile structures: NiF_2 and CoF_2. *Acta Crystallogr., Sect. B: Struct. Sci.* **1993,** *49* (4), 591-599.

48. Hepworth, M. A.; Jack, K. H.; Peacock, R. D.; Westland, G. J., The crystal structures of the trifluorides of iron, cobalt, ruthenium, rhodium, palladium and iridium. *Acta Crystallographica* **1957,** *10* (1), 63-69.

49. Molaiyan, P.; Witter, R., Surface defect‐enhanced conductivity of calcium fluoride for electrochemical applications. *Mater. Des. Process. Commun.* **2019,** *1* (4), e44.

50. Rongeat, C.; Reddy, M. A.; Witter, R.; Fichtner, M., Solid electrolytes for fluoride ion batteries: ionic conductivity in polycrystalline tysonite-type fluorides. *ACS Appl. Mater. Interfaces* **2014,** *6* (3), 2103-2110.

51. Roos, A.; Vandepol, F.; Keim, R.; Schoonman, J., Ionic conductivity in tysonite-type solid solutions $La_{1-x}Ba_xF_{3-x}$. *Solid State Ionics* **1984,** *13* (3), 191-203.

52. Orikasa, Y.; Maeda, T.; Koyama, Y.; Murayama, H.; Fukuda, K.; Tanida, H.; Arai, H.; Matsubara, E.; Uchimoto, Y.; Ogumi, Z., Transient Phase Change in Two Phase Reaction between $LiFePO_4$ and $FePO_4$ under Battery Operation. *Chem. Mater.***2013,** *25* (7), 1032-1039.

53. Jain, G.; Balasubramanian, M.; Xu, J. J., Structural studies of lithium intercalation in a nanocrystalline α-Fe_2O_3 compound. *Chem. Mater.***2006,** *18* (2), 423-434.

54. Jain, G. R.; Yang, J. S.; Balasubramanian, M.; Xu, J. J., Synthesis, electrochemistry, and structural studies of lithium intercalation of a nanocrystalline Li_2MnO_3-like compound. *Chem. Mater.***2005,** *17* (15), 3850-3860.

55. Wang, X. Q.; Hanson, J. C.; Frenkel, A. I.; Kim, J. Y.; Rodriguez, J. A., Time-resolved studies for the mechanism of reduction of copper oxides with carbon monoxide: Complex behavior of lattice oxygen and the formation of suboxides. *J Phys. Chem. B* **2004,** *108* (36), 13667-13673.

56. Haruyama, J.; Okazaki, K. I.; Morita, Y.; Nakamoto, H.; Matsubara, E.; Ikeshoji, T.; Otani, M., Two-phase reaction mechanism for fluorination and defluorination in fluoride-shuttle batteries: A first-principles study. *ACS Appl. Mater. Interfaces* **2020,** *12* (1), 428-435.

57. Zu, C.-X.; Li, H., Thermodynamic analysis on energy densities of batteries. *Energy Environ. Sci.* **2011,** *4* (8), 2614–2624.

Chapter 3 Cu–Pb Nanocomposite: toward Room-Temperature Cycling Cathode Materials

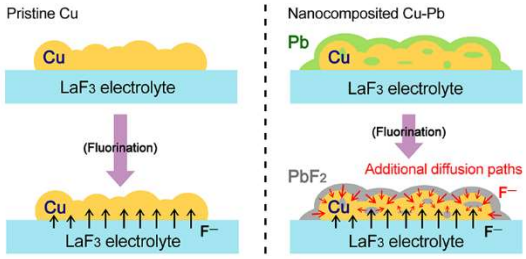

All-solid-state fluoride-ion batteries (FIBs) are regarded as attractive alternatives to traditional energy storage systems because of their high energy density; however, they are not applicable at room temperature owing to sluggish ion transport in both the electrolyte and electrode. In this study, a rational design of a Cu–Pb nanocomposite is reported, which was tested as a room-temperature cathode material for all-solid-state FIBs. Following electrochemical pretreatment, self-generated PbF_2 could act as a fast fluoride-ion conductor and consequently enhance the kinetics of the Cu/CuF_2 phase transition process upon cycling. The detailed reaction mechanism and phase transition process were verified using X-ray absorption near edge structure. The Cu–Pb nanocomposite could realize reversible (de)fluorination at room temperature with high performance and good cyclability.

3.1 Introduction

During the past few decades, lithium-ion batteries (LIBs) have been intensively researched because of their high efficiency and reversibility in practical applications; however, their energy/power densities are approaching physicochemical limitations. [1-5] New battery systems that employ Na^+, K^+, Mg^{2+}, Zn^{2+}, Al^{3+}, or Cl^- as the charge carrier have been developed. [6-12] But these systems all suffer from poor kinetics and stability because of heavy and multivalent charge-transfer ions. The concept of all-solid-state fluoride-ion batteries (FIBs), which have been considered to possess superior electrochemical stability and good ion mobility owing to the high electronegativity and light weight of monovalent fluoride anions, had already been conceived in the 1970s. [13-20] Real prototypes of all-solid-state FIBs were not successfully established until this decade, when tysonite-type (MF_3, M = La, Ce) and fluorite-type (MF_2, M = Ca, Sr, Ba) compounds were found to be suitable for solid-state electrolytes. [21]

In studies concerning all-solid-state FIBs, metal/metal fluoride (M/MF_x) systems are regarded as attractive electrodes that can afford significantly high capacities through multi-electron (de)fluorination processes, and it is possible to fabricate high-potential batteries by employing suitable combinations of working and counter electrodes. Therefore, the theoretical energy densities of all-solid-state FIBs with M/MF_x electrodes can reach 5000 Wh L^{-1} or higher, substantially exceeding those of LIB materials. [22-25] However, limited by sluggish ion transport in the bulk of M/MF_x materials as well as the electrolytes, all-solid-state FIBs exhibit low capacity and undergo significant polarization under mild temperatures. [22,26,27] Furthermore, the traditional bulk-type constructions of all-solid-state batteries lead to severe problems in electrode-electrolyte interfacial contacts and long diffusion distance because of large pellet thickness, which further worsen the kinetics of the electrochemical process. [21,22,28-31]

Herein, we report a thin-film-type Cu–Pb nanocomposite as a cathode material for all-solid-state FIBs that delivers good performance at room temperature (25 °C). Thin-film cells prepared using radio frequency (RF) magnetron sputtering ensured smooth interfacial compatibility between the electrodes and electrolytes, which enhanced the kinetics of F^- transport. High-temperature-level overall performances were achieved at 25 °C owing to the creation of additional diffusion paths for F^- through the rational design of the nanocomposite and electrochemical reaction, and X-ray absorption near edge structure (XANES) was proposed toward elucidating the phase transition and reaction. The present Cu–Pb cathode

design scheme leads to ideal electrochemical properties at room temperature and provides a new strategy for the development of all-solid-state FIB cathode materials.

3.2 Expermental

3.2.1 Preparation of thin films

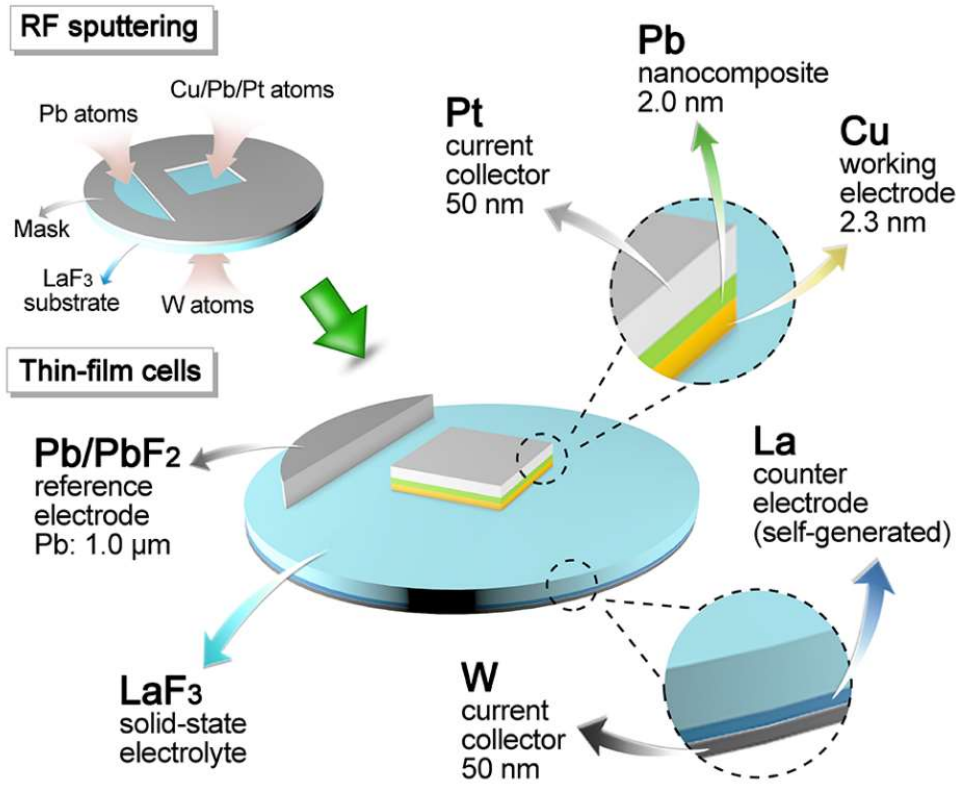

Figure 3.1 Schematic illustration of Cu–Pb nanocomposite thin-film battery. In order to show the construction more clearly, the thicknesses of the thin films were exaggerated.

Thin-film-type all-solid-state batteries were prepared using an RF sputtering machine (EIKO Engineering, Japan). As shown in **Figure 3.1**, typically, polished single-crystal LaF_3 substrates (Pier Optics, Japan) with a thickness of 0.5 mm and diameter of 15 mm were used as solid-state electrolytes. Cu, Pb, Pt, and W were deposited on the LaF_3 substrates; the RF sputtering parameters are listed in **Table 3.1**. The actual thickness and smoothness of each deposited metal were measured and confirmed via atomic force microscopy (AFM), transmission electron microscopy (TEM), and stylus profilometry (Dektak-8, Veeco, USA). The confirmations of the thickness and smoothness of each deposited metal (AFM, TEM, and profilometry characterizations) are described in a previous work. [25]

Table 3.1 The parameters of RF sputtering on LaF_3 substrate

Element	Thickness / nm	RF Sputtering Power / W
Cu	2.3 / 10	50
Pb (W.E.)	2.0 / 8.7	50
Pb (R.E.)	1000	50
Pt	50	50
W	50	120
RF Sputtering Temperature: Room temperature (~25 ˚C)		
Atmosphere: Argon; Atmosphere pressure: 1.0 Pa		

3.2.2 Electrochemical measurements

The batteries were assembled in an argon-filled glove box (Miwa, Japan). Then, pre-fluorination was carried out by connecting the reference electrode (RE) and counter electrode (CE) with a current of 8.3 μA for 300 s at 150 °C. After pre-fluorination, Pb was fluorinated into Pb/PbF_2 and the W-side LaF_3 was defluorinated into La/LaF3, which were employed as the actual RE and CE, respectively, and provided stable reference potentials. The galvanostatic charging–discharging properties were evaluated using a PARSTAT MC2000 battery testing system (Princeton Applied Research, USA) with a cut-off voltage range of 0–1.25 V at 25 and 150 °C. The theoretical capacity was calculated on the basis of the mass of pristine Cu without Pb. The ionic conductivity of the LaF_3 substrate was evaluated using electrochemical impedance spectroscopy (EIS) with a Modulab XM ECS electrochemical test system (Solartron Analytical, UK) from 10^6 to 10^{-1} Hz with an amplitude voltage of 50 mV and corresponding linear fittings at 15, 50, 80, 100, 120, and 150 °C. The details of the pre-fluorination of the Pb/PbF_2 RE and the ionic conductivity of LaF_3 are described in our previous work. [25] Impedances of Cu and Cu–Pb electrodes were also evaluated by EIS from 10^6 to 10^{-1} Hz with an amplitude voltage of 20 mV at 25 °C.

3.2.3 Characterizations

The XRD patterns were collected using an X-ray diffractometer (Rigaku Ultima IV, Japan) with Cu-Kα radiation (λ = 1.54056 Å). In order to prevent interference from strong LaF_3 diffraction signals, thin films of metals were instead deposited on mirror-polished synthetic quartz substrates. The diffraction steps were 0.02°, increasing at a rate of 0.1° per minute and the sample rotation speed was 120 rpm. Batteries for *ex situ* X-ray absorption near edge

spectroscopy (XANES) at various states of charge (SOCs) were prepared through galvanostatic charging–discharging; subsequently, samples were transferred into an analysis chamber without air exposure. The Cu K-edge XANES measurements were conducted at the BL01B1 and BL37XU beamlines (SPring-8, Hyogo, Japan). A 19-element solid-state detector was used to acquire the XANES data in partial fluorescence yield (PFY) mode.

3.3 Results and discussion

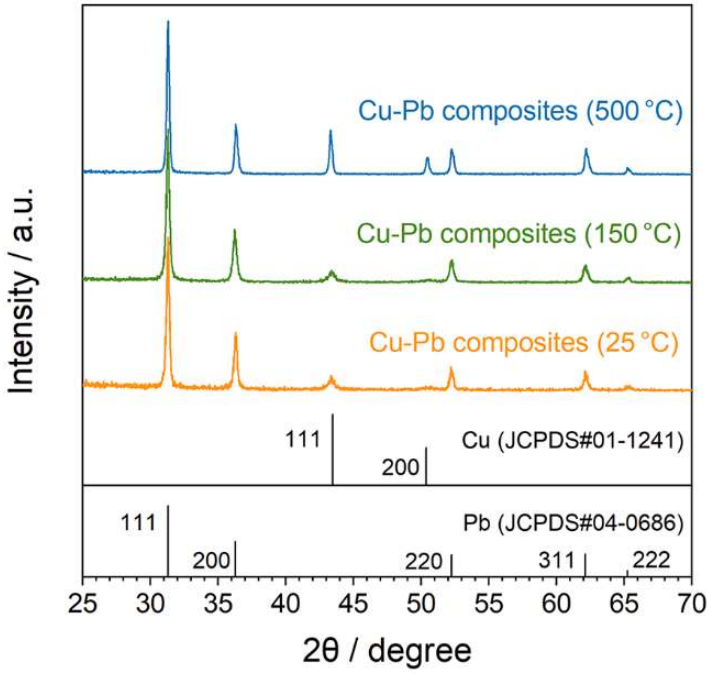

Figure 3.2 XRD patterns of as-prepared Cu–Pb thin films and those annealed at 150 and 500 °C.

Both Cu and Pb possess face-centered cubic (*fcc*) structures but are immiscible according to their phase diagram; [32] thus, no alloy or intermediate compound was generated in the Cu–Pb thin-film system. The XRD patterns of Cu–Pb nanocomposites prepared with different annealing temperatures are shown in **Figure 3.2**. All diffraction peaks were well indexed to pristine Cu (JCPDS#01-1241) and Pb (JCPDS#04-0686) with no impurities observed, and the diffraction peaks of Cu showed low intensity and broadened at 25 and 150 °C, which was attributed to the low crystallinity and the disturbance to the X-rays caused by the overlapping Pb. Even after undergoing annealing at 500 °C, the Cu and Pb phases remained separate. Except for the relative heights of the diffraction peaks, the patterns of as-prepared Cu–Pb, Cu–Pb annealed at 150 °C, and Cu–Pb annealed at 500 °C showed no obvious differences, as shown in **Table 3.2**; the lattice parameters of Cu and Pb showed no obvious changes as well. These results indicated that Cu and Pb did not form

any alloys, intermediate compounds, or solid solutions, but only the nanocomposites. Direct observation of the Cu–Pb nanocomposite through microscopy was difficult because the Cu and Pb layer thicknesses were small (2.3 and 2.0 nm, respectively). However, a cell with ten Cu–Pb layers (total thickness of ~43 nm) was prepared and examined using TEM, and the results are shown in **Figure 3.3**. The LaF_3 substrate, deposited Pt layer, and ten-layer Cu–Pb nanocomposite were identified easily in the cross-sectional TEM images and energy dispersive spectroscopy mapping images. The distribution of the Cu and Pb layers was not as uniform as expected; some local agglomerations were observed instead of clear individual layers. Considering the extremely large volumetric changes of Cu and Pb upon (de)fluorination, the inhomogeneous Cu–Pb distribution may lead to undesired distortions and contact loss upon cycling, resulting in unideal electrochemical performance fading; this is discussed in subsequent paragraphs.

Table 3.2 The lattice parameters of Cu and Pb at 25 and 150 ˚C

Temperature / ˚C	Lattice Parameters *a*	
	Cu / Å	Pb / Å
500	7.217	9.882
150	7.221	9.888
25	7.224	9.888

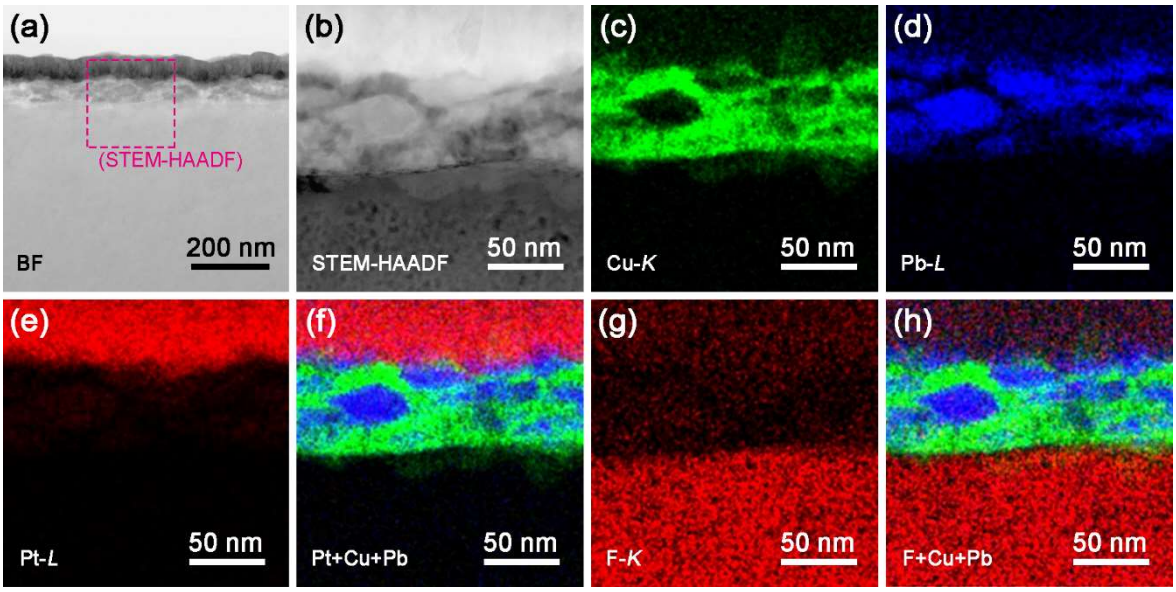

Figure 3.3 Cross-sectional TEM and corresponding EDS mapping images of as-prepared Cu-Pb nanocomposite. (a) Bright-field (BF) image, (b) High-angle annular dark-field scanning TEM (HAADF-STEM) image, and (c-h) EDS mapping images.

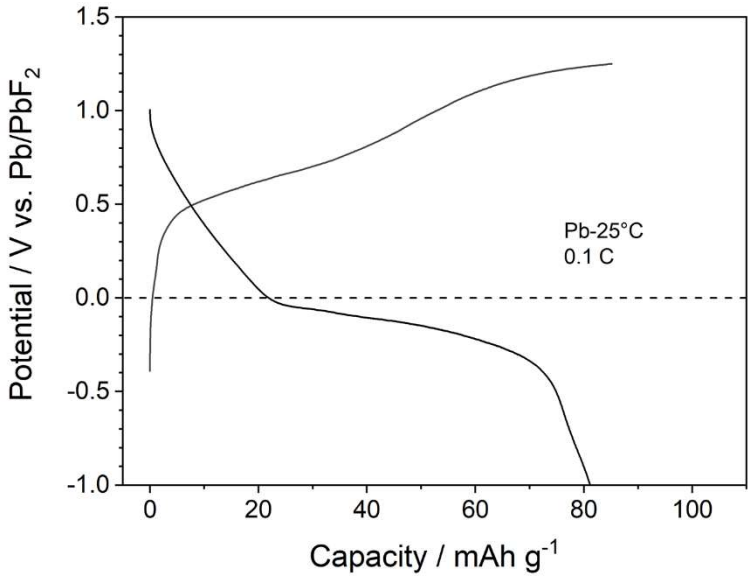

Figure 3.4 The initial charge-discharge curves of Pb at 25 ˚C.

For the galvanostatic charging–discharging tests of the Cu–Pb nanocomposites, the cut-off potential range of 0–1.25 V was selected based on considerations of the respective electrochemical behaviors of Cu and Pb. First, we had confirmed in previous study [25] that the cut-off potential range of 0–1.25 V vs. Pb/PbF_2 was suitable for the completion of the electrochemical reaction of the Cu/CuF_2 redox system. Pristine Pb possesses a theoretical working potential of 0 V vs. Pb/PbF_2; however, the overpotentials caused by polarization push the charging and discharging processes to higher and lower potentials than 0 V, respectively. Therefore, if the lower cut-off potential is limited to 0 V, then Pb cannot complete an entire charging–discharging cycle, as shown in **Figure 3.4**. Thus, within the selected cut-off potential range, Cu can undergo reversible (de)fluorination. Pb was fluorinated to PbF_2 upon initial charging, and most of the generated PbF_2 remained in the subsequent processes. PbF_2 is known as a fast F^- conductor with smooth F^- transport, [33-35] which could be exploited to provide additional F^- diffusion channels for Cu/CuF_2.

As can be seen in **Figure 3.5**, the electrochemical properties of the Cu–Pb nanocomposites significantly exceed those of pristine Cu at both 25 and 150 °C. Notably, the initial reversible capacity at room temperature (25 °C) reached up to 796.7 mAh g^{-1} at 0.1 C (1 C = 843 mA g^{-1}), which was previously thought obtainable only at 150 °C or higher. The average potential upon discharging at 25 ˚C was 0.45 V vs. Pb/PbF_2, which corresponded to high battery potential of 3.34 V if the lowest-potential Li/LiF couple was employed as counter

electrode. Under such circumstance, extremely high energy densities (**Table 3.3**), 2660.9 W h kg^{-1} gravimetrically or 23842.4 W h L^{-1} volumetrically, could be achieved, despite they were calculated based on ultrathin films which were far from practical applications. Considering the potential hysteresis upon practical charging-discharging, the practical energy densities were calculated by capacity and average potential in initial discharging.

Table 3.3 Calculation results of energy densities of Cu-Pb nanocomposites

Conditions	Temperature (˚C)	Capacity (mAh g^{-1})	Potential (V vs. Li/LiF)	Energy density	
				Gravimetric (Wh kg^{-1})	Volumetric (Wh L^{-1})
Theoretical	-	843 [25]	3.53	2975.8	26663.1
Practical	25	796.7	3.34	2660.9	23842.4
	150	870.4	3.49	3037.7	27217.7

* Density of Cu: $8.96\times10_3$ kg m^{-3}; theoretical potential: 0.64 V vs. Pb/PbF_2. [36]

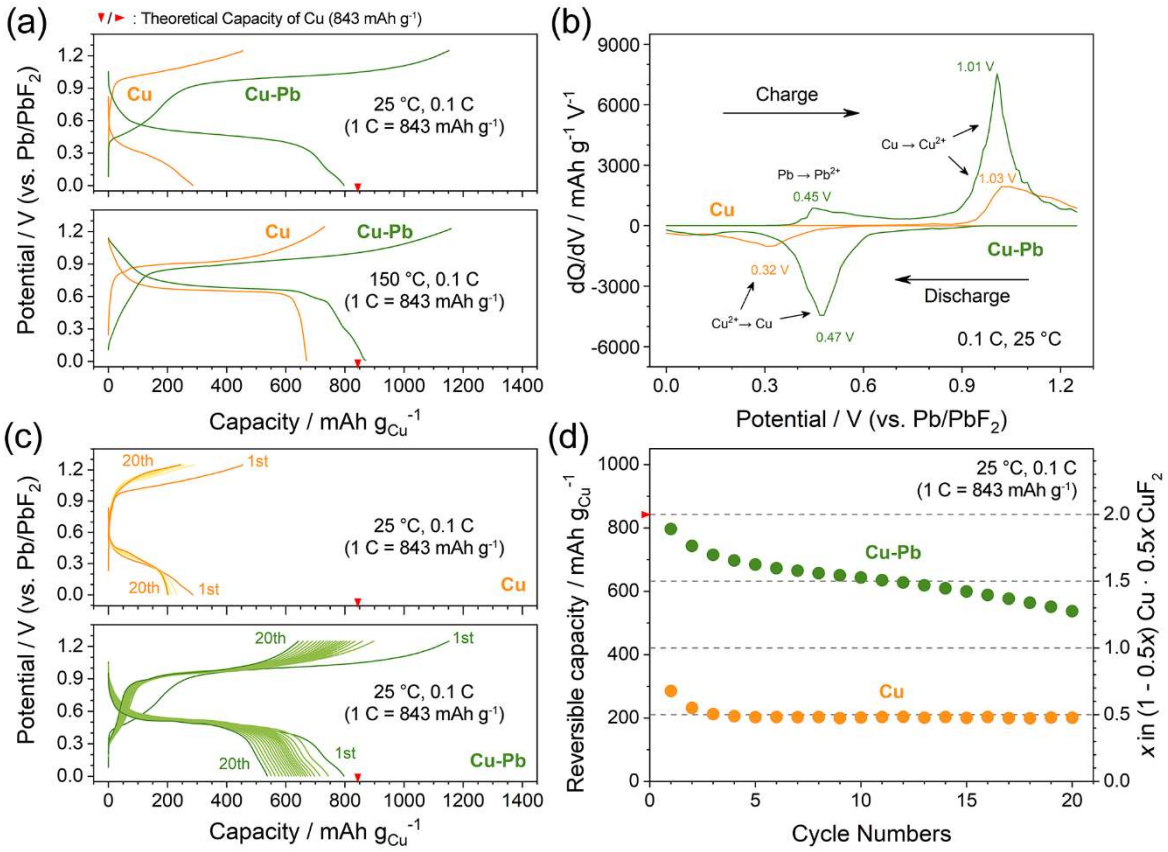

Figure 3.5 (a) Initial charge/discharge curves of Cu and Cu–Pb at 25 and 150 °C. (b) Differential capacity curves of Cu and Cu–Pb at 25 °C. (c) Charge/discharge curves and (d) cyclabilities of Cu and Cu–Pb at 25 °C over 20 cycles.

The Cu/CuF_2 transition follows a two-phase transition pattern; [25] thus, the initial reversible capacity corresponded to $x = 1.89$ in $(1 - 0.5x)Cu \cdot 0.5xCuF_2$ $(0 \leq x \leq 2)$. An additional charging plateau near 0.45 V was observed in the charge/discharge curves of the Cu–Pb nanocomposites at 25 °C (**Figure 3.5**(a)) that was not observed in the curves of pristine Cu, which was consistent with the electrochemical behavior of the Pb/PbF_2 redox system. At 150 °C, although pristine Cu can charge and discharge reversibly with outstanding electrochemical performances, Cu–Pb still delivered a higher capacity and mitigated polarization, and the additional contribution from Pb/PbF_2 redox could be observed as well.

For the Cu–Pb nanocomposites, the initial charge capacities that were much higher than the theoretical value and the low initial coulombic efficiencies suggested that irreversible Pb/PbF_2 redox (de)fluorination occurred at both temperatures, and the remaining PbF_2 consequently led to the buffered polarizations. Differential capacity (dQ/dV) curves of Cu and Cu–Pb at 25 °C clearly showed an extra peak at 0.45 V of charging process, corresponding to the irreversible Pb/PbF_2 reaction. Comparison of the charge–discharge curves of Cu and Cu–Pb over 20 cycles in Figure 3.5(c) revealed that the charging plateau of Pb almost completely disappeared after initial charging, which further substantiated our assumption of the electrochemical behavior of Pb.

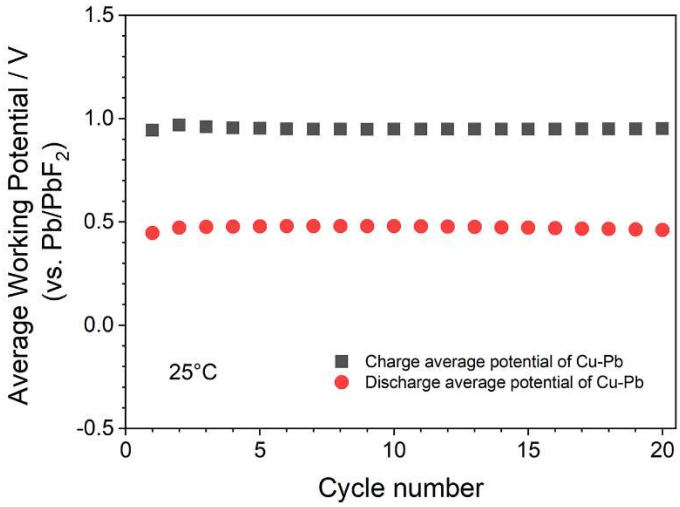

Figure 3.6 The average charge/discharge working potentials of Cu-Pb nanocomposite for 20 cycles at 25 ˚C.

After 20 cycles at 25 °C, a reversible capacity of 537.5 mAh g^{-1} was obtained ($x = 1.27$ in $(1 - 0.5x)Cu \cdot 0.5xCuF_2$ $(0 \leq x \leq 2)$, corresponding to a capacity retention of 67.5% at 0.1 C, as shown in Figure 3d. The average working potential was stable and exhibited little degradation upon long-term cycling, as shown in **Figure 3.6**. Nevertheless, the capacity fading

was still detrimental to achieving high energy density, and this can be attributed mainly to the deterioration of interfacial compatibility between the Cu electrode and LaF_3 electrolyte. During repeated (de)fluorination processes, the Cu/CuF_2 couples underwent significant volumetric expansion/contraction; the lattice volumetric change (ΔV) associated with the conversion of metallic Cu to CuF_2 can reach 195.6% (**Figure 3.7**). [25,37,38] This caused severe damage to the cathode–electrolyte contact. Moreover, the aforementioned inhomogeneous nanoscale distribution of the Cu and Pb thin films (Figure 3.3) may lead to excessive deformation in these local areas, further aggravating the contact loss between the cathode and electrolyte.

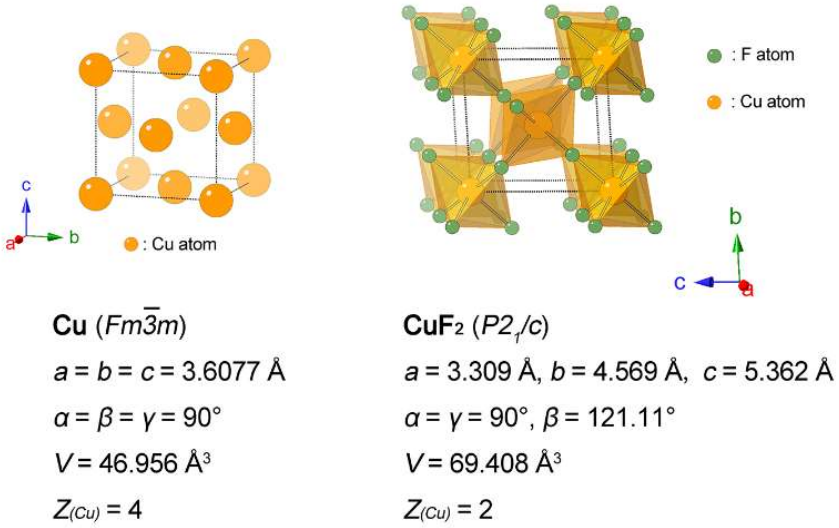

Figure 3.7 The schematically illustration of Cu and CuF_2 crystal models. Note that the relative sizes of atoms in this figure do not represent the real values.

Ex situ XANES analyses were performed to clarify the effects of nanocomposition in detail. To obtain better signals, the Cu and Pb thicknesses of the XANES samples were increased to 10 and 8.7 nm, respectively. As shown in **Figure 3.8**(a), several points on the charge/discharge curves were selected based on the SOC at 150 °C to represent various degrees of fluorination. From the Cu K-edge XANES spectra, the tendency of Cu to transform into CuF_2 could be clearly observed upon charging, as well as the reversible transformation from CuF_2 to Cu upon discharging. The respective amounts of the Cu and CuF_2 phases at various SOCs were obtained from the linear fitting results of the XANES data (Figure 3.8b). Early in the charging process (near the *Chg-80* point), the amount of CuF_2 changed little, indicating that Cu/CuF_2 did not act as the main redox system at this stage. Later in the charging–discharging process, the amount of CuF_2 increased and decreased almost linearly, which was indicative of the aforementioned Cu/CuF_2 two-phase transition reaction. The thorough Cu-to-CuF_2

conversion in the fully charged state (CuF_2 amount of 96.9%) also suggests that the transformation from Cu to CuF_2 exhibited good kinetics even considering the low ionic conductivity of LaF_3 electrolytes at 25 °C (~2.4×10^{-6} S cm^{-1}). [25]

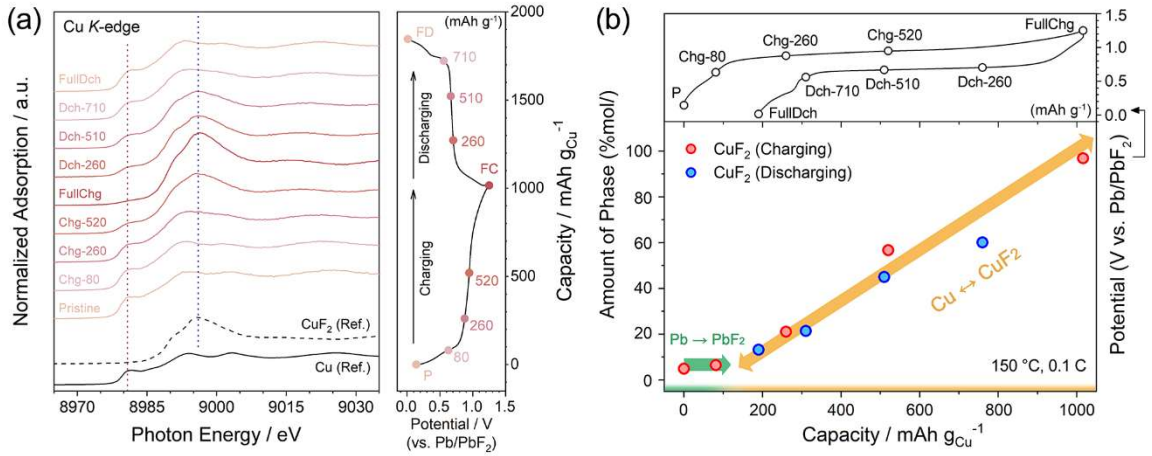

Figure 3.8 (a) Cu K-edge XANES patterns of Cu–Pb composites with various SOCs upon initial cycling. (b) Fitting of amount of CuF_2 phase upon charging and discharging.

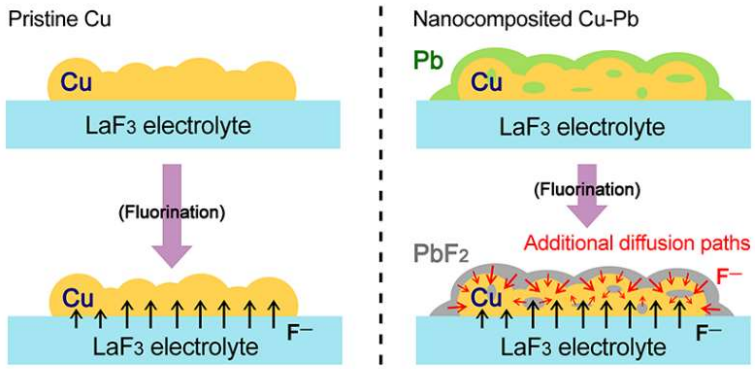

Figure 3.9 Schematically illustration of the extra F^- diffusion pathways provided by nano-composited PbF_2.

In the Cu–Pb nanocomposite, the F^- diffusion capability in the cathode bulk was greatly enhanced by additional diffusion pathways provided by the PbF_2, a fast ion conductor. Based on the respective working potentials of Pb/PbF_2 and Cu/CuF_2 redox systems, the irreversible Pb/PbF_2 transition occurred before the Cu/CuF_2 transition; therefore, the entire fluorination process for Cu was accompanied and facilitated by the fast ion conductor, PbF_2, which was generated in advance and was beneficial for establishing a kinetically smooth reaction environment and thus led to the thorough charging and discharging of Cu, as schematically illustrated in **Figure 3.9**.

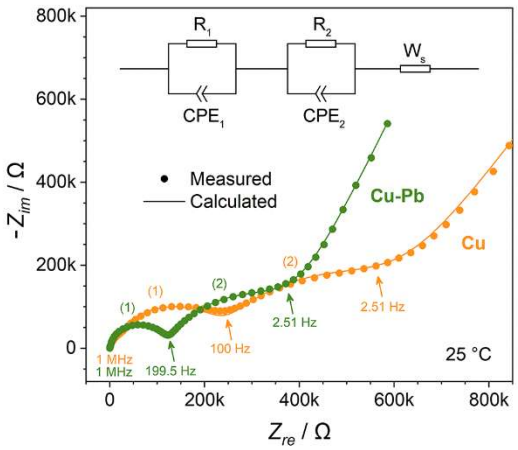

Figure 3.10 Nyquist plots, fitting results, and corresponding equivalent circuit of Cu and Cu-Pb.

The impedances of Cu and Cu–Pb were evaluated by electrochemical impedance spectroscopies (EIS), as shown in **Figure 3.10**. In equivalent circuit, R, CPE and W_s represented resistances, constant phase elements and finite-diffusion Warburg resistance, respectively, where the high-frequency and medium-frequency semicircles could be assigned to grain-boundary (which can be observed in Cu-bulk TEM images in our previous work [39]) and charge-transfer effects in working electrode. [40] Despite the suppressed impedance in Cu–Pb verified the promotion effect of nanocomposite strategy. However, such suppressions on impedances were not so significant as the optimizations on electrochemical performances. One possible reason is, PbF_2 externally provided better diffusion environments to Cu, instead of intrinsically changing the nature of Cu metal. The promotions of Cu–Pb is difficult to clearly elucidated by only EIS result due to the lack of quantitatively analyzing ways of respective contributions from Cu or Pb component. Since the ionic conductivity of the LaF_3 substrate at 25 °C is low, the high efficiency of the Cu–Pb nanocomposite cathode indicates that this is a new possibility for the design of high-performance all-solid-state FIBs. Unlike other well-researched all-solid-state battery systems, the overall properties of FIBs are constrained by not only electrolytes but also the kinetics of electrodes; thus, proper optimization of the electrode can also lead to significant improvements.

3.4 Conclusion

Thin-film-type Cu–Pb nanocomposites were prepared via RF magnetron sputtering and tested as cathode materials for all-solid-state FIBs in the cut-off voltage range of 0–1.25 V. At 25 °C, the Cu–Pb nanocomposite exhibited a high reversible capacity of 796.7 mAh g^{-1} at 0.1 C and capacity retention of 67.5% after 20 cycles. The electrochemical process was clarified

using galvanostatic electrochemical tests and XANES analyses. The entire reaction involved prior irreversible fluorination of Pb to PbF_2, followed by reversible conversion of Cu to CuF_2. PbF_2, which acted as a fast fluoride-ion conductor, provided additional F ion diffusion pathways surrounding metallic Cu, thus remarkably enhancing the ion transport kinetics even at mild temperatures. Although a proper electrolyte is still urgently required for rapid and smooth fluorination, the rational design of this cathode composite was valuable for obtaining ideal electrochemical properties, which gave us new insights for the future development of all-solid-state FIBs.

Reference

1. Armand, M.; Tarascon, J. M., Building Better Batteries. *Nature* **2008,** *451* (7179), 652-657.

2. Islam, M. S.; Fisher, C. A. J., Lithium and Sodium Battery Cathode Materials: Computational Insights into Voltage, Diffusion and Nanostructural Properties. *Chem. Soc. Rev.* **2014,** *43* (1), 185-204.

3. Janek, J.; Zeier, W. G., A Solid Future for Battery Development. *Nat. Energy* **2016**, *1*, 16141.

4. Chu, S.; Cui, Y.; Liu, N., The Path towards Sustainable Energy. *Nat. Mater.* **2017**, *16* (1), 16-22.

5. Grey, C.; Tarascon, J., Sustainability and In Situ Monitoring in Battery Development. *Nat. Mater.* **2017**, 16 (1), 45-56.

6. Delmas, C.; Braconnier, J. J.; Fouassier, C.; Hagenmuller, P., Electrochemical Intercalation of Sodium in Na_xCoO_2 Bronzes. *Solid State Ionics* **1981**, *3–4*, 165-169.

7. Aurbach, D.; Lu, Z.; Schechter, A.; Gofer, Y.; Gizbar, H.; Turgeman, R.; Cohen, Y.; Moshkovich, M.; Levi, E., Prototype Systems for Rechargeable Magnesium Batteries. *Nature* **2000**, *407* (6805), 724-727.

8. Xu, C.; Li, B.; Du, H.; Kang, F., Energetic Zinc Ion Chemistry: the Rechargeable Zinc Ion Battery. *Angew. Chem. Int. Ed.* **2012**, *51* (4), 933-935.

9. Jian, Z.; Luo, W.; Ji, X., Carbon Electrodes for K-Ion Batteries. *J. Am. Chem. Soc* **2015**, *137* (36), 11566-11569.

10. Lin, M. C.; Gong, M.; Lu, B.; Wu, Y.; Wang, D. Y.; Guan, M.; Angell, M.; Chen, C.; Yang, J.; Hwang, B. J.; Dai, H., An Ultrafast Rechargeable Aluminium-Ion Battery. *Nature* **2015**, *520* (7547), 325-328.

11. Zhao, X.; Zhao-Karger, Z.; Wang, D.; Fichtner, M., Metal Oxychlorides as Cathode Materials for Chloride Ion Batteries. *Angew. Chem. Int. Ed.* **2013**, 52 (51), 13621-13624.

12. Gao, P.; Reddy, M. A.; Mu, X.; Diemant, T.; Zhang, L.; Zhao-Karger, Z.; Chakravadhanula, V. S.; Clemens, O.; Behm, R. J.; Fichtner, M., VOCl as a Cathode

for Rechargeable Chloride Ion Batteries. *Angew. Chem. Int. Ed.* **2016**, *55* (13), 4285-4290.

13. Kosacki, I., Physical Properties and Applications of $Cd_{1-x}Pb_xF_2$ Superionic Crystals. *Appl. Phys. A* **1989**, *49* (4), 413-424.

14. Schoonman, J.; Wolfert, A., Solid-state Galvanic Cells with Fast Fluoride Conducting Electrolytes. *Solid State Ionics* **1981**, *3*, 373-379.

15. Hagenmuller, P.; Réau, J.-M.; Lucat, C.; Matar, S.; Villeneuve, G., Ionic Conductivity of Fluorite-Type Fluorides. *Solid State Ionics* **1981**, *3*, 341-345.

16. Schoonman, J.; Wapenaar, K. E. D.; Oversluizen, G.; Dirksen, G. J., Fluoride-Conducting Solid Electrolytes in Galvanic Cells. *J. Electrochem. Soc.* **1979**, *126* (5), 709-713.

17. Danto, Y.; Poujade, G.; Pistre, J.; Lucat, C.; Salardenne, J., A $Pb|PbF_2|BiF_3|Bi$ Thin Solid Film Reversible Galvanic Cell. *Thin Solid Films* **1978**, *55* (3), 347-354.

18. Schoonman, J., A Solid-State Galvanic Cell with Fluoride-Conducting Electrolytes. *J. Electrochem. Soc.* **1976**, *123* (12), 1772-1775.

19. Kennedy, J. H.; Hunter, J. C., Thin-Film Galvanic Cell $Pb/PbF_2/PbF_2$, CuF_2/Cu. *J. Electrochem. Soc.* **1976**, *123* (1), 10-14.

20. Baukal, W., Electrochemical Secondary Cells Which Contains Only Solid Material. *Ger. Offen.* **1971**, *GWXXBX DE* 2017128.

21. Reddy, M. A.; Fichtner, M., Chapter 3 - Fluoride Cathodes for Secondary Batteries. In *Advanced Fluoride-Based Materials for Energy Conversion*, Nakajima, T.; Groult, H., Eds. Elsevier: **2015**; pp 51-76.

22. Thieu, D. T.; Fawey, M. H.; Bhatia, H.; Diemant, T.; Chakravadhanula, V. S. K.; Behm, R. J.; Kübel, C.; Fichtner, M., CuF_2 as Reversible Cathode for Fluoride Ion Batteries. *Adv. Funct. Mater.* **2017**, *27* (31), 1701051.

23. Rongeat, C.; Reddy, M. A.; Witter, R.; Fichtner, M., Nanostructured Fluorite-Type Fluorides as Electrolytes for Fluoride Ion Batteries. *J. Phys. Chem. C* **2013**, *117* (10), 4943-4950.

24. Fawey, M. H.; Chakravadhanula, V. S. K.; Munnangi, A. R.; Rongeat, C.; Hahn, H.; Fichtner, M.; Kübel, C., First Results from In Situ Transmission Electron

Microscopy Studies of All-Solid-State Fluoride Ion Batteries. *J. Power Sources* **2020,** *466*, 228283.

25. Zhang, D.; Yamamoto, K.; Ochi, A.; Wang, Y.; Yoshinari, T.; Nakanishi, K.; Nakano, H.; Miki, H.; Nakanishi, S.; Iba, H.; Uchiyama, T.; Watanabe, T.; Amezawa, K.; Uchimoto, Y., Understanding the Reaction Mechanism and Performances of 3d Transition Metal Cathodes for All-solid-state Fluoride Ion Batteries. *J. Mater. Chem. A* **2021**, *9*, 406-412.

26. Zhang, L.; Reddy, M. A.; Gao, P.; Diemant, T.; Jürgen Behm, R.; Fichtner, M., Study of All-Solid-State Rechargeable Fluoride Ion Batteries Based on Thin-Film Electrolyte. *J. Solid State Electrochem.* **2016**, *21* (5), 1243-1251.

27. Mohammad, I.; Witter, R., Testing Mg as an Anode Against BiF_3 and SnF_2 Cathodes for Room Temperature Rechargeable Fluoride Ion Batteries. *Mater. Lett.* **2019**, *244*, 159-162.

28. Rongeat, C.; Anji Reddy, M.; Diemant, T.; Behm, R. J.; Fichtner, M., Development of New Anode Composite Materials for Fluoride Ion Batteries. *J. Mater. Chem. A* **2014**, *2* (48), 20861-20872.

29. Zhang, L.; Anji Reddy, M.; Fichtner, M., Development of Tysonite-Type Fluoride Conducting Thin Film Electrolytes for Fluoride Ion Batteries. *Solid State Ionics* **2015**, *272*, 39-44.

30. Anji Reddy, M.; Fichtner, M., Batteries Based on Fluoride Shuttle. *J. Mater. Chem.* **2011**, *21* (43), 17059-17062.

31. Zhang, L.; Reddy, M. A.; Fichtner, M., Electrochemical Performance of All Solid-State Fluoride-Ion Batteries Based on Thin-Film Electrolyte Using Alternative Conductive Additives and Anodes. *J. Solid State Electrochem.* **2017**, *22* (4), 997-1006.

32. Chakrabarti, D. J.; Laughlin, D. E., The Cu−Pb (Copper-Lead) System. *Bull. Alloy Phase Diagr.* **1984**, *5* (5), 503-510.

33. Boyce, J.; Mikkelsen Jr, J.; O'keeffe, M., Ion Dynamics and Sublattice Melting in the Superionic Conductor PbF_2. *Solid State Commun.* **1977**, *21* (10), 955-958.

34. Ito, Y.; Koto, K.; Yoshikado, S.; Ohachi, T.; Kanamaru, F.; Mukoyama, T., Variable-Temperature X-Ray Diffraction Analysis of the Behavior of the Mobile

Fluorine Ions in a Superionic Conductor, β-PbF_2. *J. Solid State Chem.* **1991**, *95* (1), 94-98.

35. Berastegui, P.; Hull, S., Structure and Conductivity of Some Fluoride Ion Conductors. *Solid State Ionics* **2002**, *154*, 605-608.

36. Motohashi, K.; Nakamura, T.; Kimura, Y.; Uchimoto, Y.; Amezawa, K., Influence of Microstructures on Conductivity in Tysonite-Type Fluoride Ion Conductors. *Solid State Ionics*, **2019**, *338*, 113-120.

37. Owen, E. A.; Yates, E. L., Precision Measurements of Crystal Parameters Locality: Synthetic Sample: at T = 18 °C. *Philos. Mag.* **1933**, *15*, 472-488.

38. Fischer, P.; Hälg, W.; Schwarzenbach, D.; Gamsjäger, H., Magnetic and Crystal Structure of Copper (II) Fluoride. *J. Phys. Chem. Solids* **1974**, *35* (12), 1683-1689.

39. Nakano, H.; Matsunaga, T.; Mori, T.; Nakanishi, K.; Morita, Y.; Ide, K.; Okazaki, K.-i.; Orikasa, Y.; Minato, T.; Yamamoto, K.; Ogumi, Z.; Uchimoto, Y., Fluoride-Ion Shuttle Battery with High Volumetric Energy Density. *Chem. Mater.* **2020**, *33*, 459-466.

40. Cangaz, S.; Hippauf, F.; Reuter, F. S.; Doerfler, S.; Abendroth, T.; Althues, H.; Kaskel, S., Enabling High-Energy Solid-State Batteries with Stable Anode Interphase by the Use of Columnar Silicon Anodes. *Adv. Energy Mater.* **2020**, *10*, 2001320.

Chapter 4 Reversible and Fast (De)fluorination of Cu_2O Cathode Material: One Step toward Practical Application

All-solid-state fluoride-ion batteries (FIBs) are regarded as promising energy storage devices; however, currently proposed cathodes fail to meet the requirements for practical applications in terms of high energy density and high rate capability. Herein, we report the first use of stable and low-cost cuprous oxide (Cu_2O) as a cathode material for all-solid-state FIBs with reversible and fast (de)fluorination behavior. A phase-transition reaction mechanism involving Cu^+/Cu^{2+} redox for charge compensation was confirmed, using the combination of electrochemical methods and X-ray absorption spectroscopy. The first discharge capacity was approximately 220 mAh g^{-1}, and fast capacity fading was observed in the first five cycles, which was ascribed to partial structural amorphization. Compared to those of simple metal/metal fluoride systems, the material showed a superior rate capability, with a first discharge capacity of 110 mAh g^{-1} at 1 C. The rate-determining step and probable structural evolutions were investigated as well. It is believed that the comprehensive investigations of Cu_2O as a cathode material described in this work can lead to new understandings on all-solid-state FIBs.

4.1 Introduction

The extensive application of energy storage devices has changed our lifestyles tremendously and spawned many new industries such as electronic vehicles and smart devices. [1-3] In particular, the commercialization of lithium-ion batteries (LIBs) has contributed greatly to the establishment of an intelligent and sustainable society; however, LIBs are facing bottlenecks in terms of energy/power density and safety. [1-5] In recent decades, many new concepts for batteries have been proposed as potential alternatives for LIBs, such as battery systems that employ Na^+, K^+, Mg^{2+}, Zn^{2+}, Ca^{2+}, Al^{3+}, F^-, or Cl^- as charge carriers, which have significantly expanded the strategies for developing next-generation batteries with high energy and power densities. [6-16]

All-solid-state fluoride-ion batteries (FIBs) have received widespread attention because of the high electronegativity of fluorine. This leads to extraordinary anodic electrochemical stability, resulting in superior reliability for solid-state utilization. In early studies, including our recent ones, simple metal/metal fluoride (M/MF_x) systems were first utilized as electrode materials with high theoretical capacities. [6, 17-24] Using M/MF_x systems, it is theoretically feasible to fabricate batteries with high energy densities because the working potential can exceed 3 V if suitable cathode-anode combinations are selected. However, close-packed metal atoms (e.g., Cu, Co, Ni, Bi, etc.) provide no diffusion path for F anions in conversion-type M/MF_x systems; as a result, M/MF_x systems inevitably suffer from thorough atomic rearrangements and undesired volumetric changes upon (de)fluorination, which have been proven in previous studies to be devastating for the electrode-electrolyte interfaces of all-solid-state batteries. [18, 19, 23, 25, 26]

In addition to M/MF_x systems, those with topotactic host materials with accessible lattices, such as perovskite-, Ruddlesden–Popper-, and schafarzikite-type materials, have also attracted widespread attention owing to their high structural reversibility and F intercalation tolerance [27-32] However, these intercalation-type materials usually have heavy molecules, and the large mass ratios of the electrochemically inactive components lower the overall energy densities. Theoretical calculations for MXenes [33] and layered electrides [34] as electrode materials for FIBs have also been reported recently, but no experimental results have been reported thus far.

Herein, we introduce the use of cuprous oxide (Cu_2O) with highly reversible (de)fluorination behavior as a new cathode material for all-solid-state FIBs. Besides the

metal/metal fluoride (M/MF_x) systems that theoretically has a 100% conversion percentage of pristine metals, Cu_2O has an extremely high content of redox species (Cu^+) and thus high theoretical capacity compared to those of topotactic oxides and oxyfluorides. Meanwhile, the Cu_2O cathode also possesses highly accessible non-close-packed Cu-O configurations; as expected, it was found to exhibit a much-improved rate capability compared to that of a Cu/CuF_2-based cathode. [19] X-ray absorption spectroscopic (XAS) results revealed a typical phase-transition reaction mechanism and investigated the structural evolutions, as well as the possible causes of the initial capacity fading. Kinetic factors that affect (de)fluorination were also discussed based on Kolmogorov–Johnson–Mehl–Avrami (KJMA) theory.

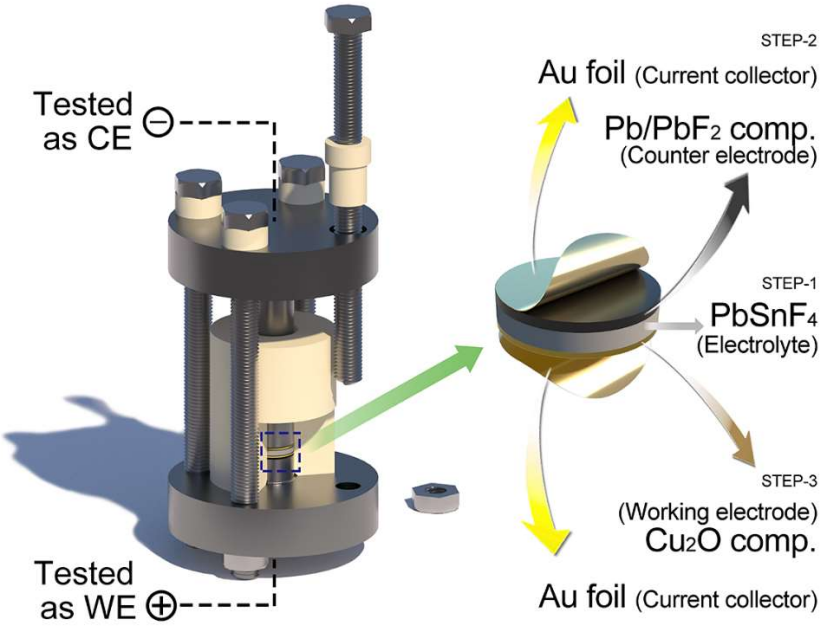

Figure 4.1 Illustration of bulk-type cells used for evaluation of Cu_2O cathode material.

To the best of our knowledge, this is the first study of Cu_2O as a new candidate for a cathode material for all-solid-state FIBs. Thus far, the extraordinary performance of Cu_2O (particularly the high performance at a current density of 375 mA g^{-1}) using a bulk-type all-solid-state cell (**Figure 4.1**) seems to be the best result among all related studies. [6, 17-32] The mixed-anion nature of fluorinated Cu_2O also lead to some new considerations. It is hoped that this result will deepen our understanding on the development of new capable alternatives for all-solid-state FIBs, as well as bring new considerations toward the possibilities of practical applications of all-solid-state FIBs, considering the low-cost, highly commercialized and chemical stable characteristics of Cu_2O materials.

4.2 Experimental

4.2.1 Material preparation

The $PbSnF_4$ solid electrolyte was prepared using a mechanochemical method. Stoichiometric amounts of SnF_2 (99%, Kojundo, Japan) and PbF_2 (99.9%, Kojundo, Japan) were ground using an agate mortar and pestle in an argon-filled glove box (Miwa, Japan) and then transferred to a milling vial. The mechanochemical synthesis was carried out using planetary ball mills (Fritsch Pulverisette7 premium line, Germany) with ZrO_2 balls under a rotation speed of 600 rpm for 12 h. The $PbSnF_4$ materials were acquired after the ball-milled powder was calcined at 400 °C for 1 h. The Cu_2O cathode composites were obtained by mixing commercial Cu_2O nanopowder (US Research Nanomaterials, USA), $PbSnF_4$, and acetylene black (AB) using ZrO_2 balls under a ball-milling rotation speed of 100 rpm for 12 h. Similarly, the Pb/PbF_2 anode composites were acquired by mixing PbF_2, $PbSnF_4$, and vapor-grown carbon fiber (VGCF, Showa Denko, Japan) using ZrO_2 balls under a rotation speed of 300 rpm for 12 h, and then grinding the ball-milled powder with a certain amount of Pb powder using an agate mortar and pestle. The Cu_2O:$PbSnF_4$:AB and Pb:PbF_2:$PbSnF_4$:VGCF mass ratios were 25:70:5 and 15:15:60:10, respectively.

4.2.2 Battery assembly

The electrochemical properties were evaluated using a bulk-type cell with all powders pressed into a pellet, as shown in Figure 4.1. All battery assembly procedures were performed in an argon-filled glove box. Typically, $PbSnF_4$ powder was placed in an insulating cell die (Φ10 mm, PEEK) and pre-pressed under a pressure of 100 MPa for 5 min. Then, the Cu_2O cathode composites, Pb/PbF_2 anode composites, and two pieces of Au current collectors (CCs) were placed on the opposite sides of the $PbSnF_4$ pellet. Lastly, the CC/cathode/electrolyte/anode/CC cell was pressed under a pressure of 360 MPa for 5 min.

4.2.3 Electrochemical tests

The galvanostatic charging-discharging properties and galvanostatic intermittent titration technique (GITT) were evaluated and performed HJ1020mSD8 battery testing systems (Hokuto Denko, Japan) with a cut-off voltage range of 0.4–1.5 V at 140 °C, the galvanostatic charging-discharging properties were evaluated and the galvanostatic intermittent titration technique (GITT) was performed; for the GITT, the cell was relaxed at

open circuit voltage (OCV) for 10 h to allow it to reach a quasi-equilibrium state after each galvanostatic step, which lasted for 4 h at 0.01 C (1 C = 375 mA g^{-1}). The ionic conductivity of the $PbSnF_4$ solid electrolyte was evaluated via electrochemical impedance spectroscopy (EIS) using a Modulab XM ECS electrochemical test system (Solartron Analytical, UK) in the frequency range of 10^6 to 10^{-1} Hz with an amplitude voltage of 50 mV. The activation energy (E_a) was calculated using the Arrhenius equation based on temperature-dependent EIS measurements at 25, 50, 75, 100, 125, and 140 °C. The electrochemical window of $PbSnF_4$ at 140 °C was measured using linear sweep voltammetry (LSV) with a sweep rate of 0.2 mV s^{-1}. The potentiostatic intermittent titration technique (PITT) was conducted using an HZ-5000 electrochemical test system (Hokuto Denko, Japan) with a potential step of 0.02 V; the potential step was narrowed to 0.01 V near the charging plateau to acquire more detailed information. The apparent F^- diffusion coefficients were calculated from the PITT results using the equation (4-1): [35-37]

$$D_{\mathrm{PITT}} = \frac{d \ln I(t)}{dt} \frac{4L^2}{\pi^2}, t \gg \frac{L^2}{D_{PITT}} \qquad (4-1)$$

where D is the diffusion coefficient, L (cm) is the diffusion length (regarded as the cathode thickness), and $I(t)$ (A) is the recorded transient current as a function of time, t.

4.2.4 Characterizations

The XRD patterns were collected using an X-ray diffractometer with Cu Kα radiation (λ = 1.54056 Å, Rigaku Ultima IV, Japan). Rietveld refinement was performed using GSAS and EXPGUI software. [38] The microscale morphologies and energy dispersive spectroscopy (EDS) spectra were examined and recorded using a field emission S-3400N scanning electron microscope (Hitachi, Japan) and a J2100F transmission electron microscope (JEOL, Japan), respectively.

Ex situ Cu K-edge and Cu $L_{2,3}$-edge X-ray absorption spectroscopy (XAS) measurements were conducted at the BL01B1, BL14B2 and BL27SU beamlines at SPring-8 (Hyogo, Japan), respectively. To acquire the XAS data in the partial fluorescence yield (PFY) mode, a 19-element solid-state detector and a silicon drift detector were used for the Cu K-edge and Cu $L_{2,3}$-edge measurements, respectively. High-energy X-ray diffraction (HEXRD) was performed at the BL02B2 beamline at SPring-8 with wavelengths of 0.41313 and 0.41269 Å, which were calibrated using CeO_2.

4.3 Results and discussion

4.3.1 Phase and compositions

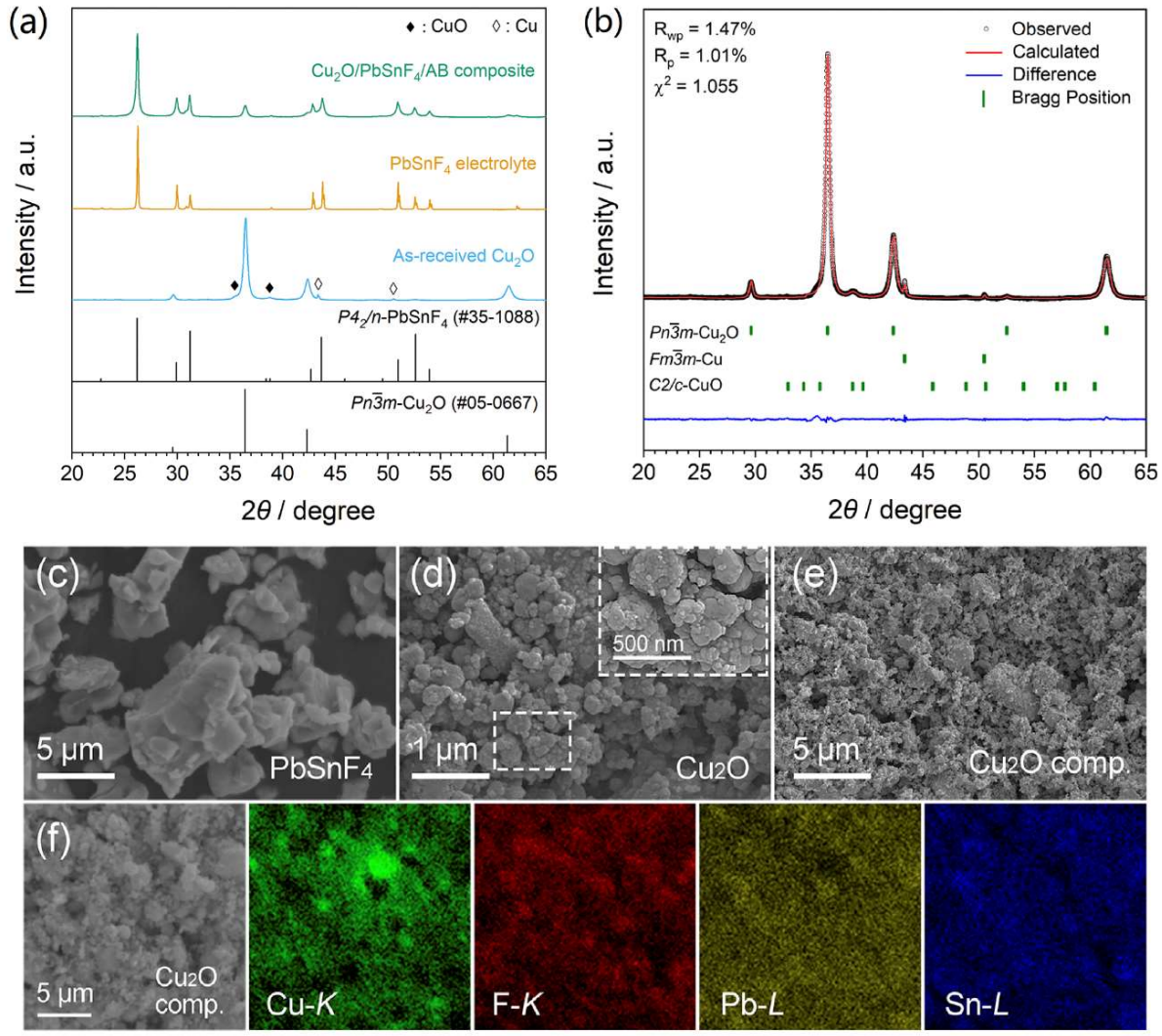

Figure 4.2 (a) XRD patterns and (b) Rietveld refinement results of as-received Cu_2O, and (c–e) scanning electron microscopy images of as-prepared $PbSnF_4$ electrolyte, as-received Cu_2O, and $Cu_2O/PbSnF_4$/AB composite. (f) Elemental distributions of Cu, F, Pb, and Sn in $Cu_2O/PbSnF_4$/AB composite from EDS mapping.

The XRD patterns of as-received Cu_2O, the as-prepared $PbSnF_4$ electrolyte, and the $Cu_2O/PbSnF_4$/AB composite are shown in **Figure 4.2**(a). Rietveld refinement revealed that as-received Cu_2O had a cubic structure (space group of $Pn\bar{3}m$, JCPDS#05-0667) with a lattice parameter a of 4.27079 Å and 1.44 wt.% and 8.24 wt.% of Cu and CuO impurities, respectively (Figure 4.2(b)). All diffraction peaks of $PbSnF_4$ were well indexed to a tetragonal β'-structure with a space group of $P4_2/n$ (JCPDS#35-1088), and the peaks of the $Cu_2O/PbSnF_4$/AB composites corresponded well with only the $Pn\bar{3}m$-Cu_2O and $P4_2/n$-$PbSnF_4$ phases because

the carbon species (AB) was amorphous; no impurities were observed. The morphologies of the $PbSnF_4$, Cu_2O, and cathode composites are shown in Figure 4.2(c) to (f). The large $PbSnF_4$ particles and Cu_2O active material nanoparticles were distributed homogeneously after ball milling, as can be seen in Figure 1e and 1fzaih, which confirmed that contact between the electrolyte and cathode was sufficient and thus there were enough diffusion paths for F anions.

4.3.2 Electrochemical performance

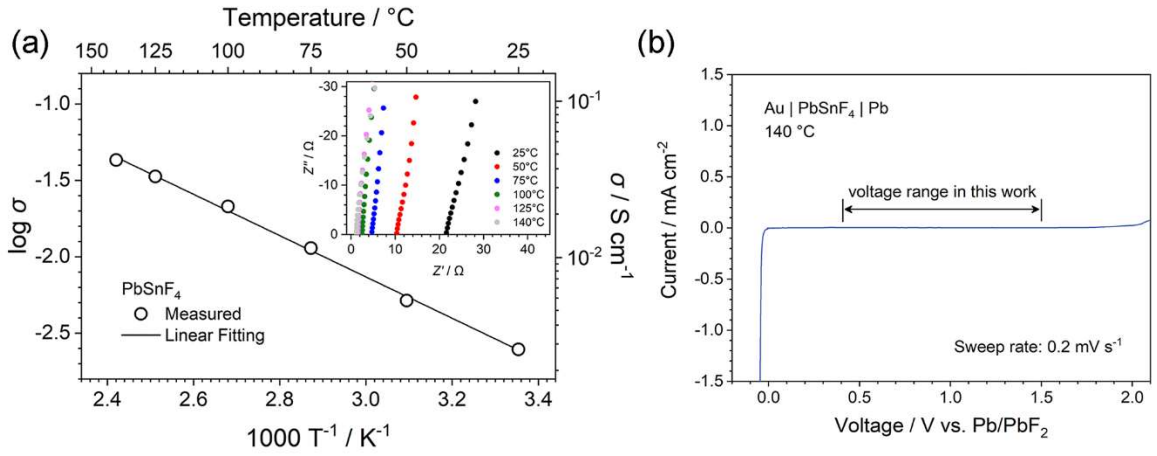

Figure 4.3 (a) The ionic conductivities and corresponding Arrhenius linear fitting, and the Nyquist plots of $PbSnF_4$ at temperatures (inset) of 25, 50, 75, 100, 125, 140 ˚C, respectively. (b) Linear sweep voltammograms (LSV) of $PbSnF_4$ from 0 V to 3 V and to -3 V (vs. Pb/PbF_2) at 140 ˚C.

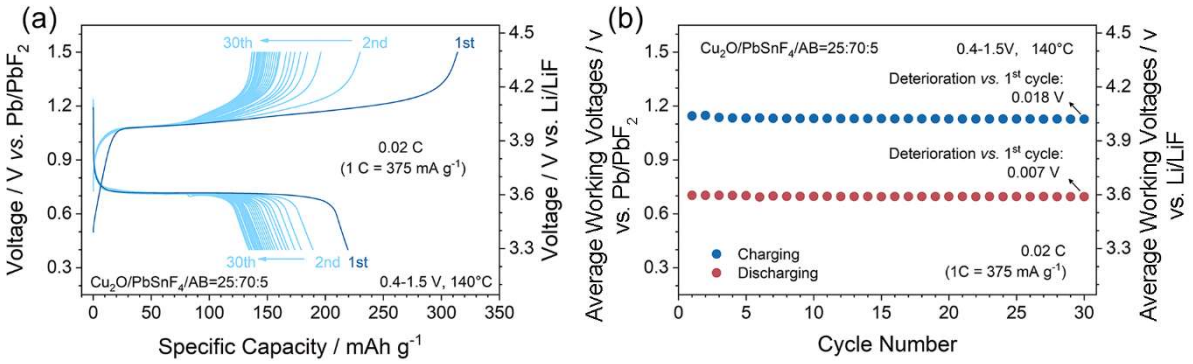

Figure 4.4 (a) Charge/discharge profiles and (b) average working voltages deteriorations for cycles 1–30 of Cu_2O cathode at 0.02 C (1 C = 375 mA g^{-1}).

$PbSnF_4$ was used as the solid electrolyte in this work because of its superior ionic conductivity (~10^{-2} S cm^{-1} at 140 °C) and low activation energy (~0.30 eV), which were determined using electrochemical impedance spectroscopy, as shown **Figure 4.3**(a), and proven to be similar to reported values. [39-43] Although the electrochemical window of $PbSnF_4$ is not as wide as that of commonly used $La_{0.9}Ba_{0.1}F_{2.9}$, [44, 45] it is electrochemically stable within the voltage range employed in this study (0.4–1.5 V vs. Pb/PbF_2), as shown in Figure 4.3(b).

In the case of Cu_2O active material, a high capacity of 375 mAh g^{-1} can be obtained theoretically, assuming that the $Cu^{(I)}$ species in Cu_2O are completely transformed into $Cu^{(II)}$ upon oxidation and vice versa. The Cu_2O material exhibited reversible charge/discharge behavior within the given cut-off voltage range (0.4–1.5 V, **Figure 4.4**(a)). At 0.02 C (7.5 mA g^{-1}), charge and discharge capacities of 313.9 and 219.5 mAh g^{-1} were delivered, respectively, and a reversible capacity of 131.5 mAh g^{-1} remained after 35 cycles. The undesired capacity fading during the first five cycles was remarkable, and the factors responsible for such fading will be discussed in later sections. The average working potentials were stable (Figure 4.4(b)), with potential deteriorations of 0.018 and 0.007 V for charging and discharging after 30 cycles, respectively. The cyclabilities were tested at various C rates, as shown in **Figure 4.5**. At a rate of 1 C (375 mA g^{-1}, corresponding to 1900 μA cm^{-2}), a competitive reversible capacity of 110 mAh g^{-1} was delivered in initial cycle; 61 mAh g^{-1} remained after 35 cycles. Such capability of fast fluorination is initially achieved in all-solid-state FIBs compared with previous studies, [23, 31, 46, 47] indicating that all-solid-state FIBs have started to pursue better practical performance that attempt to benchmark against those of LIBs instead of being regarded as a conceptional battery device with only theoretical feasibility, despite it is tough for new battery systems.

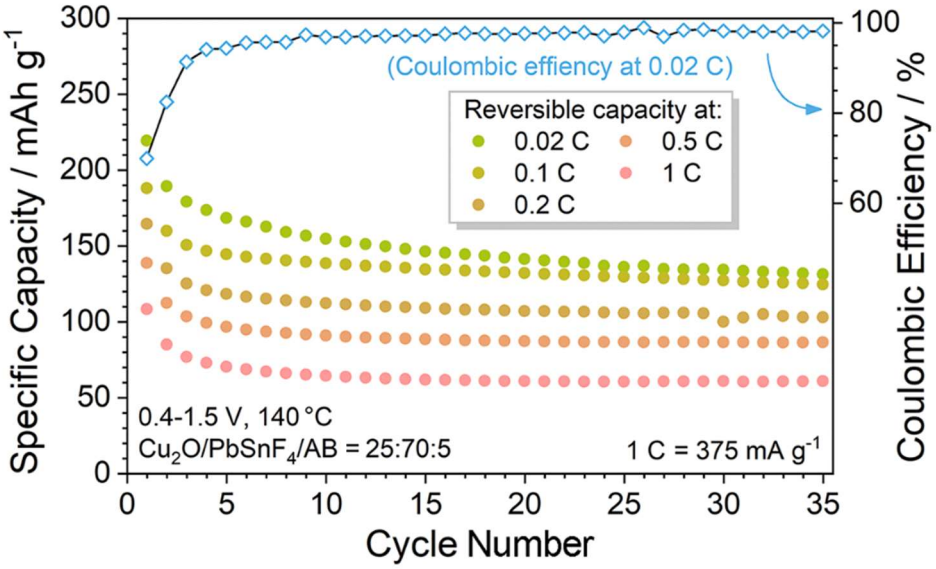

Figure 4.5 Cyclabilities at various C rates of Cu_2O cathode material.

It is worth interpreting that Pb/PbF_2 is one of most popular anode materials with ideal non-polarizing electrode behavior: the potential is always constant because the reaction proceeds in a two-phase routine, [25, 26, 48] and the potential does not change even when a small current flows due to the large exchange current density. These merits help to acquire accurate evaluations on Cu_2O properties; but Pb/PbF_2 has relatively high potential, which plays a role

more like reference electrode. In some cases of employing Pb/PbF_2 as anode, the discharging cut-off voltage can be even minus, which was also called "forced discharge" by O. Clemens et al.[11] In terms of practical applications, La/LaF_3 anodes with lower potentials (-2.41 V vs. Pb/PbF_2) have be utilized in many previous studies. [17-20, 46] A preliminary assessment of $Cu_2O||LaF_3$ cell compared with typical $LiCoO_2||$graphite was given in **Table 4.1**, where higher energy density can be achieved in $Cu_2O||LaF_3$ cell; particularly, the volumetric energy density of $Cu_2O||LaF_3$, which is more meaningful for practical application, is almost twice that of $LiCoO_2||$graphite. If more ideal anode (such as Li/LiF which possesses the lowest electrode potential among various M/MF_x compound) can be practically employed as anode, the cell voltage can be further increased, as we have marked in the right-side axis of Fig. 2a. Likewise, in order to absolutely avoid undesired fluorinations that might lead to extra behavior (plateau and capacity), we employed Au foils as current collectors for lab-level research, whereas stainless-steel or carbon-coated Al foils are practically capable of being current collector as well. [30, 31]

Table 4.1. The comparison of gravimetric/volumetric energy densities of $Cu_2O||LaF_3$ FIB and typical $LiCoO_2||$graphite LIB.

	$LiCoO_2||$graphite (LIB)	$Cu_2O||LaF_3$ (FIB)
Capacity of cathode (mAh g^{-1})	150	220
Density of cathode (g cm^{-3})	5.05	6.00
Capacity of anode (mAh g^{-1})	370	410
Density of anode (g cm^{-3})	2.00	5.94
Gravity ratio (cathode:anode)	0.403	0.536
Volume ratio (cathode:anode)	1.02	0.541
Average cell potential (V)	3.70	3.10
Gravimetric enegy density (Wh kg^{-1})	395	440
Volumetric enegy density (Wh L^{-1})	1390	2650

* The extra parts (current collector, electrolyte, battery shell, separator, conductive species, binder, etc.) were not involved into calculation because they can be solved by engineering ways and are not intrinsic factors.

** The capacity ratio of cathode to anode in the full cell was fitted to 1.0.

4.3.3 Phase-transition processes

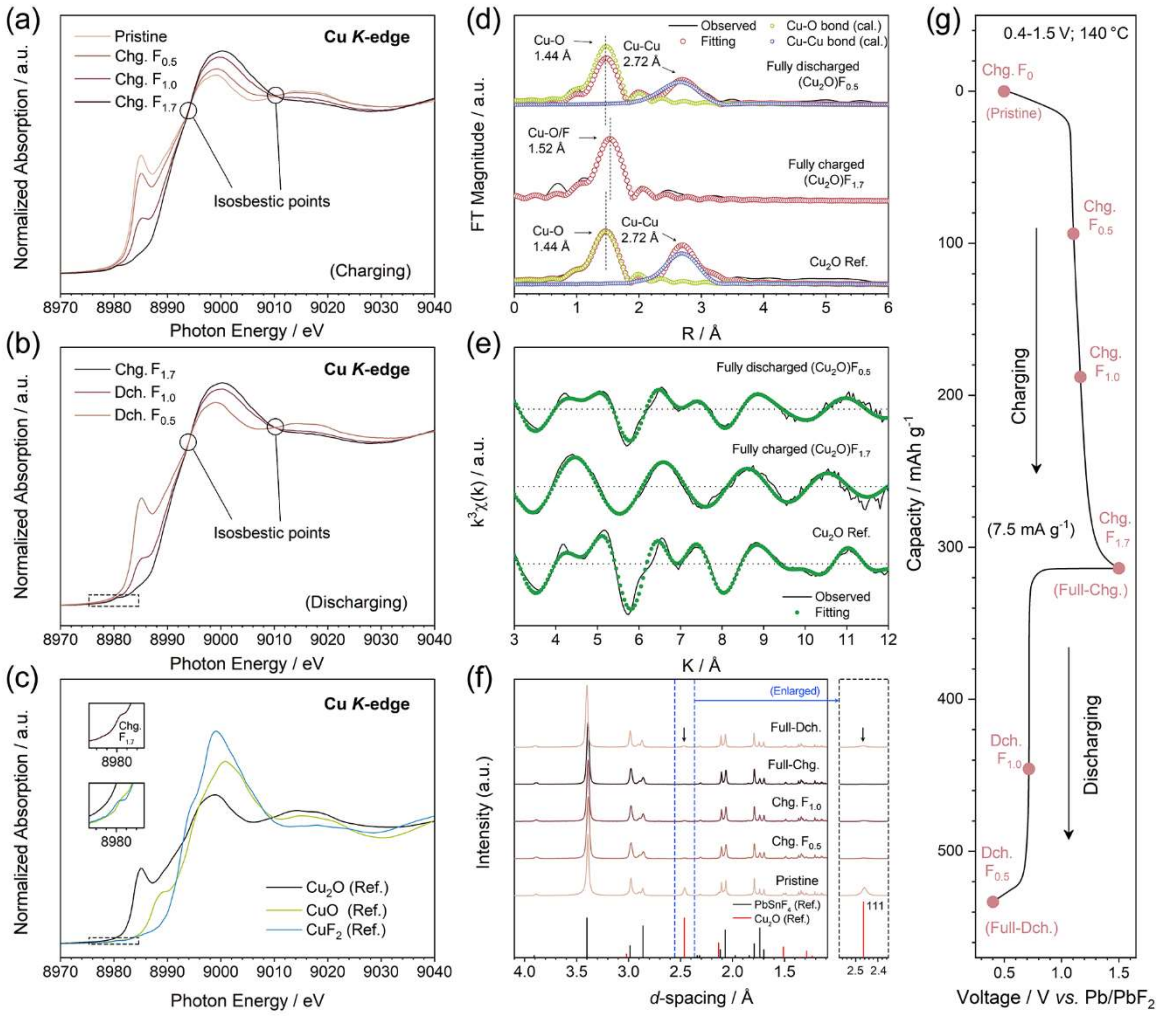

Figure 4.6 Charge compensation and structure-related informations. (a-c) Ex situ Cu K-edge XANES spectra obtained upon (a) charging and (b) discharging, and (c) standard spectra of Cu_2O, CuO, and CuF_2 reference samples. (d) R-space and (e) K-space patterns of Cu K-edge EXAFS spectra of pristine, fully charged, and fully discharged samples. (f) Ex situ HEXRD patterns of Cu_2O materials upon initial charging. These data were collected according to (g) ex situ points in the initial cycle.

The phase transitions and structural evolutions were analyzed using ex situ XAS. Ex situ samples in various states of charge (SOCs) were acquired by controlling the overall fluoride ion content upon charging (Chg.) and discharging (Dch.) in the Cu_2O lattice (denoted as Chg./Dch. F_x, $0 \leq x \leq 2$). The samples were then transferred to the analysis chamber without air exposure. The Cu K-edge X-ray absorption near edge structure (XANES) patterns obtained upon charging and discharging are shown in **Figure 4.6**(a), (b) and (c), and the ex situ points are displayed in Figure 4.6(g). The spectrum of the pristine sample was consistent with a Cu_2O reference (-Ref.) spectrum, and a clear tendency of the pristine state to convert to the fully

charged state was observed upon charging. The peak at ~8985 eV is typical of $Cu^{(I)}$ species. For $Cu^{(I)}$ compounds, the excitations of K-shell electrons to 4*p* splitting orbitals lead to two transitions: $1s \rightarrow 4p_{xy}$ (~8985 eV) and $1s \rightarrow 4p_z$ (~8998 eV). Linear coordinated ligands on Cu_2O would increase the energy of the $1s \rightarrow 4p_z$ transition; thus, the $1s \rightarrow 4p_{xy}$ peak appears at a lower energy. [49-51] The gradual disappearance of the peak at 8985 eV proved that Cu^+ donated increasingly to the overall capacities upon charging.

The XANES spectrum of the fully charged sample (Chg. $F_{1.7}$) differed from those of CuO-Ref. and CuF_2-Ref, while a very small pre-edge peak appeared at ~8980.5 eV (Figure 4.6(c)). This peak was assigned to the $1s \rightarrow 3d$ transition, which cannot occur for $Cu^{(0)}$ or $Cu^{(I)}$ compounds because of their fully occupied 3*d* orbitals (strictly speaking, there should be Cu 3*d* and O 2*p* hybridized orbitals here). [49, 52] This pre-edge peak was regarded as a signature of $Cu^{(II)}$ species, which can affirm that the reversible Cu^+/Cu^{2+} redox was the main contributor to charge compensation.

To understand the phase transition process, Cu K-edge extended X-ray absorption fine structure (EXAFS) spectra were obtained and are shown in Figure 4.6(d) and 4.6(e). For a Cu_2O-based lattice, there should be two peaks representing Cu-O and Cu-Cu interactions. However, only one main peak for Cu-O/F was observed in the EXAFS spectrum of the fully charged sample (Chg. $F_{1.7}$), which suggested that F anions may occupy sites that have similar coordination environments to O sites. The Cu-Cu interactions disappeared nearly completely and could not be further fitted. Correspondingly, the ex situ HEXRD patterns (Figure 4.6(f)) also showed the gradual disappearance of Cu_2O diffractions upon charging with no new diffractions. These results indicated the amorphization of Cu_2O after charging. The amorphization was partially reversible, based on the reappearance of Cu-Cu interactions (EXAFS) and Cu_2O diffractions (ex situ HEXRD), which also supported the inference from XANES that the Cu_2O structure can be recovered upon discharging.

However, the lattice recovery upon discharging was incomplete, which may have led to low coulombic efficiency and the consequent capacity fading in cycles 1–5, as shown in Figure 4.4. Poor ion transport also induced more complications, because excessively large amounts of electrolyte and carbon species were necessary in the cathode composites, which made direct observation of the active materials using transmission electron microscopy challenging.

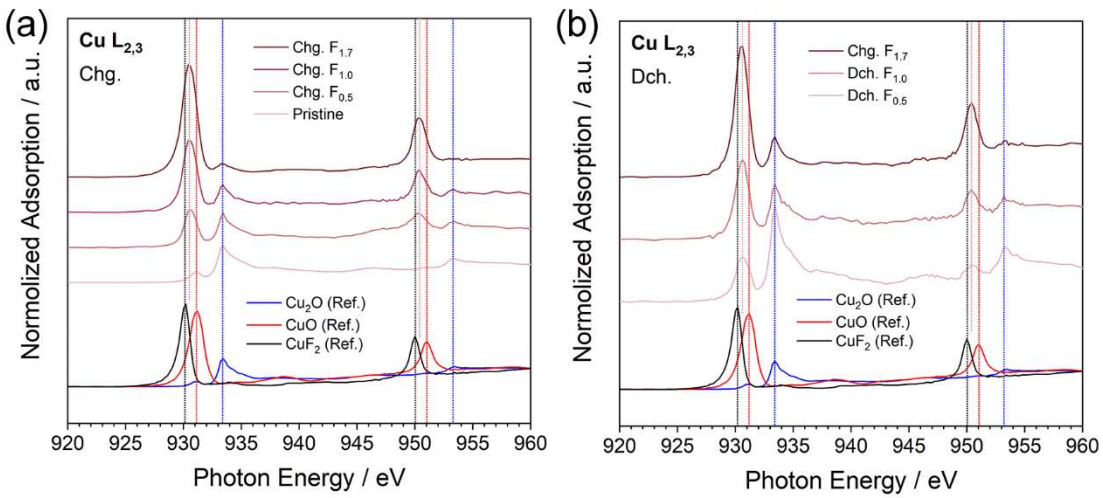

Figure 4.7 Ex situ Cu $L_{2,3}$-edge XAS spectra of Cu_2O material upon (a) charging and (b) discharging.

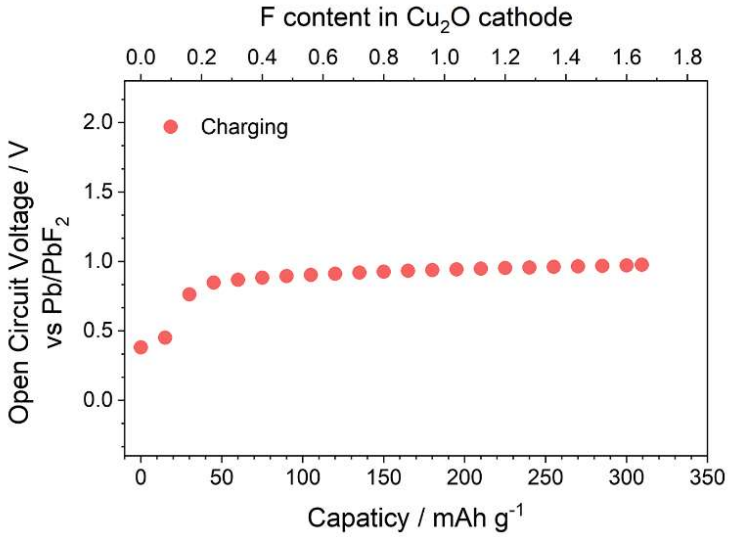

Figure 4.8 Open circuit voltages of Cu_2O materials obtained by galvanostatic intermittent titration technique (GITT) curve upon initial cycle.

Note that a pair of isosbestic points appeared at 8994 and 9010 eV in XANES patterns (Figure 4.6 (a) and (b)), indicating a phase-transition mechanism. [18, 53-56] The isosbestic points were at the same positions following the discharging and charging processes, and a clear transferring tendency was observed. Furthermore, the spectrum of the fully discharged sample (Dch. $F_{0.5}$) was identical to that of Cu_2O-Ref., which indicates that the Cu_2O structure is recoverable after cycling. The Cu $L_{2,3}$-edge XAS spectra (**Figure 4.7**) showed reversible increases/decreases in the white-line peaks, which were at fixed positions of 930.4 and 950.4 eV throughout cycling instead of continuously shifting, and this was also consistent with the Cu K-edge XAS results. The galvanostatic intermittent titration technique (GITT) was performed to gain further understanding of the reaction process (**Figure 4.8**). Except at the

very beginning of charging, the OCV values were stable; the very slight increase in the OCV in each step was ascribed to insufficient relaxation time in practical battery tests. This is considered to be further evidence of a typical phase-transition reaction mechanism, which has been suggested by XANES, because the Gibbs formation energy for the conversion from the clear parent phase to the product phase remains unchanged with phase-transition control. [48]

4.3.4 Kinetics and rate-determining step

The superior rate capabilities of Cu_2O were compared with those of materials from previous studies; the (de)fluorination process was highly reversible even under a high current density (1 C rate, 375 mA g^{-1}; perhaps the highest current density applied for all-solid-state FIBs thus far). We compared the rate capabilities of Cu_2O materials with that of a Cu thin film reported in our previous paper, [19] and the results are shown in **Figure 4.9**(a). Surprisingly, the rate capability of Cu_2O was much better than that of Cu, even that Cu_2O was under much worse reaction environments and much longer diffusion lengths, because the electrochemical performance of Cu_2O was evaluated using bulk-type cells, whereas that of Cu was evaluated using ideal thin-film cells. The average particle size of Cu_2O was approximately 50–60 nm (Figure 4.9(b)), suggesting that the diffusion length for Cu_2O was also greater than that in the Cu thin film (10 nm in thickness). These results indicate the excellent (de)fluorination kinetics of Cu_2O.

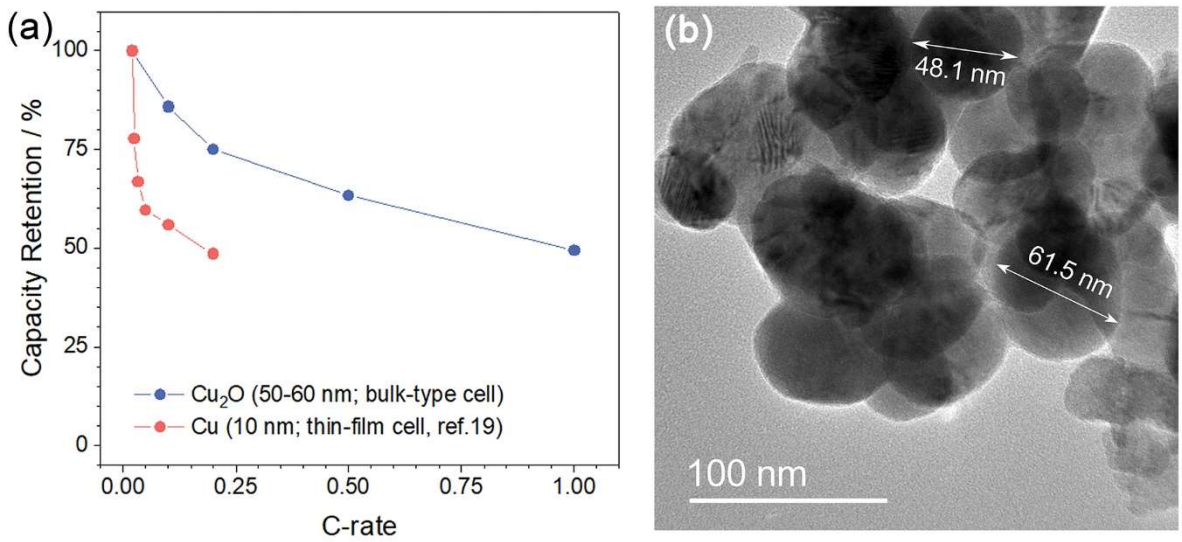

Figure 4.9 (a) Comparisons of rate capabilities of Cu_2O in this study and a Cu thin-film system from previous report. [19] (b) Transmission electron microscopic (TEM) images of Cu_2O nanoparticles.

The apparent F^- diffusion coefficients (**Figure 4.10**(a)) were calculated based on the potentiostatic intermittent titration technique (PITT, see *Experimental* section), which were ~10^{-11} to ~10^{-10} cm^2 s^{-1} at 140 °C in the steady phase transition range and were comparable to those of LIB cathode materials, such as $LiCoO_2$, $LiFePO_4$, $LiMn_2O_4$, at room temperature (**Table 4.2**), [35, 36, 57-59] further indicating that ion transport in a non-close-packed Cu_2O configuration is enhanced compared to that in close-packed Cu bulk. The high diffusion coefficient is indicative of smooth ion diffusion in Cu_2O; hence, some other factors besides ion diffusion may be responsible for the inferior kinetics of Cu_2O. The rate-determining step was investigated in detail based on KJMA theory. [60-63]

According to KJMA model, the volumetric fraction (V) of product in phase-transition mechanism is subjected to the following correlation,

$$V = 1 - \exp(-kt^n) \qquad (4-2)$$

where k, t and n are rate constant, time and Avrami exponent, respectively. The equation (4-2) can be rearranged as:

$$\ln\ln\left[\frac{1}{1-V}\right] = n\ln t + \ln k \qquad (4-3)$$

Therefore, the Avrami exponent n can be obtained by plotting and linear-fitting ln ln [1/(1-V)] *vs.* ln t. The Avrami exponent n is further explained as:

$$n = a + bc \qquad (4-4)$$

The value of a represents the nucleation rate as a function of time, where $a = 0$, $0 < a < 1$, $a = 1$ and $a > 1$ refer to zero, decreasing, constant and increasing nucleation rate, respectively. The values of b and c describe the phase-growth dimension (b = 1, 2, 3 for 1D, 2D, 3D growth, respectively) and rate-determining step (c = 1 for phase-boundary-movement controlled and c = 0.5 for diffusion controlled). The crystalline fractions V are calculated by SOCs, which was acquired by integrating the current densities upon chronoamperometric process as a function of time.

The transient current of the potential step from 1.08 to 1.09 V (Figure 4.10(b)) suggested typical nucleation and growth behavior of a two-phase-transition electrochemical reaction. The increase in current from point (i) represents the nucleation process that produces a large number of new phase boundaries, and the current reaches a maximum at point (ii); the subsequent current decrease from points (ii) to (iii) represents the nuclei growth that leads to the merging of phase boundaries. [64]

Table S2. The comparison of ionic diffusion coefficient in Cu_2O and typical LIB cathodes.

FIB cathode	$D(F^-)$ / $cm^2\ s^{-1}$	LIB cathode	$D(Li^+)$ / $cm^2\ s^{-1}$
Cu_2O	10^{-11} to 10^{-10} (140 °C)	$LiCoO_2$	10^{-12} to 10^{-10} (25 °C)
		$LiFePO_4$	10^{-14} to 10^{-12} (25 °C)
		$LiMn_2O_4$	10^{-13} to 10^{-11} (25 °C)

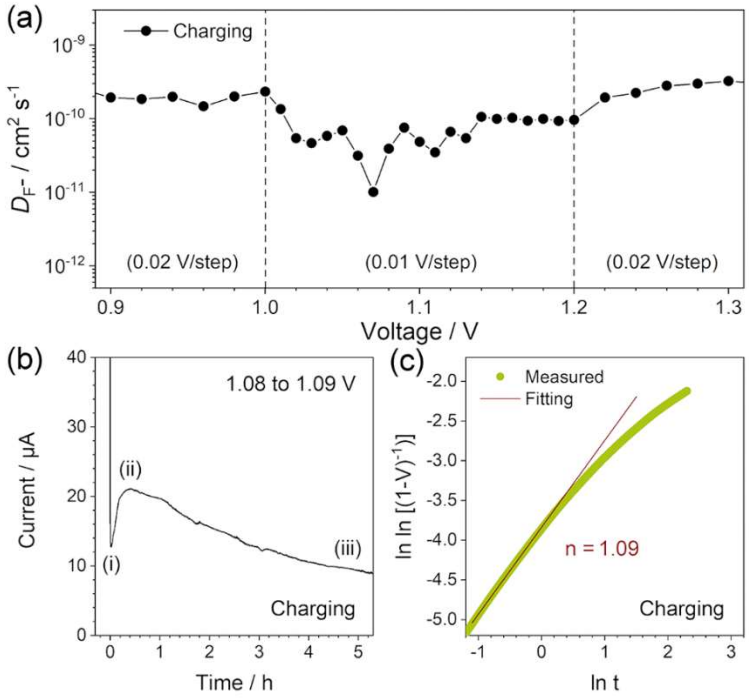

Figure 4.10 (a) Apparent F^- diffusion coefficients (D_F-) calculated from PITT results. (b) Current response in potential-step chronoamperometry measurements at step of 1.08–1.09 V and (c) corresponding KJMA analysis.

The fitting results revealed an Avrami exponent n of 1.09 (Figure 4.10 (c)) at the beginning of the nuclei growth process, which can be explained as phase-boundary-movement-controlled one-dimensional growth with a decreasing nucleation rate. There is no smooth coherent path at the interface between the Cu_2O parent phase and the fully discharged amorphous phase; the barrier of ion transport caused by lattice mismatch seems to be constant and there is no reason for it to monotonically increase. Therefore, such an environment should be kinetically unsuitable for diffusion-controlled models because diffusion-controlled growth usually obeys a parabolic principle, $r = A(Dt)^{0.5}$, where r is the particle radius. [65] Moreover, according to the PITT calculation results (Figure 4.10(a)), the diffusion coefficient is already comparable to those of LIB cathode materials; thus, the diffusion process is less likely to be the rate-determining step.

4.3.5 Presumptions about structural evolution

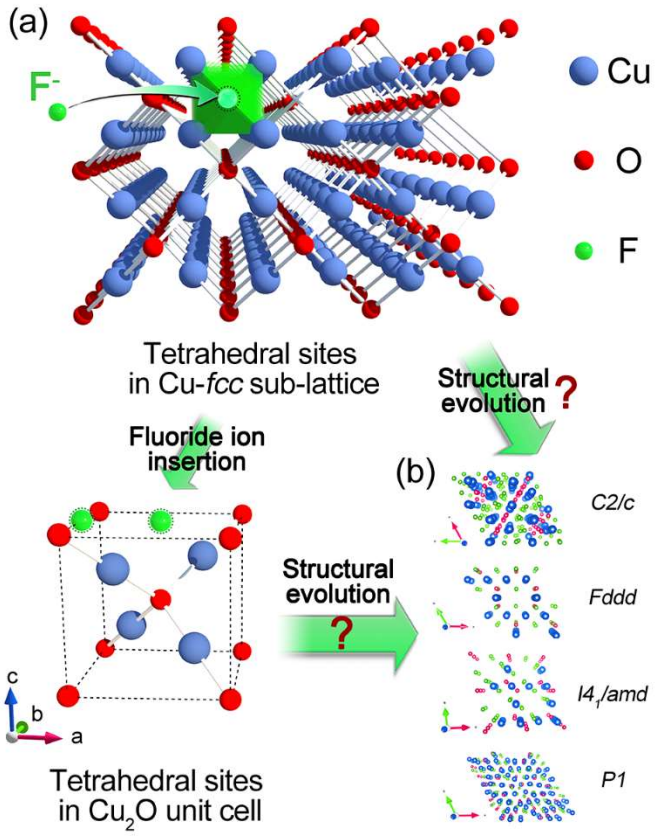

Figure 4.11 (a) Probable tetrahedral sites and (b) configurations for "topotactic Cu_2O" hypothesis.

There are three presumptions regarding the possible structures of the charged products. First, the fundamental Cu-O configurations may remain unchanged, and fluoride ions occupy the anionic vacancies in the Cu_2O lattice, namely, the "topotactic Cu_2O" hypothesis. Specifically, the lattice of the starting material, $Pn\bar{3}m$-Cu_2O, consists of straight-line O-Cu-O units with the Cu atoms arranged as a face-centered cubic (*fcc*) sub-lattice and O atoms occupying some of the tetrahedral sites in the Cu-*fcc* sub-lattice, as shown in **Figure 4.11**(a), and the unoccupied sites could create continuous channels along the <100> direction family. However, there would be six F atoms in each unit lattice if all tetrahedral sites are occupied, namely Cu_2OF_3. It is difficult to explain why and how only four of these six sites are occupied because all six tetrahedral sites are equivalent. This configuration has not yet been proven to be thermodynamically stable. The octahedral sites in the Cu-*fcc* sub-lattice also create continuous channels along <110> (**Figure 4.12**), but the length of the Cu-F interactions will be different from that of the Cu-O interactions, which is not consistent with the EXAFS analysis

results. As a result, it is more likely that F anions preliminarily occupy the tetrahedral sites in the Cu_2O lattice upon charging.

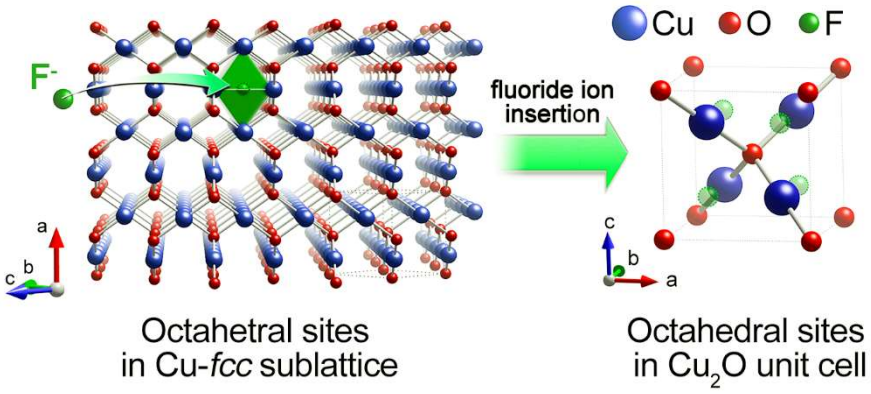

Figure 4.12 Octahedral sites in the Cu-*fcc* sublattice and the continuous channels along [011] direction for "topotactic Cu_2O" hypothesis.

Second, considering the phase-transition characteristics of Cu_2O, one might naturally suppose that the following reaction producing the imagined fully charged product, Cu_2OF_2, occurs:

$$0.5x\ Cu_2O + x\ F^- \rightarrow\ 0.5x\ Cu_2OF_2 + x\ e^-\ \ (0 \le x \le 2) \qquad (4-5)$$

To the best of our knowledge, there are no previous reports of the synthesis or characterization of Cu_2OF_2; however, four models (Figure 4.11(b)) have been acquired based on theoretical calculations using the online database, *Materials Project*. These four models are in accordance with the Cu-O/F interactions observed in the EXAFS spectra, but the absence of Cu-Cu interactions obviated further analysis.

Moreover, the four calculated Cu_2OF_2 models are regarded as thermodynamically unstable substances that produce CuF_2 and CuO; therefore, the immediate conversion of Cu_2OF_2 to CuF_2/CuO nanocomposites was considered to be the third circumstance. As shown in Figure 4.7, in the case of Chg. $F_{1.7}$, the white-line peaks in the Cu $L_{2,3}$-edge spectrum appeared at fixed positions between CuF_2 and CuO; the Cu L-edge XAS results do not eliminate the possibility of a conversion reaction. However, under such circumstances, it is difficult to explain the role of O, because CuF_2 can independently transform into Cu through a CuF_2/Cu phase-transition mechanism, which possess a completely different working potential (Cu/Cu^{2+} vs. Cu^+/Cu^{2+} redox) and has been reported by previous studies. [18, 23, 46] Meanwhile, the fully discharged products would be the composites of Cu and CuO, which are less likely to

regenerate Cu_2O; no reports about reactions between CuF_2 and CuO have been found thus far. As a result, more decisive proof of the validity of the CuF_2-CuO hypothesis is required.

4.4 Conclusions

Cu_2O with reversible Cu^+/Cu^{2+} redox was evaluated as a cathode material for all-solid-state FIBs. The phase-transition mechanism was substantiated by a combination of electrochemical evidence and XAS results. Compared to those of various reported materials, Cu_2O delivered high capacities and impressive retentions under high current densities. The fast capacity fading in the first several cycles was attributed to the partially irreversible amorphization that occurred upon charging, as indicated by ex situ HEXRD and Cu K-edge EXAFS results. The KJMA equation suggested that phase-boundary movement was the rate-determining step. The probable reaction patterns and F occupancy were also discussed based on the structural characteristics of the Cu_2O lattice combined with EXAFS analysis. In conclusion, this study initially displayed the promising potentials of fast fluorination of cathode materials for all-solid-state FIBs, which pushed all-solid-state FIBs one step closer to practical applications. In the future works, the developments of non-toxic (for example, Pb-free) and high-performance electrolyte and anode are also important. It is believed that studies on Cu_2O will bring about more strategies for developing high-performance all-solid-state FIBs.

Reference

1. Grey, C.; Tarascon, J., Sustainability and in situ monitoring in battery development. *Nat. Mater.* **2017,** *16* (1), 45-56.

2. Chu, S.; Cui, Y.; Liu, N., The path towards sustainable energy. *Nat. Mater.* **2017,** *16* (1), 16-22.

3. Armand, M.; Tarascon, J. M., Building better batteries. *Nature* **2008,** *451* (7179), 652-657.

4. Yabuuchi, N.; Kubota, K.; Dahbi, M.; Komaba, S., Research development on sodium-ion batteries. *Chem. Rev.* **2014,** *114* (23), 11636-11682.

5. Islam, M. S.; Fisher, C. A. J., Lithium and sodium battery cathode materials: computational insights into voltage, diffusion and nanostructural properties. *Chem. Soc. Rev.* **2014,** *43* (1), 185-204.

6. Anji Reddy, M.; Fichtner, M., Batteries based on fluoride shuttle. *J. Mater. Chem.* **2011,** *21* (43), 17059-17062.

7. Zhao, S.; Han, B.; Zhang, D.; Huang, Q.; Xiao, L.; Chen, L.; Ivey, D. G.; Deng, Y.; Wei, W., Unravelling the reaction chemistry and degradation mechanism in aqueous Zn/MnO_2 rechargeable batteries. *J. Mater. Chem. A* **2018,** *6* (14), 5733-5739.

8. Wang, M.; Jiang, C.; Zhang, S.; Song, X.; Tang, Y.; Cheng, H. M., Reversible calcium alloying enables a practical room-temperature rechargeable calcium-ion battery with a high discharge voltage. *Nat. Chem.* **2018,** *10* (6), 667-672.

9. Davis, V. K.; Bates, C. M.; Omichi, K.; Savoie, B. M.; Momcilovic, N.; Xu, Q.; Wolf, W. J.; Webb, M. A.; Billings, K. J.; Chou, N. H.; Alayoglu, S.; McKenney, R. K.; Darolles, I. M.; Nair, N. G.; Hightower, A.; Rosenberg, D.; Ahmed, M.; Brooks, C. J.; Miller, T. F., 3rd; Grubbs, R. H.; Jones, S. C., Room-temperature cycling of metal fluoride electrodes: Liquid electrolytes for high-energy fluoride ion cells. *Science* **2018,** *362* (6419), 1144-1148.

10. Ponrouch, A.; Frontera, C.; Barde, F.; Palacin, M. R., Towards a calcium-based rechargeable battery. *Nat. Mater.* **2016,** *15* (2), 169-72.

11. Lin, M. C.; Gong, M.; Lu, B.; Wu, Y.; Wang, D. Y.; Guan, M.; Angell, M.; Chen, C.; Yang, J.; Hwang, B. J.; Dai, H., An ultrafast rechargeable aluminium-ion battery. *Nature* **2015,** *520* (7547), 325-328.

12. Jian, Z.; Luo, W.; Ji, X., Carbon Electrodes for K-Ion Batteries. *J. Am. Chem. Soc.* **2015,** *137* (36), 11566-11569.

13. Zhao, X.; Zhao-Karger, Z.; Wang, D.; Fichtner, M., Metal oxychlorides as cathode materials for chloride ion batteries. *Angew. Chem. Int. Ed. Engl.* **2013,** *52* (51), 13621-13624.

14. Xu, C.; Li, B.; Du, H.; Kang, F., Energetic zinc ion chemistry: the rechargeable zinc ion battery. *Angew. Chem. Int. Ed. Engl.* **2012,** *51* (4), 933-935.

15. Aurbach, D.; Lu, Z.; Schechter, A.; Gofer, Y.; Gizbar, H.; Turgeman, R.; Cohen, Y.; Moshkovich, M.; Levi, E., Prototype systems for rechargeable magnesium batteries. *Nature* **2000,** *407* (6805), 724-7.

16. Delmas, C.; Braconnier, J. J.; Fouassier, C.; Hagenmuller, P., Electrochemical intercalation of sodium in Na_xCoO_2 bronzes. *Solid State Ionics* **1981,** *3–4* (AUG), 165-169.

17. Zhang, D.; Yoshinari, T.; Yamamoto, K.; Kitaguchi, Y.; Ochi, A.; Nakanishi, K.; Miki, H.; Nakanishi, S.; Iba, H.; Watanabe, T.; Uchiyama, T.; Orikasa, Y.; Amezawa, K.; Uchimoto, Y., Cu–Pb Nanocomposite Cathode Material toward Room-Temperature Cycling for All-Solid-State Fluoride-Ion Batteries. *ACS Appl. Energy Mater.* **2021,** *4* (4), 3352-3357.

18. Zhang, D.; Yamamoto, K.; Ochi, A.; Wang, Y.; Yoshinari, T.; Nakanishi, K.; Nakano, H.; Miki, H.; Nakanishi, S.; Iba, H.; Uchiyama, T.; Watanabe, T.; Amezawa, K.; Uchimoto, Y., Understanding the reaction mechanism and performances of 3d transition metal cathodes for all-solid-state fluoride ion batteries. *J. Mater. Chem. A* **2021,** *9* (1), 406-412.

19. Yoshinari, T.; Zhang, D.; Yamamoto, K.; Kitaguchi, Y.; Ochi, A.; Nakanishi, K.; Miki, H.; Nakanishi, S.; Iba, H.; Uchiyama, T.; Watanabe, T.; Matsunaga, T.; Amezawa, K.; Uchimoto, Y., Kinetic analysis and alloy designs for metal/metal fluorides toward high rate capability for all-solid-state fluoride-ion batteries. *J. Mater. Chem. A* **2021,** *9* (11), 7018-7024.

20. Nakano, H.; Matsunaga, T.; Mori, T.; Nakanishi, K.; Morita, Y.; Ide, K.; Okazaki, K. I.; Orikasa, Y.; Minato, T.; Yamamoto, K.; Ogumi, Z.; Uchimoto, Y., Fluoride-Ion Shuttle Battery with High Volumetric Energy Density. *Chem Mater* **2021,** *33* (1), 459-466.

21. Molaiyan, P.; Witter, R., Surface defect‐enhanced conductivity of calcium fluoride for electrochemical applications. *Mater. Des. Process. Commun.* **2019,** *1* (4), e44.

22. Mohammad, I.; Witter, R., Testing Mg as an anode against BiF3 and SnF2 cathodes for room temperature rechargeable fluoride ion batteries. *Materials Letters* **2019,** *244*, 159-162.

23. Zhang, L.; Reddy, M. A.; Gao, P.; Diemant, T.; Jürgen Behm, R.; Fichtner, M., Study of all solid-state rechargeable fluoride ion batteries based on thin-film electrolyte. *J. Solid State Electrochem.* **2016,** *21* (5), 1243-1251.

24. Rongeat, C.; Reddy, M. A.; Diemant, T.; Behm, R. J.; Fichtner, M., Development of new anode composite materials for fluoride ion batteries. *J. Mater. Chem. A* **2014,** *2* (48), 20861-20872.

25. Haruyama, J.; Okazaki, K. I.; Morita, Y.; Nakamoto, H.; Matsubara, E.; Ikeshoji, T.; Otani, M., Two-Phase Reaction Mechanism for Fluorination and Defluorination in Fluoride-Shuttle Batteries: A First-Principles Study. *ACS Appl. Mater. Interfaces* **2020,** *12* (1), 428-435.

26. Zhang, L.; Anji Reddy, M.; Fichtner, M., Development of tysonite-type fluoride conducting thin film electrolytes for fluoride ion batteries. *Solid State Ionics* **2015,** *272*, 39-44.

27. Nowroozi, M. A.; Wissel, K.; Donzelli, M.; Hosseinpourkahvaz, N.; Plana-Ruiz, S.; Kolb, U.; Schoch, R.; Bauer, M.; Malik, A. M.; Rohrer, J.; Ivlev, S.; Kraus, F.; Clemens, O., High cycle life all-solid-state fluoride ion battery with La_2NiO_{4+d} high voltage cathode. *Commun. Mater.* **2020,** *1* (1), 27.

28. Vasala, S.; Jakob, A.; Wissel, K.; Waidha, A. I.; Alff, L.; Clemens, O., Reversible Tuning of Magnetization in a Ferromagnetic Ruddlesden–Popper‐Type Manganite by Electrochemical Fluoride‐Ion Intercalation. *Adv. Electron. Mater.* **2019,** *6* (2), 1900974.

29. Nowroozi, M. A.; de Laune, B.; Clemens, O., Reversible Electrochemical Intercalation and Deintercalation of Fluoride Ions into Host Lattices with Schafarzikite-Type Structure. *ChemistryOpen* **2018,** *7* (8), 617-623.

30. Nowroozi, M. A.; Ivlev, S.; Rohrer, J.; Clemens, O., La_2CoO_4: a new intercalation based cathode material for fluoride ion batteries with improved cycling stability. *J. Mater. Chem. A* **2018,** *6* (11), 4658-4669.

31. Nowroozi, M. A.; Wissel, K.; Rohrer, J.; Munnangi, A. R.; Clemens, O., $LaSrMnO_4$: Reversible Electrochemical Intercalation of Fluoride Ions in the Context of Fluoride Ion Batteries. *Chem Mater* **2017,** *29* (8), 3441-3453.

32. Clemens, O.; Rongeat, C.; Reddy, M. A.; Giehr, A.; Fichtner, M.; Hahn, H., Electrochemical fluorination of perovskite type $BaFeO_{2.5}$. *Dalton Trans.* **2014,** *43* (42), 15771-15778.

33. Yang, X.-Y.; Luo, W.; Ahuja, R., Fluoride ion batteries: Designing flexible M2CH2 (M=Ti or V) MXenes as high-capacity cathode materials. *Nano Energy* **2020,** *74*, 104911.

34. Hartman, S. T.; Mishra, R., Layered electrides as fluoride intercalation anodes. *J. Mater. Chem. A* **2020,** *8* (46), 24469-24476.

35. Wen, C. J.; Boukamp, B. A.; Huggins, R. A.; Weppner, W., Thermodynamic and Mass Transport Properties of "LiAl" *J. Electrochem. Soc.* **1979,** *126* (12), 2258-2266.

36. Toby, B. H., EXPGUI, a graphical user interface for GSAS. *J. Appl. Crystallogr.* **2001,** *34* (2), 210-213.

37. Zhu, Y.; Wang, C., Galvanostatic Intermittent Titration Technique for Phase-Transformation Electrodes. *J. Phys. Chem. C* **2010,** *114* (6), 2830-2841.

38. Xie, J.; Imanishi, N.; Zhang, T.; Hirano, A.; Takeda, Y.; Yamamoto, O., Li-ion diffusion kinetics in $LiFePO_4$ thin film prepared by radio frequency magnetron sputtering. *Electrochim. Acta* **2009,** *54* (20), 4631-4637.

39. Zhang, D.; Nakano, H.; Yamamoto, K.; Tanaka, K.; Yahara, T.; Imai, K.; Mori, T.; Miki, H.; Nakanishi, S.; Iba, H.; Watanabe, T.; Uchiyama, T.; Amezawa, K.; Uchimoto, Y., Rate-Determining Process at Electrode/Electrolyte Interfaces for All-

Solid-State Fluoride-Ion Batteries. *ACS Appl. Mater. Interfaces* **2021,** *13* (25), 30198-30204.

40. Liu, L.; Yang, L.; Liu, M.; Li, X.; Shao, D.; Luo, K.; Wang, X.; Luo, Z., SnF_2-based fluoride ion electrolytes $MSnF_4$ (M = Ba, Pb) for the application of room-temperature solid-state fluoride ion batteries. *J. Alloys Compd.* **2020,** *819*, 152983.

41. Castiglione, M.; Madden, P. A.; Berastegui, P.; Hull, S., The crystal structure of α-$PbSnF_4$ and its anion diffusion mechanism. *J. Phys. Condens. Matter* **2005,** *17* (6), 845-861.

42. Sorokin, N. I.; Fedorov, P. P.; Nikol'skaya, O. K.; Nikeeva, O. A.; Rakov, E. G.; Ardashnikova, E. I., Electrical properties of $PbSnF_4$ materials prepared by different methods. *Inorg. Mater.* **2001,** *37* (11), 1178-1182.

43. Réau, J.-M.; Lucat, C.; Portier, J.; Hagenmuller, P.; Cot, L.; Vilminot, S., Etude des proprietes structurales et electrioues d'un nouveau conducteur anionique: $PbSnF_4$. *Mater. Res. Bull.* **1978,** *13* (9), 877-882.

44. Grenier, A.; Porras-Gutierrez, A. G.; Body, M.; Legein, C.; Chrétien, F.; Raymundo-Piñero, E.; Dollé, M.; Groult, H.; Dambournet, D., Solid Fluoride Electrolytes and Their Composite with Carbon: Issues and Challenges for Rechargeable Solid State Fluoride-Ion Batteries. *J. Phys. Chem. C* **2017,** *121* (45), 24962-24970.

45. Stefan, I. C.; Jacobson, C. P.; Visco, S. J.; De Jonghe, L. C., Solid-State Electrochemistry of Fluoride Ionic Conductive Materials. In *Electrochemical Society Meeting*, Honolulu, Hawaii, 2004.

46. Thieu, D. T.; Fawey, M. H.; Bhatia, H.; Diemant, T.; Chakravadhanula, V. S. K.; Behm, R. J.; Kübel, C.; Fichtner, M., CuF_2 as Reversible Cathode for Fluoride Ion Batteries. *Adv. Funct. Mater.* **2017,** *27* (31), 1701051.

47. de Laune, B. P.; Rees, G. J.; Marco, J. F.; Hah, H. Y.; Johnson, C. E.; Johnson, J. A.; Berry, F. J.; Hanna, J. V.; Greaves, C., Topotactic Fluorine Insertion into the Channels of $FeSb_2O_4$-Related Materials. *Inorg. Chem.* **2017,** *56* (16), 10078-10089.

48. Zu, C.-X.; Li, H., Thermodynamic analysis on energy densities of batteries. *Energ Environ Sci* **2011,** *4* (8), 2614–2624.

49. Gaur, A.; Shrivastava, B. D., A Comparative Study of the Methods of Speciation Using X-ray Absorption Fine Structure. *Acta Phys. Pol. A* **2012,** *121* (3), 647-652.

50. Kim, W. B.; Lee, J. S., Quantitative XANES analysis of cuprous dibromide complex formed in the oxidative carbonylation of phenols. *J. Phys. Chem. B* **2003,** *107* (35), 9195-9202.

51. Kau, L. S.; Spirasolomon, D. J.; Pennerhahn, J. E.; Hodgson, K. O.; Solomon, E. I., X-Ray Absorption-Edge Determination of the Oxidation-State and Coordination-Number of Copper - Application to the Type-3 Site in Rhus-Vernicifera Laccase and Its Reaction with Oxygen. *J. Am. Chem. Soc.* **1987,** *109* (21), 6433-6442.

52. Chou, C. H.; Pong, W. F.; Lin, I. N.; Tsai, S. F., X-Ray Absorption Fine-Structure (Xafs) Study of the High-Tc Superconductor Pb-Bi-Sr-Ca-Cu-O System. *Chinese J Phys* **1991,** *29* (3), 263-282.

53. Orikasa, Y.; Maeda, T.; Koyama, Y.; Murayama, H.; Fukuda, K.; Tanida, H.; Arai, H.; Matsubara, E.; Uchimoto, Y.; Ogumi, Z., Transient Phase Change in Two Phase Reaction between $LiFePO_4$ and $FePO_4$ under Battery Operation. *Chem Mater* **2013,** *25* (7), 1032-1039.

54. Jain, G.; Balasubramanian, M.; Xu, J. J., Structural Studies of Lithium Intercalation in a Nanocrystalline α-Fe_2O_3 Compound. *Chem Mater* **2006,** *18* (2), 423-434.

55. Jain, G. R.; Yang, J. S.; Balasubramanian, M.; Xu, J. J., Synthesis, electrochemistry, and structural studies of lithium intercalation of a nanocrystalline Li_2MnO_3-like compound. *Chem Mater* **2005,** *17* (15), 3850-3860.

56. Wang, X. Q.; Hanson, J. C.; Frenkel, A. I.; Kim, J. Y.; Rodriguez, J. A., Time-resolved studies for the mechanism of reduction of copper oxides with carbon monoxide: Complex behavior of lattice oxygen and the formation of suboxides. *J. Phys. Chem. B* **2004,** *108* (36), 13667-13673.

57. Xia, H.; Lu, L.; Ceder, G., Li diffusion in $LiCoO_2$ thin films prepared by pulsed laser deposition. *J Power Sources* **2006,** *159* (2), 1422-1427.

58. Aurbach, D.; Levi, M. D.; Levi, E.; Teller, H.; Markovsky, B.; Salitra, G.; Heider, U.; Heider, L., Common electroanalytical behavior of Li intercalation processes into graphite and transition metal oxides. *J. Electrochem. Soc.* **1998,** *145* (9), 3024-3034.

59. Xie, J.; Kohno, K.; Matsumura, T.; Imanishi, N.; Hirano, A.; Takeda, Y.; Yamamoto, O., Li-ion diffusion kinetics in $LiMn_2O_4$ thin films prepared by pulsed laser deposition. *Electrochim. Acta* **2008,** *54* (2), 376-381.

60. Orikasa, Y.; Maeda, T.; Koyama, Y.; Minato, T.; Murayama, H.; Fukuda, K.; Tanida, H.; Arai, H.; Matsubara, E.; Uchimoto, Y.; Ogumi, Z., Phase Transition Analysis between $LiFePO_4$ and $FePO_4$ by In-Situ Time-Resolved X-ray Absorption and X-ray Diffraction. *J. Electrochem. Soc.* **2013,** *160* (5), A3061-A3065.

61. Avrami, M., Granulation, Phase Change, and Microstructure Kinetics of Phase Change. III. *J. Chem. Phys.* **1941,** *9* (2), 177-184.

62. Avrami, M., Kinetics of Phase Change. II Transformation‐Time Relations for Random Distribution of Nuclei. *J. Chem. Phys.* **1940,** *8* (2), 212-224.

63. Avrami, M., Kinetics of Phase Change. I General Theory. *J. Chem. Phys.* **1939,** *7* (12), 1103-1112.

64. Oyama, G.; Yamada, Y.; Natsui, R.-i.; Nishimura, S.-i.; Yamada, A., Kinetics of Nucleation and Growth in Two-Phase Electrochemical Reaction of Li_xFePO_4. *J. Phys. Chem. C* **2012,** *116* (13), 7306-7311.

65. Ranganathan, S.; Von Heimendahl, M., The three activation energies with isothermal transformations: applications to metallic glasses. *J. Mater. Sci.* **1981,** *16* (9), 2401-2404.

Chapter 5 High-energy Cu_3N Cathode Material Involving Nitrogen Redox with Novel Intercalation Preference

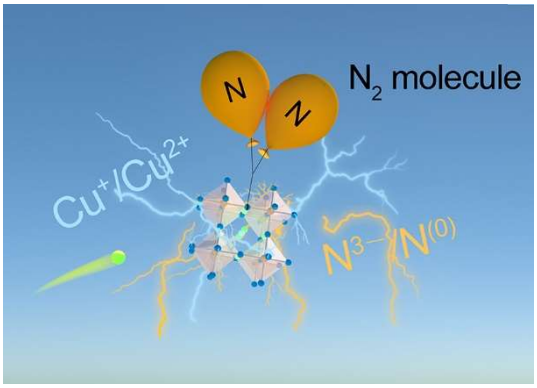

All-solid-state fluoride-ion batteries (FIBs) have received extensive attention as candidates for next-generation energy storage devices; however, promising cathodes with high energy density is still lacking. In this study, Cu_3N cathode material is developed and studied for all-solid-state fluoride-ion batteries, which delivers high reversible capacity of ~550 mAh g^{-1} due to a multielectron-transferred fluorination process. A simultaneous contribution from mixed cationic/anionic redox for charge compensation, as long as the generation of molecular N_2 at highly charged states, have been proved by X-ray absorption spectroscopy and resonant inelastic X-ray scattering techniques. Moreover, a novel intercalation preference that F^- occupied not only perovskite A site but also face-centered sites of Cu_3N lattice was observed as well. Not only the utilization of N redox as main contributor for charge compensation, but also the numerous intercalation number and the occupied sites of F^-, are for the first time reported.

5.1 Introduction

All-solid-state fluoride-ion batteries (FIBs) have been regarded as one of promising alternates for conventional lithium-ion batteries (LIBs) which have met tough bottlenecks on energy/power densities.[1-7] Employing monovalent F anions as charge carriers, great electrochemical stabilities could be realized owing to the high electronegativity of F element; meanwhile, it is promising to achieve excellent overall energy density due to the multielectron nature per redox center of many basic fluorination reactions. Previous studies have shown that all-solid-state FIB employing a pair of metal/metal fluoride (M/MF_y) electrodes could deliver ultrahigh theoretical energy densities, for instance, ~5000 Wh L^{-1} or 2000 Wh kg^{-1} for some representative 3*d* transition metals, based on two-phase-type $M + yF^- \rightarrow MF_y + ye^-$ (M = various metal species) reactions.[5-7] However, in the case of practical applications, two-phase-type M/MF_y systems have been suffering from severe lattice mismatches between parent and fluorinated phases, leading to large strain energy and sluggish phase-transition kinetics. The large volumetric changes upon phase-transition reaction can easily lead to exfoliations between active materials and solid electrolyte, which is largely harmful for long-term cycling of all-solid-state batteries.[7, 8]

Intercalation-type oxide and oxyfluoride materials ($LaSrMnO_4$, La_2CoO_4, Sr_2MnO_3F, etc.) that obey a topotactic fluorination pattern have also been intensively researched in recent years.[9, 10] These materials possess robust frameworks that allow highly reversible F^- (de)intercalation at certain sites without large-scale volumetric expansion/contractions. Such robustness is realized by a relatively complex lattice with large intercalation sites or channels, where a large part of structural components helps to hold the framework but does not contribute to capacity. For example, in $LaSrMnO_4$, rock-salt La/Sr-O layers provide large rooms for F^- intercalation, whereas La/Sr components, which take 65.6% of molecular mass, do not make any contribution for charge compensations. As a result, $LaSrMnO_4$ only delivers a capacity of 155 mAh g^{-1} even in the case of two F^- intercalation.[9]

Therefore, as a result of comparing the electrochemical performances between simple M/MF_y and intercalation-type systems, it is necessary and important to consider the trade-off among theoretical energy density, fluorination kinetics and configurational complexibility. Specifically, simple M/MF_y systems deliver higher energy densities in a sluggish and structure-damage way; however, a well-constructed perovskite-related lattice enable highly reversible F^- (de)intercalation but deliver low energy. Exploiting rare-earth elements (La, Ce, etc) is also uneconomic from the angle of practical applications. Consequently, it has become more

interesting and challenging to find a subtle balance between basic phase-transition-type M/MF_y systems and complex intercalation-type perovskite derivatives, that is, to achieve fast fluorination in a simple (to ensure high energy densities) but highly accessible structure (to ensure high intercalation tolerance). In our very recent work, we have successfully employed Cu_2O as high-energy cathode material for all-solid-state FIBs.[11] The highly accessible non-close-packed Cu-O configuration has exerted important effects to fast (de)fluorination, resulting in extraordinary rate capabilities. The F^- intercalation into Cu_2O lattice by an electrochemical method was believed to have induced a local mixed-anion coordination (Cu-O/F), which was for the first time reported thus far. The mixed-anion coordination might could differentiate the binding energy, leading to facilitated F^- diffusion and (de)fluorination reaction.[11, 12] Further, it also deserves deeper investigation for the potential effects on tuning crystal field splitting of Cu-X (X = mixed anions, such as O/F in fluorinated Cu_2O materials) polyhedrons and controlling band gaps of FIB electrode materials upon long-term cycling.

Herein, we report cuprous nitride (Cu_3N) with highly accessible anti-ReO_3 structure as a high-energy cathode material for all-solid-state FIBs, where both Cu and N redox were involved as charge-compensation contributors. Cu_3N can be a great exemplification of "balance strategy": reversible cationic and anionic redoxes (Cu^+ and N^{3-}) allow up to six electrons to participate charge-compensation processes upon (de)fluorination; as a result, Cu_3N cathode material is hopeful for achieving high energy density. Meanwhile, the cubic Cu_3N lattice that contains linear N-Cu-N bonds provides a plenty of accessible anionic vacancies for F^- (de)intercalation. N redox that makes simultaneous contribution along with Cu redox was for the first time confirmed and the formation of molecular N_2 was as well detected by N K-edge X-ray absorption spectroscopies (XAS) and resonant inelastic X-ray scattering (RIXS) techniques. Moreover, a novel intercalation behavior in Cu_3N lattices was verified, where the intercalated F anions do not at first occupy the A site of the perovskite-like Cu_3N lattice, but the face-centered sites. Such intercalation preference is totally beyond the conventional cognitions for heteroatoms intercalation in Cu_3N lattice.

5.2 Experimental

5.2.1 Materials preparation

Cuprous nitride (Cu_3N) was synthesized using Cu_2O nano-powder and urea as Cu and N resources, respectively.[13] Typically, 0.200 g of commercialized Cu_2O nanoparticles (US Research Nanomaterials, 99.86%) and 0.168 g of urea (Wako, 99.9%) were mixed, then put

into a 25 mL Teflon autoclave and reacted at 190 ˚C for 6 h. The products were collected and washed by deionized water and ethanol for several times and finally dried overnight. Solid electrolyte $La_{0.9}Ba_{0.1}F_{2.9}$ (LBF) was prepared by mechanochemical method. Stoichiometric amount of LaF_3 (99.9%, Kojundo) and BaF_2 (99.9%, Kojundo) were mixed and milled by planetary ball mills (Fritsch Pulverisette7 premium line, Germany) using ZrO_2 balls under a rotation speed of 600 rpm for 12 h, then pelletized and sintered at 1000 ˚C for 4 h. Cathode and anode composites were acquired by mixing certain amounts of active materials (Cu_3N and PbF_2, respectively) with solid electrolyte LBF and vapor grown carbon fiber (VGCF, Showa Denko, Japan) using ZrO_2 balls under a rotation speed of 300 rpm for 12 h; for anode composites, some Pb powder were added and mixed by an agate pestle and mortar after ball-milling. The mass ratios of cathode and anode composites were Cu_3N:LBF:VGCF = 3:6:1 and PbF_2:Pb:LBF:VGCF = 3:2:4:1, respectively.

5.2.2 Electrochemical measurement

Electrochemical tests were evaluated by bulk-type cells. Similar to the procedures described in our previous studies, 0.15 g of LBF, 0.01 g of cathode composite, 0.05 g of anode composite and two pieces of Au current collectors were put into a PEEK insulator (10 mm diameter) and pelletized under a pressure of 360 MPa for 5 min. All operations of battery assembling were finished in an Ar-filled glove box.

The galvanostatic charging-discharging properties were tested using SD-8 battery testing systems (Hokuto Denko, Japan). Considering the electrochemical stability windows of solid electrolyte LBF, the maximum voltage range was restrained from -1.5 to 3.0 V at 140 °C. The ionic conductivity of LBF was evaluated by electrochemical impedance spectroscopy (EIS) via a Solartron analytical Modulab XM ECS electrochemical test system within the frequency range of 10^6 to 10^{-1} Hz with an amplitude voltage of 50 mV. The activation energy (E_a) was evaluated by Arrhenius equation using temperature dependent EIS results at 25, 50, 75, 100, 125 and 150˚C, respectively.

5.2.3 Characterization of materials

The powder X-ray diffraction (XRD) data were recorded using a Rigaku Ultima IV X-ray diffractometer with Cu Kα radiation (λ = 1.54056 Å). The Rietveld refinement was processed by JANA software.[14] The analyses related to crystallographic information were supported by VESTA.[15] The microscale morphologies and energy dispersive spectroscopy

(EDS) were acquired using a Hitachi S-3400N field emission scanning electron microscope (SEM). Ex situ Cu K-edge, Cu $L_{2,3}$-edge, F K-edge and N K-edge X-ray absorption spectroscopy (XAS) measurements were carried out at BL14B2 and BL27SU beamlines in SPring-8 synchrotron-radiation facility, respectively. The XAS data were acquired in partial fluorescence yield (PFY) mode by a 19-element solid-state detector for Cu K-edge and a silicon drift detector for Cu $L_{2,3}$-edge, F K-edge and N K-edge, respectively. Resonant inelastic X-ray scattering (RIXS) measurements were performed at BL07LSU in SPring-8 utilizing a grazing flat-field-type high-resolution soft X-ray emission spectrometer.[16] Soft XAS were recorded in advance for determining the proper excitation energies of X-ray emission spectroscopy (XES). The samples were supported on the holders by carbon tape and transferred to the measurement chamber without any exposures to air or moisture; all operations are carried out in an Argon-atmosphere glovebox. The samples kept moving slowly with a speed of 2.4 μm s^{-1} upon RIXS measurements to avoid radiation damage from high-energy beam.

5.3 Results and discussion

5.3.1 Phase and compositions

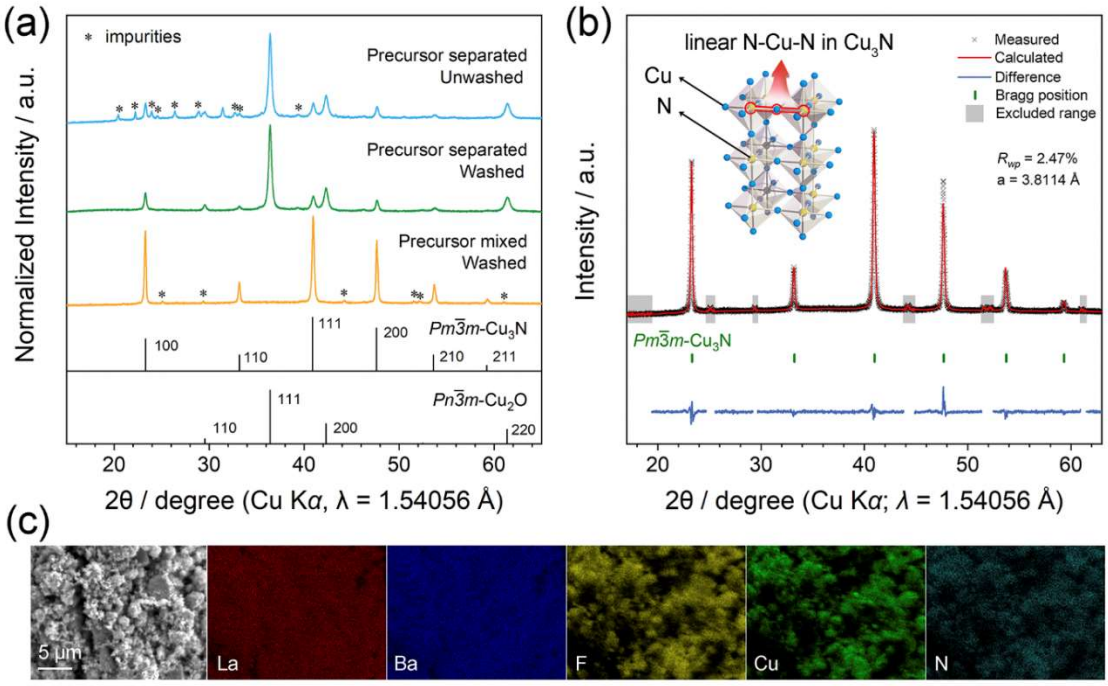

Figure 5.1 (a) X-ray diffraction patterns upon various synthetic conditions, (b) Rietveld refinement of as-prepared Cu_3N material and (c) morphology and elemental distributions of Cu_3N/LBF/VGCF cathode composite.

A pure cubic Cu_3N phase (space group: $Pm\bar{3}m$) with anti-ReO_3 structure was obtained after the reaction in Teflon autoclaves at 190 °C for 6 h, as shown in **Figure 5.1**(a), and a few unknown impurities (organic residents from urea) were observed; a homogenous mixture of starting Cu_2O and urea and proper washing after reaction can be important for obtaining single phase Cu_3N. The 2-fold coordinated N-Cu-N straight-line configuration in Cu_3N lattice created sufficient anionic vacancies surrounding the Cu^+ center; the lattice parameter a of 3.8114 Å (see Figure 1b) indicated a large-size void that allows smooth F^- intercalation as well. Tiny and uniform nanoparticles of as-prepared Cu_3N and homogeneous mixture of Cu_3N/LBF/VGCF cathode composites were confirmed according to SEM and EDS mapping images.

5.3.2 Electrochemistry

For fabricating an all-solid-state fluoride-ion cell, $La_{0.9}Ba_{0.1}F_{2.9}$ (LBF) was utilized as solid electrolyte. **Figure 5.2** shows the ionic conductivities which were calculated by EIS results using Arrhenius models. At 140 °C, LBF has an acceptable ionic conductivity of ~5 × 10^{-4} S cm^{-1} with an activation energy of 0.436 eV, which is similar to the values in previous studies.[17-19] This conductivity is sufficient for reversibly cycling of batteries. LBF possess greatly wide electrochemical stability windows (beyond 5 V) which was beneficial to entirely assess the performance of Cu_3N from a wide voltage range.[20]

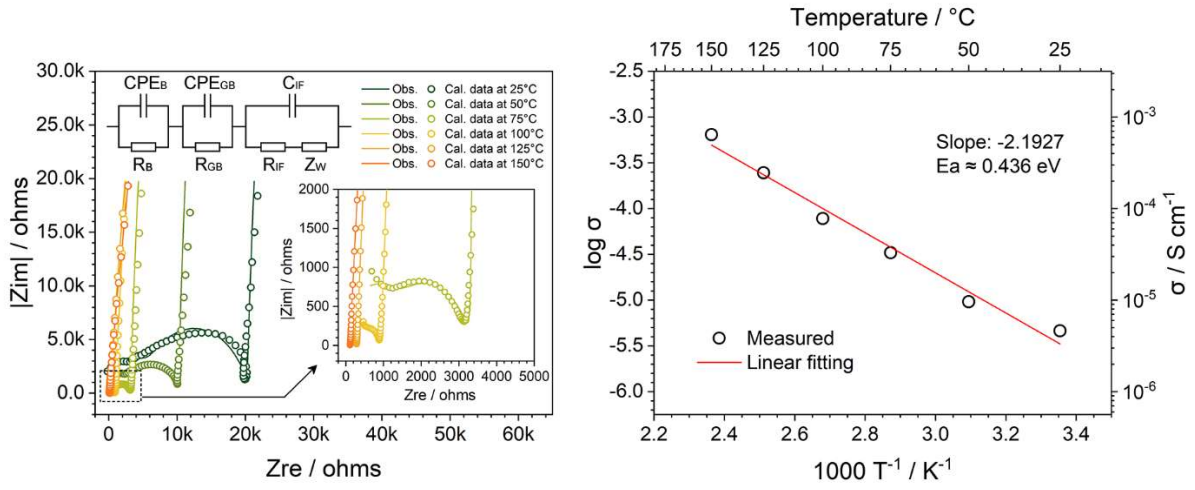

Figure 5.2 Nyquist plots, equivalent circuits, ionic conductivities and corresponding Arrhenius linear fitting of LBF at temperatures of 25, 50, 75, 100, 125 and 150 °C, respectively.

Cu_3N exhibited highly reversible charge-discharge behaviors as shown in **Figure 5.3**. Cut-off ranges were manipulated by various fluorination degrees (denoted as Chg. F=x, where x = 1 to 6 in Cu_3NF_x formula), namely, the number of intercalated F^- in Cu_3N lattice, upon

initial charging process. The (de)intercalation of each F^- corresponded to a capacity of approx. 130 mAh g^{-1}. The maximum of x in Cu_3NF_x was set as six, corresponding to the ending of both Cu^+/Cu^{2+} and $N^{3-}/N^{(0)}$ redox where N might irreversibly release in the form of gaseous N_2. Two plateaus occurred upon first charge process located at x of 0 to ~2.0 and ~2.0 to ~3.5 in Cu_3NF_x formula, respectively, as well as a slope after them. Notice that in the case of Chg. F=2, the capacity of each cycle gradually increased (as the dash line in the inset figure shows), indicating the occurrence of an accumulated capacity which might be caused by the ongoing contributions of N redox, which will be discussed in following sections.

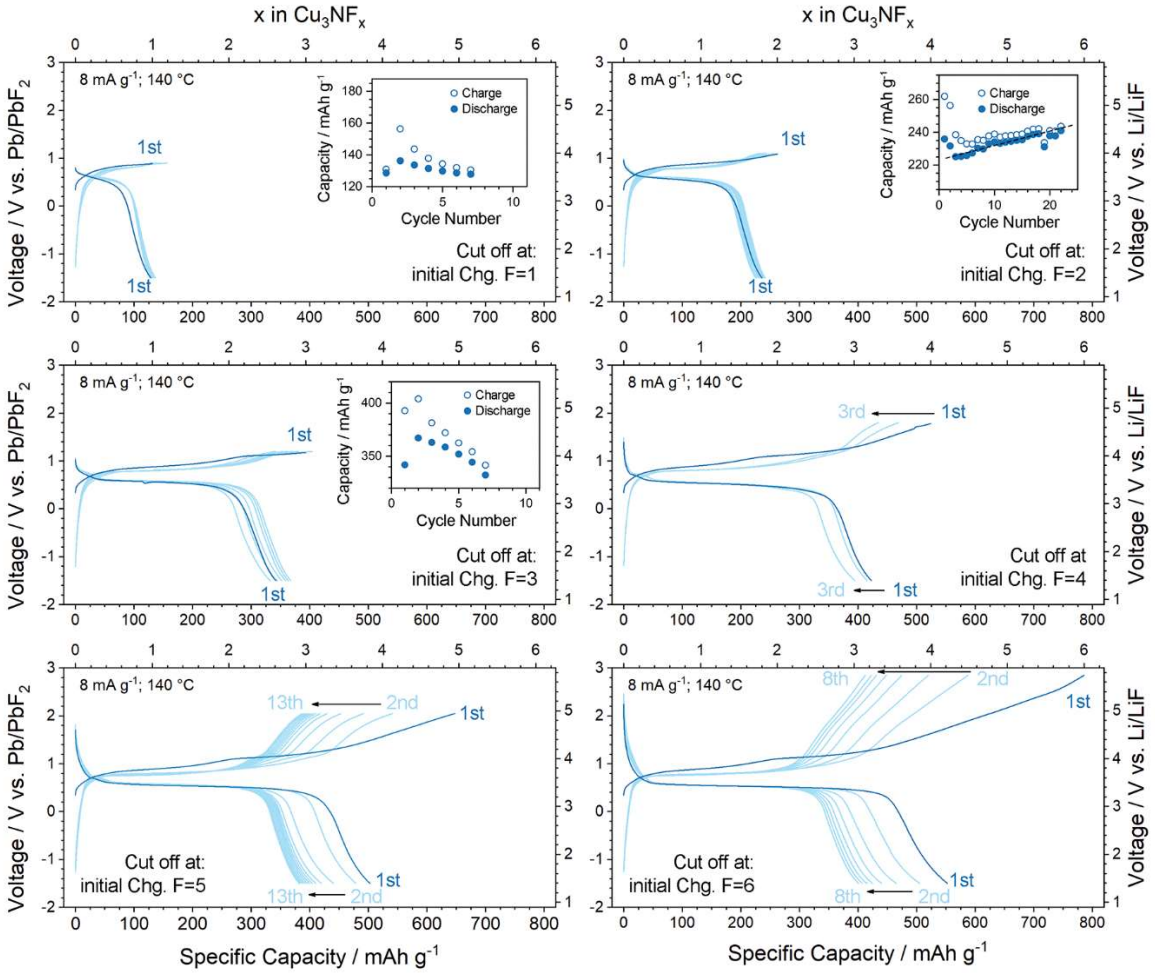

Figure 5.3 Charge-discharge curves of Cu_3N materials cut off at 1, 2, … , 6 of F^- intercalations upon initial charging. For samples of Chg. F=1, Chg. F=2 and Chg. F=3, cyclabilities were displayed in the insets for emphasizing the accumulated capacity at Chg. F=2 state where the black dash line is plot for guiding the eyes.

In the cases of Chg. F=6.0, Cu_3N materials surprisingly delivered an initial reversible capacity of 552 mAh g^{-1} at a current density of 8 mA g^{-1}. Despite that the initial coulombic efficiencies for Chg. F=4.0, Chg. F=5.0 and Chg. F=6.0 were relatively unsatisfactory, the reversible capacities were stabilized to near 400 mAh g^{-1} after several cycles, corresponding a

steady and reliable (de)intercalation of three F anions. If the initial fluorination degrees were constrained within the range of $x \leq 3.0$, better capacity retentions could be obtained. Within the steady (de)fluorination range (near three F (de)intercalation), the average voltage were ~0.95 V and 0.5 V vs. Pb/PbF_2 for charging and discharging process, respectively.

It is worth emphasizing that the Pb/PbF_2 was employed as anode because of its smooth fluorination which is beneficial for accurately evaluating the electrochemical behavior of cathode Cu_3N; however, the working voltage of Pb/PbF_2 was relatively high.[11] From the angle of practical application, an anode with much lower voltage such as La/LaF_3 (−2.41 V vs. Pb/PbF_2) shall be more suitable for achieving higher energy density. Based on the initial reversible capacity in the case of Chg. F=6 state, we can estimate the energy densities of a $Cu_3N||LaF_3$ cell and compare them with those of commercialized $LiCoO_2$||graphite cell, as shown in **Table 5.1**. The $Cu_3N||LaF_3$ cell can deliver energy densities of 1.7- (gravimetric) and 2.9-fold (volumetric) that of $LiCoO_2$||graphite cell, where volumetric energy density is significantly important for practical applications. In an ideal case of Li/LiF anode which has the lowest electrode voltage (−2.89 V vs. Pb/PbF_2) among most M/MF_x couples, the cell voltage could be further increased (see the right-side axis of **Figure 5.3**).

Table 5.1. The comparison of gravimetric/volumetric energy densities of $Cu_3N||LaF_3$ FIB and typical $LiCoO_2$||graphite LIB.

	$LiCoO_2$||graphite (LIB)	$Cu_3N\|\|LaF_3$ (FIB)
Capacity of cathode (mAh g^{-1})	150	550
Density of cathode (cm^{-3})	5.05	5.84
Capacity of anode (mAh g^{-1})	370	410
Density of anode (cm^{-3})	2.00	5.94
Gravity ratio (cathode:anode)	0.403	1.34
Volume ratio (cathode:anode)	1.02	1.32
Average cell potential (V)	3.70	2.90
Gravimetric enegy density (Wh kg^{-1})	395	680
Volumetric enegy density (Wh L^{-1})	1390	4020

* The extra battery components (current collector, electrolyte, battery shell, separator, conductive species, binder, etc.) were not involved into calculation because they can be solved by engineering ways and are not intrinsic factors.

** The capacity ratio of cathode to anode in the full cell was fixed to 1.0.

Rate capability was studied at a theoretically safe (namely, no risk of fully transition to CuF_2 nor N_2 release) state, Chg. F=2, as shown in **Figure 5.4**. Cu_3N material realized reversible charge/discharge at a current density of 200 mA g^{-1}; the capacity of a similar Cu/LBF/VGCF (as-purchased Cu nano-powder) composite fast decayed even at an unvaried current density of 5 mA g^{-1}. As well, the accumulated capacity of Cu_3N can be observed when the current density returned to 5 mA g^{-1} at last (also see the inset of Chg. F=2 in Figure 5.3).

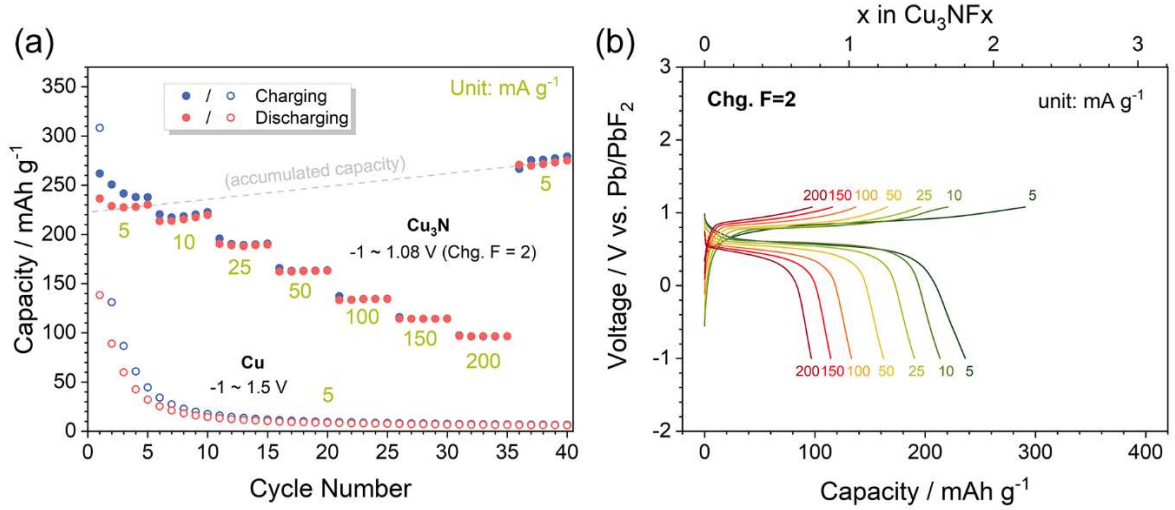

Figure 5.4 Rate capabilities of Cu_3N in the case of Chg. F=2 state. (a) Comparison between capacities of Cu_3N at various current densities and Cu at 5 mA g^{-1} and (b) corresponding charge-discharge curves of Cu_3N material.

5.3.3 Charge compensation mechanisms

Charge compensation mechanism was revealed by XAS measurements. In Cu K-edge spectra (**Figure 5.5**(a)), the pre-edge shoulder at approx. 8981 eV was ascribed to the excitation of K-shell electrons of Cu^+ species to 4*p* orbitals. The linear N-Cu-N coordination might result in the splitting of $4p_{xy}$ and $4p_z$, leading to the multi-shoulder feature of $1s \rightarrow 4p$ transition, which was also observed in many other Cu-containing compounds with low coordination number of Cu^+ center.[21-23] The gradual absence of this pre-edge shoulder from Chg. F=1 state to Chg. F=3 or Chg. F=4 indicated the donation of Cu^+ species to charge compensation. Meanwhile, after Chg. F=3 state, a tiny peak of $1s \rightarrow 3d$ transitions occurred at approx. 8976 eV; since the 3*d* orbital was fully occupied in $Cu^{(0)}$ and Cu^+ ($3d^{10}4s^1$ and $3d^{10}$ state, respectively), this tiny 3*d*-hole peak was regarded as a signature of Cu^{2+} species ($3d^9$ state). [21, 23] Therefore, Cu^+/Cu^{2+} redox was thought as a main contributor for charge compensation upon Cu_3N charging. This was supported by the results of Cu L_3-edge spectra as well, as shown in Figure 5.5(b). The broadened peak at 934 eV, which represented the $2p_{2/3} \rightarrow 4s$ transition, disappeared

as F gradually intercalating; correspondingly, the white-line peak at 930 eV of $2p_{2/3} \rightarrow 3d$, which exists only in Cu^{2+} species, increased rapidly. Also, such changes were successive throughout the charging process, further indicating that Cu^{+}/Cu^{2+} kept contributing for charge compensation upon charging process. [24-29]

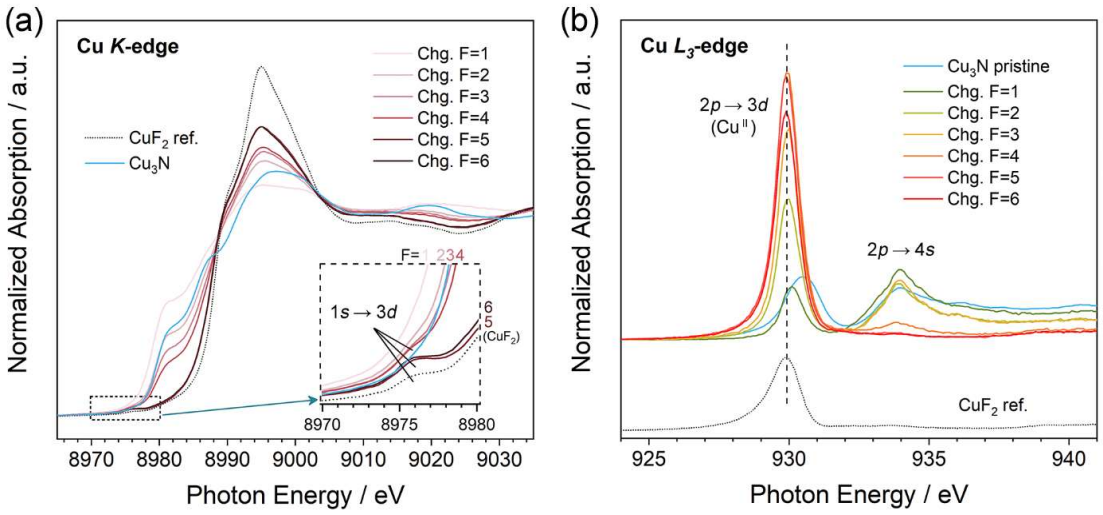

Figure 5.5 Ex situ (a) Cu K-edge and (b) Cu L_3-edge XAS patterns of Cu_3N material at various fluorination states upon initial charging.

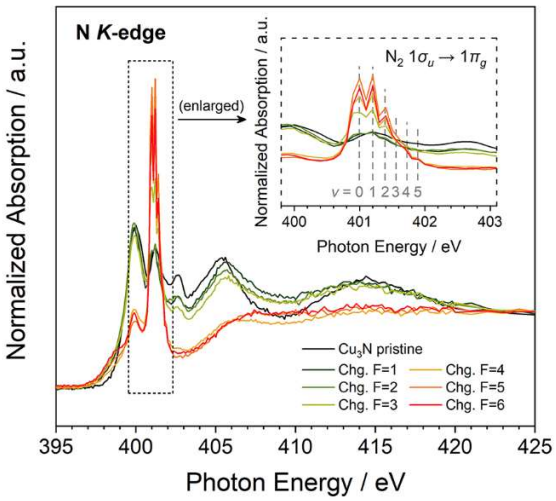

Figure 5.6 Ex situ N K-edge XAS patterns of Cu_3N at various fluorination states upon initial charging.

However, in the cases of high-fluorination-degree samples such as Chg. F=4.0, Chg. F=5.0 and Chg. F=6.0, they all delivered high capacities in initial several cycles that have exceeded the capability of sole Cu^{+}/Cu^{2+} redox (three F^{-} (de)intercalation, approx. 390 mAh g^{-1}), indicating that N redox had also reversibly participated the charge-compensation processes. The results of N K-edge XAS were shown in **Figure 5.6**. The near-edge interactions in N K-edge spectra of pristine Cu_3N are originated from N 1*s* → hybridized N 2*p*-Cu 3*d*

orbitals and N 1*s* → hybridized N 2*p*-Cu 4*sp* orbitals.[30-39] After Chg. F=3 state, a group of sharp multiple peaks occurred at approx. 401 eV. These multiple peaks are assigned to the vibrational excitations (vibrational substates of v = 0, 1, 2, 3, …), which accompany with an electronic excitation due to different bonding geometry between initial and final states, of N $1\sigma_u \rightarrow 1\pi_g$ transition in N_2 molecule.[40-44] The occasion of molecular N_2 occurrence is subtle: it has been verified that Cu^{+}/Cu^{2+} redox kept contributing for charge compensation from the beginning of charging process (Figure 5.5), however, molecular N_2 also occurred at as early as Chg. F=3 state even it is a three-electron ($N^{3-}/N^{(0)}$) process. Therefore, $N^{3-}/N^{(0)}$ redox reaction might have started in early stage as well, which made simultaneous contribution with Cu^{+}/Cu^{2+} redox for charge compensation owing to the largely overlapped Cu 3*d* and N 2*p* orbitals in Cu_3N material.

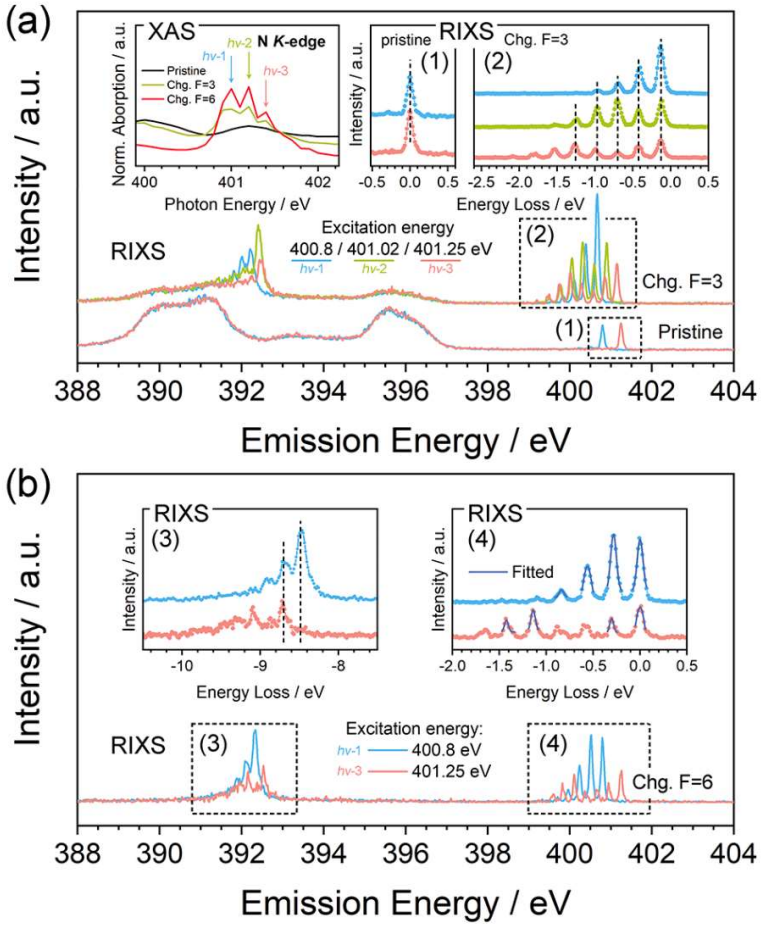

Figure 5.7 RIXS results of Cu_3N at (a) pristine and Chg. F=3 and (b) Chg. F=6 states. The inset figures showed the elastic peaks and corresponding scattering behaviors which were calibrated to energy loss. Three different incident energies represented the various vibrational state, v = 0, 1 and 2, in the N K-edge XAS results, respectively. The accurate incident energies for RIXS were remeasured and determined to be 400.8, 401.02 and 401.25 eV since there is a systematic energy difference in various beamlines (BL27SU for XAS and BL07LSU for RIXS).

As a result, we have selected three key ex situ points, namely, pristine, Chg. F=3 and Chg. F=6 states, for investigating N redox by N K-edge RIXS, as shown in **Figure 5.7**. Three excitation energies that represent the vibration levels, $v = 0$, 1 and 2 of π^* resonance (see Figure 6 and "XAS" inset of Figure 5.7(a)), were chosen for gauging the X-ray emission spectroscopies (XES). In both cases of Chg. F=3 and Chg. F=6 states, elastic peaks and corresponding behaviors at energy-loss range of -2.0 to 0 eV (scattering to ground state $^1\Sigma_g^+$) and -10.0 to -8.0 eV (scattering to ground state $a^1\Pi_g$) can be clearly observed in the case of an excitation energy of 400.8 eV ($v = 0$). Higher excitation energy of 401.02 eV ($v = 1$) and 401.25 eV ($v = 2$) resulted in the increases of peak intensities at higher energy loss, which is assigned to the increased vibrational final-state excitation.[45] These results strongly indicated the generation of molecular N_2 in charged-state Cu_3N material. Moreover, the molecular N_2 occurred at an early state of charging, Chg. F=3, indicating that N redox has started to make contribution to charge compensation at even earlier stage; consequently, the aforementioned "accumulated capacity" occurred at Chg. F=2 sample became understandable, since the Chg. F=2 state might be close to the threshold of N redox participation.

5.3.4 Discussion on fluorination preference and structural evolution

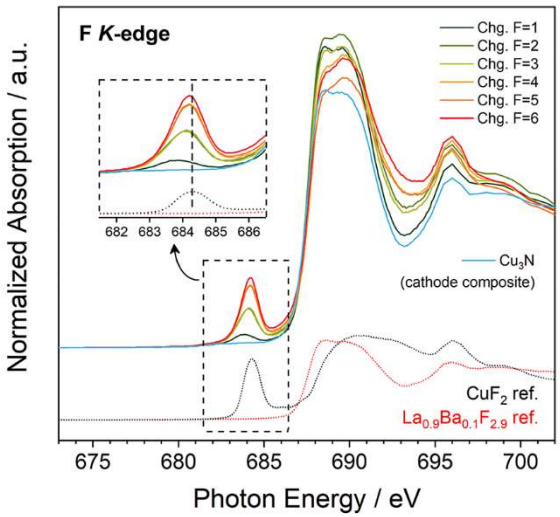

Figure 5.8 Ex situ F K-edge XAS patterns of Cu_3N at various fluorination states upon initial charging.

It is necessary to investigate the process of structural evolution, considering the multielectron process that has been achieved in Cu_3N material. The transforming tendency of F K-edge XAS results (**Figure 5.8**) were consistent with those of Cu electronic structures (Figure 5.5). All samples have similar post-edge fine structures (≥ 687 eV) which were assigned to the majority of F^- in LBF solid electrolyte. As F^- intercalation proceeded, a pre-edge peak

occurred at 684.3 eV and gradually increased. This pre-edge peak is highly possible to be relevant to the formation of e_g orbital originated from F 2*p*-Cu 3*d* hybridization, which was observed in F K-edge XAS result of CuF_2 as well.[46, 47]

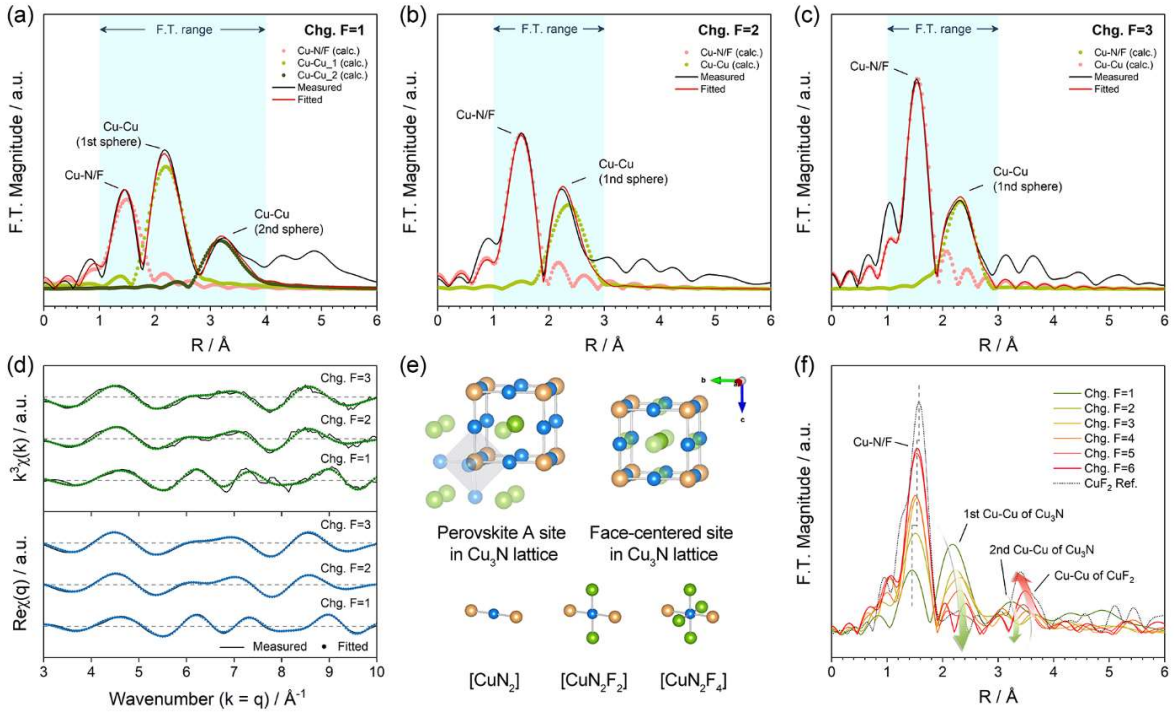

Figure 5.9 EXAFS results and corresponding FEFF calculations for charged Cu_3N at (a) Chg. F=1, (b) Chg. F=2 and (c) Chg. F=3 states, and (d) the fitting results in K and Q space in these cases. The fitting is based on (e) "face-centered" model which leads to $[CuN_2F_2]$ or $[CuN_2F_4]$ mixed-anion polyhedrons. (f) The EXAFS results showed highly CuF_2-like patterns at Chg. F=5 and Chg. F=6 fluorinated states.

Extended X-ray absorption fine structures (EXAFS) were studied to elucidate the structural evolution upon fluorination of Cu_3N lattice, as shown in **Figure 5.9**. Since we have verified that Cu and N redox have made simultaneous contributions to charge-compensation process, there is little possibility, before Chg. F=4 states, that N species have been fully oxidized to $N^{(0)}$ state and released as gaseous N_2. From Chg. F=1 to Chg. F=3 state (Figure 5.9 (a) to (c)), the F^- intercalation did not result in an independent Cu-F interaction but an increased Cu-N interaction, indicating that F^- occupied sites with same coordination environment as N anions and formed a mixed-anionic $[CuN_2F_x]$ unit, which as well in accordance with the formation of Cu-F hybridization in F K-edge XAS results. We simulated a fluorination model, which matched well with EXAFS results (Figure 5.9 (a) to (d)), that F^- occupied face-centered sites in Cu_3N lattice; these sites exactly have equivalent coordination environment with that of N. On the basis of "face-centered occupation" model, a linear N-Cu-N coordination induced at least four surrounding anionic vacancies of Cu in an assumed $[CuX_6]$ (X = N or F) octahedron,

as shown in Figure 8e. The effective simulations for further fluorinated samples (Chg. F=5 and Chg. F=6) can be difficult because complete oxidations of both Cu and N species might have happened with an end product of CuF_2 because of high risk of N_2 loss.

Interestingly, such intercalation behavior can be unique compared with many pioneering studies on similar (anti-)ReO_3-type configurations. As is known, ReO_3-type lattice is highly related to perovskite structure (ABO_3, A and B are cations), where the A site of perovskite structure become empty (Figure 5.9(e)). The absence of A site in Cu_3N lattice induces large rooms, enabling the accommodation of heteroatoms. It has been extensively studied of the intercalations of various heteroatoms into A site to form an (anti-)perovskite-structure Cu_3NX compound (X = Li, Pd, Rh, Ru, Zn, Ni, Cd, Cu, Fe, Ti, Ag, La, Ce, N, etc.) by DFT calculation;[48-59] many of them have been synthesized and investigated by experimental methods, which were also in accordance with DFT calculation results. In most cases of Cu_3NX compound, X is a metal element which exists as cationic or metallic state; usually, a part of Cu^+ in Cu_3N will be inevitably substituted by X cation, which will be captured inside the lattice as an A-site $Cu^{(0)}$ instead of phase-separated metallic Cu. N. Bashian et al. have carried out electrochemical fluorinations of ReO_3, where they induced approx. 0.6 F^- into ReO_3 lattice using a fluoride-ion cell; the intercalation of F^- to vacant A site would not break the symmetry within parent perovskite structure.[60] Meanwhile, they also found an interesting "migration model" with significantly low energy, that Re atom has migrated from the corner of lattice to the tetrahedral sites created by three O atoms and one inserted F atoms, and formed a [ReO_3F] tetrahedron. M. Matsutakes et al. realized dopant of F^- into Cu_3N by chemical methods and directly observed the A-site occupation of F^- in the perovskite-structure Cu_3NF.[61]

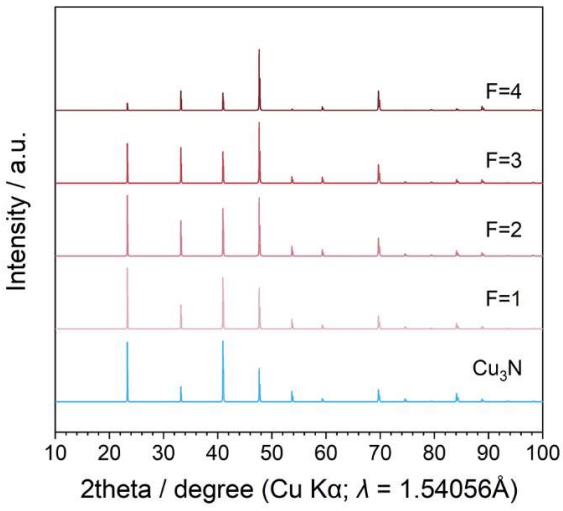

Figure 5.10 Theoretical XRD patterns of various assumed Cu_3NF_x (x = 1, 2, 3 and 4) models.

However, in the case of Cu_3N material in all-solid-state fluoride-ion batteries, such model, namely, one F^- intercalated into vacant A site and formed a perovskite Cu_3NF ("perovskite A-site occupation" model), seems insufficient and somehow incorrect, because much more F^- (far more than one) have been intercalated into one single Cu_3N lattice; the coordination was not consistent with "perovskite A-site occupation" model either. From the calculated diffraction patterns, it is found that the F occupations at both perovskite A site and face-centered site do not break the symmetry of primitive Cu_3N structure, as shown in **Figure 5.10**. More decisive evidence is required to determine the structural evolutions.

5.4 Conclusion

High-energy Cu_3N involving both Cu and N redox was evaluated as cathode material for all-solid-state FIBs. Reversible charge-discharge behavior with relatively low polarizations as well as excellent rate capability have been verified. N redox as one of major contributors to charge compensation was observed by combining XAS result with RIXS investigation. Cu and N redox gave simultaneous contributions to charge compensation, leading to multiple F^- intercalation into one lattice. This unique behavior of heteroatom intercalation in Cu_3N lattice is beyond the conventional cognations based on the perovskite model that the heteroatom X occupied the A site of Cu_3NX perovskite, which is for the first time reported. On the basis of up to six F^- intercalation, it is promising for Cu_3N-based all-solid-state FIBs to achieve much higher volumetric energy density compared with currently commercialized LIBs.

Reference

1. Armand, M.; Tarascon, J. M., Building better batteries. *Nature* **2008,** *451* (7179), 652-657.

2. Chu, S.; Cui, Y.; Liu, N., The path towards sustainable energy. *Nat. Mater.* **2017,** *16* (1), 16-22.

3. Grey, C.; Tarascon, J., Sustainability and in situ monitoring in battery development. *Nat. Mater.* **2017,** *16* (1), 45-56.

4. Xiao, A. W.; Galatolo, G.; Pasta, M., The case for fluoride-ion batteries. *Joule* **2021**.

5. Anji Reddy, M.; Fichtner, M., Batteries based on fluoride shuttle. *J. Mater. Chem.* **2011,** *21* (43), 17059-17062.

6. Thieu, D. T.; Fawey, M. H.; Bhatia, H.; Diemant, T.; Chakravadhanula, V. S. K.; Behm, R. J.; Kübel, C.; Fichtner, M., CuF_2 as Reversible Cathode for Fluoride Ion Batteries. *Adv. Funct. Mater.* **2017,** *27* (31), 1701051.

7. Zhang, D.; Yamamoto, K.; Ochi, A.; Wang, Y.; Yoshinari, T.; Nakanishi, K.; Nakano, H.; Miki, H.; Nakanishi, S.; Iba, H.; Uchiyama, T.; Watanabe, T.; Amezawa, K.; Uchimoto, Y., Understanding the reaction mechanism and performances of 3d transition metal cathodes for all-solid-state fluoride ion batteries. *J. Mater. Chem. A* **2021,** *9* (1), 406-412.

8. Yoshinari, T.; Zhang, D.; Yamamoto, K.; Kitaguchi, Y.; Ochi, A.; Nakanishi, K.; Miki, H.; Nakanishi, S.; Iba, H.; Uchiyama, T.; Watanabe, T.; Matsunaga, T.; Amezawa, K.; Uchimoto, Y., Kinetic analysis and alloy designs for metal/metal fluorides toward high rate capability for all-solid-state fluoride-ion batteries. *J. Mater. Chem. A* **2021,** *9* (11), 7018-7024.

9. Nowroozi, M. A.; Wissel, K.; Rohrer, J.; Munnangi, A. R.; Clemens, O., $LaSrMnO_4$: Reversible Electrochemical Intercalation of Fluoride Ions in the Context of Fluoride Ion Batteries. *Chem. Mater.* **2017,** *29* (8), 3441-3453.

10. Nowroozi, M. A.; Ivlev, S.; Rohrer, J.; Clemens, O., La_2CoO_4: a new intercalation based cathode material for fluoride ion batteries with improved cycling stability. *J. Mater. Chem. A* **2018,** *6* (11), 4658-4669.

11. Zhang, D.; Yamamoto, K.; Wang, Y.; Gao, S.; Uchiyama, T.; Watanabe, T.; Takami, T.; Matsunaga, T.; Nakanishi, K.; Miki, H.; Iba, H.; Amezawa, K.; Maeda, K.; Kageyama, H.; Uchimoto, Y., Reversible and Fast (De)fluorination of High-Capacity Cu_2O Cathode: One Step Toward Practically Applicable All-Solid-State Fluoride-Ion Battery. *Adv. Energy Mater.* **2021**.

12. Kageyama, H.; Hayashi, K.; Maeda, K.; Attfield, J. P.; Hiroi, Z.; Rondinelli, J. M.; Poeppelmeier, K. R., Expanding frontiers in materials chemistry and physics with multiple anions. *Nat. Commun.* **2018,** *9* (1), 772.

13. Reichert, M. D.; White, M. A.; Thompson, M. J.; Miller, G. J.; Vela, J., Preparation and Instability of Nanocrystalline Cuprous Nitride. *Inorg. Chem.* **2015,** *54* (13), 6356-62.

14. Petříček, V.; Dušek, M.; Palatinus, L., Crystallographic Computing System JANA2006: General features. *Z. Kristallogr. Cryst. Mater.* **2014,** *229* (5), 345-352.

15. Momma, K.; Izumi, F., VESTA 3 for three-dimensional visualization of crystal, volumetric and morphology data. *J. Appl. Cryst.* **2011,** *44* (6), 1272-1276.

16. Harada, Y.; Kobayashi, M.; Niwa, H.; Senba, Y.; Ohashi, H.; Tokushima, T.; Horikawa, Y.; Shin, S.; Oshima, M., Ultrahigh resolution soft X-ray emission spectrometer at BL07LSU in SPring-8. *Rev. Sci. Instrum.* **2012,** *83* (1), 013116.

17. Zhang, L.; Anji Reddy, M.; Fichtner, M., Development of tysonite-type fluoride conducting thin film electrolytes for fluoride ion batteries. *Solid State Ionics* **2015,** *272*, 39-44.

18. Rongeat, C.; Reddy, M. A.; Witter, R.; Fichtner, M., Solid electrolytes for fluoride ion batteries: ionic conductivity in polycrystalline tysonite-type fluorides. *ACS Appl. Mater. Interfaces* **2014,** *6* (3), 2103-2110.

19. Rongeat, C.; Reddy, M. A.; Witter, R.; Fichtner, M., Nanostructured Fluorite-Type Fluorides As Electrolytes for Fluoride Ion Batteries. *J. Phys. Chem. C* **2013,** *117* (10), 4943-4950.

20. Grenier, A.; Porras-Gutierrez, A. G.; Body, M.; Legein, C.; Chrétien, F.; Raymundo-Piñero, E.; Dollé, M.; Groult, H.; Dambournet, D., Solid Fluoride Electrolytes and Their Composite with Carbon: Issues and Challenges for

Rechargeable Solid State Fluoride-Ion Batteries. *J. Phys. Chem. C* **2017,** *121* (45), 24962-24970.

21. Gaur, A.; Shrivastava, B. D., A Comparative Study of the Methods of Speciation Using X-ray Absorption Fine Structure. *Acta Phys. Pol. A* **2012,** *121* (3), 647-652.

22. Kim, W. B.; Lee, J. S., Quantitative XANES analysis of cuprous dibromide complex formed in the oxidative carbonylation of phenols. *J. Phys. Chem. B* **2003,** *107* (35), 9195-9202.

23. Kau, L. S.; Spirasolomon, D. J.; Pennerhahn, J. E.; Hodgson, K. O.; Solomon, E. I., X-Ray Absorption-Edge Determination of the Oxidation-State and Coordination-Number of Copper - Application to the Type-3 Site in Rhus-Vernicifera Laccase and Its Reaction with Oxygen. *J. Am. Chem. Soc.* **1987,** *109* (21), 6433-6442.

24. Fioretti, A. N.; Schwartz, C. P.; Vinson, J.; Nordlund, D.; Prendergast, D.; Tamboli, A. C.; Caskey, C. M.; Tuomisto, F.; Linez, F.; Christensen, S. T.; Toberer, E. S.; Lany, S.; Zakutayev, A., Understanding and Control of Bipolar Self-Doping in Copper Nitride. *J. Appl. Phys.* **2016,** *119* (18), 181508.

25. Dong, C. L.; Mattesini, M.; Augustsson, A.; Wen, X. G.; Zhang, W. X.; Yang, S. H.; Persson, C.; Ahuja, R.; Lüning, J.; Chang, C. L.; Guo, J. H., Electronic structure and surface structure of Cu_2S nanorods from polarization dependent X-ray absorption spectroscopy. *J. Electron Spectrosc. Relat. Phenom.* **2006,** *151* (1), 64-70.

26. George, S. J.; Lowery, M. D.; Solomon, E. I.; Cramer, S. P., Copper L-edge spectral studies: a direct experimental probe of the ground-state covalency in the blue copper site in plastocyanin. *J. Am. Chem. Soc.* **2002,** *115* (7), 2968-2969.

27. Carniato, S.; Luo, Y.; Ågren, H., Theoretical study of the near-edge Cu *L* x-ray absorption spectrum of copper phthalocyanine. *Phys. Rev. B* **2001,** *63* (8).

28. Flipse, C. F.; van der Laan, G.; Johnson, A. L.; Kadowaki, K., Soft-x-ray absorption spectroscopy of electron-doped $(Nd,Sm)_{2-x}Ce_xCuO_{4-\delta}$ compounds. *Phys. Rev. B Condens. Matter* **1990,** *42* (4), 1997-2002.

29. Grioni, M.; Goedkoop, J. B.; Schoorl, R.; de Groot, F. M.; Fuggle, J. C.; Schafers, F.; Koch, E. E.; Rossi, G.; Esteva, J.; Karnatak, R. C., Studies of copper

valence states with Cu L_3 x-ray-absorption spectroscopy. *Phys. Rev. B Condens. Matter* **1989,** *39* (3), 1541-1545.

30. Esaka, F.; Furuya, K.; Shimada, H.; Imamura, M.; Matsubayashi, N.; Sato, H.; Nishijima, A.; Kawana, A.; Ichimura, H.; Kikuchi, T., Comparison of surface oxidation of titanium nitride and chromium nitride films studied by x-ray absorption and photoelectron spectroscopy. *J. Vac. Sci. Technol* **1997,** *15* (5), 2521-2528.

31. Fioretti, A. N.; Schwartz, C. P.; Vinson, J.; Nordlund, D.; Prendergast, D.; Tamboli, A. C.; Caskey, C. M.; Tuomisto, F.; Linez, F.; Christensen, S. T.; Toberer, E. S.; Lany, S.; Zakutayev, A., Understanding and Control of Bipolar Self-Doping in Copper Nitride. *J. Appl. Phys.* **2016,** *119* (18).

32. Kaspar, T. C.; Ney, A.; Mangham, A. N.; Heald, S. M.; Joly, Y.; Ney, V.; Wilhelm, F.; Rogalev, A.; Yakou, F.; Chambers, S. A., Structure of epitaxial (Fe,N) codoped rutile TiO_2 thin films by x-ray absorption. *Phys. Rev. B* **2012,** *86* (3).

33. Li, X.; An, L.; Chen, X.; Zhang, N.; Xia, D.; Huang, W.; Chu, W.; Wu, Z., Durability enhancement of intermetallics electrocatalysts via N-anchor effect for fuel cells. *Sci. Rep.* **2013,** *3*, 3234.

34. Modin, A.; Kvashnina, K. O.; Butorin, S. M.; Werme, L.; Nordgren, J.; Arapan, S.; Ahuja, R.; Fallberg, A.; Ottosson, M., Electronic structure of Cu_3N films studied by soft x-ray spectroscopy. *J. Phys. Condens. Matter* **2008,** *20* (23), 235212.

35. Sahoo, G.; Kashikar, R.; Jain, M. K.; Nanda, B. R. K., Tailoring p- and n- type semiconductor through site selective oxygen doping in Cu_3N: density functional studies. *Mater. Res. Express* **2016,** *3* (6).

36. Shang, H.; Zhou, X.; Dong, J.; Li, A.; Zhao, X.; Liu, Q.; Lin, Y.; Pei, J.; Li, Z.; Jiang, Z.; Zhou, D.; Zheng, L.; Wang, Y.; Zhou, J.; Yang, Z.; Cao, R.; Sarangi, R.; Sun, T.; Yang, X.; Zheng, X.; Yan, W.; Zhuang, Z.; Li, J.; Chen, W.; Wang, D.; Zhang, J.; Li, Y., Engineering unsymmetrically coordinated Cu-S_1N_3 single atom sites with enhanced oxygen reduction activity. *Nat. Commun.* **2020,** *11* (1), 3049.

37. Shimada, H.; Fukao, T.; Minami, H.; Ukai, M.; Fujii, K.; Yokoya, A.; Fukuda, Y.; Saitoh, Y., Nitrogen K-edge X-ray absorption near edge structure (XANES)

spectra of purine-containing nucleotides in aqueous solution. *J. Chem. Phys.* **2014,** *141* (5), 055102.

38. Soto, G.; de la Cruz, W.; Farías, M. H., XPS, AES, and EELS characterization of nitrogen-containing thin films. *J. Electron Spectrosc. Relat. Phenom.* **2004,** *135* (1), 27-39.

39. Tanaka, I.; Mizoguchi, T.; Yamamoto, T., XANES and ELNES in Ceramic Science. *J. Am. Ceram. Soc.* **2005,** *88* (8), 2013-2029.

40. Bjorneholm, O.; Nilsson, A.; Sandell, A.; Hernnas, B.; Martensson, N., Vibrationally selective autoionization of physisorbed molecular nitrogen. *Phys. Rev. B Condens. Matter* **1994,** *49* (3), 2001-2004.

41. Kimberg, V.; Lindblad, A.; Söderström, J.; Travnikova, O.; Nicolas, C.; Sun, Y. P.; Gel'mukhanov, F.; Kosugi, N.; Miron, C., Single-Molecule X-Ray Interferometry: Controlling Coupled Electron-Nuclear Quantum Dynamics and Imaging Molecular Potentials by Ultrahigh-Resolution Resonant Photoemission and Ab InitioCalculations. *Phys. Rev. X* **2013,** *3* (1).

42. Miron, C.; Nicolas, C.; Travnikova, O.; Morin, P.; Sun, Y.; Gel'mukhanov, F.; Kosugi, N.; Kimberg, V., Imaging molecular potentials using ultrahigh-resolution resonant photoemission. *Nat. Phys.* **2011,** *8* (2), 135-138.

43. Neeb, M.; Rubensson, J. E.; Biermann, M.; Eberhardt, W., Coherent excitation of vibrational wave functions observed in core hole decay spectra of O_2, N_2 and CO. *J. Electron Spectrosc. Relat. Phenom.* **1994,** *67* (2), 261-274.

44. Song, H. J.; Shin, H. J.; Chung, Y.; Lee, J. C.; Lee, M. K., X-ray absorption and photoelectron spectroscopic study of plasma-nitrided SiO_2 film. *J. Appl. Phys.* **2005,** *97* (11).

45. Kjellsson, L.; Ekholm, V.; Agåker, M.; Såthe, C.; Pietzsch, A.; Karlsson, H. O.; Jaouen, N.; Nicolaou, A.; Guarise, M.; Hague, C.; Lüning, J.; Chiuzbăian, S. G.; Rubensson, J. E., Resonant inelastic x-ray scattering at the N_2 π^* resonance: Lifetime-vibrational interference, radiative electron rearrangement, and wave-function imaging. *Phys. Rev. A* **2021,** *103* (2).

46. Hu, Z.; Kaindl, G.; Warda, S. A.; Reinen, D.; de Groot, F. M. F.; Müller, B. G., On the electronic structure of Cu(III) and Ni(III) in $La_2Li_{1/2}Cu_{1/2}O_4$, $Nd_2Li_{1/2}Ni_{1/2}O_4$, and Cs_2KCuF_6. *Chem. Phys.* **1998,** *232* (1-2), 63-74.

47. Nakai, S.; Kawata, A.; Ohashi, M.; Kitamura, M.; Sugiura, C.; Mitsuishi, T.; Maezawa, H., Core-exciton absorption in the F K absorption spectra of 3d transition-metal fluorides. *Phys. Rev. B Condens. Matter* **1988,** *37* (18), 10895-10897.

48. Wu, Z.; Chen, H.; Gao, N.; Zhang, E.; Yang, J.; Yang, T.; Li, X. a.; Huang, W., Ab initio calculations of the structural, elastic, electronic and optical properties of Cu_3N as well as Cu_3NLa and Cu_3NCe compounds. *Comput. Mater. Sci.* **2014,** *95*, 221-227.

49. Pierson, J. F.; Horwat, D., Addition of silver in copper nitride films deposited by reactive magnetron sputtering. *Scr. Mater.* **2008,** *58* (7), 568-570.

50. Wang, J.; Li, F.; Liu, X.; Zhou, H.; Shao, X.; Qu, Y.; Zhao, M., Cu_3N and its analogs: a new class of electrodes for lithium ion batteries. *J. Mater. Chem. A* **2017,** *5* (18), 8762-8768.

51. Hou, Z. F., Effects of Cu, N, and Li intercalation on the structural stability and electronic structure of cubic Cu_3N. *Solid State Sci.* **2008,** *10* (11), 1651-1657.

52. Pereira, N.; Dupont, L.; Tarascon, J. M.; Klein, L. C.; Amatucci, G. G., Electrochemistry of Cu_3N with Lithium A Complex System with Parallel Processes. *J. Electrochem. Soc.* **2003,** *150* (9).

53. Hahn, U.; Weber, W., Electronic structure and chemical-bonding mechanism of Cu_3N, Cu_3NPd, and related Cu(I) compounds. *Phys. Rev. B Condens. Matter* **1996,** *53* (19), 12684-12693.

54. Li, X.; Hector, A. L.; Owen, J. R., Evaluation of Cu_3N and CuO as Negative Electrode Materials for Sodium Batteries. *J. Phys. Chem. C* **2014,** *118* (51), 29568-29573.

55. Moreno-Armenta, M. G.; Pérez, W. L.; Takeuchi, N., First-principles calculations of the structural and electronic properties of Cu_3MN compounds with M = Ni, Cu, Zn, Pd, Ag, and Cd. *Solid State Sci.* **2007,** *9* (2), 166-172.

56. Gulo, F.; Simon, A.; Kohler, J.; Kremer, R. K., Li-Cu exchange in intercalated Cu_3N--with a remark on Cu_4N. *Angew. Chem.* **2004,** *43* (15), 2032-4.

57. Pierce, J. W.; McKinzie, H. L.; Vlasse, M.; Wold, A., Preparation and properties of molybdenum fluoro-bronzes. *J. Solid State Chem.* **1970,** *1* (3-4), 332-338.

58. Ji, A.; Li, C.; Cao, Z., Ternary Cu_3NPd_x exhibiting invariant electrical resistivity over 200K. *Appl. Phys. Letters* **2006,** *89* (25).

59. Fan, X. Y.; Wu, Z. G.; Zhang, G. A.; Li, C.; Geng, B. S.; Li, H. J.; Yan, P. X., Ti-doped copper nitride films deposited by cylindrical magnetron sputtering. *J. Alloys Compd.* **2007,** *440* (1-2), 254-258.

60. Bashian, N. H.; Zuba, M.; Irshad, A.; Becwar, S. M.; Vinckeviciute, J.; Rahim, W.; Griffith, K. J.; McClure, E. T.; Papp, J. K.; McCloskey, B. D.; Scanlon, D. O.; Chmelka, B. F.; Van der Ven, A.; Narayan, S. R.; Piper, L. F. J.; Melot, B. C., Electrochemical Oxidative Fluorination of an Oxide Perovskite. *Chem. Mater.* **2021,** *33* (14), 5757-5768.

61. Matsuzaki, K.; Harada, K.; Kumagai, Y.; Koshiya, S.; Kimoto, K.; Ueda, S.; Sasase, M.; Maeda, A.; Susaki, T.; Kitano, M.; Oba, F.; Hosono, H., High-Mobility p-Type and n-Type Copper Nitride Semiconductors by Direct Nitriding Synthesis and In Silico Doping Design. *Adv. Mater.* **2018,** *30* (31), e1801968.

Chapter 6 Understanding Cationic/Anionic Redox of Topotactic $Ca_{0.85}CuO_2$ Cathode Materials

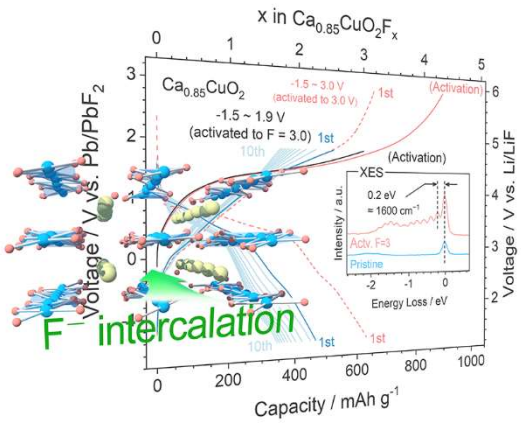

All-solid-state fluoride-ion batteries (FIBs), in which monovalent fluoride anions are employed as charge carriers, are regarded as attractive options owing to high theoretical energy densities from multielectron fluorination reactions. As a result, deeper understanding toward anionic redox in topotactic cathode materials is strongly required. In this study, $Ca_{0.85}CuO_2$ with an infinite-layer-related structure, where O redox is nominally main contributor for charge compensation, is evaluated as cathode material for all-solid-state FIBs. Through X-ray absorption spectroscopy and resonant inelastic X-ray scattering, the remarkable participation of O redox as well as the formation of molecular O_2 in $Ca_{0.85}CuO_2$ lattice has been confirmed. The transformation of charge-compensation pattern from “anionic redox as principal” in initial activation to “co-participation of cationic/anionic redox” in following cycles has been revealed as well.

6.1 Introduction

All-solid-state fluoride-ion batteries (FIBs) have received many attentions due to high electrochemical stability of F anion as charge carriers.[1-6] Owing to the multielectron nature of most fluorination process, it is highly promising for FIBs to achieve excellent theoretical energy densities which largely exceed those of conventional lithium-ion batteries (LIBs). For example, the simple metal/metal fluoride (M/MF_x) delivers high theoretical energy density of over 2000 Wh kg^{-1} or 5000 Wh L^{-1}.[5-8] However, M/MF_x systems were proved to obey a two-phase-type reaction pattern with exceedingly large volumetric changes which are devastating interfacial behaviors between electrode and solid electrolytes, leading to fast capacity deteriorations upon cycling.[5, 9]

Topotactic host materials, such as perovskite-, Ruddlesden−Popper-, schafarzikite-type materials, etc., are particularly attractive due to their high structural reversibility and F intercalation tolerance, compared with widely used M/MF_x systems.[10-16] It is vitally important for topotactic materials to have anionic vacancies surrounding cationic coordination centers as F^- intercalation sites. Therefore, the host materials with low-coordination environment of cations can be promising candidates for the use of F (de)intercalations. Moreover, unlike M/MFx materials that have a starting valency of 0 (metallic state), transition metals in topotactic materials have relatively elevated oxidation states, leading to decreased capabilities of these transition metals for charge compensation. As a result, the involvement of anionic species for charge compensation is substantial for realizing high energy densities, which has been extensively applied in the studies of LIBs.[17-21]

Herein, we introduced $Ca_{0.85}CuO_2$ as high-energy cathode material for all-solid-state FIBs with an infinite-layer-related modulated chain structure. Slightly distorted square planar [CuO_4] provide sufficient rooms for F^- intercalation. Reversible fluorinations as well as ultrahigh capacities were exhibited, where the charge-compensation mechanism involving both cationic and anionic redox was investigated by X-ray absorption spectroscopies (XAS) and resonant inelastic X-ray scattering (RIXS) techniques. The light molecular mass of $Ca_{0.85}CuO_2$ leads to high capacity of ~206.8 mAh g^{-1} for each intercalated F^-. Interestingly, a transition of charge-compensation pattern from “anionic redox as principal” to “co-participation of cationic/anionic redox” was revealed. It is hoped that the explorations toward anionic redox behaviors in this study could lead to better understandings on fluorination reactions and facilitate the future development of high-energy fluoride-ion batteries.

6.2 Experimental

6.2.1 Materials preparation

$Ca_{0.85}CuO_2$ was synthesized via a solid-state routine. Typically, stoichiometric amounts of $CaCO_3$ (Aldrich) and CuO (Aldrich) were ball-milled using ethanol as medium, then dried, pelletized and sintered at 800 °C for 20 h under O_2 flow. The sintering process shall be repeated for at least 6 times with immediate re-grinding and X-ray diffraction checking after each sintering until a pure single phase was obtained. The $CaCO_3$/CuO precursor could also be hand-ground by mortar and pestle, whereas more sintering times will be required compared with that of ball-milled precursor. Solid electrolyte $La_{0.9}Ba_{0.1}F_{2.9}$ (LBF), cathode composite ($Ca_{0.85}CuO_2$/LBF/VGCF = 3:6:1 in mass ratio) and anode composite (PbF2/Pb/LBF/VGCF = 3:2:4:1 in mass ratio) were prepared by ball milling, which has been described in detail in Section 5.2.1.

6.2.2 Electrochemical measurement

Electrochemical performances were studied utilizing bulk-type all-solid-state cells. Similar to the procedures described in our previous studies,[4] 0.15 g of LBF, 0.01 g of cathode composite, 0.05 g of anode composite and two pieces of Au current collectors were put into a PEEK insulator (10 mm of inner diameter) and pressed at 360 MPa. All operations of battery assembly were carried out in an Ar-filled glove box without any exposure to air or moisture. The galvanostatic charging-discharging tests were proceeded using Hokuto Denko SD-8 battery testing systems, which was cut off within a voltage range of −1.5 to 3.0 V.

6.2.3 Characterizations

The XRD patterns were collected using an Rigaku Ultima IV X-ray diffractometer with Cu Kα radiation (λ = 1.54056 Å). The analyses on crystallographic structures were supported by VESTA.[22] The high-energy X-ray diffractions (HEXRD) were performed at BL02B2 beamline in SPring-8 synchrotron-radiation facility with wavelength of 0.41385 Å and calibrated by CeO_2. The microscale morphologies and energy dispersive spectroscopy (EDS) were recorded using a field emission S-3400N scanning electron microscope (SEM, Hitachi, Japan).

Ex situ Cu K-edge, Cu $L_{2,3}$-edge, F K-edge and O K-edge X-ray absorption spectroscopy (XAS) measurements were conducted at BL14B2 and BL27SU beamlines in

SPring-8 synchrotron-radiation facility, respectively. A 19-element solid-state detector for Cu K-edge and a silicon drift detector for Cu $L_{2,3}$-edge, F K-edge and O K-edge XAS were used to acquire the data in partial fluorescence yield (PFY) mode.

RIXS measurements were performed at BL07LSU in SPring-8 utilizing a grazing flat-field-type high-resolution soft X-ray emission spectrometer.[23] Proper excitation energies of O K-edge X-ray emission spectroscopy (XES) were determined by beforehand soft XAS. The samples were supported on the holders by carbon tape and transferred to the measurement chamber; all operations are carried out in an Argon-atmosphere glovebox. Slow movements with a speed of 2.4 μm s^{-1} upon RIXS measurements to avoid high-energy beam damage.

6.3 Results and discussion

6.3.1 Synthesis, phase and compositions

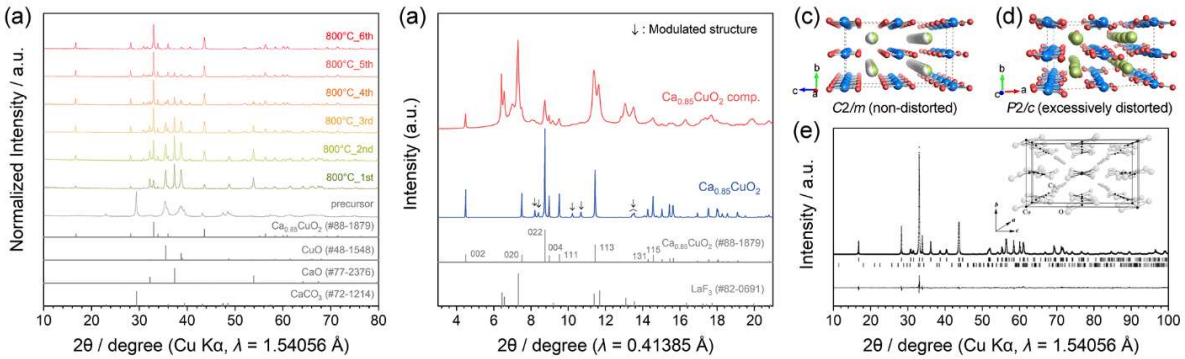

Figure 6.1 (a) XRD patterns of phase transition process of $Ca_{0.85}CuO_2$ material upon sintering. (b) HEXRD patterns of single-phase $Ca_{0.85}CuO_2$ and as-prepared $Ca_{0.85}CuO_2$/LBF/VGCF cathode composite. (c) *C*2/*m*-$Ca_{0.85}CuO_2$ and (d) *P*2/*c*-$Ca_{0.833}CuO_2$ models representing perfect non-distorted and excessively distorted structures which are available from crystallographic database. (e) A previously reported $Ca_{0.824}CuO_2$ material with incommensurately modulated crystal structure, reproduced from ref. 24.

Repeated sinters-regrinds are required to obtain a pure-phase $Ca_{0.85}CuO_2$ owing to the slow interdiffusion of Ca and Cu. As can be seen in **Figure 6.1**(a), the $CaCO_3$/CuO precursor rapidly transformed to $Ca_{0.85}CuO_2$ after the first sinter mixed with large amounts of residual CaO and CuO; these residues gradually disappeared with increased diffractions of target $Ca_{0.85}CuO_2$ upon following sinters. Some extra peaks out of target $Ca_{0.85}CuO_2$ diffractions (marked as ↓ symbols in Figure 6.1(b)) can be observed which were assigned to the distortions in a modulated substructure.[24, 25] Unlike $Ca_{0.86}Sr_{0.14}CuO_2$, which is known as its tetragonal infinite-layer structure and promising properties in terms of superconductivities where the planar

square [CuO_4] units form [CuO_2]$_\infty$ layers separated by Ca/Sr atoms,[26-28] strontium-free $CaCuO_2$ material possess a more complex structure. By the solid-state synthetic routine, it has been proved that Ca/Cu = 0.85 is the largest ratio that could be realized; however, in this case, the crystal structure is incommensurately modulated, and each Cu-O bond has its own length and angle distinct from those of other Cu-O bonds.[24, 25] The comparison between two related models, *C*2/*m*-$Ca_{1-x}CuO_2$[24] and *P*2/*c*-$Ca_{0.833}CuO_2$, with non-distorted (not any substructure diffractions) and excessively distorted (too many substructure diffractions than those of $Ca_{0.85}CuO_2$ in this work) crystal structures are displayed in Figure 6.1 (c) and (d), respectively. The most possible crystal structure of our as-prepared $Ca_{0.85}CuO_2$ shall be the one described by M. Isobe et al. (Figure 6.1(e)),[24] where *F*2/*m*-*F*2/*m* space groups were utilized to analyze the modulated sub-systems, which is beyond the discussion of this study.

6.3.2 Electrochemistry

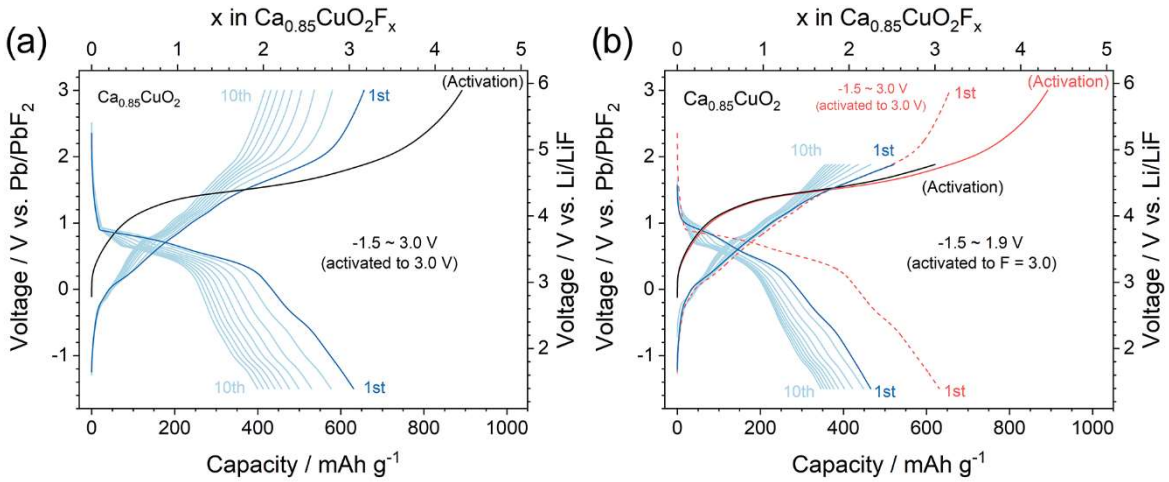

Figure 6.2 Electrochemical behaviors of $Ca_{0.85}CuO_2$ cut-off at (a) Actv. 3.0 V and (b) Actv. F=3 states. The curves of activation and 1st cycles in (a) are also plotted in (b) by pink color for comparison.

As shown in **Figure 6.2**, after activated to 3.0 V (a capacity of ~890 mAh g^{-1} was delivered in this process, denoted as "Actv. 3.0 V" state), the initial discharging and charging capacities were as large as 630 and 655 mAh g^{-1} within the cut-off range of 3.0 to −1.5 V, indicating that reversible fluorination was realized in $Ca_{0.85}CuO_2$ cathode material. For the starting $Ca_{0.85}CuO_2$ material, since Cu had a high oxidation state (even higher than +2 valence, which will be discussed later), O species shall be the main contributor to charge compensation upon activation. The activation process represented the intercalation of ~4.3 F^-, which is beyond the capability of O oxidation (maximum 4 electrons). Therefore, Cu species was thought to be further oxidized toward +3 valency as the rest part of charge compensation. After

10 cycles, the reversible capacity decreased to ~400 mAh g^{-1}, corresponding to a capacity retention of 63.4 %.

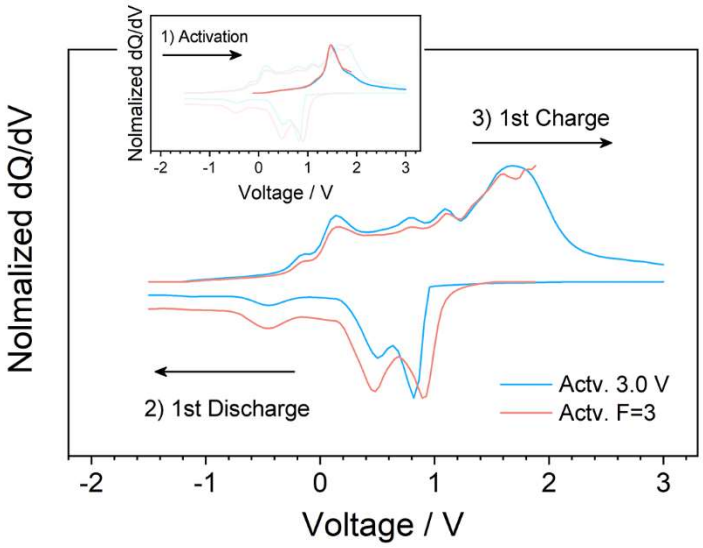

Figure 6.3 The dQ/dV curves of $Ca_{0.85}CuO_2$ cathode material cut-off at Actv. 3.0 V and Actv. F=3 states upon activation (inset), 1st discharging and 1st charging.

Notice that the electrochemical behaviors of activation and of following cycles were different, there should be a change of contribution ratios from each redox species. However, firstly, the unideal circumstance that O turned to gaseous and were totally lost should be considered. In this case, the $Ca_{0.85}CuO_2$ was completely transformed to $Ca_{0.85}CuF_x$ compound, which should obey a M/MF_x reaction routine as we described in Chapter 2 and 3. To avoid such circumstance, the activation capacity was constrained to that of three F^- intercalation (approx. 620 mAh g^{-1}, denoted as "Actv. F=3" state) and the final voltage was recorded; the following cycles will be cut-off from -1.5 V to this recorded voltage. The cyclability within Actv. F=3 controlment was shown in Figure 6.2(b). Similarly, in the case of Actv. F=3 state, the electrochemical behavior also changed after activation. Importantly, electrochemical behaviors in following cycles will not be largely influenced by various activation conditions; in both cases of Actv. 3.0 V and Actv. F=3 states, the behaviors of following cycles were identical, which was strongly indicated by the dQ/dV results (**Figure 6.3**) as well. Consequently, it is thought that the complete O_2 loss did not happen at Actv. 3.0 V state, otherwise the assumed products of $Ca_{0.85}CuF_{4.3}$ in Actv. 3.0 V state (complete loss of O) and $Ca_{0.85}CuO_2F_3$ in Actv. F=3 state (theoretically non-loss of O) were supposed to exhibit different discharging behaviors. As a result, the capacity fading shall not be caused by complete O loss of $Ca_{0.85}CuO_2$ in Actv. 3.0 V state.

6.3.3 Charge compensation mechanisms

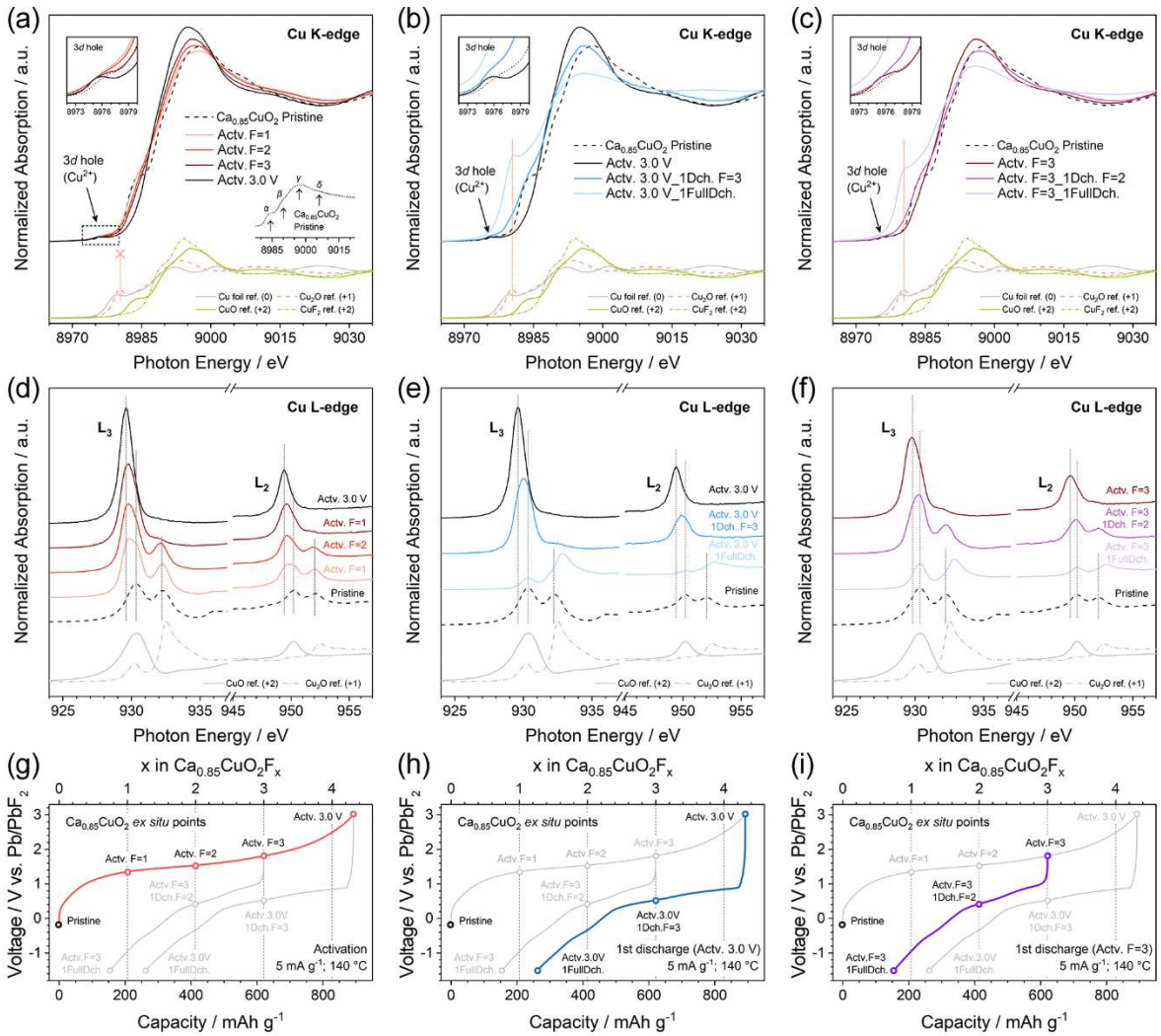

Figure 6.4 Ex situ (a-c) Cu K-edge and (d-f) Cu L-edge XAS patterns of $Ca_{0.85}CuO_2$ upon (g) activation process, (h) 1st discharging after Actv. 3.0 V state and (i) 1st discharging after Actv. F=3 state.

Charge-compensation mechanisms were investigated by XAS technique. Ex situ Cu K-edge XAS results were displayed in **Figure 6.4** (a) to (c). The near-edge features of pristine $Ca_{0.85}CuO_2$ were well consistent with previously reported results, where the starting valence of Cu shall be no less than +2. Firstly, totally four peaks, α, β, γ and δ, can be observed in the pattern of pristine $Ca_{0.85}CuO_2$, representing $1s \rightarrow 4p_{xy}$ (α) and $1s \rightarrow 4p_z$ (γ) transitions and their shake-down counterparts (β, δ), respectively.[29-31] Specifically, in the case of square-planar [CuO_4] coordination, the dipole-allowed one-electron transition $1s \rightarrow 4p_{xy}$ leads to two peaks with final-stage configurations of $1s^1 3d^{10} L^{-1} 4p_{xy}^1$ (α) and $1s^1 3d^9 4p_{xy}^1$ (β), respectively, where L^{-1} denotes a pole on Cu ligand (and so does $1s \rightarrow 4p_z$ transition).[29] This Cu ligand pole also results in the occurrence of partial $3d^{10}$ state in Cu^{2+} (normally $3d^9$) species; as a result, the tiny

3*d*-hole peak at ~8976 eV (1s → 3*d* transition), which is usually regarded as a signature of Cu^{2+} species, cannot be observed at pristine, Actv. F=1 and Actv. F=2 states.[30, 31] Upon charging process (Figure 6.4(a)), since the gradual F^- intercalation might lead to the Cu-F hybridization and create a local non-planar [CuO_4F_x] polyhedral coordination, α and γ peaks disappeared and the 3*d*-hole peak reoccurred, which further confirmed the above interpretations.

Upon 1st discharging, in both cases of Actv. 3.0 V (Figure 6.4(b)) and Actv. F=3 (Figure 6.4(c)), a large shoulder at ~8980 eV gradually occurred, demonstrating the $1s \rightarrow 4p_{xy}$ transition of Cu^+ species which located at lower energy than that of Cu^{2+} species (~8985 eV).[30, 31] Such changes indicated an increased contribution from Cu species to charge compensation upon discharging (further reduced to +1) than that upon activation (start valence of +2).

The results of Cu L-edge XAS were in line with those of Cu K-edge XAS, as shown in Figure 6.4 (d) to (f). The white-line peaks of pristine $Ca_{0.85}CuO_2$ at ~930 (L_3 edge) and ~950 eV (L_2 edge) were assigned to transitions from $2p_{3/2}$ and $2p_{1/2}$ to 3*d* orbital, respectively;[32] however, two shoulders occurred at ~1.5 eV above those of L_3 and L_2 white-line peaks. Similar to those shake-down shoulders in Cu K-edge XAS patterns, these L-edge shoulders were also assigned to the Cu ligand pore, which is also known as the characteristic of a Zhang-Rice singlet in the case of planar Cu-O coordination.[33, 34] Explicitly, the Cu species in pristine $Ca_{0.85}CuO_2$ shall involve partial transitions from $3d^8$ to $\underline{2p}3d^9$ and $\underline{2p}3d^{10}\underline{L}$ ($\underline{2p}$ and $\underline{L}$ denote the holes on Cu 2*p* orbitals and on Cu-O ligand) final states.[33-37] This also demonstrated the higher nominal oxidation state of Cu in $Ca_{0.85}CuO_2$ formula other than normal Cu^{2+}, because $\underline{2p}3d^{10}\underline{L}$ configuration was actually indicative of a delocalized doping hole on Cu 3*d* – O 2*p* hybridized orbitals in planar [CuO_4] coordination.[36]

Upon activation, the characteristics of pristine $Ca_{0.85}CuO_2$ gradually transformed to a single white-line peak at lower energy, which was caused by a purer and smoother Cu 2*p* to 3*d* transitions after fluorination compared to that of pristine $Ca_{0.85}CuO_2$. This indicated a higher oxidation state (emptier 3*d* orbital) and less Cu-O ligand hole (non-planar [CuO_4F_x] polyhedral), which was as well consistent with the Cu K-edge results. Similarly, upon 1st discharging, the white-line peak at ~930 eV (Cu 2*p* to 3*d*) disappeared; instead, a new peak, distinctive to the ligand-hole shoulder (~932 eV) in pristine $Ca_{0.85}CuO_2$, gradually occurred at ~933 eV, which suggested the appearance of Cu^+ species (strong Cu 2*p* to 4*s* transition).[32, 35, 38-41] The abovementioned speculations were firmly supported by the results of F K-edge XAS as shown

in **Figure 6.5**, where the pre-edge peak at ~684 eV reversibly occurred and disappeared upon activation and following discharging, which strongly implied the Cu 3*d* – F 2*p* (de)hybridization processes.[42, 43] The post-edge structures were assigned to the F species in LBF solid electrolyte.

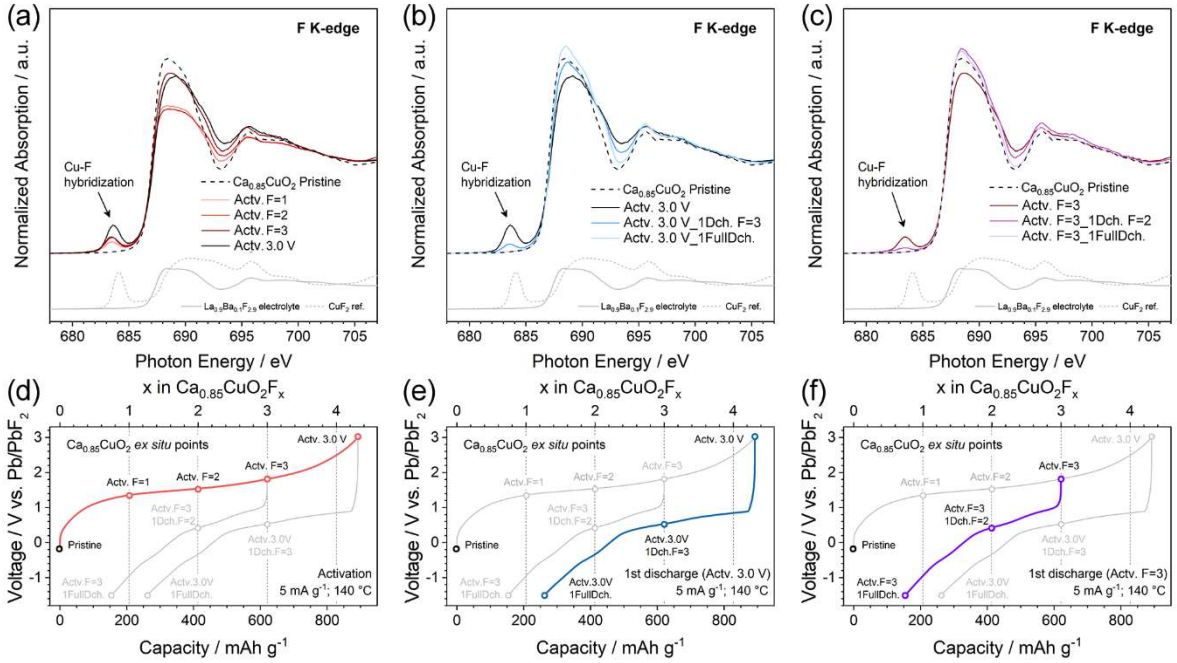

Figure 6.5 Ex situ (a-c) F K-edge XAS patterns of $Ca_{0.85}CuO_2$ cathode material upon (d) activation process, (e) 1st discharge after Actv. 3.0 V state and (f) 1st discharge after Actv. F=3 state.

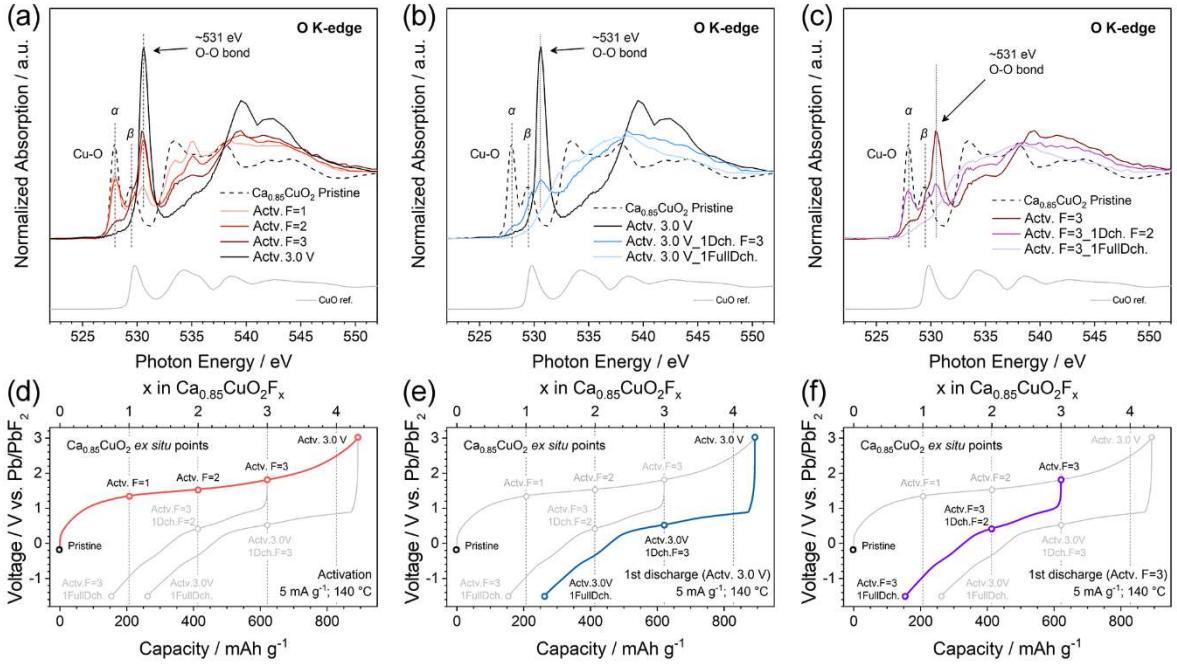

Figure 6.6 Ex situ (a-c) O K-edge XAS patterns of $Ca_{0.85}CuO_2$ cathode material upon (d) activation process, (e) 1st discharge after Actv. 3.0 V state and (f) 1st discharge after Actv. F=3 state.

The contribution of O redox to charge compensation was clarified by O K-edge XAS. As shown in **Figure 6.6**, the occurrences of doublet pre-edge peaks α and β are due to same reason as those of shake-down peaks and shoulders in Cu K-edge and Cu L-edge XAS patterns, namely, transitions from O 1*s* to Cu 3*d* – O 2*p* hybridized orbitals (β) and to Cu 3*d* – O 2*p* hybridized orbitals with a doping ligand hole (α).[37, 44] Upon activation, a sharp feature at excitation energy of ~531 eV gradually occurred, strongly implying the involvement of oxidized O species in charge compensation; notice that the ~531 eV feature was much stronger and sharper than those of previously reported materials,[17-20] which was ascribed to the absolutely major contribution to charge compensations of O species in $Ca_{0.85}CuO_2$ material. Upon discharging (Figure 5(b) and (c)), the ~531 eV feature reversibly disappeared, whereas the O K-edge XAS patterns at fully discharged states (in the cases of Actv. 3.0 V and Actv. F=3) did not recover to the starting pattern, indicating that O redox was not totally reversible.

RIXS results further revealed the nature of ~531 eV peak in O K-edge XAS, as shown in **Figure 6.7**, The zero-loss elastic peak and accompanied vibrational features at energy loss −2.0 to 0 eV (scattering to ground state $^3\Sigma_g^-$), and a characteristic structure at energy loss −8.0 to −6.5 eV (scattering to ground state $B'^3\Pi_g$),[45] as well as the vibrational frequency of ~1600 cm^{-1}, were clearly observed, demonstrating the formation of molecular O species at Chg. F=3 state.[19, 20]

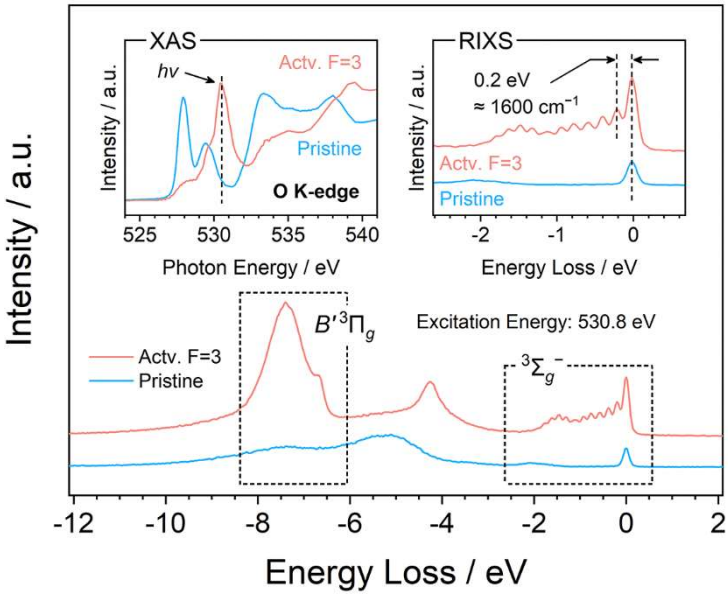

Figure 6.7 O K-edge RIXS patterns of $Ca_{0.85}CuO_2$ at pristine and Actv. F=3 states. The incident energy was set as that of the sharp feature near ~531 eV in XAS pattern (left side inset), which was calibrated as 530.8 eV for RIXS measurements due to the systematic energy difference in various beamlines (BL27SU for XAS and BL07LSU for RIXS).

Comprehensively considering the aforementioned XAS results, the charge-compensation processes could be concluded as follows. Upon initial charging, O species was the absolutely major contributor to charge compensation, accompanied with a slightly further oxidation of Cu species from a starting valency of no less than +2 to higher value. However, upon discharging, O redox was partially irreversible and did not contribute as much as it has done upon charging. Instead, Cu species were further reduced to +1 state, indicating an increased contribution from Cu species compared with that upon initial charging. This charge-compensation patterns were repeated in following cycle, leading to a different charging behavior compared with that of initial charging. The XAS results upon second charging process strongly supported our analyses, as shown in **Figure 6.8**.

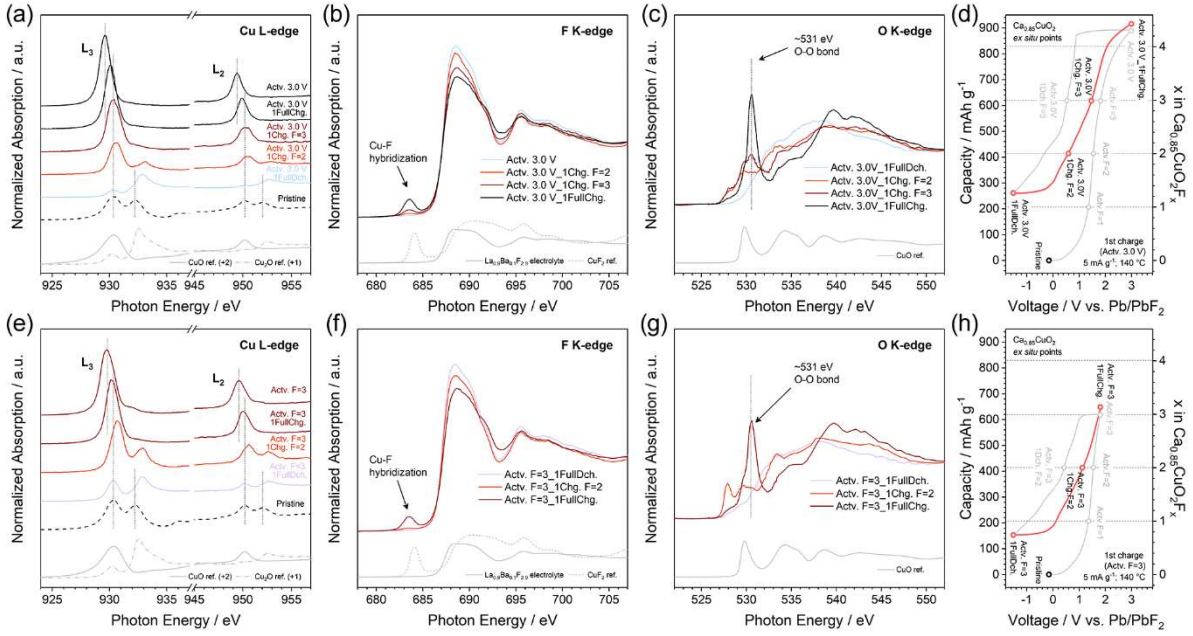

Figure 6.8 Ex situ (a, e) Cu L-edge, (b, d) F K-edge and (c, g) O K-edge XAS results of $Ca_{0.85}CuO_2$ upon 1st charging process in the cases of activated to (d) Actv. 3.0 V and (h) Actv. F=3 states.

6.4 Conclusion

Reversible (de)fluorinations were achieved in $Ca_{0.85}CuO_2$ cathode material for all-solid-state fluoride-ion batteries. A capacity of ~890 mAh g^{-1} (~4.3 F^- intercalation) was delivered in an initial activation process, utilizing anionic redox as main contributor to charge compensation. In following cycles, a reversible capacity of ~630 mAh g^{-1} (~3.1 F^- intercalation) was maintained with varied contribution ratios from cationic and anionic redox. By XAS results, the charge-compensation mechanisms were investigated in detail, accompanied with confirming the oxidation state of O redox through RIXS results.

Reference

1. Armand, M.; Tarascon, J. M., Building better batteries. *Nature* **2008,** *451* (7179), 652-657.

2. Grey, C.; Tarascon, J., Sustainability and in situ monitoring in battery development. *Nat. Mater.* **2017,** *16* (1), 45-56.

3. Chu, S.; Cui, Y.; Liu, N., The path towards sustainable energy. *Nat. Mater.* **2017,** *16* (1), 16-22.

4. Zhang, D.; Yamamoto, K.; Wang, Y.; Gao, S.; Uchiyama, T.; Watanabe, T.; Takami, T.; Matsunaga, T.; Nakanishi, K.; Miki, H.; Iba, H.; Amezawa, K.; Maeda, K.; Kageyama, H.; Uchimoto, Y., Reversible and Fast (De)fluorination of High-Capacity Cu_2O Cathode: One Step Toward Practically Applicable All-Solid-State Fluoride-Ion Battery. *Adv. Energy Mater.* **2021**, 2102285.

5. Zhang, D.; Yamamoto, K.; Ochi, A.; Wang, Y.; Yoshinari, T.; Nakanishi, K.; Nakano, H.; Miki, H.; Nakanishi, S.; Iba, H.; Uchiyama, T.; Watanabe, T.; Amezawa, K.; Uchimoto, Y., Understanding the reaction mechanism and performances of 3d transition metal cathodes for all-solid-state fluoride ion batteries. *J. Mater. Chem. A* **2021,** *9* (1), 406-412.

6. Anji Reddy, M.; Fichtner, M., Batteries based on fluoride shuttle. *J. Mater. Chem.* **2011,** *21* (43), 17059-17062.

7. Xiao, A. W.; Galatolo, G.; Pasta, M., The case for fluoride-ion batteries. *Joule* **2021**.

8. Thieu, D. T.; Fawey, M. H.; Bhatia, H.; Diemant, T.; Chakravadhanula, V. S. K.; Behm, R. J.; Kübel, C.; Fichtner, M., CuF_2 as Reversible Cathode for Fluoride Ion Batteries. *Adv. Funct. Mater.* **2017,** *27* (31), 1701051.

9. Yoshinari, T.; Zhang, D.; Yamamoto, K.; Kitaguchi, Y.; Ochi, A.; Nakanishi, K.; Miki, H.; Nakanishi, S.; Iba, H.; Uchiyama, T.; Watanabe, T.; Matsunaga, T.; Amezawa, K.; Uchimoto, Y., Kinetic analysis and alloy designs for metal/metal fluorides toward high rate capability for all-solid-state fluoride-ion batteries. *J. Mater. Chem. A* **2021,** *9* (11), 7018-7024.

10. Zaheer, W.; Andrews, J. L.; Parija, A.; Hyler, F. P.; Jaye, C.; Weiland, C.; Yu, Y.-S.; Shapiro, D. A.; Fischer, D. A.; Guo, J.; Velázquez, J. M.; Banerjee, S., Reversible Room-Temperature Fluoride-Ion Insertion in a Tunnel-Structured Transition Metal Oxide Host. *ACS Energy Lett.* **2020,** *5* (8), 2520-2526.

11. Nowroozi, M. A.; Wissel, K.; Donzelli, M.; Hosseinpourkahvaz, N.; Plana-Ruiz, S.; Kolb, U.; Schoch, R.; Bauer, M.; Malik, A. M.; Rohrer, J.; Ivlev, S.; Kraus, F.; Clemens, O., High cycle life all-solid-state fluoride ion battery with La_2NiO_{4+d} high voltage cathode. *Commun. Mater.* **2020,** *1* (1), 27.

12. Nowroozi, M. A.; Ivlev, S.; Rohrer, J.; Clemens, O., La_2CoO_4: a new intercalation based cathode material for fluoride ion batteries with improved cycling stability. *J. Mater. Chem. A* **2018,** *6* (11), 4658-4669.

13. Nowroozi, M. A.; de Laune, B.; Clemens, O., Reversible Electrochemical Intercalation and Deintercalation of Fluoride Ions into Host Lattices with Schafarzikite-Type Structure. *ChemistryOpen* **2018,** *7* (8), 617-623.

14. Nowroozi, M. A.; Wissel, K.; Rohrer, J.; Munnangi, A. R.; Clemens, O., $LaSrMnO_4$: Reversible Electrochemical Intercalation of Fluoride Ions in the Context of Fluoride Ion Batteries. *Chem Mater* **2017,** *29* (8), 3441-3453.

15. de Laune, B. P.; Rees, G. J.; Marco, J. F.; Hah, H. Y.; Johnson, C. E.; Johnson, J. A.; Berry, F. J.; Hanna, J. V.; Greaves, C., Topotactic Fluorine Insertion into the Channels of $FeSb_2O_4$-Related Materials. *Inorg. Chem.* **2017,** *56* (16), 10078-10089.

16. Clemens, O.; Rongeat, C.; Reddy, M. A.; Giehr, A.; Fichtner, M.; Hahn, H., Electrochemical fluorination of perovskite type $BaFeO_{2.5}$. *Dalton Trans.* **2014,** *43* (42), 15771-15778.

17. Luo, K.; Roberts, M. R.; Hao, R.; Guerrini, N.; Pickup, D. M.; Liu, Y. S.; Edstrom, K.; Guo, J.; Chadwick, A. V.; Duda, L. C.; Bruce, P. G., Charge-compensation in 3*d*-transition-metal-oxide intercalation cathodes through the generation of localized electron holes on oxygen. *Nat. Chem.* **2016,** *8* (7), 684-91.

18. Yabuuchi, N.; Nakayama, M.; Takeuchi, M.; Komaba, S.; Hashimoto, Y.; Mukai, T.; Shiiba, H.; Sato, K.; Kobayashi, Y.; Nakao, A.; Yonemura, M.; Yamanaka, K.; Mitsuhara, K.; Ohta, T., Origin of stabilization and destabilization in solid-state redox reaction of oxide ions for lithium-ion batteries. *Nat. Commun.* **2016,** *7*, 13814.

19. House, R. A.; Maitra, U.; Perez-Osorio, M. A.; Lozano, J. G.; Jin, L.; Somerville, J. W.; Duda, L. C.; Nag, A.; Walters, A.; Zhou, K. J.; Roberts, M. R.; Bruce, P. G., Superstructure control of first-cycle voltage hysteresis in oxygen-redox cathodes. *Nature* **2020,** *577* (7791), 502-508.

20. House, R. A.; Rees, G. J.; Pérez-Osorio, M. A.; Marie, J.-J.; Boivin, E.; Robertson, A. W.; Nag, A.; Garcia-Fernandez, M.; Zhou, K.-J.; Bruce, P. G., First-cycle voltage hysteresis in Li-rich 3*d* cathodes associated with molecular O_2 trapped in the bulk. *Nat. Energy* **2020,** *5* (10), 777-785.

21. Ji, H.; Wu, J.; Cai, Z.; Liu, J.; Kwon, D.-H.; Kim, H.; Urban, A.; Papp, J. K.; Foley, E.; Tian, Y.; Balasubramanian, M.; Kim, H.; Clément, R. J.; McCloskey, B. D.; Yang, W.; Ceder, G., Ultrahigh power and energy density in partially ordered lithium-ion cathode materials. *Nat. Energy* **2020,** *5* (3), 213-221.

22. Momma, K.; Izumi, F., VESTA 3 for three-dimensional visualization of crystal, volumetric and morphology data. *J. Appl. Cryst.* **2011,** *44* (6), 1272-1276.

23. Harada, Y.; Kobayashi, M.; Niwa, H.; Senba, Y.; Ohashi, H.; Tokushima, T.; Horikawa, Y.; Shin, S.; Oshima, M., Ultrahigh resolution soft X-ray emission spectrometer at BL07LSU in SPring-8. *Rev. Sci. Instrum.* **2012,** *83* (1), 013116.

24. Isobe, M.; Kimoto, K.; Takayama-Muromachi, E., Modulated Crystal Structure and Spin/Hole Arrangement in the Chain Compound Ca_xCuO_2 (x = 0.8240). *J. Phys. Soc. Japan* **2002,** *71* (3), 782-789.

25. Milat, O.; Van Tendeloo, G.; Amelinckx, S.; Babu, T. G. N.; Greaves, C., Structural variants of $Ca_{0.85}CuO_2$ ($Ca_{5+x}Cu_6O_{12}$). *J. Solid State Chem.* **1992,** *101* (1), 92-114.

26. Lombardi, A.; Mali, M.; Roos, J.; Brinkmann, D.; Mangelschots, I. I., Temperature dependence of the sublattice magnetization of the antiferromagnet $Ca_{0.85}Sr_{0.15}CuO_2$. *Phys. Rev. B Condens. Matter* **1996,** *54* (1), 93-96.

27. Kikkawa, S.; Er, G.; Kato, N.; Kanamaru, F., Superconductivity in the Infinite-layered $Sr_{1-x}La_xCuO_2$ and Preparation of $CaCuO_2$ by Sol-gel Method. *J. Jpn. Soc. Powder Powder Metall.* **1993,** *40* (2), 175-178.

28. Siegrist, T.; Zahurak, S. M.; Murphy, D. W.; Roth, R. S., The parent structure of the layered high-temperature superconductors. *Nature* **1988,** *334* (6179), 231-232.

29. Colonna, S.; Arciprete, F.; Balzarotti, A.; Balestrino, G.; Medaglia, P. G.; Petrocelli, G., EXAFS study of the $[BaCuO_2]_2/[(Ca,Sr)CuO_2]_n$ artificial superconducting superlattices. *Phys. C: Supercond.* **2000,** *334* (1-2), 64-76.

30. Gaur, A.; Shrivastava, B. D., A Comparative Study of the Methods of Speciation Using X-ray Absorption Fine Structure. *Acta Phys. Pol. A* **2012,** *121* (3), 647-652.

31. Kau, L. S.; Spirasolomon, D. J.; Pennerhahn, J. E.; Hodgson, K. O.; Solomon, E. I., X-Ray Absorption-Edge Determination of the Oxidation-State and Coordination-Number of Copper - Application to the Type-3 Site in Rhus-Vernicifera Laccase and Its Reaction with Oxygen. *J. Am. Chem. Soc.* **1987,** *109* (21), 6433-6442.

32. Dong, C. L.; Mattesini, M.; Augustsson, A.; Wen, X. G.; Zhang, W. X.; Yang, S. H.; Persson, C.; Ahuja, R.; Lüning, J.; Chang, C. L.; Guo, J. H., Electronic structure and surface structure of Cu_2S nanorods from polarization dependent X-ray absorption spectroscopy. *J. Electron Spectrosc. Relat. Phenom.* **2006,** *151* (1), 64-70.

33. Aruta, C.; Ghiringhelli, G.; Dallera, C.; Fracassi, F.; Medaglia, P. G.; Tebano, A.; Brookes, N. B.; Braicovich, L.; Balestrino, G., Hole redistribution across interfaces in superconducting cuprate superlattices. *Phys. Rev. B* **2008,** *78* (20).

34. Zhang, F. C.; Rice, T. M., Effective Hamiltonian for the superconducting Cu oxides. *Phys. Rev. B Condens. Matter* **1988,** *37* (7), 3759-3761.

35. Flipse, C. F.; van der Laan, G.; Johnson, A. L.; Kadowaki, K., Soft-x-ray absorption spectroscopy of electron-doped $(Nd,Sm)_{2-x}Ce_xCuO_{4-\delta}$ compounds. *Phys. Rev. B Condens. Matter* **1990,** *42* (4), 1997-2002.

36. Bianconi, A.; Castellano, A. C.; De Santis, M.; Rudolf, P.; Lagarde, P.; Flank, A. M.; Marcelli, A., $L_{2,3}$ xanes of the high T_c superconductor $YBa_2Cu_3O_{\sim 7}$ with variable oxygen content. *Solid State Commun.* **1987,** *63* (11), 1009-1013.

37. Huang, M. J.; Deng, G.; Chin, Y. Y.; Hu, Z.; Cheng, J. G.; Chou, F. C.; Conder, K.; Zhou, J. S.; Pi, T. W.; Goodenough, J. B.; Lin, H. J.; Chen, C. T., Determination of hole distribution in $Sr_{14-x}Ca_xCu_{24}O_{41}$ using soft x-ray absorption spectroscopy at the Cu L_3 edge. *Phys. Rev. B* **2013,** *88* (1), 014520.

38. Grioni, M.; Goedkoop, J. B.; Schoorl, R.; de Groot, F. M.; Fuggle, J. C.; Schafers, F.; Koch, E. E.; Rossi, G.; Esteva, J.; Karnatak, R. C., Studies of copper

valence states with Cu L_3 x-ray-absorption spectroscopy. *Phys. Rev. B Condens. Matter* **1989,** *39* (3), 1541-1545.

39. Carniato, S.; Luo, Y.; Ågren, H., Theoretical study of the near-edge Cu *L* x-ray absorption spectrum of copper phthalocyanine. *Phys. Rev. B* **2001,** *63* (8).

40. George, S. J.; Lowery, M. D.; Solomon, E. I.; Cramer, S. P., Copper L-edge spectral studies: a direct experimental probe of the ground-state covalency in the blue copper site in plastocyanin. *J. Am. Chem. Soc.* **2002,** *115* (7), 2968-2969.

41. Fioretti, A. N.; Schwartz, C. P.; Vinson, J.; Nordlund, D.; Prendergast, D.; Tamboli, A. C.; Caskey, C. M.; Tuomisto, F.; Linez, F.; Christensen, S. T.; Toberer, E. S.; Lany, S.; Zakutayev, A., Understanding and Control of Bipolar Self-Doping in Copper Nitride. *J. Appl. Phys.* **2016,** *119* (18), 181508.

42. Nakai, S.; Kawata, A.; Ohashi, M.; Kitamura, M.; Sugiura, C.; Mitsuishi, T.; Maezawa, H., Core-exciton absorption in the F K absorption spectra of 3d transition-metal fluorides. *Phys. Rev. B Condens. Matter* **1988,** *37* (18), 10895-10897.

43. Hu, Z.; Kaindl, G.; Warda, S. A.; Reinen, D.; de Groot, F. M. F.; Müller, B. G., On the electronic structure of Cu(III) and Ni(III) in $La_2Li_{1/2}Cu_{1/2}O_4$, $Nd_2Li_{1/2}Ni_{1/2}O_4$, and Cs_2KCuF_6. *Chem. Phys.* **1998,** *232* (1-2), 63-74.

44. Hu, Z.; Drechsler, S. L.; Málek, J.; Rosner, H.; Neudert, R.; Knupfer, M.; Golden, M. S.; Fink, J.; Karpinski, J.; Kaindl, G.; Hellwig, C.; Jung, C., Doped holes in edge-shared CuO_2 chains and the dynamic spectral weight transfer in X-ray absorption spectroscopy. *Europhys. Lett.* **2002,** *59* (1), 135-141.

45. Hennies, F.; Pietzsch, A.; Berglund, M.; Fohlisch, A.; Schmitt, T.; Strocov, V.; Karlsson, H. O.; Andersson, J.; Rubensson, J. E., Resonant inelastic scattering spectra of free molecules with vibrational resolution. *Phys. Rev. Lett.* **2010,** *104* (19), 193002.

Chapter 7 Rate-determining Process at Electrode /electrolyte Interfaces of All-solid-state Fluoride-ion Batteries

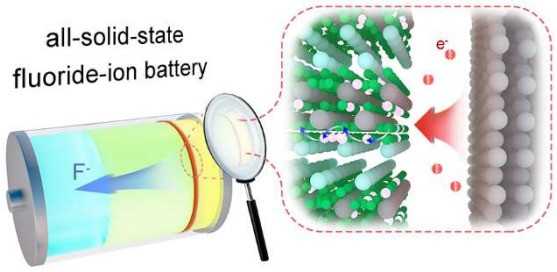

Developing high-performance solid electrolytes that are operable at room temperature is one of the toughest challenges related to all-solid-state fluoride-ion batteries (FIBs). In this study, tetragonal β-$Pb_{0.78}Sn_{1.22}F_4$, a promising solid electrolyte material for mild-temperature applications, was modified through annealing under various atmospheres using thin-film models. The annealed samples exhibited preferential growth and enhanced ionic conductivities. The rate-determining factor for electrode/electrolyte interface reactions in all-solid-state FIBs was also investigated by comparing β-$Pb_{0.78}Sn_{1.22}F_4$ with representative fluoride-ion- and lithium-ion-conductive materials, namely LaF_3, CeF_3, and $Li_7La_3Zr_2O_{12}$. The overall rate constant of the interfacial reaction, k^0, which included both mass and charge transfers, was determined using chronoamperometric measurements and Allen-Hickling simulations. Arrhenius-type correlations between k^0 and temperature indicated that activation energies calculated from k^0 and ionic conductivities (σ_{ion}) were highly consistent. The results indicated that the mass transfer (electrolyte-side fluoride-ion conduction) should be the rate-determining process at the electrode/electrolyte interface. β-$Pb_{0.78}Sn_{1.22}F_4$, with a large σ_{ion} value, had a larger k^0 value than that of $Li_7La_3Zr_2O_{12}$. Therefore, it is hoped that the development of high-conductivity solid electrolytes can lead to all-solid-state FIBs with superior rate capabilities similar to those of all-solid-state Li-ion batteries.

7.1 Introduction

Recently, battery systems that utilize multielectron transfer reactions have been demanded for the development of portable devices and hybrid electric vehicles owing to the unsatisfactory energy/power densities of widely applied lithium-ion batteries (LIBs). [1–3] However, the multivalent charge carriers of some new battery concepts, for example, Zn^{2+}, Mg^{2+}, and Al^{3+}, undergo much stronger Coulombic interactions than monovalent Li ions do; consequently, ion mobility is inferior, leading to lower overall battery power. [4–12] Recently, fluoride-ion batteries (FIBs) employing monovalent fluoride anions as charge carriers have been reported frequently; in these batteries, F^- is shuttled back and forth due to multielectron transfer reactions, such as two-phase transitions between metals and metal fluorides. [13–15] Meanwhile, some tysonite-type, fluorite-type, and PbF_2-based compounds and their derivatives, such as $La_{1-x}Ba_xF_{3-x}$, $Pb_{2-x}Sn_xF_4$, and $BaSnF_4$, are known as fast F-ion conductors with relatively high ionic conductivities. [13,16–25] Aqueous fluoride-ion batteries that exhibit ultrahigh fluoride-ion conductivity (~10^{-2} to 10^{-1} S cm^{-1}) have also been fabricated in a latest report, for which the future development is highly expected. [26] However, in current stage, it is greatly challengeable to achieve high energy density in aqueous systems compared with all-solid-state systems due to problems such as dissolution of active materials, narrow electrochemical windows, etc. Therefore, all-solid-state FIBs have been regarded as promising alternatives with high energy/power densities and favorable battery kinetics.

In our previous study,[14,27-28] we demonstrated that the 3d-transition-metal cathode (Cu, Co and Ni) and self-generated La/LaF_3 anode in thin-film all-solid-state FIBs show clear charge–discharge behavior. The combinations of Cu, Co and Ni cathodes and representative anodes (La/LaF_3, Ce/CeF_2, Pb/PbF_2, etc.) possess high energy density in theory as listed in **Table 7.1**, and the practical thin-film cells delivered high capacities that were almost equal to the theoretical values at 150 °C. However, the reversible capacity at 25 °C was less than half the value at 150 °C, and the polarization became exceedingly large.[14] For practical applications, the operation temperature of all-solid-state FIBs must be lowered; thus, the development of electrolytes with smooth ion conduction is very important, and this requires a better understanding of the rate-determining factor for the interactions between the electrode and electrolyte.

Among the many solid electrolytes for FIBs, tetragonal β-$Pb_{2-x}Sn_xF_4$ compounds have attracted much attention because of their ultrahigh ionic conductivities at room temperature;

Table 7.1. Theoretical energy densities of representative cathode-anode combinations[14,27-28]

Electrode Potential vs. Pb/PbF_2		Cell voltage (V)	Capacity (cathode based, mAh g^{-1})	Energy density	
Cathode (V)	Anode (V)			Gravimetric (Wh kg^{-1})	Volumetric (Wh L^{-1})
Cu/CuF_2 (0.65)	La/LaF_3 (-2.41)	3.06	843.5	2581	23127
Cu/CuF_2 (0.65)	Ce/CeF_3 (-2.37)	3.02	843.5	2547	22824
Co/CoF_3 (0.64)	La/LaF_3 (-2.41)	3.05	1364.4	4161	37037
Co/CoF_3 (0.64)	Ce/CeF_3 (-2.37)	3.01	1364.4	4106	36551
Ni/NiF_2 (0.07)	La/LaF_3 (-2.41)	2.47	913.3	2256	20082
Ni/NiF_2 (0.07)	Ce/CeF_3 (-2.37)	2.44	913.3	2229	19838

they exhibit the highest ionic conductivities (~2.2×10^{-3} S cm^{-1}) at 25 °C, which are comparable to those of Li-ion solid electrolytes. [22,23] The high conductivities of $Pb_{2-x}Sn_xF_4$ materials even at room temperature are decided by its special crystal structure, in which there is a large number of distortions created by the stereo-activity of the $Sn^{(II)}$ lone pairs, consequently many disorders and defects at F anion sites. These disorders and defects are believed to be the major contributors to the mass transfer in $Pb_{2-x}Sn_xF_4$ bulks. [22,29-31] However, strict kinetic analysis of the electrode/electrolyte interface using common bulk-type cells is difficult because the addition of electrolyte into electrode powders, which is necessary for a bulk-type all-solid-state cell, leads to complex interfacial conditions, constraining quantitative studies.

In this study, we designed effective thin-film models to determine the rate-determining processes for the reactions at the interface between metal electrodes and solid electrolytes. A tetragonal β-$Pb_{0.78}Sn_{1.22}F_4$ thin film was prepared using pulsed laser deposition (PLD) and employed as a fluoride-ion solid electrolyte. Proper annealing treatments were conducted to tailor the crystallographic orientations of the as-deposited thin films, leading to reliable ionic conductivities and activation energies for further analysis. In addition to β-$Pb_{0.78}Sn_{1.22}F_4$, three typical solid electrolytes for FIBs and LIBs, namely LaF_3, CeF_3, and $Li_7La_3Zr_2O_{12}$, were also assessed using the optimized Butler-Volmer equation,[32] which revealed the relationship between mass transfer and overall interfacial processes. To the best of our knowledge, this paper reports the first quantitative treatment of the interfacial reaction kinetics in all-solid-state FIBs.

7.2 Experimental

7.2.1 Thin-film models & electrode deposition

Based on the various physicochemical characteristics and origins of solid electrolytes, four types of thin-film models were utilized in this study. Single-crystal LaF_3 and CeF_3 substrates and mirror-polished $Li_7La_3Zr_2O_{12}$ (LLZO) substrates were purchased and used without further treatment, and β-$Pb_{0.78}Sn_{1.22}F_4$ thin films were deposited on quartz substrates via PLD (Lotis Tii LS-2137, Belarus) using a homemade $Pb_{0.78}Sn_{1.22}F_4$ target. For the commercial LaF_3, CeF_3, and LLZO substrates, three-electrode (**Figure 7.1**a) or two-electrode (Figure 7.1b) models were employed. For β-$Pb_{0.78}Sn_{1.22}F_4$ thin films, a homemade three-electrode model (Figure 7.1c) with a β-$Pb_{0.78}Sn_{1.22}F_4$ thickness of 4.68 μm was utilized for chronoamperometric measurements. Commercial interdigitated array (IDA, Figure 7.1d) microelectrodes with 69 intervals and a β-$Pb_{0.78}Sn_{1.22}F_4$ thickness of 400 nm were utilized for alternating current (AC) impedance measurements. Counter electrodes (CEs), reference electrodes (REs), and current collectors were prepared by depositing all necessary metals onto solid electrolytes using radio-frequency magnetron sputtering (Eiko, Japan). Li thin films were deposited using vacuum evaporation. The thickness and size of each metal are given in Figure 7.1 and **Table 7.2**.

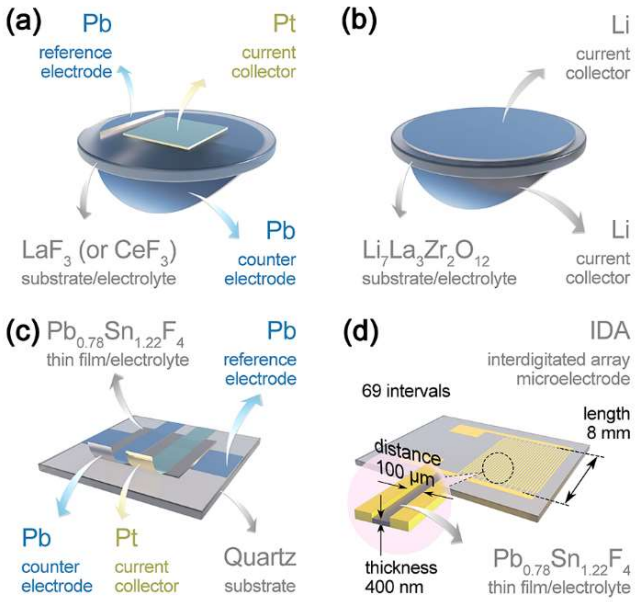

Figure 7.1 Schematic illustrations of (a) three-electrode model for LaF_3 and CeF_3, (b) two-electrode model for LLZO, (c) three-electrode model for chronoamperometric measurements of β-$Pb_{0.78}Sn_{1.22}F_4$ and (d) IDA microelectrodes for AC impedance measurements of β-$Pb_{0.78}Sn_{1.22}F_4$.

Table 7.2 Parameters of various metal thin films

Thin film	Size	
	Cell in Figure 1(a)	Cell in Figure 1(c)
Pt current collector	5 mm × 5 mm × 50 nm	15 mm × 2 mm × 50 nm
Pb reference electrode	1 μm (thickness)	15 mm × 2 mm × 200 nm
Pb counter electrode	Φ 12 mm × 1 μm	15 mm × 6 mm × 200 nm
$Pb_{0.78}Sn_{1.22}F_4$	–	8 mm × 8 mm × 4.68 μm

RF Sputtering parameters (for Pt, Pb): Power 50 W; atmosphere Ar 1.0 Pa; temperature 25 ˚C.

7.2.2 Preparation of *β*-$Pb_{0.78}Sn_{1.22}F_4$

Stoichiometric amounts of PbF_2 and SnF_2 (99.9%, Kojundo, Japan) were weighed and mixed using an agate pestle and mortar; the selection of this composition ($Pb_{0.78}Sn_{1.22}F_4$) will be explained in the *Results and Discussion* section. The mixtures were pre-pelletized and processed by cold isostatic pressing (CIP, Sansho Industry CPA-50, Japan) under a pressure of 200 MPa for 5 min. The CIP-processed pellets were used as PLD targets without other treatments. A Q-switch Nd^{3+}:YAG 4ω laser beam (λ = 266 nm) with a pulse energy of 20 mJ and a laser frequency of 10 Hz was applied. The base atmosphere during PLD was either 10^{-4} Pa Ar or 10^{-2} Pa NF_3. After the desired thickness (4.68 μm) was attained, some *β*-$Pb_{0.78}Sn_{1.22}F_4$ samples underwent further annealing at 110 °C under various atmospheres, namely 10^5 Pa Ar, 10^{-2} Pa NF_3, and 10 Pa NF_3, to adjust the crystallographic preferential growth.

7.2.3 Cell fabrication

For the three-electrode models, the working electrode (WE) was constructed using an *in situ* generation method. After the WE and CE were connected, a constant current flow was applied at 150 °C, leading to the reduction of the metal fluoride near the WE-side current collector (Pt, as shown in **Figure 7.2**) to the metal, and the CE-side Pb thin film was partially fluorinated to afford Pb/PbF_2. As a result, the cell remained in an intermediate state of charge (SoC), which was beneficial for an accurate evaluation of the kinetics because the large nucleation barriers at the initial stage (0% or 100% SoC) have already been overcome. Therefore, reliable electrode/electrolyte interfaces were successfully established *in situ*. Similarly, the RE-side Pb thin film was also partially fluorinated through an *in situ*

electrochemical method; thus, equilibrium-state Pb/PbF_2, which has been proven to offer stable reference potentials, was employed as a practical RE.[14]

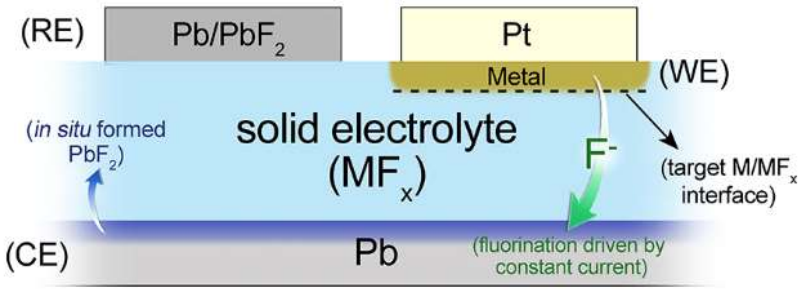

Figure 7.2 Schematic illustrations of in situ generation of M/MF_x interface due to constant current.

7.2.4 Characterizations & Electrochemical measurement

X-ray diffraction (XRD) was conducted using an X-ray diffractometer (Rigaku Ultima IV) using Cu-Kα radiation (λ = 1.54056 Å). The cross-sectional morphologies of the β-$Pb_{0.78}Sn_{1.22}F_4$ thin films were examined using scanning electron microscopy (SEM, SU-6600, Hitachi) with an acceleration voltage of 1.0 kV, as shown in **Figure 7.3**.

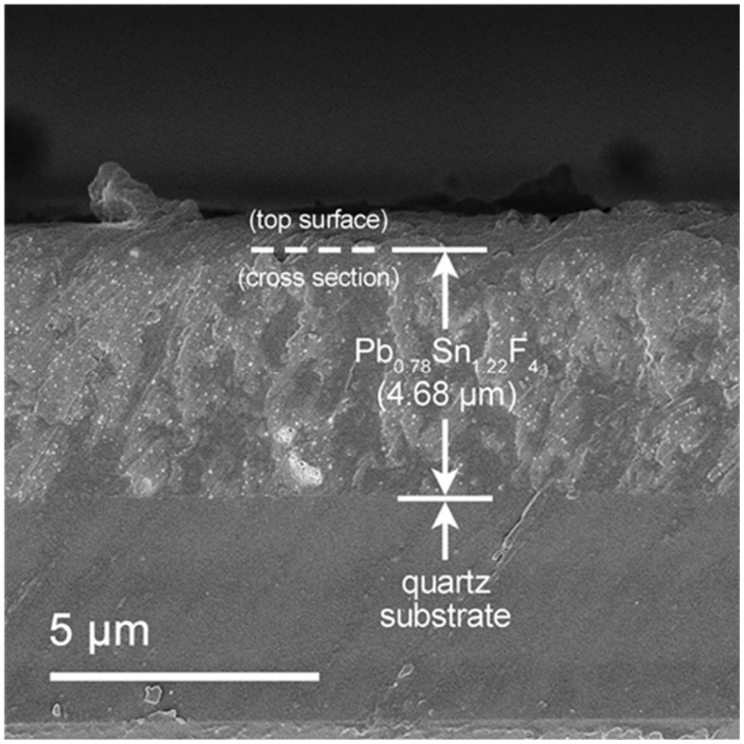

Figure 7.3 Cross-sectional SEM image of as-deposited $Pb_{0.78}Sn_{1.22}F_4$ thin film in the model of Figure 7.1c.

Constant currents were applied using a battery testing system (PARSTAT MC2000, Princeton Applied Research, USA) for SoC adjustments, RE pre-fluorination rendering, and

chronoamperometric measurements of the exchange current densities. Ionic conductivities were determined via electrochemical impedance spectroscopy (EIS) using an electrochemical workstation (Modulab XM-ECS, Solartron Analytical, UK) with a frequency range of 10^6 to 10^{-1} Hz and an amplitude voltage of 20 mV at various temperatures. The activation energies were calculated using the Arrhenius equation. The exchange current density patterns were recorded under different potentials vs. Pb/PbF_2 using chronoamperometric measurements.

7.3 Results and discussion

7.3.1 Phase and ionic conductivity of β-$Pb_{0.78}Sn_{1.22}F_4$

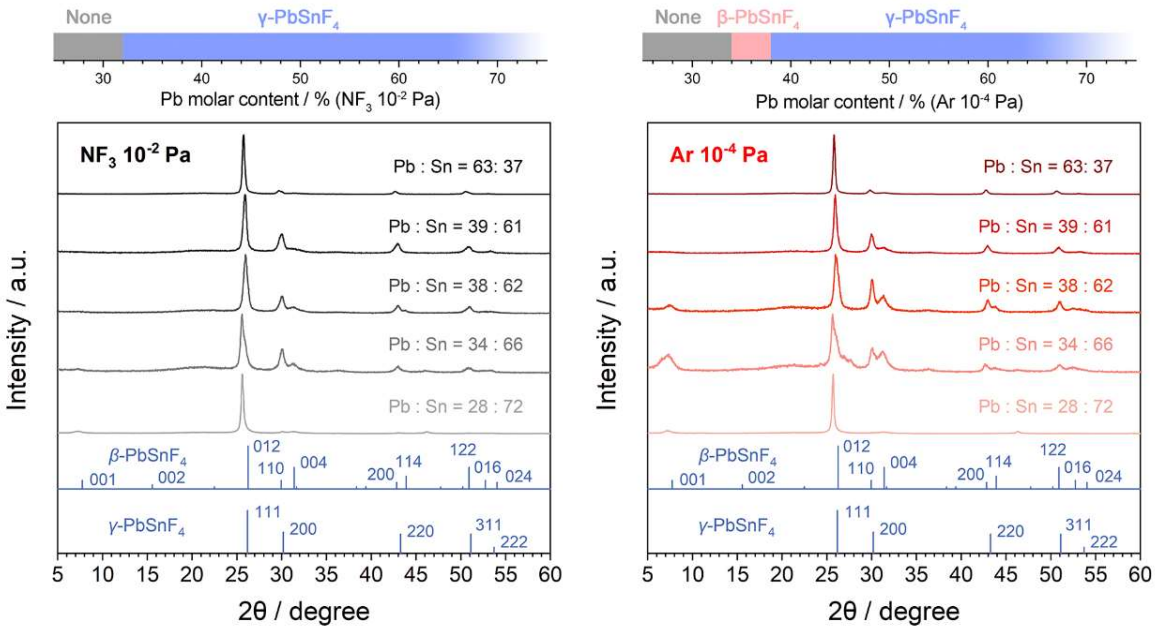

Figure 7.4 XRD patterns of $Pb_{2-x}Sn_xF_4$ deposited under various compositions and base atmospheres.

$Pb_{2-x}Sn_xF_4$ with various compositions and different base atmospheres (10^{-4} Pa Ar or 10^{-2} Pa NF_3) for PLD was studied by XRD; however, the β phase was observed only under certain conditions and with certain compositions (**Figure 7.4**). A composition of $Pb_{0.78}Sn_{1.22}F_4$ and a base atmosphere of 10^{-4} Pa Ar were employed for PLD, and a tetragonal β-phase with a space group of *P4*/*nmm* was acquired, as shown in **Figure 7.5**. The relative intensities of some peaks were different from those of the theoretical pattern, which was attributed to low crystallinity, preferential growth, and an uncertain amount of F defects.

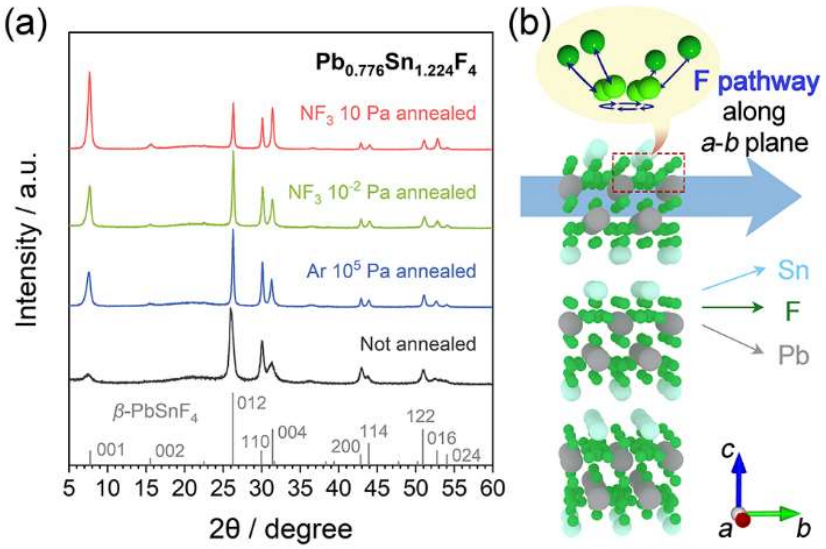

Figure 7.5 (a) XRD patterns of β-$Pb_{0.78}Sn_{1.22}F_4$ thin films obtained under various ex-post annealing atmospheres. (b) Schematic illustrations of crystal structures and possible F anion conduction pathways.

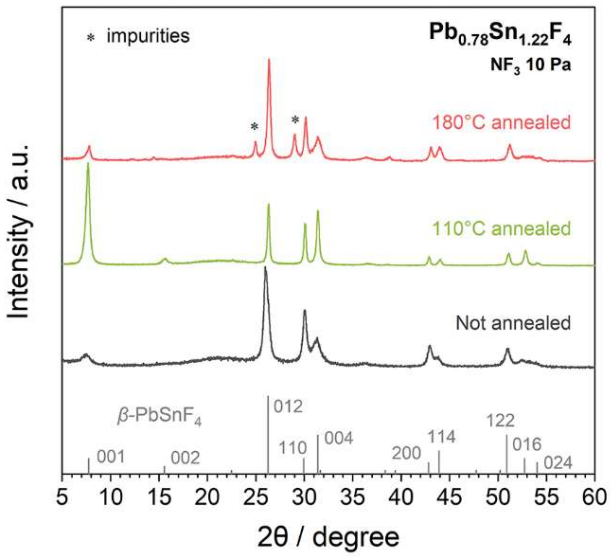

Figure 7.6 XRD of $Pb_{0.78}Sn_{1.22}F_4$ thin films obtained at various annealing temperatures (NF_3 10 Pa).

The preferential growth can be modified through proper ex-post annealing: annealing at 110 °C (higher or lower temperatures led to inferior crystallinity or undesired impurities, see **Figure 7.6**) for 12 h improved the crystallinity remarkably and changed the structural orientation. The intensity of the (001) diffraction increased significantly and was 1.6 times that of the (012) peak after annealing under a 10 Pa NF_3 atmosphere, whereas in theory, it should be only 0.2 times the intensity (**Table 7.3**). Such growth is usually indicative of a larger grain size along the *c*-axis compared to those along the *a*- and *b*-axes, which is thought to be beneficial for F-ion conduction. According to Fujisaki et al., [33] the undulate channels between Sn and Pb layers along the *a*-*b* plane of a β-structure are highly likely to be the main conduction

pathways for F anions, as illustrated in Figure 7.5b. Therefore, it is reasonable that a proper (001)-preferential orientation can lead to better conductivity compared to equiaxed grains.

Table 7.3 Comparisons of XRD peak intensity in Figure 7.5(a)

$Pb_{0.78}Sn_{1.22}F_4$ samples	Theoretical $I_{(001)}/I_{(012)}$	Practical $I_{(001)}/I_{(012)}$
Not annealed	0.2	0.16231
Ar 10^5 Pa annealed		0.41161
NF_3 10^{-2} Pa annealed		0.52113
NF_3 10 Pa annealed		1.54225

*The peak intensity was roughly compared using integrated peak area after background functioning and elimination.

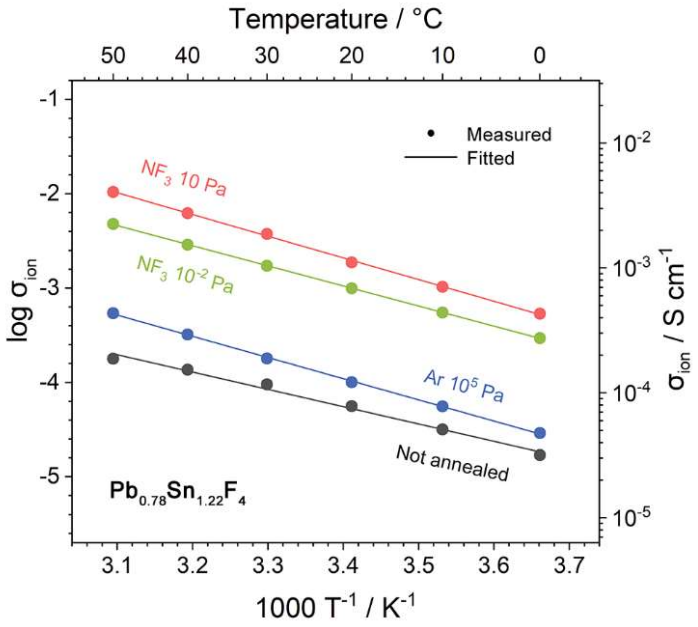

Figure 7.7 Linear fitting plots of log σ_{ion} vs. 1000 T^{-1} for β-$Pb_{0.78}Sn_{1.22}F_4$ thin films annealed under various annealing conditions, calculated from EIS results.

The ionic conductivities (σ_{ion}) of the four samples are shown in **Figure 7.7** and the Nyquist plots and equivalent circuits for curve fitting are given in **Figure 7.8**, where CPE_{gb}, CPE_b, R_{gb}, R_b, and W in the equivalent circuits represent the constant phase elements (CPE) and resistances (R) on the grain boundary (*gb*) and in bulk (*b*) and the Warburg resistance, respectively. After annealing, the ionic conductivities were clearly enhanced, and the samples with the strongest (001) diffractions, that is, the samples annealed under 10 Pa NF_3, also exhibited the highest σ_{ion} values. Therefore, the sample annealed under 10 Pa NF_3 was selected for further kinetic analysis.

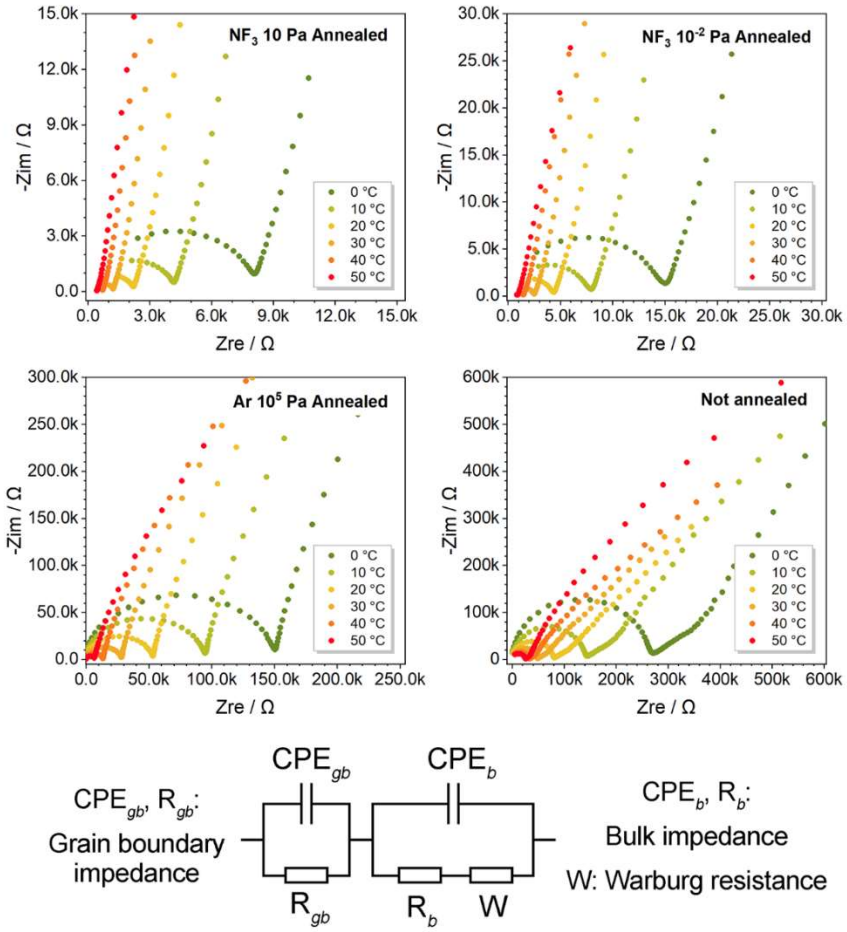

Figure 7.8 Nyquist plots of $Pb_{0.78}Sn_{1.22}F_4$ annealed by various atmospheres and equivalent circuits for fitting.

7.3.2 Analysis of interfacial reaction processes

The two main probable types of rate-determining processes at electrode/electrolyte interfaces are charge-transfer and mass-transfer processes.[34] Generally, when a charge-transfer process determines the rate of the electrode reaction, the current density, i, is related to the overpotential, η, according to the Butler-Volmer equation:[34]

$$i = -i_0 \left[exp\left(\frac{-\alpha n F \eta}{RT}\right) - exp\left(\frac{(1-\alpha) n F \eta}{RT}\right) \right] \qquad (7-1)$$

where i_0, α, n, F, R, and T are the exchange current density, transfer coefficient, number of electrons exchanged in the charge transfer reaction, Faraday constant, gas constant, and temperature, respectively. Rearrangement of Equation (7-1) gives the Allen-Hickling equation,[34]

$$ln\left[\frac{i}{1-exp(nF\eta/RT)}\right] = ln\, i_0 - \frac{\alpha n F}{RT}\eta \qquad (7-2)$$

By measuring the correlation between i and η under charge-transfer-limited conditions, i_0 (as a kinetic parameter of the electrode reaction) can be determined from the intercept of the Allen-Hickling plot, $\ln[i/(1 - e^{nF\eta/RT})]$ vs. η. Therefore, the kinetics of charge transfer reactions can be studied using the i_0 obtained from the Allen-Hickling plot. [35,36]

However, Equations (7-1) and (7-2) cannot be applied for mass-transfer-controlled processes. Mizusaki et al. derived the following modified rate equation for a heterogeneous chemical reaction that does not assume any rate-determining process: [32]

$$pA + qB \leftrightarrow p'C + q'D \qquad (7-3)$$

where p, q, p', and q' are the numbers of moles of species A, B, C, and D, respectively. The rate of Reaction (7-3), v, can be expressed as Equation (7-4):

$$v = k{a_A}^p {a_B}^q - k'{a_c}^{p'} {a_D}^{q'} \qquad (7-4)$$

where k and k' are the reaction rate constants for the forward and reverse processes of the reversible reaction, respectively, and a_X is the activity of species X (X = A, B, C, or D). According to the basic thermodynamic relationships represented by Equations (7-5) and (7-6),

$$a_X = exp\left(\frac{\mu_X - {\mu_X}^0}{RT}\right) \qquad (7-5)$$

$$\Delta G = -nFE = (p'\mu_C + q'\mu_D) - (p\mu_A + q\mu_B) \qquad (7-6)$$

v can be converted to

$$v = k^0\left[exp\left(\frac{\alpha nFE}{RT}\right) - exp\left(\frac{-(1-\alpha)nFE}{RT}\right)\right] \qquad (7-7)$$

where k^0 can be determined using Equation (7-8),

$$k^0 = k\, exp[-(n{\mu_A}^0 + m{\mu_B}^0)/RT] \qquad (7-8)$$

The value of α in Equation (7-7) composes a portion of the ΔG contribution, increasing the chemical potential of the reactants (i.e., $p\mu_A + q\mu_B$ in Equation (7-6)). The remaining portion of ΔG, that is, $(1 - \alpha)$, decreases the chemical potential of the products (i.e., $p'\mu_C + q'\mu_D$ in Equation (6)). The reaction rate in Equation (7-7), v, is proportional to the current density in Equation (1), i, according to the following relationship: [34]

$$|i| = nFv \qquad (7-9)$$

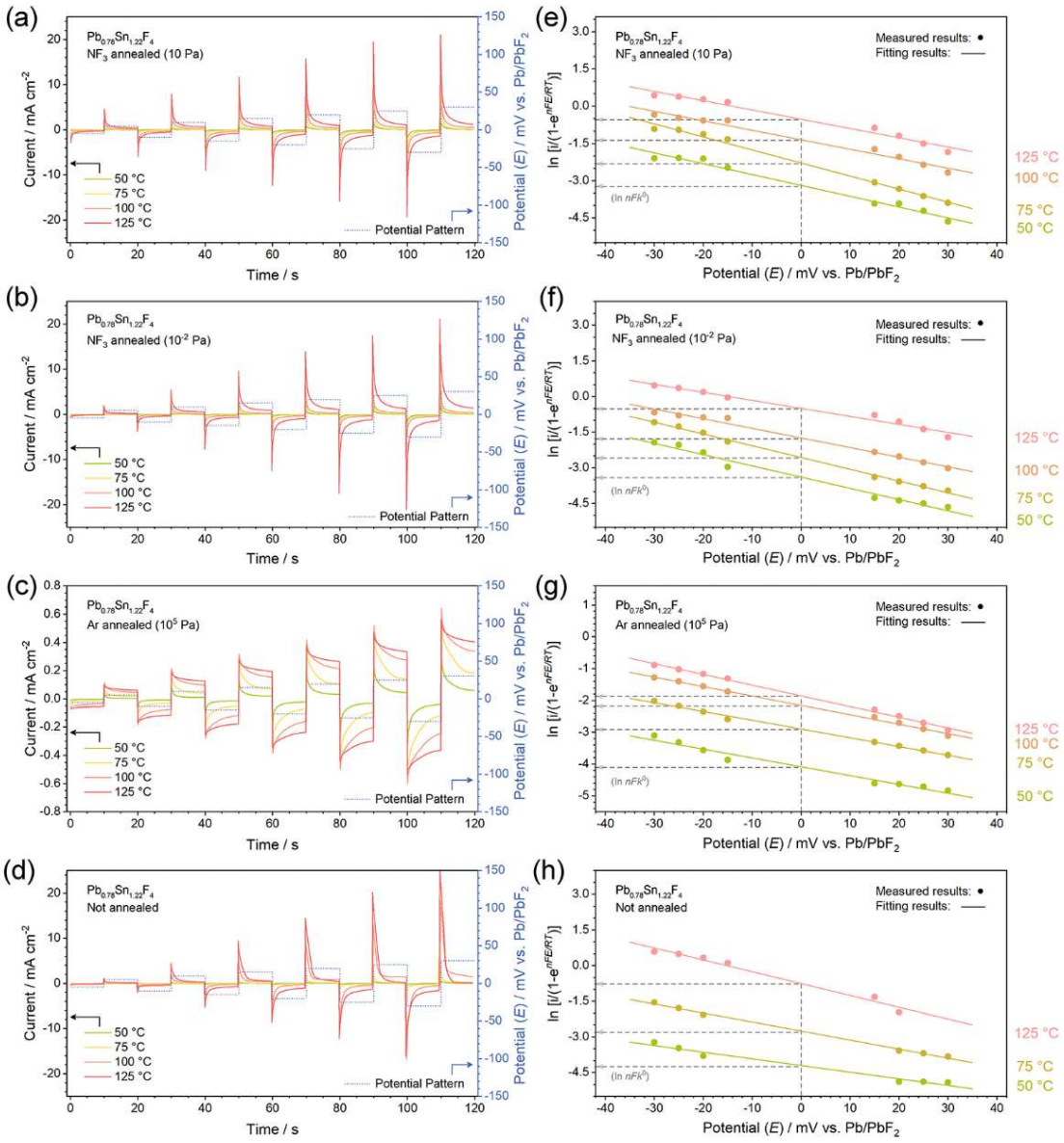

Figure 7.9 (a-d) Exchange current densities and (e-h) corresponding Allen-Hickling-type plots of β-$Pb_{0.78}Sn_{1.22}F_4$ thin films at various annealing temperatures and atmospheres.

Therefore, Equations (7-1) and (7-7) are identical. Similarly, an Allen-Hickling-type equation can be obtained by rearranging Equation (7-7), in which nFk^0 acts as a kinetic parameter, as i_0 does in Equation (7-2):

$$ln\left[\frac{i}{1-exp\left(\frac{nFE}{RT}\right)}\right] = ln\, nFk^0 - \frac{\alpha nF}{RT}E \qquad (7-10)$$

Equation (7-10) is derived from Reaction (7-3), where no rate-determining process is assumed; thus, it is valid for both charge transfer and mass transfer. The relationship between i and E in Equation (7-10) was determined using chronoamperometry, in which the current

response for each step decreased monotonically and became steady at the end. The values of the steady current were used to plot the Allen-Hickling-type relationships. The exchange current densities and corresponding Allen-Hickling-type plots are shown in **Figure 7.9**. The point at $E = 0$ of the linear fitted results on the Allen-Hickling-type plots gives the specific ln nFk^0 value at each applied temperature.

7.3.3 Rate-determining factor

The kinetic parameter nFk^0 showed Arrhenius behavior (**Figure 7.10**a) and its logarithm can be well fitted linearly against the inverse of temperature (K).[37] The activation energy (E_a) of β-$Pb_{0.78}Sn_{1.22}F_4$ annealed under 10 Pa NF_3 and those of LaF_3, CeF_3, and LLZO (Figure 7.10b), which were obtained from the fitting results of log nFk^0 vs. 1000 T^{-1} correlations, were compared. Meanwhile, the Arrhenius plots and E_a calculated using the conventional EIS method (log σ_{ion} vs. 1000 T^{-1}) are shown in Figures 7.10c and 7.10d. The E_a values obtained using the Allen-Hickling model and EIS method differed slightly but show identical changing tendencies if the four electrolytes are listed in a specific order.

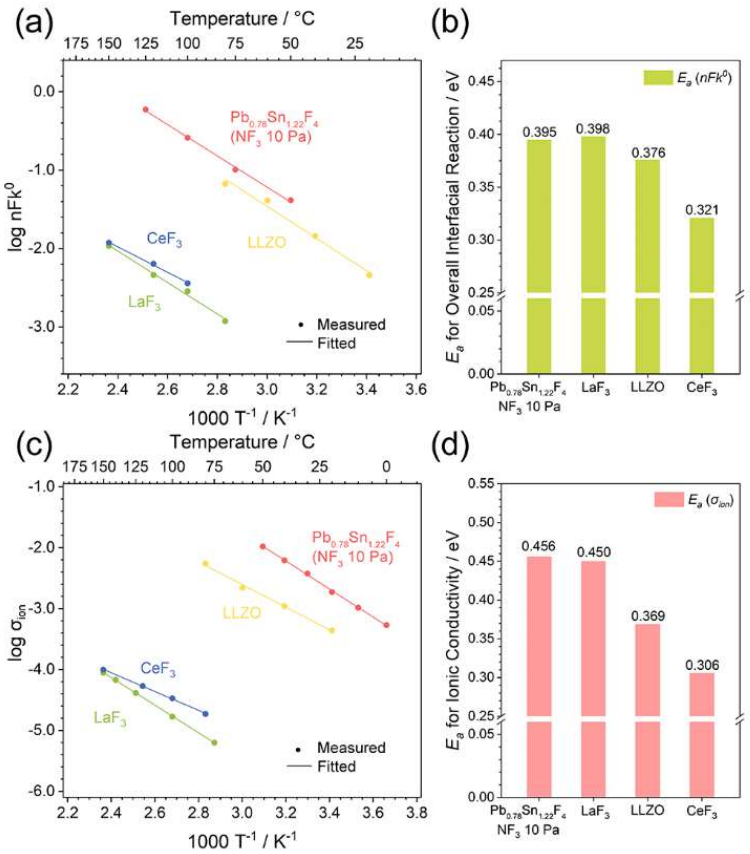

Figure 7.10 Arrhenius plots and calculated activation energies of (a,b) overall interfacial reactions and (c,d) specific contributions from ion conduction.

Here, E_a (nFk^0) and E_a (σ_{ion}) indicate the energy barriers required to overcome the entire interfacial process (overall) and a particular ion conduction process (mass transfer only), respectively. Therefore, it is highly reasonable to believe that the rates of the overall interfacial reactions are determined by electrolyte-side ion conduction. Here, Allen-Hickling model, which was usually applicable for only charge-transfer process, was utilized in interfacial reactions that involve mass transfer and correlated with the ionic conductivity. Similar tendency has been reported in many all-solid-state electrochemical devices. [38-43]

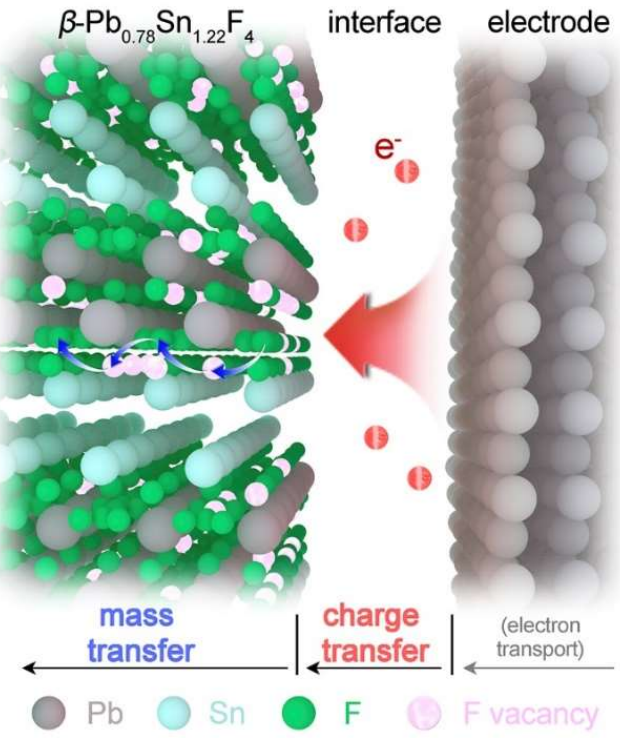

Figure 7.11 Schematic illustration of mass/charge transfer processes at an electrode/electrolyte interface. Sizes and scales here do not represent practical values.

A schematic illustration explaining the rate-determining process at the electrode/electrolyte interfaces of all-solid-state FIBs is shown in **Figure 7.11**. Electrons are transported from the current collector, via the electrode bulk, to the electrode/electrolyte interface. The passing of electrons through the interface (charge transfer) is accompanied by the transport of surficial F ions toward the opposite direction through F vacancies in the electrolyte lattices (mass transfer); these two processes are mutually dependent because of charge compensation. The inferior ion conduction process is dominant and is the major contributor to the interfacial reactions; therefore, the E_a values of ionic conduction and the overall reactions were similar and exhibited identical tendencies.

7.3.4 Discussion

As is mentioned above, the rates of electrode reactions for other solid-state battery systems, such as all-solid-state LIBs, [38,39] solid oxide fuel cells, [40–42] and Ag|AgSi|I_2-type cells, [43] have also been reported to be limited by ion conduction. A comparison of ionic conductivities (σ_{ion}) and kinetic parameters (nFk^0), shown in Figure 6, reveal a clear linear correlation, showing similar tendencies to those in the study of Uchida et al.[40] That is, if ion transport from/to the active sites was the rate-determining step, there would be a linear correlation between the exchange current density and the bulk ionic conductivity.

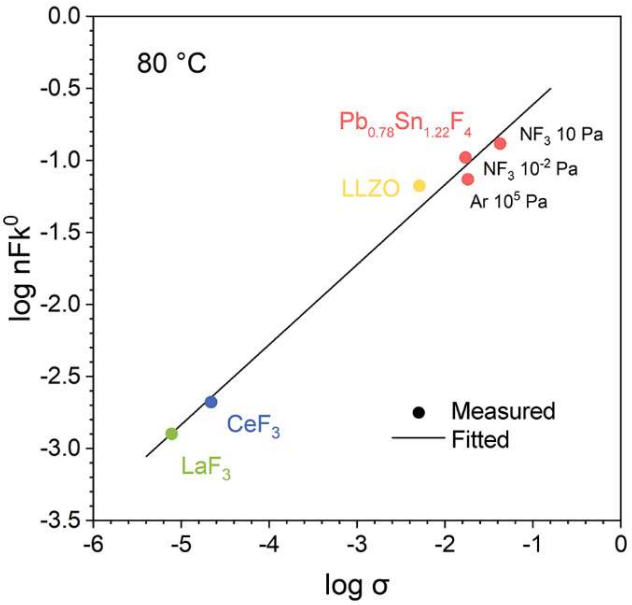

Figure 7.12 Correlations and linear fittings between ionic conductivity and kinetic parameters.

Since LaF_3, CeF_3, and LLZO are representative fluoride-ion and lithium-ion solid electrolytes, the comparison results in **Figure 7.12** prove the universality of the conclusion of this work. Therefore, it is believed that high rate capabilities can be achieved in all-solid-state FIBs, as in LIBs, if solid electrolytes with high ionic conductivities are employed. Consequently, the improvement in the ionic conductivity of the solid electrolyte was considered to play a crucial role in decreasing the operating temperature and increasing the power of all-solid-state FIBs.

7.4 Conclusion

In this study, tetragonal β-$Pb_{0.78}Sn_{1.22}F_4$ thin films were prepared using PLD and evaluated as fast fluoride-ion conductors. Proper annealing was conducted to tune the

preferential growth, optimizing the ionic conductivities. An Allen-Hickling-type equation reported by Mizusaki et al., which was derived from a general reaction with no assumed constraints, was utilized to analyze the interfacial reactions of β-$Pb_{0.78}Sn_{1.22}F_4$ and three representative solid fluoride-ion and lithium-ion electrolytes, namely LaF_3, CeF_3, and LLZO. The calculation results gave the overall kinetic parameters, which exhibited Arrhenius behavior. Comparison of the activation energies obtained using this Allen-Hickling-type equation (Equation 7-10) and the conventional EIS method suggested that the ionic conductivities dictate the rate-determining processes of electrode/electrolyte reactions in all-solid-state FIBs.

Reference

1. Armand, M.; Tarascon, J. M., Building Better Batteries. *Nature* **2008,** *451* (7179), 652-657.

2. Chu, S.; Cui, Y.; Liu, N., The Path towards Sustainable Energy. *Nat. Mater.* **2017,** *16* (1), 16-22.

3. Islam, M. S.; Fisher, C. A. J., Lithium and Sodium Battery Cathode Materials: Computational Insights into Voltage, Diffusion and Nanostructural Properties. *Chem. Soc. Rev.* **2014,** *43* (1), 185-204.

4. Besenhard, J. O.; Winter, M., Advances in Battery Technology: Rechargeable Magnesium Batteries and Novel Negative-Electrode Materials for Lithium Ion Batteries. *ChemPhysChem* **2002,** *3* (2), 155-159.

5. Aurbach, D.; Weissman, I.; Gofer, Y.; Levi, E., Nonaqueous Magnesium Electrochemistry and Its Application in Secondary Batteries. *Chem. Rec.* **2003,** *3* (1), 61-73.

6. Levi, E.; Gofer, Y.; Aurbach, D., On the Way to Rechargeable Mg Batteries: the Challenge of New Cathode Materials. *Chem. Mater.* **2010,** *22* (3), 860-868.

7. Muldoon, J.; Bucur, C. B.; Oliver, A. G.; Sugimoto, T.; Matsui, M.; Kim, H. S.; Allred, G. D.; Zajicek, J.; Kotani, Y., Electrolyte Roadblocks to a Magnesium Rechargeable Battery. *Energy Environ. Sci.* **2012,** *5* (3), 5941-5950.

8. Kamath, G.; Narayanan, B.; Sankaranarayanan, S. K., Atomistic Origin of Superior Performance of Ionic Liquid Electrolytes for Al-ion Batteries. *Phys. Chem. Chem. Phys.* **2014,** *16* (38), 20387-20391.

9. Wang, H. L.; Gu, S. C.; Bai, Y.; Chen, S.; Zhu, N.; Wu, C.; Wu, F., Anion-Effects on Electrochemical Properties of Ionic Liquid Electrolytes for Rechargeable Aluminum Batteries. *J. Mater. Chem. A* **2015,** *3* (45), 22677-22686.

10. Lin, M. C.; Gong, M.; Lu, B.; Wu, Y.; Wang, D. Y.; Guan, M.; Angell, M.; Chen, C.; Yang, J.; Hwang, B. J.; Dai, H., An Ultrafast Rechargeable Aluminium-Ion Battery. *Nature* **2015,** *520* (7547), 325-328.

11. Liao, M.; Wang, J.; Ye, L.; Sun, H.; Wen, Y.; Wang, C.; Sun, X.; Wang, B.; Peng, H., A Deep-cycle Aqueous Zinc-ion Battery Containing an Oxygen-deficient Vanadium Oxide Cathode. *Angew. Chem., Int. Ed.* **2020,** *59* (6), 2273-2278.

12. Zhao, S.; Han, B.; Zhang, D.; Huang, Q.; Xiao, L.; Chen, L.; Ivey, D. G.; Deng, Y.; Wei, W., Unravelling the Reaction Chemistry and Degradation Mechanism in Aqueous Zn/MnO_2 Rechargeable Batteries. *J. Mater. Chem. A* **2018,** *6* (14), 5733-5739.

13. Anji Reddy, M.; Fichtner, M., Batteries Based on Fluoride Shuttle. *J. Mater. Chem.* **2011,** *21* (43), 17059-17062.

14. Zhang, D.; Yamamoto, K.; Ochi, A.; Wang, Y.; Yoshinari, T.; Nakanishi, K.; Nakano, H.; Miki, H.; Nakanishi, S.; Iba, H.; Uchiyama, T.; Watanabe, T.; Amezawa, K.; Uchimoto, Y., Understanding the Reaction Mechanism and Performances of 3*d* Transition Metal Cathodes for All-solid-state Fluoride Ion Batteries. *J. Mater. Chem. A* **2021,** *9* (1), 406-412.

15. Thieu, D. T.; Fawey, M. H.; Bhatia, H.; Diemant, T.; Chakravadhanula, V. S. K.; Behm, R. J.; Kübel, C.; Fichtner, M., CuF_2 as Reversible Cathode for Fluoride Ion Batteries. *Adv. Funct. Mater.* **2017,** *27* (31), 1701051.

16. Gschwind, F.; Rodriguez-Garcia, G.; Sandbeck, D. J. S.; Gross, A.; Weil, M.; Fichtner, M.; Hörmann, N., Fluoride Ion Batteries: Theoretical Performance, Safety, Toxicity, and a Combinatorial Screening of New Electrodes. *J. Fluorine Chem.* **2016,** *182*, 76-90.

17. Rongeat, C.; Reddy, M. A.; Diemant, T.; Behm, R. J.; Fichtner, M., Development of New Anode Composite Materials for Fluoride Ion Batteries. *J. Mater. Chem. A* **2014,** *2* (48), 20861-20872.

18. Rongeat, C.; Reddy, M. A.; Witter, R.; Fichtner, M., Solid Electrolytes for Fluoride Ion Batteries: Ionic Conductivity in Polycrystalline Tysonite-type Fluorides. *ACS Appl. Mater. Interfaces* **2014,** *6* (3), 2103-2110.

19. Düvel, A.; Ruprecht, B.; Heitjans, P.; Wilkening, M., Mixed Alkaline-earth Effect in the Metastable Anion Conductor $Ba_{1-x}Ca_xF_2$ ($0 \leq x \leq 1$): Correlating Long-range Ion Transport with Local Structures Revealed by Ultrafast ^{19}F MAS NMR. *J. Phys. Chem. C* **2011,** *115* (48), 23784-23789.

20. Patro, L. N.; Hariharan, K., Fast Fluoride Ion Conducting Materials in Solid State Ionics: An Overview. *Solid State Ionics* **2013,** *239*, 41-49.

21. Ahmad, M. M.; Yamada, K.; Okuda, T., Conductivity Spectra and Comparative Scaling Studies of Polycrystalline $PbSnF_4$. *Solid State Ionics* **2004,** *167* (3-4), 285-292.

22. Murakami, M.; Morita, Y.; Yonemura, M.; Shimoda, K.; Mori, M.; Koyama, Y.; Kawaguchi, T.; Fukuda, K.; Ishikawa, Y.; Kamiyama, T.; Uchimoto, Y.; Ogumi, Z., High Anionic Conductive Form of $Pb_xSn_{2-x}F_4$. *Chem. Mater.* **2019,** *31* (18), 7704-7710.

23. Uno, M.; Onitsuka, M.; Ito, Y.; Yoshikado, S., Synthesis and Evaluation of $Pb_{1-x}Sn_xF_2$ by Mechanical Milling. *Solid State Ionics* **2005,** *176* (31-34), 2493-2498.

24. Karkera, G.; Reddy, M.; Fichtner, M., Recent Developments and Future Perspectives of Anionic Batteries. *J. Power Sources* **2021**, *481*, 228877.

25. Nowroozi, M.; Mohammad, I.; Molaiyan, P.; Wissel, K.; Munnangi, A.; Clemens, O., Fluoride Ion Batteries – Past, Present, and Future. *J. Mater. Chem. A* **2021**, *9* (10), 5980-6012.

26. Li, X., Tang, Y., Zhu, J., Lv, H., Xu, Y., Wang, W., Zhi, C., Li, H., Initiating a Room-Temperature Rechargeable Aqueous Fluoride-Ion Battery with Long Lifespan through a Rational Buffering Phase Design. *Adv. Energy Mater.* **2021**, *11* (14), 2003714.

27. Nakano, H., Matsunaga, T., Mori, T., Nakanishi, K., Morita, Y., Ide, K., Okazaki, K., Orikasa, Y., Minato, T., Yamamoto, K., Ogumi, Z., Uchimoto, Y., Fluoride-Ion Shuttle Battery with High Volumetric Energy Density. *Chem. Mater.* **2021**, *33* (1), 459-466.

28. Motohashi, K., Nakamura, T., Kimura, Y., Uchimoto, Y., Amezawa, K., Influence of Microstructures on Conductivity in Tysonite-Type Fluoride Ion Conductors. *Solid State Ionics* **2019**, *338*, 113-120.

29. Castiglione, M., Madden, P. A., Berastegui, P., Hull, S., The Crystal Structure of α-PbSnF4 and Its Anion Diffusion Mechanism. *J. Phys. Condens. Matter* **2005**, *17*, 845-861.

30. Liu, L., Yang, L., Liu, M., Li, X., Shao, D., Luo, K., Wang, X., Luo, Z., SnF_2-Based Fluoride Ion Electrolytes $MSnF_4$ (M = Ba, Pb) for the Application of Room-Temperature Solid-State Fluoride Ion Batteries. *J. Alloy. Compd.* **2020**, *819*, 152983.

31. Dénès, G., Milova, G. Madamba, M.C., Perfiliev, M., Structure and Ionic Transport of $PbSnF_4$ Superionic Conductor. *Solid State Ionics* **1996**, *86-88*, 77-82.

32. Mizusaki, J., Model for Solid Electrolyte Gas Electrode Reaction Kinetics; Key Concepts, Basic Model Construction, Extension of Models, New Experimental Techniques for Model Confirmation, and Future Prospects. *Electrochemistry* **2014,** *82* (10), 819-829.

33. Fujisaki, F.; Mori, K.; Yonemura, M.; Ishikawa, Y.; Kamiyama, T.; Otomo, T.; Matsubara, E.; Fukunaga, T., Mechanical Synthesis and Structural Properties of the Fast Fluoride-ion Conductor $PbSnF_4$. *J. Solid State Chem.* **2017,** *253*, 287-293.

34. Bard, A. J.; Faulkner, L. R., *Electrochemical Methods*. Wiley: New York, 2001.

35. Kato, Y.; Ishihara, T.; Ikuta, H.; Uchimoto, Y.; Wakihara, M., A High Electrode-Reaction Rate for High-Power-Density Lithium-Ion Secondary Batteries by the Addition of a Lewis Acid. *Angew. Chem., Int. Ed.* **2004,** *43* (15), 1966-1969.

36. Kato, Y.; Ishihara, T.; Uchimoto, Y.; Wakihara, M., Charge-transfer Reaction Rate of Li^+/Li Couple in Poly(ethylene glycol) Dimethyl Ether Based Electrolytes. *J. Phys. Chem. B* **2004,** *108* (15), 4794-4798.

37. Xu, J.; Farrington, G. C., A Microelectrode Study of Lithium Electrokinetics in Poly(ethylene glycol dimethyl ether) and 1,2-Dimethoxyethane. *J. Electrochem. Soc.* **2019,** *142* (10), 3303-3309.

38. Chiku, M.; Tsujiwaki, W.; Higuchi, E.; Inoue, H., Microelectrode Studies on Kinetics of Charge Transfer at an Interface of Li Metal and Li_2S-P_2S_5 Solid Electrolytes. *Electrochemistry* **2012,** *80* (10), 740-742.

39. Chiku, M.; Tsujiwaki, W.; Higuchi, E.; Inoue, H., Determination of the Rate-determining Step in the Electrochemical Oxidation of Li Metal at the Li Negative Electrode/Li_2S-P_2S_5 Solid Electrolyte Interface. *J. Power Sources* **2013,** *244*, 675-678.

40. Uchida, H.; Yoshida, M.; Watanabe, M., Effects of Ionic Conductivities of Zirconia Electrolytes on Polarization Properties of Platinum Anodes in Solid Oxide Fuel-cells. *J Phys. Chem.* **1995,** *99* (10), 3282-3287.

41. Uchida, H.; Yoshida, M.; Watanabe, M., Effect of Ionic Conductivity of Zirconia Electrolytes On The Polarization Behavior of Various Cathodes in Solid Oxide Fuel Cells. *J. Electrochem. Soc.* **1999,** *146* (1), 1-7.

42. Watanabe, M.; Uchida, H.; Yoshida, M., Effect of Ionic Conductivity of Zirconia Electrolytes on the Polarization Behavior of Ceria-Based Anodes in Solid Oxide Fuel Cells. *J. Electrochem. Soc.* **1997,** *144* (5), 1739-1743.

43. Takahashi, T.; Yamamoto, O., Polarization of the Solid-Electrolyte Cell $Ag/Ag_3SI/I_2$. *Electrochim. Acta* **1966,** *11* (7), 911-917.

Chapter 8 General Conclusion

All-solid-state fluoride-ion batteries (FIBs) exhibit highly potential as competitive candidates for next-generation energy storage devices, which is highly promising to achieve excellent energy densities that greatly exceed those of commercialized lithium-ion batteries (LIBs). In terms of several crucial problems related to further applications of all-solid-state FIBs, including phase-transition patterns, charge-compensation mechanism, and structural evolutions of typical cathode materials, as well as basic kinetics factors of electrolyte/electrode interfaces or electrolytes, various strategies have been pointedly proposed. Generally, comprehensive understandings on basic fluorination reactions are gained the by establishing effective models that facilitate the evaluation of electrochemical tests as well as phase-transition processes. Furthermore, high-energy cathode materials are designed and developed by employing multielectron fluorination reactions, upon which the cognations on the involvement of various cationic/anionic redox are expanded as well assisted by synchrotron-radiation X-ray spectroscopic techniques.

Herein, the results of the above discussion were summarized. In chapter 1, by introducing and comparing the respective working principles of LIBs and all-solid-state FIBs, the purpose, briefly, designing and studying Cu-based cathode material for all-solid-state FIBs, are presented. In Chapter 2 and 3, metal and metal-based nanocomposites were evaluated as excellent cathode materials for all-solid-state FIBs by thin-film models, where the two-phase reaction pattern is clearly proved by experimental evidence for the first time. In Chapter 4 to 6, the first uses of several Cu-based topotactic cathode materials for all-solid-state FIBs, including Cu_2O, Cu_3N and $Ca_{0.85}CuO_2$, are reported, where the electrochemical behaviors, charge-compensation mechanism and structural evolutions are studied in detail. In Chapter 7, based on β-$Pb_{0.78}Sn_{1.22}F_4$ system, the rate-determining factor for electrode/electrolyte interface reactions in all-solid-state FIBs is studied. The results strongly imply the high possibility to achieve superior rate capabilities in all-solid-state FIBs similar to those in all-solid-state LIBs. Prospects for the future developments of rechargeable all-solid-state FIBs are provided from diverse perspectives in each chapter as well.

List of publications

1. **Zhang, D.;** Yamamoto, K.*; Ochi, A.; Wang, Y.; Yoshinari, T.; Nakanishi, K.; Nakano, H.; Miki, H.; Nakanishi, S.; Iba, H.; Uchiyama, T.; Watanabe, T.; Amezawa, K.; Uchimoto, Y., Understanding the Reaction Mechanism and Performances of 3d Transition Metal Cathodes for All-solid-state Fluoride Ion Batteries. *J. Mater. Chem. A* **2021**, 9, 406-412. DOI: 10.1039/d0ta08824b. (**Chapter 2**)

2. **Zhang, D.;** Yoshinari, T.; Yamamoto, K.*; Kitaguchi, Y.; Ochi, A.; Nakanishi, K.; Miki, H.; Nakanishi, S.; Iba, H.; Watanabe, T.; Uchiyama, T.; Orikasa, Y.; Amezawa, K.; Uchimoto, Y., Cu–Pb Nanocomposite Cathode Material toward Room-temperature Cycling for All-solid-state Fluoride-ion Battery. *ACS Appl. Energy Mater.* **2021**, 4, 3352-3357. DOI: 10.1021/acsaem.0c03087. (**Chapter 3**)

3. **Zhang, D.;** Yamamoto, K.*; Wang, Y.; Gao, S.; Uchiyama, T.; Watanabe, T.; Takami, T.; Matsunaga, T.; Nakanishi, K.; Miki, H.; Iba, H.; Amezawa, K.; Maeda, K.; Kageyama, H.; Uchimoto, Y., Reversible and Fast (De)fluorination of High-capacity Cu_2O Cathode: One Step Toward Practically Applicable All-solid-state Fluoride-Ion Battery. *Adv. Energy Mater.* **2021**, in press. DOI: 10.1002/aenm.202102285. (**Chapter 4**)

4. **Zhang, D.;** Yamamoto, K.*; Gao, S.; Cao, Z.; Wang, Y.; Uchiyama, T.; Watanabe, T.; Matsunaga, T.; Takami, T.; Nakanishi, K.; Miki, H.; Iba, H.; Amezawa, K.; Maeda, K.; Kageyama, H.; Uchimoto, Y., High-energy Cu_3N Cathode Material Involving Nitrogen Redox for All-solid-state Fluoride-ion Batteries. *J. Am. Chem. Soc.* In revision. (**Chapter 5**)

5. **Zhang, D.;** Gao, S.; Cao, Z.; Wang, Y.; Uchiyama, T.; Nakanishi, K.; Matsunaga T.; Tassel, C.; Takami, T.; Watanabe, T.; Miki, H.; Iba, H.; Amezawa, K.; Maeda, K.; Kageyama, H.; Yamamoto, K.*; Uchimoto, Y., Understanding the Cationic/Anionic Redox of Topotactic $Ca_{0.85}CuO_2$ Cathode Materials for High-energy All-solid-state Fluoride-ion Batteries. *J. Am. Chem. Soc.* In revision. (**Chapter 6**)

6. **Zhang, D.;** Nakano, H.; Yamamoto, K.*; Tanaka, K.; Yahara, T.; Imai, K.; Mori, T; Miki, H.; Nakanishi, S.; Iba, H.; Watanabe, T.; Uchiyama, T.; Amezawa, K.; Uchimoto, Y., Rate-determining Process at Electrode/electrolyte Interfaces for All-

solid-state Fluoride-ion Batteries. *ACS Appl. Mater. Interfaces* **2021**, 13, 30198-30204. DOI: 10.1021/acsami.1c06947. (**Chapter 7**)

7. Yoshinari, T.[1]; **Zhang, D.[1] (co-first author);** Yamamoto, K.*; Kitaguchi, Y.; Ochi, A.; Nakanishi, K.; Miki, H.; Nakanishi, S.; Iba, H.; Uchiyama, T.; Watanabe, T.; Matsunaga, T.; Amezawa, K.; Uchimoto, Y., Kinetic Analysis and Alloy Designs for Metal/Metal Fluorides toward High Rate Capability for All-solid-state Fluoride Ion batteries. *J. Mater. Chem. A* **2021**, 9, 7018-7024. DOI: 10.1039/d0ta12055c.

8. Wang, Y.; Yamamoto, K.*; Tsujimoto, Y.; Matsunaga, T.; **Zhang, D.;** Cao, Z.; Nakanishi, K.; Uchiyama, T.; Watanabe, T.; Takami, T.; Miki, H.; Iba, H.; Maeda, K.; Kageyama, H.; Uchimoto, Y., Anion substitution at apical sites of Ruddlesden–Popper-type cathodes toward high power density for all-solid-state fluoride ion battery. *Chem. Mater.* **2022**, 34, 609-616. DOI: 10.1021/acs.chemmater.1c03189.

9. Zhang, C; Wei, B.; Wang, M.; Zhang, D.; Uchiyama, T.; Liang, C.; Chen, L.; Uchimoto, Y.; Zhang, R.; Wang, P.; Wei, W., Regulating oxygen covalent electron localization to enhance anionic redox reversibility of lithium-rich layered oxide cathodes. *Energy Storage Mater.* **2022**, 46, 515-522. DOI: 10.1016/j.ensm.2022.01.038.

10. Gao, S.; Tassel, C.; Broux, T.; Saito, T.; **Zhang, D.;** Yamamoto, K.; Yoruk, E.; Okada, K.; Kageyama, H., Na_3ZnH_5 – A sodium-conducting metal hydride antiperovskite. *Inorg. Chem.* **2021**, in revision.

Acknowledgement (致谢)

The ancients were often fascinated in watching the stars.

Since those stars are unknown and mysterious, it shall be worthy for the ancients to try to understand it. Similarly, since I doubt whether I possess the character of concentrating on something unknown, it is also worthy for me to dedicate my energetic days to this doctorate degree.

This is a quite tough process which relied on not only my own insistence, but also the support and care from my supervisor Professor Yoshiharu Uchimoto, who invited me to join his lab when I was confused to future choices at the end of my master's courses. He gave me sufficient guidance and provided us excellent experimental conditions during the past few years. Assistant professors, Kentaro Yamamoto and Tomoki Uchiyama, gave me a lot of helps in daily experiments. Senior/junior fellows, Yanchang Wang, Zulai Cao, and Yao Xiao also became my close comrades due to daily dining or hard nightshift experiments in synchrotron-radiation facility, SPring-8. Meanwhile, I sincerely appreciate Professor Weifeng Wei in State Key Laboratory of Powder Metallurgy, Central South University, and all members in his lab, for the comprehensive research skills and knowledges I have learned during my master's period, which really helped me a lot.

My parents, families, childhood friends, and Zhihong Zhong, Shuai Zhao, Jianling Liu, three friends in my university period, as well as *7-518* roommates, they have been supporting me during past few years. Affected by COVID-19 pandemic, it is a great pity that I cannot share joys nor difficulties they have encountered before. Gratefully, their loves can always heal me.

The greatest luck for me, is that I met my girlfriend, Shenghan, who is filling my life by her unconditional understands, supports, and loves. She is facing similar situations of chasing unknowns as I am; I have fallen into her beauty and kindness, as well as her knowledge and wisdom. It is a great honor for me to fight with her against future challenge, whatever the challenge is.

古人常观星入定。

因为星星未知且神秘，求之而不得的古人值得痴迷观星而忘我；因为想证明自己仍有能为未知事物而忘我的品质，在青春年华值得追求一个博士学位。

这个过程很累很难，不仅要自己咬牙坚持，亦承蒙太多人提携照顾：内本喜晴教授向硕士毕业时候有些迷茫的我发出邀请信，并在这几年里提供了耐心的指导、充分的支持和优良的实验条件。两位助教山本健太郎和内山智贵在日常科研生活中给予了诸多关照和帮助。几位师兄弟王彦昌、曹祖涞、肖遥则是同步辐射出差值夜班或是日常三餐的亲密战友。此时也越发感激中南大学粉末冶金国家重点实验室韦伟峰教授以及所有实验室成员，我硕士期间在那里获得的全方位的科研技能训练为我博士求学旅程助力颇多。

父母和家人，几位发小，大学同窗钟志洪、赵帅、刘渐陵，以及 7 舍 518 寝室所有成员，是我在异国读书的最大后盾。受新冠疫情影响，身为晚辈，却难以分担家人责任；身为人友，却错过许多他们的重要时刻。他们的爱与支持让我从不疲惫。

最大的幸运时遇到了我的女朋友高胜寒。她是对我充满理解、支持与爱的人生另一半。她和我走在同样的追求未知的道路上，我既沉迷于她的美丽与善良，也折服于她的学识与聪慧。能与她并肩战斗——既是对学问，也是对未来的生活——令我充满斗志。

We are pursuing those true knowledges that might not be so profound yet no one has ever cognized. We are just struggling to describe the “boundary” constrained by objective rules which have long been written in the freezing essence of the universe, so that we can understand the availability of our freedom. Coincidentally, this is consistent to the social behavior of human beings, namely, try to find how wild our freedom could be. The modern people chasing unknowns and those ancients watching the stars are sharing their minds and spirits.

Now, it seem that I start to know the core of “rules” or “boundaries”; this is the most valuable knowledge I have obtained during my doctoral studies. To become a Doctor of Philosophy, though I might never become a true philosopher, I luckily caught an enlightened moment. May this moment long last.

Having been fed by my motherland, including all tuition fees and scholarships for my master’s and doctoral studies, I can always freely plan my life and my study, like a light-hearted kid. Now, it is time to feed her back. How joyful it is!

The following professors, staffs and fellow students are acknowledged as well: Seunghoon Yang, Yadan Ren, Saeko Otani, Prof. Koji Nakanishi (SPring-8), Prof. Yoshiyuki Matsunaga, Dr. Toshiki Watanabe, Ms. Shigeki Shimura, Ms. Yumiko Saito, Ms. Yukiko Nakaji, Ms. Aki Gakiuchi, Dr. Xiao Gao, Dr. Takahiro Yoshinari, Dr. Yingying Zhou, Dr. Chen Liu, Dr. Feilure Tuerxun, Dr. Masakuni Takahashi, Hiroyuki Nakaki, Aika Ochi, Shuo Cao, Zhiwei Mu, Zhuoran Li, Xian Shi, Xiaohan Mei, Aierxiding, Weijie Cao, Wenli Pan, Yunfei Gao, et al.

我们在追求一些未必深奥却从未有人涉足的真知。那些客观规则早就写在了宇宙冰冷的肌理当中，我们只是尝试描画出这规则的边界，以便我们尽可能在允许范围内达到充分的自由：这与人类的宏观社会行为又是如此相似。从这个角度看，孜孜求索的今人，与观星入定的古人，心意一直相通。

如今，我似乎正在更加清晰地认识规则与边界，这是求学过程于我最大的意义。博士，虽并非博古通今之士，却也难得一刻精神的通透。愿此刻永恒。

我蒙受祖国的恩惠，一直无忧无虑读书至今，像一个自由散漫了很多年的孩子。如今终于能回头反哺母亲，幸甚！

同级生：梁胜勋、任亚丹、大谷纱惠子；课题组内外诸多教职员：中西康次先生（Spring-8）、松永利之先生、渡边稔树先生、志村滋子、斋藤裕美子、中路有希子、垣内亚希；诸多前辈后辈：高啸、吉成宏崇、周莹莹、刘辰、Tuerxun Feilure、高桥胜国、中木宽之、越智爱果、曹硕、母志为、李卓然、石现、梅笑寒、艾尔西丁、曹伟杰、潘雯丽、高云飞等，此处一并表示感谢。

Datong Zhang (張 大同),

in Kyoto University, November 2021

※著作権等

Understanding the reaction mechanism and performances of 3d transition metal cathodes for all-solid-state fluoride ion batteries
Datong Zhang,Kentaro Yamamoto, Aika Ochi, Yanchang Wang, Takahiro Yoshinari, Koji Nakanishi, Hiroyuki Nakano, Hidenori Miki, Shinji Nakanishi, Hideki Iba, Tomoki Uchiyama, Toshiki Watanabe, Koji Amezawa and Yoshiharu Uchimoto
Journal of Materials Chemistry A, 2021, 9, 406-412.
doi: 10.1039/d0ta08824b

Cu-Pb Nanocomposite Cathode Material toward Room-Temperature Cycling for All-Solid-State Fluoride-Ion Batteries
Datong Zhang, Takahiro Yoshinari, Kentaro Yamamoto, Yuya Kitaguchi, Aika Ochi, Koji Nakanishi, Hidenori Miki, Shinji Nakanishi, Hideki Iba, Toshiki Watanabe, Tomoki Uchiyama, Yuki Orikasa, Koji Amezawa, and Yoshiharu Uchimoto
ACS Applied Energy Materials, 2021, 4, 3352-3357
doi: 10.1021/acsaem.0c03087

Reversible and Fast (De)fluorination of Cu2O Cathode Material: One Step toward Practical Application
Datong Zhang, Kentaro Yamamoto, Yanchang Wang, Shenghan Gao, Tomoki Uchiyama, Toshiki Watanabe, Tsuyoshi Takami, Toshiyuki Matsunaga, Koji Nakanishi, Hidenori Miki, Hideki Iba, Koji Amezawa, Kazuhiko Maeda, Hiroshi Kageyama, Yoshiharu Uchimoto
Advanced Energy Materials, 2021, Accepted
doi: 10.1002/aenm.202102285

Rate-determining Process at Electrode /electrolyte Interfaces of All-solid-state Fluoride-ion Batteries
Datong Zhang, Hiroyuki Nakano, Kentaro Yamamoto, Kenta Tanaka, Tatsuma Yahara, Kazuyuki Imai, Takuya Mori, Hidenori Miki, Shinji Nakanishi, Hideki Iba, Toshiki Watanabe, Tomoki Uchiyama, Koji Amezawa, and Yoshiharu Uchimoto
ACS Applied Materials & Interfaces, 2021, 13, 30198-30204
doi: 10.1021/acsami.1c06947